January 2011

Aerosol Route Synthesis and Applications of Doped Nanostructured Materials

Manoranjan Sahu
Washington University in St. Louis

WASHINGTON UNIVERSITY IN SAINT LOUIS

School of Engineering and Applied Science

Department of Energy, Environmental & Chemical Engineering

Dissertation Examination Committee:

Pratim Biswas, Chair
Da-Ren Chen
Young-Shin Jun
Günter Oberdörster
Sankar M. L. Sastry
Yinjie Tang

Aerosol Route Synthesis and Applications of Doped Nanostructured Materials

by

Manoranjan Sahu

A dissertation presented to the Graduate School of Arts and Sciences of Washington University in partial fulfillment of the requirements for the degree of Doctor of Philosophy

August, 2011

Saint Louis, MO

Abstract of Dissertation

Aerosol Route Synthesis and Applications of Doped Nanostructured Materials

by

Manoranjan Sahu

Doctor of Philosophy in Energy, Environmental and Chemical Engineering

Washington University in St. Louis, 2011

Professor Pratim Biswas, Chairperson

Nanotechnology presents an attractive opportunity to address various challenges in air and water purification, energy, and other environment issues. Thus, the development of new nanoscale materials in low-cost scalable synthesis processes is important. Furthermore, the ability to independently manipulate the material properties as well as characterize the material at different steps along the synthesis route will aide in product optimization. In addition, to ensure safe and sustainable development of nanotechnology applications, potential impacts need to be evaluated. In this study, nanomaterial synthesis in a single-step gas phase reactor to continuously produce doped metal oxides was demonstrated. Copper-doped TiO_2 nanomaterial properties (composition, size, and crystal phase) were independently controlled based on nanoparticle formation and growth mechanisms dictated by process control parameters. Copper dopant found to significantly affect TiO_2 properties such as particle size, crystal phase, stability in the suspension, and absorption spectrum (shift from UV to visible light absorption). The *in-situ* charge distribution characterization of the synthesized nanomaterials was carried out

by integrating a tandem differential mobility analyzer (TDMA) set up with the flame reactor synthesis system. Both singly- and doubly- charged nanoparticles were measured, with the charged fractions dependent on particle mobility and dopant concentration. A theoretical calculation was conducted to evaluate the relative importance of the two charging mechanisms, diffusion and thermo-ionization, in the flame. Nanoparticle exposure characterization was conducted during synthesis as a function of operating condition, product recovery and handling technique, and during maintenance of the reactors. Strategies were then indentified to minimize the exposure risk. The nanoparticle exposure potential varied depending on the operating conditions such as precursor feed rate, working conditions of the fume hood, ventilation system, and distance from the reactors. Nanoparticle exposure varied during product recovery and handling depending on the quantity of nanomaterial handled. Most nanomaterial applications require nanomaterials to be in solution. Thus, the role of nanomaterial physio-chemical properties (size, crystal phase, dopant types and concentrations) on dispersion properties was investigated based on hydrodynamic size and surface charge. Dopant type and concentration were found to significantly affect iso-electric point (IEP)-shifting the IEP to a high or lower pH value compared to pristine TiO_2 based on the oxidation state of the dopant. The microbial inactivation effectiveness of as-synthesized nanomaterials was investigated under different light irradiation conditions. Microbial inactivation was found to strongly depend on the light irradiation condition as well as on material properties such chemical composition, crystal phase, and particle size. The potential interaction mechanisms of copper-doped TiO_2 nanomaterial with microbes were

also explored. The studies conducted as part of this dissertation addressed issues in nanomaterial synthesis, characterization and their potential environmental applications.

Acknowledgements

I sincerely thank my advisor Professor Pratim Biswas (EECE) for providing me the wonderful opportunity to work in his research group. His guidance and enthusiastic research approach and never ending support helped me to complete this dissertation. I am grateful that he continuously encouraged excellence and independent thinking, and for the confidence he showed in me throughout these years. I would like to acknowledge Professors Sankar M. L Sastry (MACE) and Yinjie Tang (EECE) for their insightful discussions during different stages of my research work. I am especially grateful to have had the opportunity to collaborate with Professor Tang, for my microbial inactivation studies. I also thank Professors Guntur Oberdorster (U. Rochester) and Young-Shin Jun (EECE), Da-Ren Chen (EECE) Chen for their insightful discussions during the preparation of this dissertation.

I am thankful to my colleagues in the Aerosol & Quality Research Laboratory (AAQRL) for providing a stimulating work environment and for their help during my research. I would particularly like to thank Woo-Jin An, Michael Daukoru, Luis-Modesto Lopez, Soubir Basak, and all former and present members for their friendship and countless discussions. I would like to acknowledge all my friends in EECE and other departments. Particularly, I would like to thank Biplab Mukherjee, Abhas Singh, and Hare Kirshna for their friendship. I would like to thank Vikram Govindan for his friendship and kind help in many aspects during my stay in St. Louis. Special thanks to my friends in India, especially Patitapaban Das and Prashant Padhy for their friendship and never ending support throughout my life. I am also thankful to the staff of the EECE

department-Rose Baxter, Kim Coleman, Trisha Sutton, and Beth Mehringer-for all their support during my studies at Washington University.

I gratefully acknowledge financial support from the McDonnell Internationals' Scholars Academy at Washington University in St. Louis, the McDonnell Academy Global Energy and Environmental Partnership (MAGEEP) at Washington University in St. Louis, DOD-MURI grant UR523873, and NIEHS grant - 100030N.

Finally, I would like to thank my family for their understanding, constant encouragement, and continuous support during these years that I have been away from them.

Table of Contents

List of Figures

Chapter-1

Chapter-2

Chapter- 3

Chapter- 4

Chapter-5

Chapter-6

Chapter-7

Appendix-A

Appendix-B

Appendix-C

List of Tables

Chapter 1:

Introduction

1.1. An overview: Nanotechnology

Nanotechnolgy presents exciting approaches to overcome challenges in energy and the environmental sectors. It is also expected to have a great impact in electronic and medical applications. To fully realize the benefits of nanotechnology applications and to ensure their safe and sustainable development, potential impacts need to be evaluated. This dissertation addresses different challenges of nanoparticle technology, which are discussed in detail in the various chapters of this dissertation.

1.2. Background and Motivation

Nanotechnolgy has significantly advanced in a wide range of applications, such as electronics, medicine, energy, the environment, and a variety of consumer products. Nanotechnology is expected to rise far beyond the current use, and is projected to be a market of $1 trillion by 2015 [1, 2] . Nanoparticles (at least one dimension ranging from a few to several hundred nanometers) are the building blocks for all applications and they have markedly different physico-chemical properties than their bulk counterpart.

The determining factors for optimal application of nanomaterials are their size, shape, crystal phase, purity, doping species and concentration of dopant. TiO_2 is one example of a nanomaterial that has varied applications. The anatase phase of TiO_2 has higher photocatalytic activity than the rutile phase. For photo-catalytic applications, TiO_2 particles ranging from 25 to 40 nm are desirable [3], whereas for paint and pigment applications, the rutile phase of TiO_2 between 190-200 nm is preferable. Several studies

have reported that optimum loading of doping species increases photo-reactivity [4]. The electronic properties of nanomaterials also depend on the size of the particle [5, 6].

The research work in this dissertation is mainly focused on titanium dioxide, a semiconducting material, widely used in a range of applications such as air and water purification, toxic metal capture, CO_2 photo-reduction, destruction of bacteria and viruses, self cleaning building materials and photo-catalysis reactions. TiO_2 is one of the most widely used photo-catalyst because it is relatively safe, inexpensive and resists photo-corrosion. Despite the numerous applications of TiO_2 nanomaterials, some of the property limitations need to be overcome before TiO_2 can be used on a larger scale. First, TiO_2 requires near ultraviolet light energy ($\lambda < 380$ nm) for activation. Second, the relatively low quantum efficiency of the catalyst is due to fast electron and hole pair recombination need to be overcome.

Several approaches have been pursued to improve the material properties of TiO_2 including size optimization [7], compositional optimization to make suboxides [8], surface modification and doping [9-11]. Among these strategies, one promising approach is doping with foreign impurities to change the structure. Reports suggest that dopant addition enhances photoreactions as well as modifies material properties such as size and crystal structure. Dopant addition also shifts the absorption to the visible wavelengths by substituting Ti in the substitutional sites or in the interstitial sites. Dopant effects on properties of nanosized titania are not well understood. In addition, synthesis methods for doped nanomaterials with independent control of composition, size, crystal phase, and morphology have not been demonstrated. Cu-doped TiO_2 nanomaterials are the main

focus in this research work, as these materials have shown promising results in improving photocatalytic efficiency and in solar energy applications [12]. Cu-doped TiO_2 has also shown improved photocatalytic degradation [13-16], CO_2 photoreduction [17-19], and improved gas sensing [20, 21].

One research challenge is developing a readily controllable process to synthesize a wide spectrum of stable, functional, highly pure nanomaterials with well controlled properties (size, composition, crystal phase, morphology, reactivity, etc.). Developing and optimizing the synthesis process to produce large quantities of high quality materials in a low-cost scalable synthesis process requires a rigorous understanding of the underlying physical and chemical mechanisms. The use of well designed experimental systems helps in the better understanding of the material processing parameters, and nanoparticle formation pathways.

Several methods have been adopted for synthesis of pristine and doped nanomaterials. These methods include: sol gel [22-24], co-precipitation [25], mechanical alloying [15], hydrothermal [26], solvothermal, sonochemical, and photo reduction [14]. Sol-gel techniques have been used by many researchers to synthesize pristine and doped materials. It involves multiple steps such hydrolysis, drying, pulverization, and calcinations [27]. Moreover, in all the aforementioned methods, it has been difficult to synthesize material on the nanoscale level, in a predictable and intentional way, while controlling for the desired size, shape, composition, and crystal phase. Furthermore, these synthesis processes require multiple steps for preparation and are time consuming.

Gas phase synthesis methods have an advantage over other methods because of its relative ease in controlling the particle size, crystallinity, homogeneity, and degree of agglomeration [28]. Also gas phase synthesis processes are continuous, while liquid phase synthesis and mechanical alloying are batch processes with a possible variation in material properties from batch to batch. Gas phase techniques adopted for synthesizing nanomaterials include furnace aerosol reactor [29, 30], plasma reactors, laser ablation, flame aerosol reactor [31-33]. Although several synthesis methods have been demonstrated, the potential factors affecting the nanoparticle properties during the production process of both pristine and doped nanomaterials are still not fully understood. Flame aerosol reactors (FLAR) have been widely used to synthesize nanomaterials [31, 32] and also used to prepare nanostructured film for solar energy applications [33, 34]. Flame synthesis process achieves the desired properties of the nanomaterials in a single-step unlike the sol gel process. Also unlike other processes, doped particles from a FLAR can be expected to be uniformly distributed due to excellent mixing of the precursor vapors at the molecular level. Moreover, the aerosol reactor can be scaled up to synthesize large quantities of nanomaterials with controlled characteristics [35, 36]. A systematic study of the synthesis of pristine and doped nanomaterials in the FLAR would require a thorough understanding of the role of different process parameters such as feed rate, reaction environment, residence time, and doping concentration, in controlling the different physical and chemical properties of the nanomaterials, which is investigated in this dissertation.

During the high temperature synthesis, particles are charged by ions generated through chemi-ionization process, by diffusion as well as thermionic charging [32, 37-39]. Particle charging may depend on factors such as flame temperature, flame structure, mixing of the reactants, and material properties such as particle size, crystal structure, and composition. There is a need to investigate the charging characteristics of particles during the synthesis, as charge on particles strongly affect the coagulation process, influences the particle motion, and deposition pattern on substrate [40, 41]. Apart from influencing the particle properties, charge on particles affects sampling, transport, and capture [39, 42]. Magnitude of charge significantly affect the inhaled aerosol deposition in the lungs [43]. It is of practical importance to study particle charge effect on the relationship between nanoparticle exposure and lung uptake. Well designed charge characterization methodologies to measure the magnitude of charge and key parameters that govern the charging mechanisms need to be explored at different flame operating conditions. A detailed understanding of nanoparticle charge will help in accurately assess the role of charge in particle synthesis, fabricating nano-devices, measurement, and control of such particles in both fundamental and applied nanotechnology research

During synthesis in gas phase reactors, particle leakage and dispersion into the work environment may occur, exposing workers to the potentially harmful effects of these fugitive particles. Due their small size and large surface area, nanoparticles may penetrate the epithelial cells, enter the blood stream and can even move to the brain through the olfactory nerves, adversely affecting health [44]. A strong dose-response relationship was observed between particle concentration and pulmonary inflammatory

responses [45]. Many studies have reported that potential toxic effects also depend on the particle size, crystal phase composition, and chemical composition [46]. Such concerns have resulted in many groups raising issues of "safe nanotechnology", and prompted strategies to address health and safety aspects simultaneously with the adaptation of nanotechnology [9, 47, 48]. Well designed exposure assessment studies are needed for a better understanding of the health effects caused by exposure to nanoparticles, and cost effective control measures are to reduce exposure. The exposure characterization during different stages of the processing of the materials will provide guidelines to minimize the exposure risks that arise.

In parallel, accurately characterizing nanomaterials at different steps upon application, and fundamentally exploring the physical and chemical principle that determine the functionality need to be carefully considered. Changes in nanomaterial properties under different application conditions will play a crucial role in determining their performance. For example, when either released to the environment or applied as a solution, nanoparticles tend to agglomerate. Their surface is also modified by factors such as their size, shape, crystal structure, and functionalization and by environmental parameters such as pH and ionic strength [49-51]. A detailed characterization of nanoparticles dispersed in aqueous suspension and the factors affecting the dispersion behavior is critical in understanding their toxicological and photo-catalytic applications, and their environmental fate and transport behavior. Therefore, characterization methods and testing protocols must be developed to continually improve our fundamental

understanding of the structure-function relationships during different stages of nanomaterials application (e.g. as produced, as administered).

In addition, doped nanomaterial properties must be correlated with their application for optimal design of the materials, which is lacking for doped TiO_2 materials due to the unavailability of nanostructured materials with precisely controlled properties. Based on the above understanding, tailoring and exploiting the material properties for enhanced performance are essential. In this work, as-synthesized Cu-doped TiO_2 nanomaterials were applied to explore their potential anti-microbial activity and their interaction mechanisms with microbes.

1.3. Objectives

The goals, research approach, and applications explored in this study are shown in Figure 1-1. This study develops a thorough understanding of the formation of nanostructured materials with independently controlled properties. It characterizes the nanomaterials in depth at the different stages of their applications. Finally, it correlates their material properties with microbial inactivation potential and investigates interaction mechanisms. This dissertation focuses on the synthesis of TiO_2 and Cu-doped TiO_2 nanomaterials. A rigorous characterization methodology is adopted along with *in-situ* exposure characterization to simulate real life exposure scenarios of nanoparticles. The specific objectives are given below:

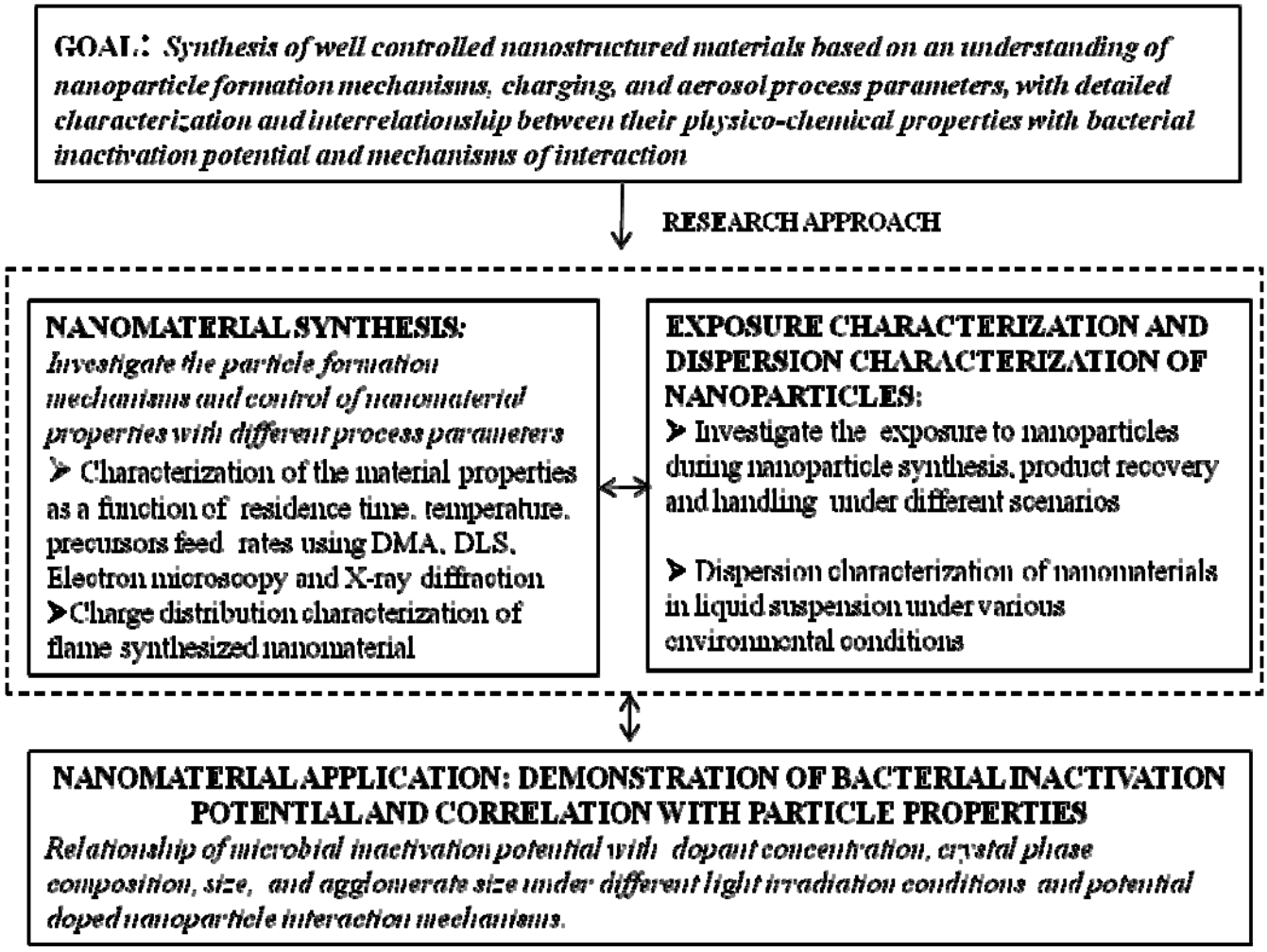

Figure 1- 1: Overview of research conducted in the dissertation

1) Process development for doped TiO_2 nanomaterial synthesis using a flame aerosol reactor (FLAR). It involves studying nanoparticles formation mechanisms and the influence of dopant on TiO_2 nanomaterial properties. The focus is on processing Cu-doped TiO_2 nanomaterials.

2) Synthesis of nanoparticles with independently controlled material properties such as composition, size, crystal phase, and morphology. This synthesis is based on an understanding of the key process parameters and nanoparticle formation mechanisms.

3) Development of an *in-situ* characterization methodology for measuring the charge distribution of the flame synthesized nanoparticles and understanding the charging mechanisms at different flame operating conditions.

4) Development of an exposure characterization methodology and quantification of exposure to nanoparticles during synthesis, during maintenance in gas phase reactors, and during product recovery and handling under different scenarios.

5) Characterization of the nanoparticles dispersion properties in water under different environmental conditions and for different physio-chemical properties.

6) Demonstration of the application of Cu-doped TiO_2 material for microbial inactivation. Exploration of potential interaction mechanisms, and their correlation with physio-chemical properties.

In summary, this dissertation addresses different research needs in nanomaterial synthesis, characterization, aggregation behavior in suspension and application for microbial inactivation. More details about the knowledge gaps and research approaches are given in the individual chapters.

1.4. Dissertation Layout

TiO_2 based nanomaterials are widely used as they are cheap and stable in adverse environmental conditions. These semiconductor metal oxides are produced in tons for various applications. Methodologies to synthesize well controlled Cu-doped TiO_2 nanomaterials are demonstrated in a single-step gas phase reactor. Detailed *in-situ* charge characterization and exposure characterization were conducted during various operations during synthesis. Several approaches were adopted for post synthesis characterization of nanoparticle to relate their application performance with properties. The studies performed as part of this dissertation were aimed to address questions on the synthesis, characterization, and application of doped TiO_2 nanomaterials. An overview of nanotechnology applications and challeneges are discussed in Chapter-1 followed by a detailed understanding of the nanomaterial synthesis in a single-step flame aerosol reactor in Chapter-2. In addition to synthesis, a detailed *in-situ* characterization methodology (Chapter-3) was undertaken to measure the charge distribution characteristics and nanoparticle exposure (Chapter-4) during different operating conditions in flame aerosol reactor. Post synthesis characterization of nanoparticle suspension was carried out in DI water to understand the surface charge and agglomeration behavior (Chaper-5). The as-synthesized doped nanomaterials were applied for microbial inactivation and relationship with physio-chemical properties of nanomaterials were established (Chapter-6, 7). A detailed summary of each chapter is discussed as below.

Chapter 2 discusses the synthesis of doped TiO_2 nanomaterials in a single-step process. A detailed investigation of the particle formation mechanisms and characterization were undertaken that allowed understanding the dopant effect on TiO_2 material properties such as size, crystal phase composition, stability in suspension and optical absorption. This flame synthesis method was also used to make V-doped TiO_2 material. The effect of annealing conditions on Cu-doped TiO_2 nanomaterial properties such as size, crystal phase, and absorption was also investigated.

Chapter 3 addresses the charge distribution of flame synthesized nanoparticles, and establishes a fundamental understanding of the two important charging mechanisms that interplay during the flame synthesis process (diffusion charging and thermo-ionization charging). The charge carried by nanoparticles during synthesis is important for nanoparticle transport, sampling, and deposition to make nanodevices. Different size particles that carry charges of both the polarities (positive and negative) in flame synthesis conditions are explored by using a differential mobility analyzer (DMA) and a tandem differential mobility analyzer (TDMA). Numerical calculations were done to identify the dominant charging mechanism at different flame operating parameters. This nanoparticle charging understanding can be extended to develop better charging to capture ultrafine aerosols.

Exposure assessment of nanoparticles is very important in the different life cycle stages of the material. During generation and production, nanoparticles can enter the working environment and pose health hazards after long term exposure. Chapter 4 presents exposure characterization methodologies and discusses the quantification of

exposure during production, product handling and recovery, and during the maintenance of gas phase reactors. The results from this study provide guidelines to minimize exposure during operation of reactors during synthesis and in other operations.

The aggregation potential and surface charge of doped nanoparticles in a liquid suspension are discussed in Chapter 5. Most nanomaterials are dispersed in liquid suspension before application. However, the nanomaterials tend to agglomerate based on altered surface charge, which finally influences their performance. The agglomeration and state of the material in suspension depend on environmental factors such as pH, ionic strength, etc. and on physio-chemical parameters such as size, crystal phase and composition, and dopant types and concentrations. The aggregation behavior is discussed for three types of doped TiO_2 nanomaterials: Cu-doped TiO_2, V-doped TiO_2 and Pt-doped TiO_2.

Nanomaterial applications depend mainly on size, composition, crystal phase and morphology. Chapters 6, 7 delineate how the composition, crystal phase, and size of Cu-doped TiO_2 affect bacterial inactivation potential for both gram positive and gram negative environmental microorganisms under different light irradiation conditions. Doped nanoparticle interaction mechanisms are explored in detail along with the agglomeration behavior of the materials in suspension. This study demonstrates that doped nanomaterials can be effectively used as antibacterial agents for water and waste water treatment. Chapter 7 summarizes the major conclusions of this dissertation and discusses its future directions and broader implications.

The experimental set ups and supporting calculation are presented in Appendix-A. The exposure potential to ultrafine particles in the outdoor environment and their chemical compositions are discussed in Appendix-C. A detailed receptror modeling approach using both positive matric factolization (PMF) and UNMIX were undertaken to separate the emissions from gasoline vehile sources from diesel vehicle sources. Finally, Appendix-D summarizes my curriculum vitae at the time of completion of this dissertation.

1.5. References

1. Maynard, A.D., *Nanotechnology: The next big thing, or much ado about nothing?* Annals of Occupational Hygiene, 2007. **51**(1): p. 1-12.
2. Nel, A., T. Xia, L. Madler, and N. Li, *Toxic potential of materials at the nanolevel.* Science, 2006. **311**(5761): p. 622-627.
3. Almquist, C.B. and P. Biswas, *Role of synthesis method and particle size of nanostructured TiO_2 on its photoactivity.* Journal of Catalysis, 2002. **212**(2): p. 145-156.
4. Choi, W.Y., A. Termin, and M.R. Hoffmann, *The Role of Metal-Ion Dopants in Quantum-Sized TiO_2 - Correlation between Photoreactivity and Charge-Carrier Recombination Dynamics.* Journal of Physical Chemistry, 1994. **98**(51): p. 13669-13679.
5. Grassian, V.H., *When Size Really Matters: Size-Dependent Properties and Surface Chemistry of Metal and Metal Oxide Nanoparticles in Gas and Liquid Phase Environments.* Journal of Physical Chemistry C, 2008. **112**(47): p. 18303-18313.
6. Jiang, J., D.R. Chen, and P. Biswas, *Synthesis of nanoparticles in a flame aerosol reactor with independent and strict control of their size, crystal phase and morphology.* Nanotechnol., 2007. **18**(28): p. 285603.

7. Gao, L. and Q.H. Zhang, *Effects of amorphous contents and particle size on the photocatalytic properties of TiO_2 nanoparticles.* Scr. Mater., 2001. **44**(8-9): p. 1195-1198.
8. Dhumal, S.Y., T.L. Daulton, J. Jiang, B. Khomami, and P. Biswas, *Synthesis of visible light-active nanostructured TiOx (x < 2) photocatalysts in a flame aerosol reactor.* Applied Catalysis B-Environmental, 2009. **86**(3-4): p. 145-151.
9. *Approach to Nanomaterial ES&H Department of Energy Nanoscale Science Research Centers, NSRC Revision 2. 6/15/07*. 2006.
10. Asahi, R., T. Morikawa, T. Ohwaki, K. Aoki, and Y. Taga, *Visible-light photocatalysis in nitrogen-doped titanium oxides.* Science, 2001. **293**(5528): p. 269-271.
11. Wang, Z.M., G.X. Yang, P. Biswas, W. Bresser, and P. Boolchand, *Processing of iron-doped titania powders in flame aerosol reactors.* Powder Technol., 2001. **114**(1-3): p. 197-204.
12. Mor, G.K., O.K. Varghese, R.H.T. Wilke, S. Sharma, K. Shankar, T.J. Latempa, K.S. Choi, and C.A. Grimes, *p-Type Cu-Ti-O Nanotube Arrays and Their Use in Self-Biased Heterojunction Photoelectrochemical Diodes for Hydrogen Generation (vol 8, pg 1906, 2008).* Nano Letters, 2008. **8**(10): p. 3555-3555.
13. Li, G.H., N.M. Dimitrijevic, L. Chen, T. Rajh, and K.A. Gray, *Role of Surface/Interfacial Cu^{2+} Sites in the Photocatalytic Activity of Coupled CuO-TiO_2 Nanocomposites.* Journal of Physical Chemistry C, 2008. **112**(48): p. 19040-19044.
14. Xu, Y., D. Liang, M. Liu, and D. Liu, *Preparation and characterization of Cu_2O–TiO:Efficient photocatalytic degradation of methylene blue.* Materials Research Bulletin, 2008. **43**: p. 3474–3482.
15. Park , H.S., D.H. Kim, S.J. Kim, and K.S. Lee, *The photocatalytic activity of 2.5 wt% Cu-doped TiO_2 nano powders synthesized by mechanical alloying.* Journal of Alloys and Compounds 2006. **415**: p. 51–55.
16. Arana, J., J.M. Dona-Rodriguez, O. Gonzalez-Diaz, E.T. Rendon, J.A.H. Melian, G. Colon, J.A. Navio, and J.P. Pena, *Gas-phase ethanol photocatalytic degradation*

study with TiO_2 doped with Fe, Pd and Cu. Journal of Molecular Catalysis a-Chemical, 2004. **215**(1-2): p. 153-160.

17. Tseng, I.H., J.C.S. Wu, and H.Y. Chou, *Effects of sol-gel procedures on the photocatalysis of Cu/TiO_2 in CO_2 photoreduction.* Journal of Catalysis, 2004. **221**(2): p. 432-440.
18. Li, Y., W.N. Wang, Z. Zhan, M.H. Woo, C.Y. Wu, and P. Biswas, *Photocatalytic reduction of CO_2 with H_2O on mesoporous silica supported Cu/TiO_2 catalysts.* Appl. Catal., B, 2011. **100**: p. 386-392.
19. Wang, W.-N., J. Park, and P. Biswas, *Rapid synthesis of nanostructured $Cu–TiO_2–SiO_2$ composites for CO_2 photoreduction by evaporation driven self-assembly.* Catalysis Science & Technology, 2011.
20. Ruiz, A.M., A. Cornet, and J.R. Morante, *Study of La and Cu influence on the growth inhibition and phase transformation of nano-TiO_2 used for gas sensors.* Sensors and Actuators B-Chemical, 2004. **100**(1-2): p. 256-260.
21. Teleki, A., N. Bjelobrk, and S.E. Pratsinis, *Flame-made Nb- and Cu-doped TiO_2 sensors for CO and ethanol.* Sensors and Actuators B-Chemical, 2008. **130**(1): p. 449-457.
22. Bhattacharyya, K., S. Varma, A.K. Tripathi, S.R. Bharadwaj, and A.K. Tyagi, *Effect of Vanadia Doping and Its Oxidation State on the Photocatalytic Activity of TiO_2 for Gas-Phase Oxidation of Ethene.* J. Phys. Chem. C 2008. **112**(112): p. 19102–19112.
23. Yang, X., C. Cao, K. Hohn, L. Erickson, R. Maghirang, D. Hamal, and K. Klabunde, *Highly visible-light active C- and V-doped TiO_2 for degradation of acetaldehyde.* Journal of Catalysis, 2007. **252**(2): p. 296-302.
24. Tian, Z.M., S.L. Yuan, S.Y. Yin, S.Q. Zhang, H.Y. Xie, J.H. Miao, Y.Q. Wang, J.H. He, and J.Q. Li, *Synthesis and magnetic properties of vanadium doped anatase TiO2 nanoparticles.* Journal of Magnetism and Magnetic Materials, 2008. **320**: p. L5–L9

25. Carotta, M.C., V. Guidia, M. Malag, B. Vendemiatia, A. Zannia, G. Martinelli, M. Sacerdoti, S. Licoccia, M.L.D. Vona, and E. Traversa, *Vanadium and tantalum-doped titanium oxide (TiTaV): a novel material for gas sensing.* Sensors and Actuators B 2005. **108**: p. 89–96.
26. Chen, X. and S.S. Mao, *Titanium Dioxide Nanomaterials: Synthesis, Properties, Modifications, and Applications.* Chem. Rev., 2007. **107**(7): p. 2891-2959.
27. Zaleska, A., *Doped TiO2-A review.* Recent Patents in Enginering, 2008. **2**: p. 157-164.
28. Kruis, F.E., H. Fissan, and A. Peled, *Synthesis of nanoparticles in the gas phase for electronic, optical and magnetic applications - A review.* Journal of Aerosol Science, 1998. **29**(5-6): p. 511-535.
29. Basak, S., K.S. Rane, and P. Biswas, *Hydrazine-assisted, low-temperature aerosol pyrolysis method to synthesize gamma-Fe_2O_3.* Chemistry of Materials, 2008. **20**(15): p. 4906-4914.
30. Namiki, N., K. Cho, P. Fraundorf, and P. Biswas, *Tubular reactor synthesis of doped nanostructured titanium dioxide and its enhanced activation by coronas and soft X-rays.* Industrial & Engineering Chemistry Research, 2005. **44**(14): p. 5213-5220.
31. Tiwari, V., J. Jiang, V. Sethi, and P. Biswas, *One-step synthesis of noble metal-titanium dioxide nanocomposites in a flame aerosol reactor.* Applied Catalysis a-General, 2008. **345**(2): p. 241-246.
32. Jiang, J., D.R. Chen, and P. Biswas, *Synthesis of nanoparticles in a flame aerosol reactor with independent and strict control of their size, crystal phase and morphology.* Nanotechnology, 2007. **18**(28).
33. Wang, Z.M., G.X. Yang, P. Biswas, W. Bresser, and P. Boolchand, *Processing of iron-doped titania powders in flame aerosol reactors.* Powder Technology, 2001. **114**(1-3): p. 197-204.
34. Thimsen, E., P. Biswas, and *Nanostructured photoactive films synthesized by a flame aerosol reactor.* Aiche Journal, 2007. **53**(7): p. 1727-1735.

35. Wegner, K. and S.E. Pratsinis, *Gas-phase synthesis of nanoparticles: scale-up and design of flame reactors.* Powder Technology, 2005. **150**(2): p. 117-122.
36. Wegner, K. and S.E. Pratsinis, *Scale-up of nanoparticle synthesis in diffusion flame reactors.* Chemical Engineering Science, 2003. **58**(20): p. 4581-4589.
37. Kim, S.H., K.S. Woo, B.Y.H. Liu, and M.R. Zachariah, *Method of measuring charge distribution of nanosized aerosols.* Journal of Colloid and Interface Science, 2005. **282**(1): p. 46-57.
38. Jiang, J., M.H. Lee, and P. Biswas, *Model for nanoparticle charging by diffusion, direct photoionization, and thermionization mechanisms.* Journal of Electrostatics, 2007. **65**(4): p. 209-220.
39. Jiang, J.K., C.J. Hogan, D.R. Chen, and P. Biswas, *Aerosol charging and capture in the nanoparticle size range (6-15 nm) by direct photoionization and diffusion mechanisms.* Journal of Applied Physics, 2007. **102**(3): p. -.
40. Kim, H., J. Kim, H.J. Yang, J. Suh, T. Kim, B.W. Han, S. Kim, D.S. Kim, P.V. Pikhitsa, and M. Choi, *Parallel patterning of nanoparticles via electrodynamic focusing of charged aerosols.* Nature Nanotechnology, 2006. **1**(2): p. 117-121.
41. Modesto-Lopez, L.B., E.J. Thimsen, A.M. Collins, R.E. Blankenship, and P. Biswas, *Electrospray-assisted characterization and deposition of chlorosomes to fabricate a biomimetic light-harvesting device.* Energy & Environmental Science, 2010. **3**(2): p. 216-222.
42. Kulkarni, P., N. Namiki, Y. Otani, and P. Biswas, *Charging of particles in unipolar coronas irradiated by in-situ soft X-rays: enhancement of capture efficiency of ultrafine particles.* Journal of Aerosol Science, 2002. **33**(9): p. 1279-1296.
43. Vincent, J.H., *On the practical signicance of electrostatic lung deposition of isomeric and 9brous aerosols.* Journal of Aerosol Science, 1985. **16**: p. 511–51.
44. Oberdorster, G., Z. Sharp, V. Atudorei, A. Elder, R. Gelein, W. Kreyling, and C. Cox, *Translocation of inhaled ultrafine particles to the brain.* Inhalation Toxicology, 2004. **16**(6-7): p. 437-445.

45. Oberdorster, G., J. Finkelstein, J. Ferin, J. Godleski, L.Y. Chang, R. Gelein, C. Johnston, and J.D. Crapo, *Ultrafine particles as a potential environmental health hazard - Studies with model particles.* Chest, 1996. **109**(3): p. S68-S69.
46. Jiang, J., G. Oberdorster, A. Elder, R. Gelein, P. Mercer, and P. Biswas, *Does nanoparticle activity depend upon size and crystal phase?* Nanotoxicology, 2008. **2**(1): p. 33-42.
47. *Exposure assessment methods: Research needs and priorities : NIOSH Report*. 2002.
48. Clarence, D.J., *Managing the effects of nanotechnology, Washington D.C Project on Emerging Nanotechnologies.* Woodrow Wilson International Center for Scholars 2008.
49. Jiang, J.K., G. Oberdorster, and P. Biswas, *Characterization of size, surface charge, and agglomeration state of nanoparticle dispersions for toxicological studies.* Journal of Nanoparticle Research, 2009. **11**(1): p. 77-89.
50. Mukherjee, B. and J.W. Weaver, *Aggregation and charge behavior of metallic and nonmetallic nanoparticles in the presence of competing similarly-charged inorganic ions.* Environmental Science & Technology, 2010. **44**(9): p. 3332-3338.
51. Suttiponparnit, K., J. Jiang, M. Sahu, S. Suvachittanont, T. Charinpanitkul, and P. Biswas, *Role of surface area, primary particle size, and crystal phase on titanium dioxide nanoparticle dispersion properties.* Nanoscale Res. Lett., 2011. **6**(27): p. 1-8.

Chapter 2:

Single-step Processing of Copper-doped Titania Nanomaterials in a Flame Aerosol Reactor

The results presented here were published in:

Sahu, M and P. Biswas, *Single-step Processing of Copper-doped Titania Nanomaterials in a Flame Aerosol Reactor*, Nanoscale Research Letters, 2011, 6, 441.

2.1. Abstract

Synthesis and characterization of long wavelength visible-light absorption Cu-doped TiO_2 nanomaterials with well-controlled properties such as size, composition, morphology, and crystal phase have been demonstrated in a single-step flame aerosol reactor. This has been feasible by a detailed understanding of the formation and growth of nanoparticles in the high temperature flame region. The important process parameters controlled were: molar feed ratios of precursors, temperature, and residence time in the high temperature flame region. The ability to vary the crystal phase of the doped nanomaterials while keeping the primary particle size constant has been demonstrated. Results indicate that increasing the copper dopant concentration promotes an anatase to rutile phase transformation, decreased crystalline nature and primary particle size, and better suspension stability. Annealing the Cu-doped TiO_2 nanoparticles increased the crystalline nature and changed the morphology from spherical to hexagonal structure. Measurements indicate a band gap narrowing by 0.8eV (2.51eV) was achieved at 15 wt% copper dopant concentration compared to pristine TiO_2 (3.31eV) synthesized under the same flame conditions. The change in the crystal phase, size, and band gap is attributed to replacement of titanium atoms by copper atoms in the TiO_2 crystal.

Key words: Nanomaterials, Cu-doped TiO_2, Crystal structure, Band gap, Flame synthesis.

2.2. Introduction

Nanosized TiO_2 has been widely used because of its stability in aqueous environments and low production cost. However, its light absorption range is limited to the ultraviolet (UV) spectrum of light due to its wide band gap (~3.2 eV). To shift the absorption range to the visible spectrum, various approaches have been pursued in the past involving size optimization [1] , compositional variation to make sub-oxides [2] , surface modification [3], and doping [4, 5, 6] to modify the TiO_2 structure. Among these methods, tailoring the band structures by incorporating a dopant into the host nanomaterial is a promising approach [6, 7, 8]. Several studies have reported enhancement of absorbtion in the visible range and photocatalytic activity on doping TiO_2 by transition metal ions like Cu, Co, V, Fe, Nb and non metal like N, S, F [4, 5, 9, 10, 11]. However, a major challenge is to process low-cost, and stable doped nanomaterials with well controlled properties that can effectively absorb visible light.

Recently, copper has been increasingly investigated as a dopant for titania [12]. Copper oxide is a narrow band gap (cupric oxide- 1.4eV, cuprous oxide-2.2eV) material which has a high absorption coefficient, but suffers from UV induced photocorrosion [12]. However, copper oxide coupled with TiO_2 has been demonstrated to be stable with improved photocatalytic degradation properties [9, 13, 14], effective CO_2 photoreduction [15, 16], improved gas sensing and enhanced H_2 production [17, 18]. It has been shown that Cu-doped TiO_2 induces more toxicity compared to TiO_2 [19]. Though a large number of studies on Cu-doped TiO_2 nanomaterials have been reported, there is little information available on the effect of dopant concentration on TiO_2 properties. Dopants

can replace Ti in the substitutional sites or be incorporated in the interstitial sites. In some cases they may segregate on the surface [21]. The creation of new energy states due to the incorporation of the dopant in the host TiO_2 alters the particle properties, electronic structure, and light absorption properties. These affect their functionality, and hence can be used in different applications [3, 8, 21, 22]. In summary, there is a need to synthesize Cu-doped nanomaterials with controlled properties (independently) which will help understand in detail the role of the dopant in altering TiO_2 properties. It is essential to have samples wherein one characteristic is varied, keeping the others the same. For example, samples of varying crystal phases while maintaining the size the same will allow to establish the dependence of biological activity with the crystal phase.

Studies have reported the preparation of various doped TiO_2 nanmaterials by multi-step liquid phase synthesis [5], gas phase spray pyrolysis, and flame synthesis methods [20, 23, 24]. Flame aerosol synthesis is a single-step process, and allows independent control of the material properties such as particle size, crystallinity, homogeneity, and degree of aggregation [25, 26]. At elevated temperatures encountered in the flame synthesis process, most dopants can diffuse rapidly [27] and be uniformly distributed due to excellent precursor vapor mixing at the molecular level [20, 21]. Furthermore, flame aerosol processing is a scalable technique that is commercially used to manufacture large quantities of nanomaterials [28].

The synthesis of Cu-doped TiO_2 in a single-step flame aerosol process is reported in this paper. A detailed characterization of the as-produced samples to understand the influence of process parameters on material properties is done. The role of key process

parameters such as molar feed ratio of precursors and dopant concentration on TiO_2 nanomaterial properties such as size, composition, crystallinity, stability in suspension, and morphology are thoroughly investigated. A method to control the crystal phase of the Cu-doped TiO_2 nanomaterial has been discussed. The effect of annealing temperature on crystal phase and microstructure of the Cu-doped TiO_2 material is reported. A formation mechanism of Cu-doped TiO_2 nanomaterial in the flame aerosol reactor is elucidated.

2.3. Experimental

2.3.1. Nanomaterial synthesis

Figure 1 shows the schematic diagram of the flame aerosol reactor system used for the synthesis of the Cu-doped TiO_2 nanomaterials. The main components of the flame aerosol reactor system are: a diffusion burner, a precursor feeding system, and a quenching and collection system. The design details of the diffusion burner used for this study is given in Jiang et al [26]. Nitrogen was passed through titanium tetra-ispopropoxide (TTIP) (99.7%, Aldrich) in a bubbler, and the saturated vapor was introduced into the central port of the burner. The bubbler containing the liquid TTIP precursor was placed in an oil bath and was maintained at a temperature of 98^{o}C. The precursor delivery tube was maintained at a temperature of 210^{o}C by a heating tape. This avoided the condensation of the precursor TTIP vapor in the delivery tube. Copper

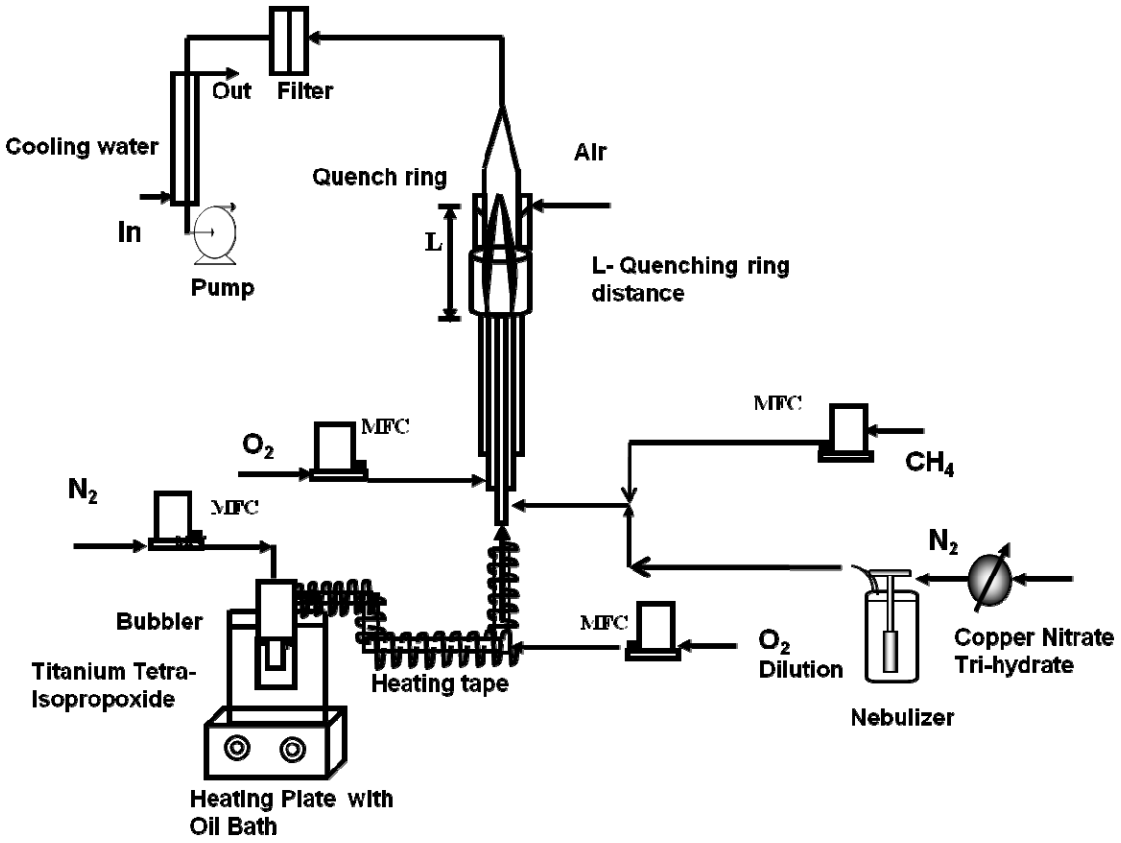

Figure 2- 1: Schematic diagram of the FLAR experimental setup used to synthesize Cu-doped TiO_2 nanoparticles

nitrate trihydrate (99.5%, VWR) was used as the dopant precursor. The dopant precursor solution was prepared by dissolving a known amount of copper nitrate in distilled water. A stainless steel collison nebulizer was used to generate fine spray droplets (less than 2μm), which were then carried by nitrogen gas into the high temperature zone of the flame. The doping percentage was varied by introducing different molar ratios of both the precursors. The overall doping concentration was varied from 0 to 15 wt%. Methane and oxygen were introduced into the second and third ports of the burner respectively to create a diffusion flame zone. The volumetric flow rates of N_2 through the TTIP bubbler and the O_2 were precisely controlled by mass flow controllers at 2 lpm and 7.5 lpm

respectively. The methane flow rate was maintained at 1.8 lpm, and varied for few of the tests. A 20 lpm flow of compressed air was supplied in a radial directon to the quenching ring for cooling. The entrained air diluted the aerosol stream and suppressed particle growth. The synthesized materials were collected using a glass microfiber filter paper (Whatman) for further characterization.

2.3.2. Material characterization

The size, morphology, and microstructure of the nanoparticles were determined by a transmission electron microscope (TEM) (Model: JEOL 2100F FE-(S) TEM) with an accelerating voltage of 200 kV and by a field emission scanning electron microscope (SEM) (Model: JEOL 7001LVF FE-SEM). The elemental analysis of the doped nanomaterial was done using energy dispersive spectroscopy (EDS) analysis integrated with a SEM. In EDS analysis, the X-rays are generated in about few microns (~2μm) in depth of the sample. Phase structures of the material were determined using an X-ray diffractometer (XRD) with Cu Kα radiation (λ=1.5418 A) (Rigaku D-MAX/A9). Zeta potential, an indicator of the stability of nanoparticles in suspensios, was measured by using a ZetaSizer Nano ZS (Malvern Instruments) dynamic light scattering instrument. Nanoparticles were dispersed in de-ionized water at a concentration of 30μg/ml and sonicated for 25 minutes using a bath sonicator (40 W, 50 kHz, 5 Fisher Scientific, Fairlawn, New Jersey) before zeta potential measurements. UV-visible absorption spectroscopy (Perkin Elmer Lambda 2S) was used to analyze the absorbance spectrum of

the nanomaterials over wavelengths ranging from 200 to 800 nm at room temperature. From the absorption spectrum, the band gap was estimated. The absorption edge was estimated to be the point where the absorption was 30% of the maximum, corresponding to where 50% of the photons were absorbed. This approach was used because of the difficulty in finding the linear region of the absorption spectrum according to conventional methods of band gap estimation [22].

2.3.3. Experimental test plan

The list of experiments performed is outlined in Table 2-1. The flow rates were

Table 2- 1: Summary of the experimental test plan

Test #	Dopant Concentration (wt %)	CH_4 (lpm)	Objective
1 A	0	1.8	Study the influence of dopant concentration on TiO_2 material properties such as size, crystal phase, suspension stability, and light absorption.
B	0.5		
C	1		
D	3		
E	5		
F	15		
2 A	3	0.8	Study the effect of methane flow rate on size and crystal phase of the material.
B		1.2	
C		1.5	
D		1.8	
3 A	1	Annealing temperature- 400^oC, 600^oC Duration of annealing under air -4 hrs	Examine the effect of annealing on phase and microstructure characteristics of Cu-doped TiO_2 nanoparticles
B	15		

controlled to maintain the same residence time in the high temperature flame (Test-1). TiO_2 was synthesized under the same experimental conditions using only TTIP as the precursor (Test-1A). Addition of dopant influences nanomaterial properties such as size, crystal structure, stability in suspension, and optical properties. The copper dopant concentration was varied from 0 to 15 wt% to process Cu-doped TiO_2 nanomaterials (Test-1(B-F)) to investigate the impact on properties. The copper dopant concentration was estimated based on the precursors feed rate to the flame. The temperature - time history in the flame impacts the particle formation and growth rates. This was varied by altering the methane flow rate from 0.8 to 1.8 lpm at a constant dopant level of 3wt% (Test-2). Annealing of the 1 and 15 wt% Cu-doped TiO_2 was conducted for 4 hrs at 400^{o}C and 600^{o}C in an atmosphere of air to examine property alterations (Test-3).

2.4. Results and Discussion

Doping TiO_2 with other atoms changes properties such as particle size, crystal structure, stability in suspension, and light absorption. The mechanism of Cu-doped TiO_2 nanoparticle formation in the flame aerosol reactor is discussed first. The effect of copper dopant on TiO_2 particle properties are discussed followed by crystal structure control of the doped TiO_2 nanomaterials. Finally, microstructure changes of Cu-doped TiO_2 are discussed under different annealing conditions.

2.4.1. Particle formation mechanism

The proposed Cu-doped TiO_2 particle formation mechanism is illustrated in Figure 2-2. This is similar to the pathways proposed by Basak [24] for multi-component

nanomaterial systems. To understand the formation mechanism of the Cu-doped TiO_2 nanoparticles in the flame aerosol reactor, pristine TiO_2 was synthesized first using TTIP only as the precursor. TTIP decomposes to form TiO_2 monomers, which then undergo subsequent growth by collision followed by sintering to form nanoparticles (Test-1A). For synthesizing Cu-doped TiO_2 particles, both the TTIP and copper nitrate precursor are fed to the high temperature flame. The nanoparticle properties such as size and composition depend on the relative decomposition kinetics and molar feed ratios of the precursors (see Figure 2-2). The decomposition rate of TTIP is given by, $k_a = 3.96 \times 10^5 \exp((-7.05 \times 10^4)/RT\ s^{-1}$ [29]. Since the kinetic data for copper nitrate precursor is not available, the decomposition rate reported for copper acetyl acetonate was assumed ($k_b = 3.02 \times 10^7 \exp((-1.15 \times 10^5)/RT)\ s^{-1}$) [30]. The two precursors form TiO_2 (formed from TTIP molecular decomposition) and CuO (formed by decomposition of copper nitrate followed by evaporation) monomers at similar time instants as their decomposition rates are similar (($k_{1,Cu} / k_{1,Ti} \sim 5$, at 2200^{o}C). Depending on the molar feed ratio of the precursors, a variety of morphologies can be formed, ranging from particles consisting of only copper oxide, particles of only TiO_2 and the particles of mixed TiO_2 and CuO. At low copper concentrations (1-5 wt%), CuO monomers are readily incorporated into the higher concentration TiO_2 clusters by a scavenging process. This is similar to the phenomenon demonstrated by Wang et al [20]. Subsequent collisional growth and sintering result in a homogenous mix of Cu-doped TiO_2 particles. However, at higher Cu feed concentration (~15wt %), apart from the collision and sintering of the

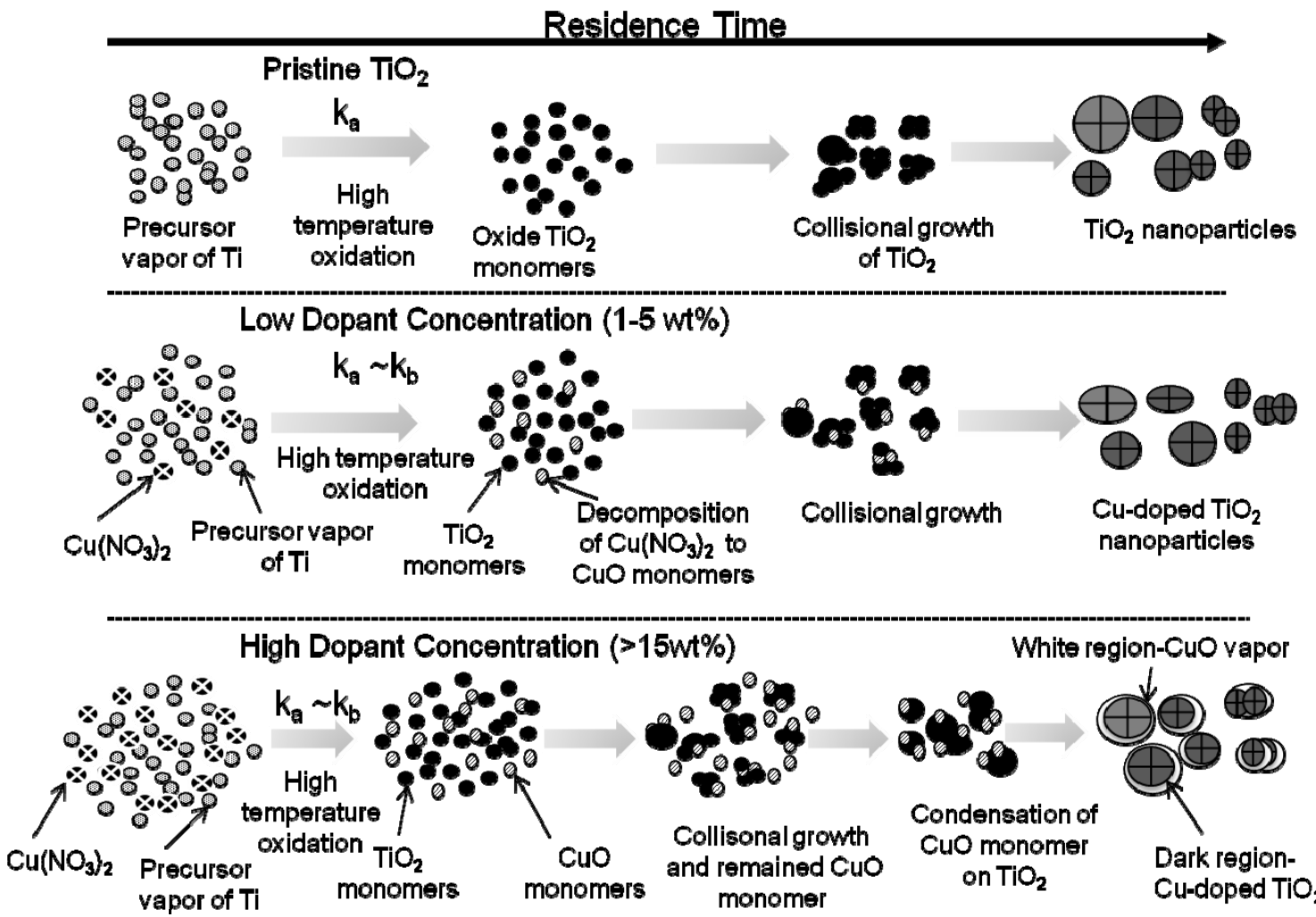

Figure 2- 2: Cu-doped TiO_2 nanoparticles formation mechanism in a FLAR reactor (Top case represents TiO_2 formation mechanism, Middle case is for low copper dopant concentration, and bottom case is for high dopant concentration).

CuO monomers and TiO_2 clusters, some of the CuO oxide monomers also condense onto the formed Cu-doped TiO_2 particles. The HR-TEM image of the synthesized 15wt% Cu-TiO_2 nanoparticles indicates regions of amorphous CuO on the particle surface. The explanation of CuO monomer condensation on the particle surface is thus corroborated (Test-1F). The nanomaterials synthesized at various dopant concentration were verified by single particle EDS analysis to be comprised of both copper and titania. No particles were found consisting of only Ti or only copper species.

2.4.2. Effect of copper dopant concentration on TiO_2 properties

2.4.2.1. Particle size analysis

Figure 2-3 shows the TEM, HR-TEM images, and primary particle size distribution of 1 wt% Cu-TiO_2 (Test-1B) and 15 wt% Cu-TiO_2 (Test-1F) samples. The particle size distribution was obtained by measuring the diameter of 200 particles from representative TEM images. As shown in the size distribution of these samples (see Figure 2-3), the particles were spherical and size decreased with increasing doping concentration. The geometric mean primary particle size obtained at 1 wt% doping was ~47 nm compared to ~33 nm obtained at 15 wt% doping. The peak broadening observed in XRD pattern (see Figure 2-4) also qualitatively explained the change in particle size and lattice expansion with doping. The crystallite size was estimated from the XRD pattern obtained using Scherrer formula. The crystallite size obtained at 1 wt% doping was 33 nm compared to 25 nm and 23 nm at 5 and 15 wt % doping concentration. It is important to note that crystallite size estimation from XRD is different from the particle size observed from the microscopic analysis. XRD

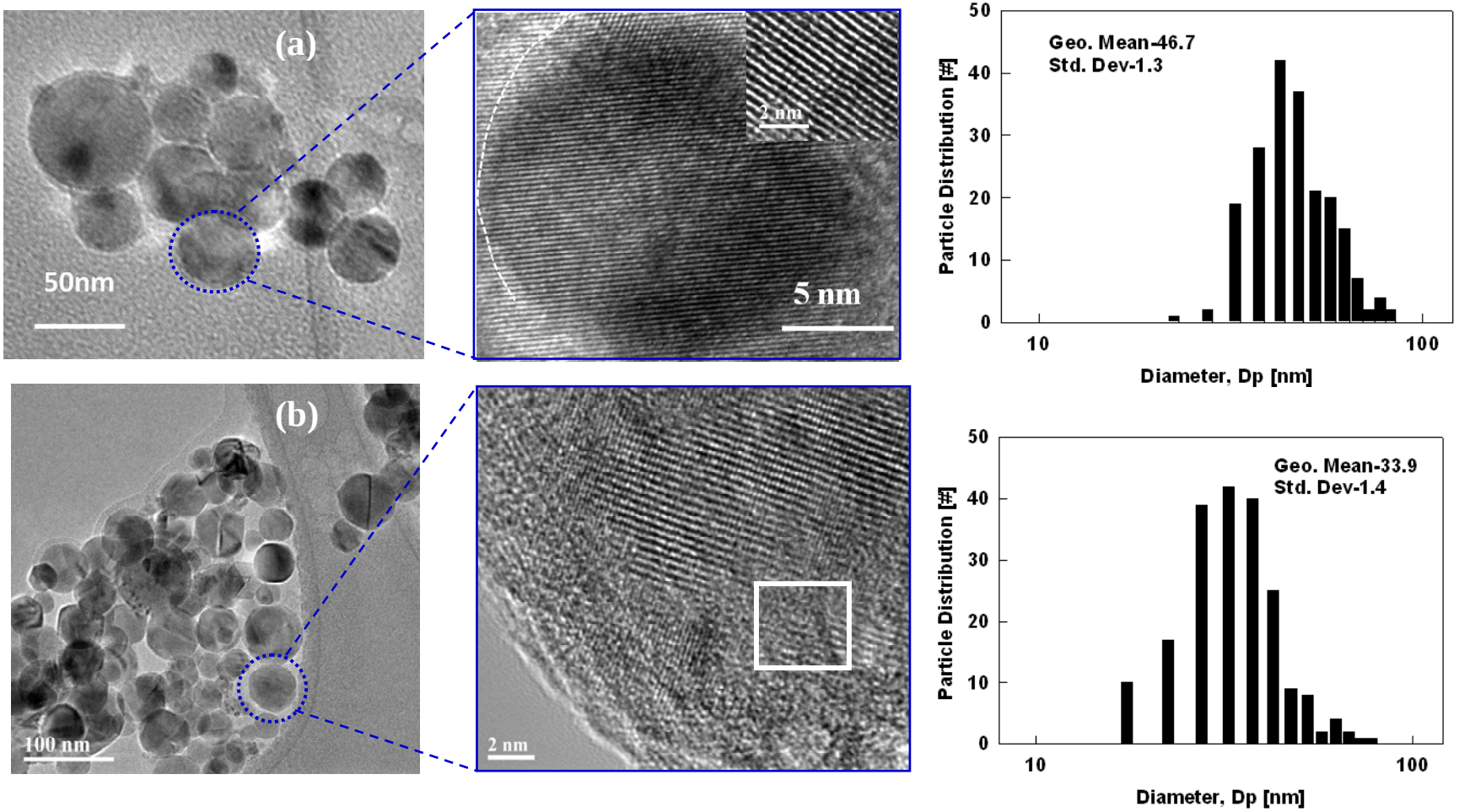

Figure 2- 3: TEM images and particle size distribution of as synthesized Cu-doped TiO_2 nanoparticles (a) 1 wt% Cu-TiO_2 and (b) 15 wt% Cu-TiO_2 (Inset is the HR-TEM image of the crystal fringes) (Size distribution of particles is plotted by measuring 200 particles)

measures the size of the small domains within the grains and one particle may consist of several crystallites based on the preparation methods [31]. The decreased particle size with increasing doping concentration is due to the inhibition of the grain growth. As evident from the HR-TEM images of the 15wt% Cu-TiO_2 (see Figure 2-3), an enhanced amorphous layer is observed on the surface. The excess CuO monomers condense on to the existing Cu-doped TiO_2 particles. Thus, particle crystallinity decreases and also prevents grain growth. Wang et al [20] observed an amorphous crystal structure and decreased grain size with an increasing Fe^{2+}/Ti^{4+} ratios consistent with our Cu-doped TiO_2 materials. Reduction in size was also observed when Li et al [3] synthesized Zn-doped SnO_2 nanomaterials. Norris et al [27] proposed a process called self purification by which dopants diffuse from inside to the surface sites of TiO_2 nanocrystals. This change in particle size with doping concentration is fundamentally a very important phenomenon for electronic structure modification. These results indicate that the particle size of the Cu-doped TiO_2 can be controlled by manipulating the dopant concentration in addition to the methods demonstrated by other researchers by controlling the precursor feed concentration and residence time of the particle in the high temperature flame [26, 32].

2.4.2.2. Crystal Phase

The functionality of TiO_2 nanomaterials for various applications depends on its crystal phase. The anatase phase of TiO_2 is preferred for photocataytic applications, whereas rutile phase is preferred for applications in pigments [1]. It is, therefore, necessary to understand the modifications in the crystal structure by incorporation of the dopants in

TiO_2. The XRD diffraction pattern of the Cu-doped TiO_2 nanomaterials synthesized at various concentrations is shown in Figure 2-4. The pristine and Cu-doped TiO_2 nanoparticles were prepared at the same flame conditions for comparison. The pristine TiO_2 was primarily anatase under the chosen processing conditions. However, with increasing dopant concentration, the transformation from anatase to rutile phase occurred, as shown in Figure 2-4 (a) from the (110) rutile peak, consistent with other studies [18, 33]. The anatase and rutile fraction were calculated according to the formula proposed by Spurr and Myers [34]. The pristine TiO_2 had 1.2% rutile content, but with increasing doping concentration to 15 wt %, the rutile phase increased to 21.8% . Even at high dopant concentration (15 wt %), no pure dopant related crystal phase was observed within the XRD detection limit. The same anatase to rutile phase transformation was observed for synthesis of Cu-doped TiO_2 by other methods [9, 35].

The similarity in ionic radius of Cu^{2+} (0.73^oA) to that of of Ti^{4+} (0.64^oA) enable copper to substitutionally replaces Ti in the titanium lattice in the flame environment, where particles are formed from the atomistic state. In the high temperature flame synthesis of Cu-doped TiO_2 nanomaterial, the copper dopant creates a higher number of defects inside the anatase phase, resulting in a faster formation and growth of a higher number of rutile nuclei[36]. At elevated temperatures, the substitution of Ti^{4+} by Cu^{2+} increases the oxygen vacancy concentration and decreases the free electron concentration. The excess of oxygen vacancies created in the TiO_2 crystal lattice is responsible for anatase to rutile phase transition [36, 37]. To satisfy the charge imbalance due to Ti^{4+} substitution by Cu^{2+}, restructuring of the neighbouring atoms takes place resulting in contraction in c-axis of anatase crystal structure to transform to more

compact rutile structure [18]. Nair et al [36] found that a dopant with an oxidation state above 4+ will reduce the oxygen vacancy concentration in the titania lattice as an interstitial impurity. Dopants with an oxidation state of 3+ or lower when placed in the titania lattice points create a charge-compensating anion vacancy [36] and cause a transformation to the rutile phase as also found in this study. At higher dopant concentration (15wt %) amorphous phase was also observed on the surface as well as in the bulk. The TEM and HR-TEM images 1 wt% and 15 wt% Cu-doped TiO_2 nanoparticles (see Figure 2-3) shows that particles at lower doping concentrations are fully crystallized, and the crystal lattice spacing corresponds to the anatase phase of TiO_2 (0.331±.03 nm), where as the particle synthesized at 15 wt% copper concentration shows both crystalline and amorphous phases of the material. The HR-TEM images confirm that Cu^{2+} doping retards the grain growth of TiO_2 nanoparticles. Similar results of decreasing crystalline nature of material were observed when Fe^{2+} and Zn^{2+} doped TiO_2 were synthesized [3, 20]. In a similar doping study, Wang et al [20] found that at higher Fe^{2+}/Ti^{4+} ratios of 0.12, more rutile and amorphous crystal structure was observed, consistent with our Cu-doped TiO_2 materials.

Figure 2-4(b) and Figure 2-4(c) represents the XRD spectra for (101) and (201) anatase peaks scanned at a very small steps of 0.004 degree for pristine and doped TiO_2 nanomaterials. It is important to note that with increasing dopant concentration, broadening of the major anatase peaks (101) and (201) was observed, which indicates a decrease in crystallite size. The shift in peak position to the right [8] with increasing dopant concentration indicates that Cu^{2+} ions replaced some Ti^{4+} ions along with the lattice expansion. The results clearly indicate that addition of dopant alters the crystal

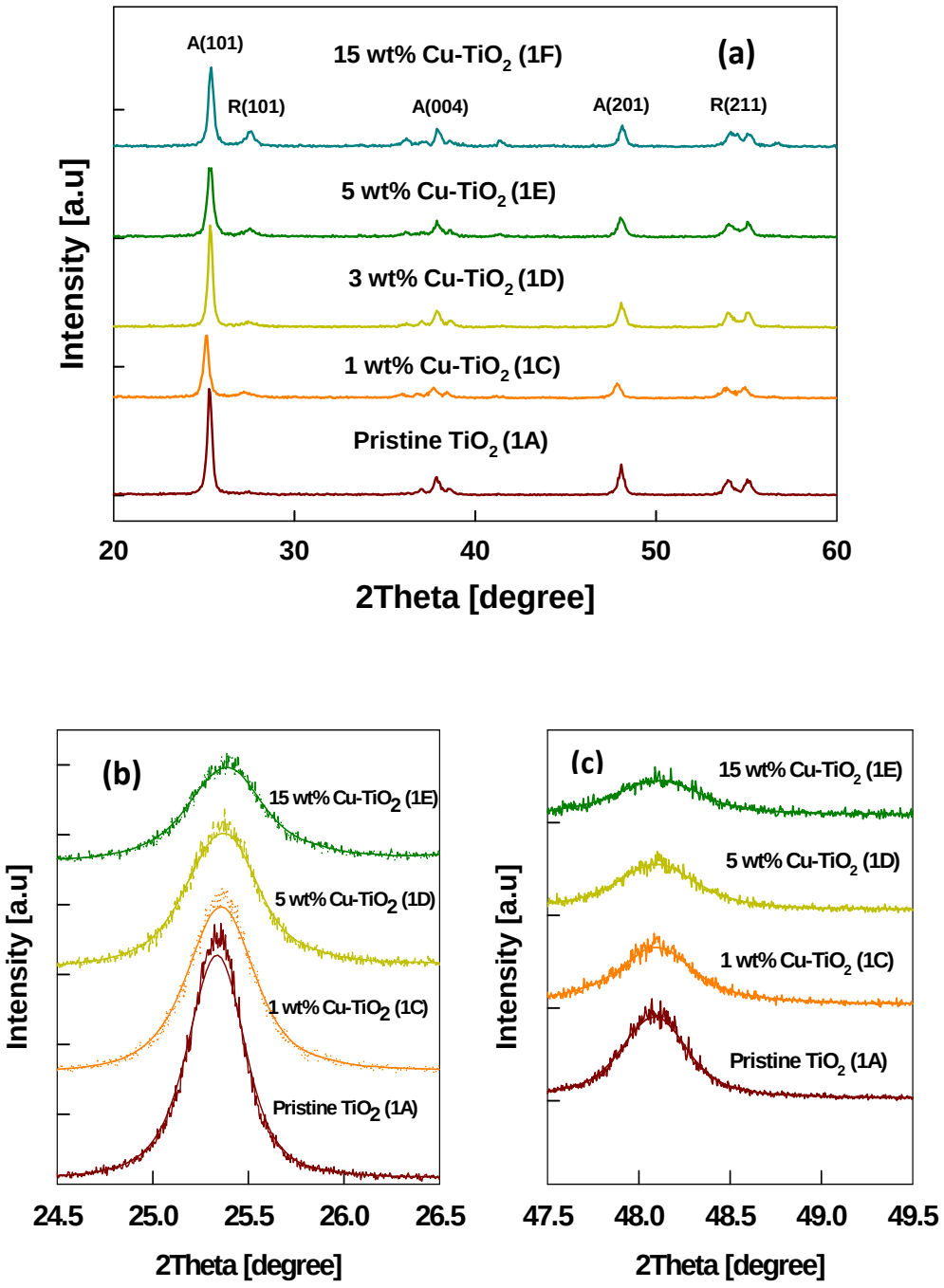

Figure 2- 4: (a) XRD spectra of as-prepared Cu-TiO_2 nanoparticles with different doing concentrations (A-anatase, R-rutile) (b) Comparison of the XRD anatase peaks of Cu-TiO_2 nanoparticles: anatase (101) peaks and (c) anatase (201) peaks (Test-1)

phase of the host nanomaterial and the degree of phase transition depends on dopant types and their concentrations.

2.4.2.4. Zeta potential and suspension stability

The dispersion characteristics of nanoparticles in aqueous suspensions influence the fate and transport, catalytic reactivity in the environmental system as well as critical in understanding for toxicological applications [38, 39]. The stability of the synthesized Cu-doped TiO_2 nanoparticles was analyzed through the measurement of zeta potential in aqueous system using de-ionized water suspension (Figure 2-5) and compared with pure TiO_2 (Test-1A) and commercial CuO. When metal oxide nanoparticles are dispersed in

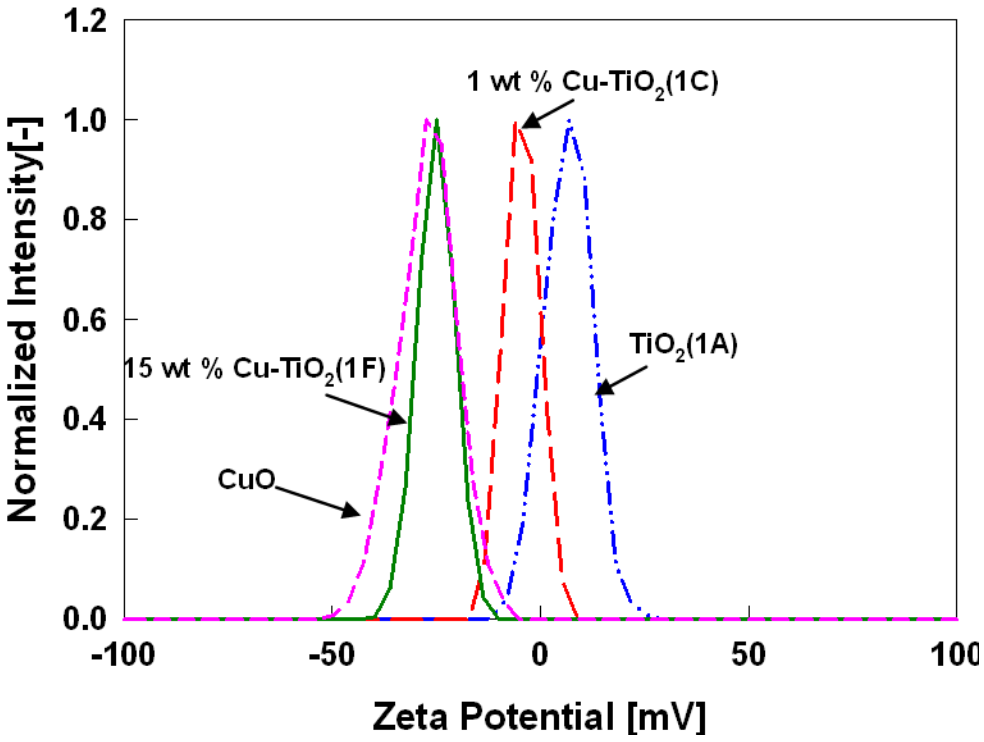

Figure 2- 5: Zeta potential measurements of Cu-doped TiO_2 nanoparticles in water suspension.

water, the hydration of the nanoparticle surface followed by protonation and deprotonation of the surface groups from the oxide surface results in a surface charge. The effective surface charge on the particle depends on the isoelectric point (IEP) in the suspension [39, 40]. The zeta potential observed for pure TiO_2 particle was +3.4mV in the suspension, as the measured pH of the suspension was 5.06, which is less than the IEP of the TiO_2(pH~6.0) and consistent with other studies [40]. However, for Cu-doped TiO2 nanoparticles, the zeta potential value decreased to -3.4mV and -25.6mV at 1 wt% (Test-1B) and 15wt% (Test-1F) copper dopant concentration. The zeta potential measured for the commercial CuO was -27.3mV which is close to the zeta potential value observed for 15 wt% Cu-TiO_2 samples (Test-1F). The high surface charge on the 15wt% Cu-TiO_2 indicates better stability of these particles over pristine TiO_2 nanoparticles in aqueous suspension. The higher zeta potential value and suspension stability of the doped nanoparticles compared to TiO_2 is attributed to charge imbalance created due to substitution of Ti^{4+} atoms by Cu^{2+} in the TiO_2 structure resulting in a more negatively charged surface. Furthermore, zeta potential values for 15 wt% Cu-TiO_2 samples being similar to pure CuO supports the presence of a copper oxide layer on the outer surface of the particles.

2.4.2.4. Light absorption properties

The absorption spectra of the resulting Cu-doped TiO_2 nanomaterials was determined by a diffusive reflectance spectroscopy measurement. The absorption spectrum of Cu-doped TiO_2 nanomaterials prepared at various dopant concentrations are shown in Figure 2-6. With increasing dopant concentration, an increased absorbance in the visible spectrum is

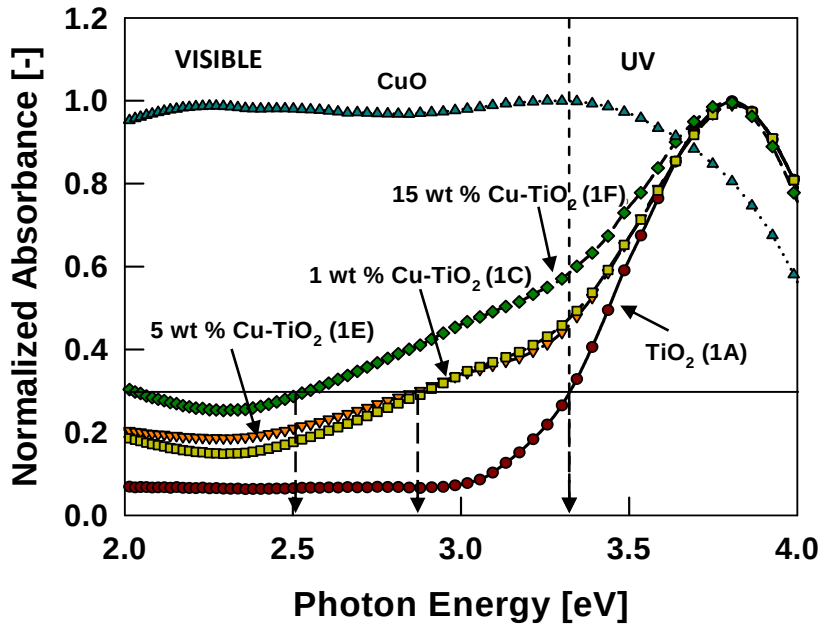

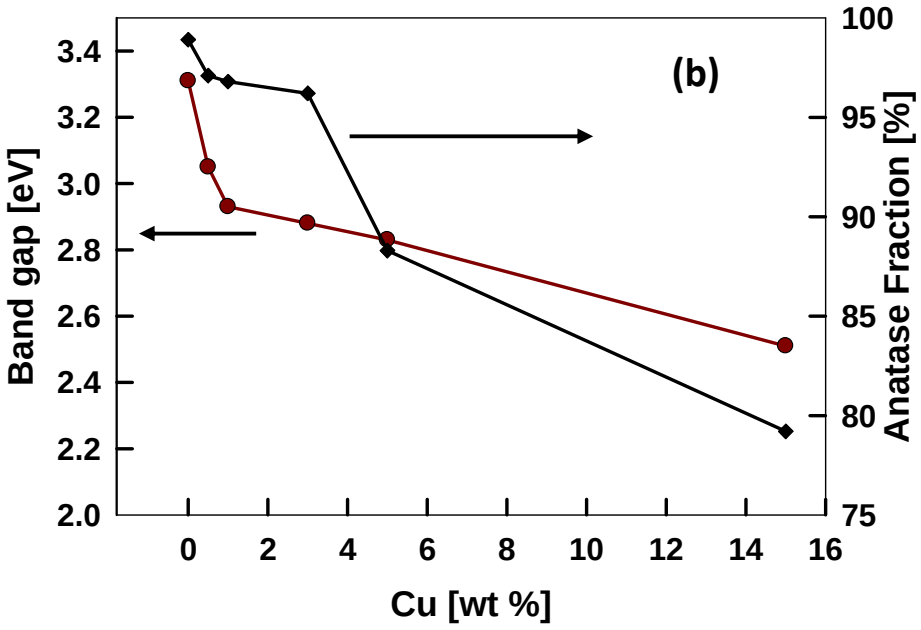

Figure 2- 6: (a) Normalized UV-visible absorption spectra measured by diffuse reflectance spectroscopy (b) Estimated band gap as a function of doping concentrations (Test-1).

observed. The estimated Eg for pristine TiO_2 was 3.31eV which is consistent with the reported value for anatase TiO_2 [22]. With increasing dopant concentration, the band gap energy decreased and was estimated to be 2.51 eV at the highest dopant concentration of 15 wt%. This change of ~0.8 eV was due to the incorporation of Cu^{2+} ions into TiO_2 crystal structure, and CuO forming a layer on the particle surface. From an experimental and theoretical study of band structure estimation of metal oxides, The results are consistent with findings of Thimsen et al [22] that the band gap energy decreases with increasing Fe concentration in anatase based TiO_2 materials.

Change in the optical absorption is due to the defect centers created by the substitution of Ti^{4+} by Cu^{2+} atoms in the TiO_2 crystal lattice. Earlier studies indicated that doping with aliovalent ions changes the local lattice symmetry and defect characteristics, which could change the absorption properties and the material properties. In Cu-dopedTiO_2, when copper ions are either located inside the bulk TiO_2 or on the surface sites, a rearrangement of the neighbor atoms take place to compensate the charge deficiency, resulting in lattice deformation. The lattice deformation affects the electronic structure causing the band gap shift [3]. Furthermore, small amounts of Cu^{2+} dopant in the lattice sites of TiO_2 introduce oxygen vacancies due to the charge compensation effect [36, 41]. Increasing the copper doping concentration increases the oxygen vacancies and probably form a newly doubly occupied oxygen vacancy as discussed in Li et al [3]. Therefore absorption of the doped nanomaterial and band gap shift may be controlled by surface effects, doping-induced vacancies, and lattice strain. It can be said that the copper modified TiO_2 structure extends its absorption to the visible spectrum of

sun light (400-700nm) effectively. Hence, these copper doped materials can be utilized for various visible-light photocatalytic applications, which have been demonstrated in several other studies [9, 18].

2.4.3. Crystal phase control of Cu-doped TiO_2 nanoparticle

The functionality of the nanomaterials depends on their properties such as particle size, crystal phase, morphology, and agglomeration [38, 40]. A recent study by Braydich-Stolle et al [42] showed that cyto-toxicity in the cells is both size and crystal structure dependent. They demonstrated that mechanism of cell death varied with different crystal structure; the anatase phase of TiO_2 being more toxic than the rutile phase. To understand the role of crystal phase of the doped nanomaterials on its functionality, it is important to independently control the crystal phase without varying the other material properties such as size. Previous studies have demonstrated that crystal phase of the TiO_2 nanoparticle can be controlled by varying the temperature in the flame (changing the methane flow rates) and quenching rate downstream of the flame [25, 26]. A similar methodology was adopted to control the crystal phase of the Cu-doped TiO_2 materials. The dopant concentration was kept constant at 3wt% and methane flow was varied from 0.8 to 1.8 lpm (Test-2, Figure 2-7(a)). The anatase phase varied from 39 % to 95%, when the methane flow was increased from 0.8 lpm to 1.2 lpm, whereas the primary particle sizes for all the cases were similar. The representative TEM micrographs and corresponding size distribution of the particles synthesized at 0.8 lpm and 1.8 lpm are shown in Figure 2-7(b-c). The geometric mean size of 31.5 and 32.3 nm were nearly the same for the two flow rate conditions. The size remained similar due to the balance

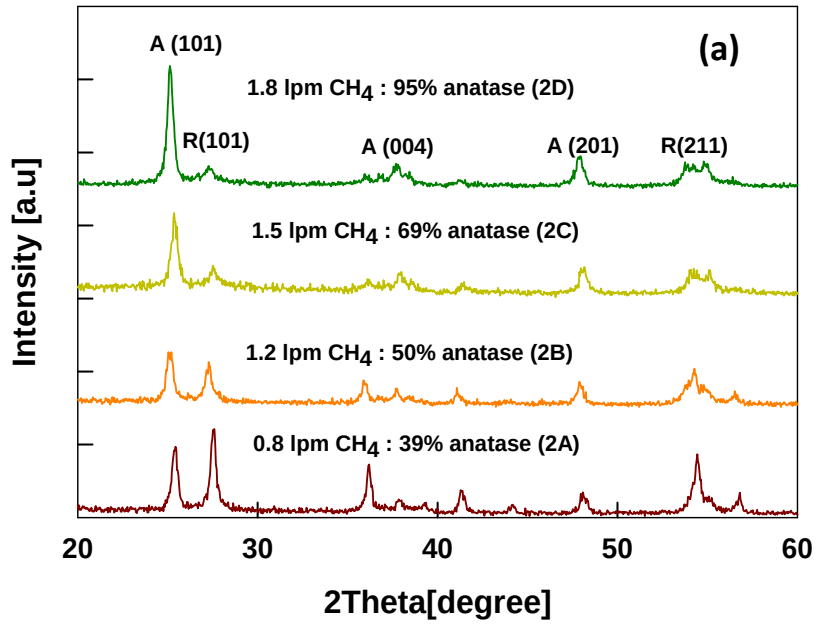

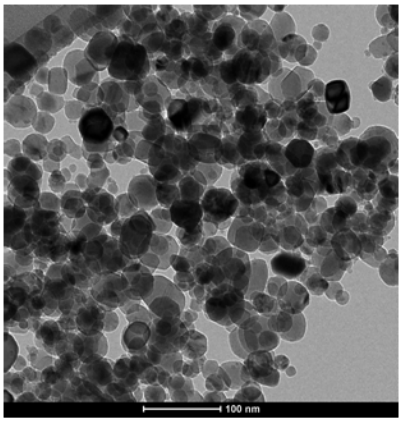

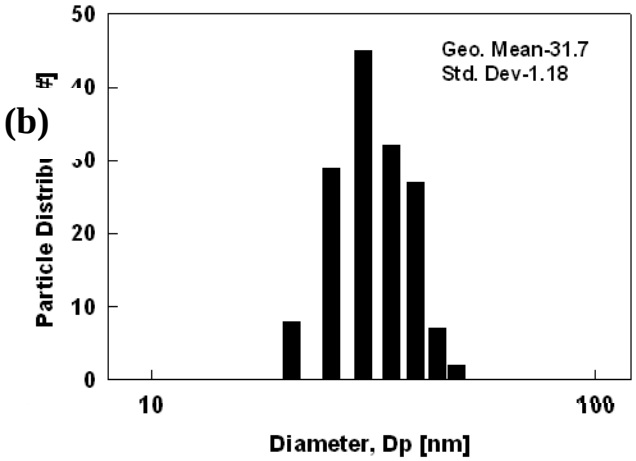

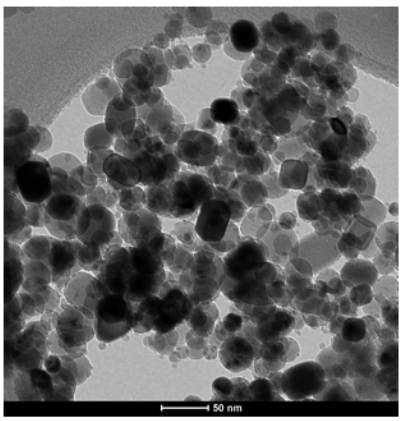

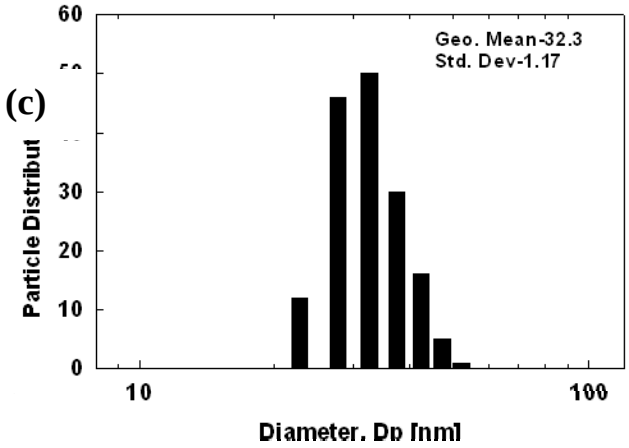

Figure 2-7: (a) XRD spectra at different methane flow rates (A-anatse, R-rutile) and particle size distribution at (b) 0.8 lpm (c) 1.2 lpm methane flow rates of as-prepared 3 wt% Cu-TiO_2 nanoparticles (Test-2).

between temperature profile and residence time in the flame at different methane flow rates. For a fixed flame operating parameters, increasing the methane flow rate increases the flame temperature but at the same time reduces the residence time in the flame. For lower methane flow rate the temperature decreases and residence time increases. It can be said that crystal phase of the Cu-doped TiO_2 nanoparticles having similar primary particle size can be controlled by manipulating the temperature and time history of the nanoparticles in the high temperature zone. These well controlled Cu-doped TiO_2 samples will be of significant importance in biological studies to elucidate the role of crystal phases without interferences from the other particle properties such as size.

2.4.4. Effect of annealing on Cu-doped TiO_2 nanoparticle properties

The morphological and structural transformation of the doped nanoparticles plays important role in photocatalytic activity by modifying the surface chemistry, crystal and electronic structure [43]. Since both amorphous and crystalline phases were observed in HR-TEM images at higher dopant concentration, the as prepared Cu-doped TiO_2 samples were annealed at different temperatures to investigate the effect on crystal structure and morphology. The 1 wt% and 15 wt% Cu-doped TiO_2 samples were annealed at temperatures of 400^{o}C and 600^{o}C for 6 hours. No phase transformation was observed at 400^{o}C. At 600^{o}C, the transformation from anatase to rutile phase was observed as shown in Figure 2-8, which is consistent with other studies [18, 44]. The anatase weight fraction decreased from 75% to 21% for the 15 wt% Cu-doped TiO_2 sample. However, the morphology of the particles changed from spherical to hexagonal structure for nanoparticles prepared at both the dopant concentrations. The crystallite size increased

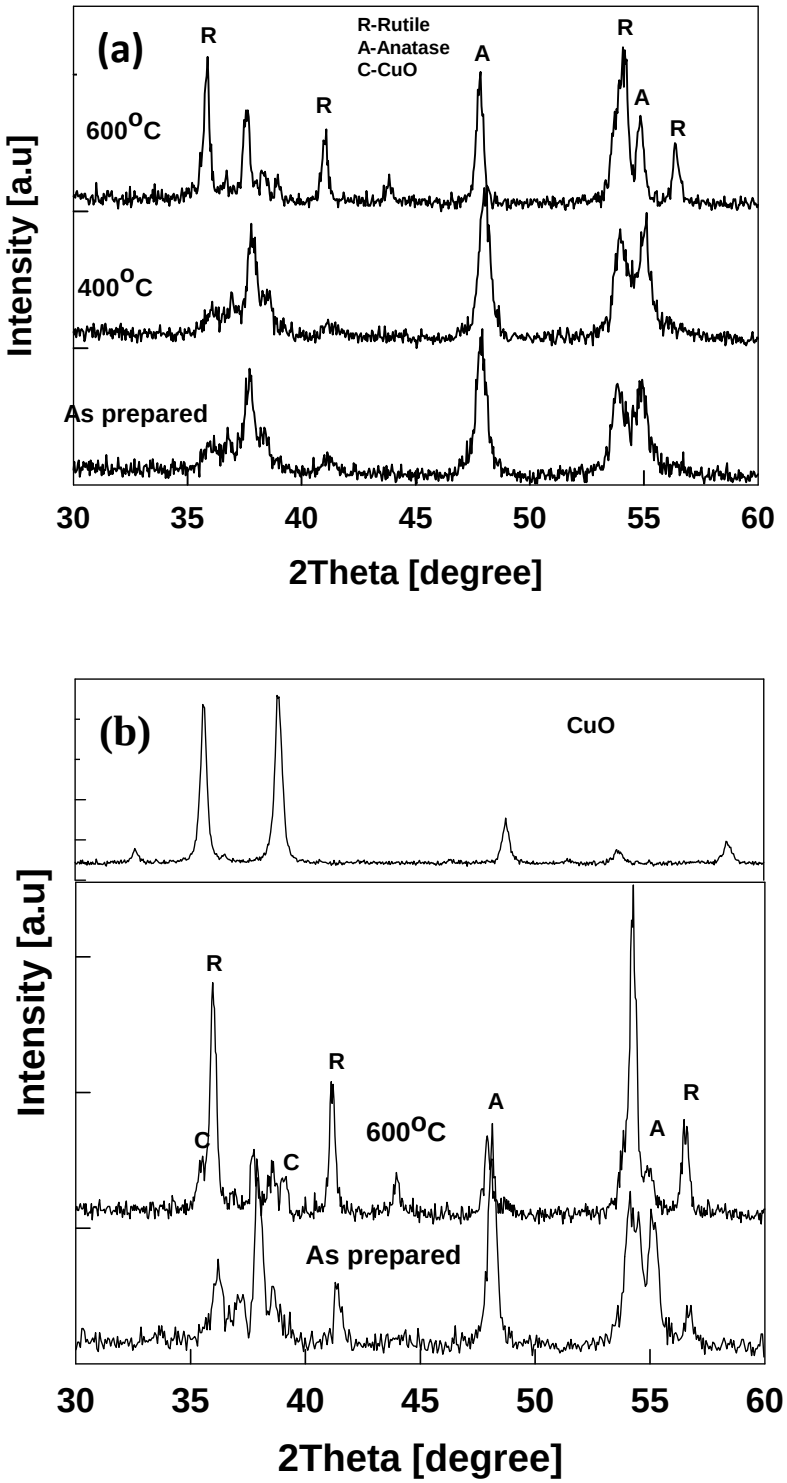

Figure 2- 7: XRD pattern of the annealed Cu-TiO_2 nanoparticles (a) 1 wt% Cu-TiO_2 (b) 15 wt% Cu-TiO_2 (A-anatse, R-rutile) (Samples were annealed for 4 hours in a furnace at constant temperature, Test-3).

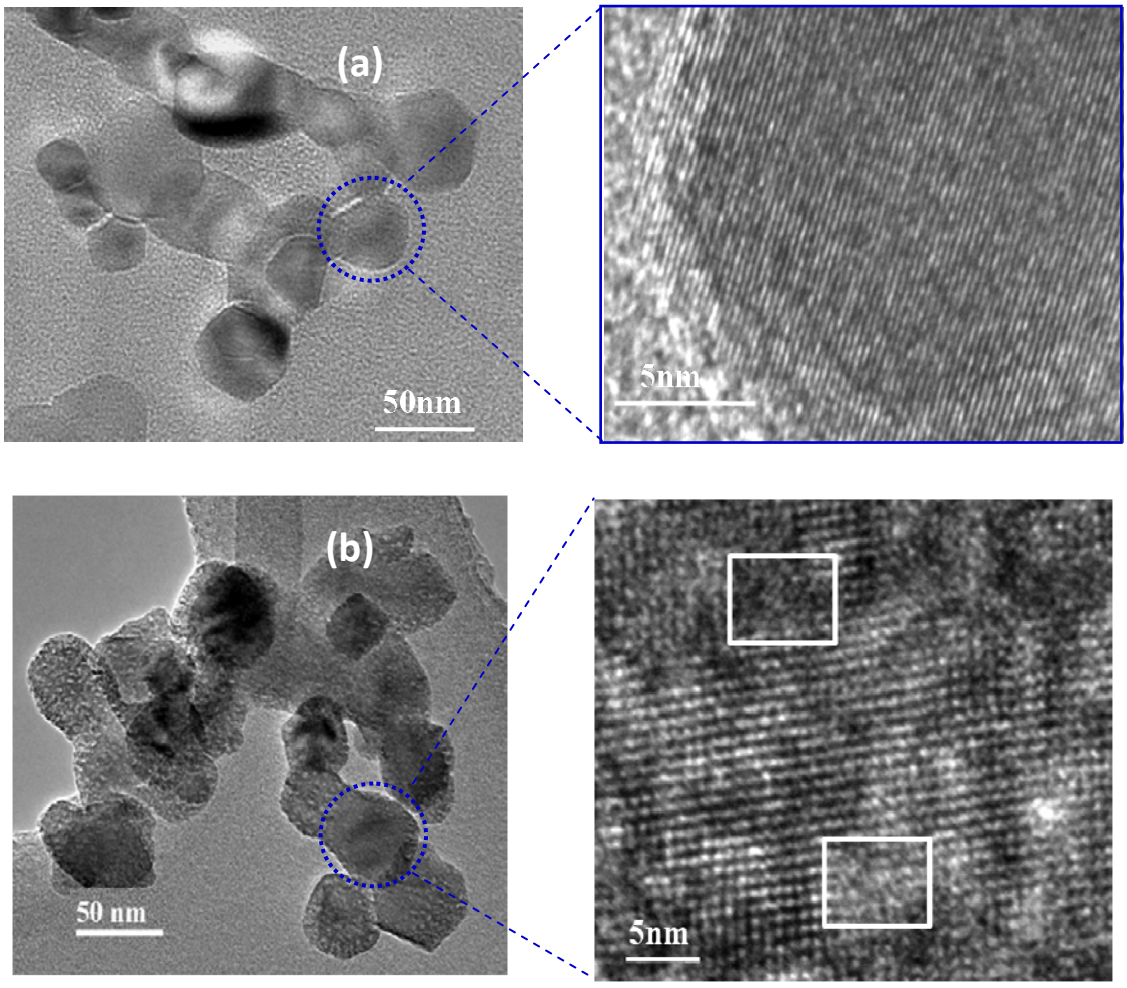

Figure 2- 8: TEM images of annealed Cu-doped TiO_2 samples (a) 1 wt% Cu-TiO_2 and (b) 15 wt% Cu-TiO_2 (Annealing temperature-600^oC, Duration of annealing-4 hours) (Test-3).

with annealing. For 15 wt% Cu-doped TiO_2 sample, the phase related to CuO was observed based on the peaks recorded at Bragg angle of 35.5^o and 39^o from the XRD pattern (Figure 2-8). The amorphous CuO present in the outer layers were annealed to form the crystalline phase in the presence of air. The HR-TEM images of samples

annealed at 600°C are shown in Figure 2-9. The figure indicates that the annealed 1 wt% Cu-doped TiO_2 particle was completely crystallized with no discontinuity in the crystal fringes as observed from HR-TEM images, similar to the as prepared 1 wt% Cu-doped TiO_2 particles. However, for the 15 wt% dopant sample, some amorphous regions were still detected as shown in Figure 2-9 (highlighted with the white squares). More detailed investigations are needed to understand the effect of dopant concentration and reaction environments on morphology change during post synthesis treatment of the initially synthesized spherical particles. The UV-vis measurements of absorption spectra of 1wt % and 15wt% Cu-doped TiO_2 annealed samples are shown in Figure 2-10 and compared with the commercially available CuO nanoparticles.

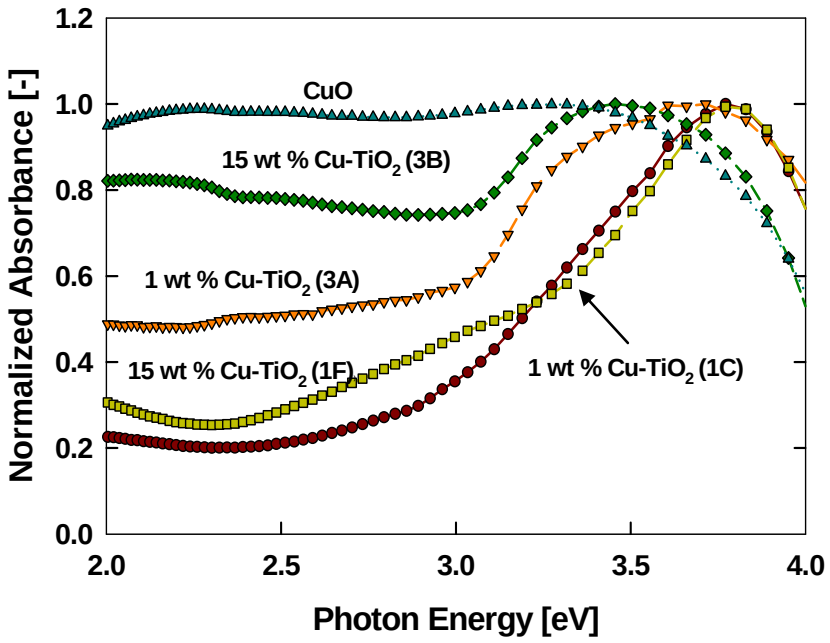

Figure 2- 9: Normalized UV-visible absorption spectra measured by diffuse reflectance spectroscopy of the annealed Cu-doped TiO_2 nanomaterials. Samples were annealed for 4 hours at 600°C (Test-3).

Annealing of the 15 wt% Cu-TiO_2 increased the absorption compared to the as prepared samples in the visible spectrum mainly because of enhanced crystalline CuO formation. It is clear from the results that post-synthesis annealing can alter the doped TiO_2 nanomaterial properties such as size, crystal structures as well as absorption properties, thus influencing eventual functionality and performance.

2.5. Conclusions

Cu-doped TiO_2 nanoparticles were synthesized in a diffusion flame aerosol reactor and the properties were readily varied by controlling the processing conditions. The increase in dopant concentration caused the transformation from anatase to rutile phase of TiO_2 due to replacement of Ti^{4+} by Cu^{2+} in the crystal structure of TiO_2. A decrease in primary particle size was also observed. The doped nanomaterials exhibited better aqueous suspension stability compared to pristine TiO_2 due to charge imbalance created. The annealing of the doped samples resulted in the phase segregation and crystallization of CuO for the higher dopant concentration samples. Spectroscopy measurements confirm a shift in the absorption to visible frequencies, due to crystal structure modification.

2.6. References

1. Almquist, C. B.; Biswas, P., Role of synthesis method and particle size of nanostructured TiO_2 on its photoactivity. *J. Catal.* **2002,** *212*, 145-156.
2. Dhumal, S. Y.; Daulton, T. L.; Jiang, J.; Khomami, B.; Biswas, P., Synthesis of visible light-active nanostructured TiOx (x < 2) photocatalysts in a flame aerosol reactor. *Appl. Catal., B* **2009,** *86*, 145-151.
3. Li, L. P.; Liu, J. J.; Su, Y. G.; Li, G. S.; Chen, X. B.; Qiu, X. Q.; Yan, T. J., Surface doping for photocatalytic purposes: relations between particle size, surface

modifications, and photoactivity of SnO_2:Zn^{2+} nanocrystals. *Nanotechnol.* **2009,** *20*, 155706.

4. Asahi, R.; Morikawa, T.; Ohwaki, T.; Aoki, K.; Taga, Y., Visible-light photocatalysis in nitrogen-doped titanium oxides. *Science* **2001,** *293*, 269-271.
5. Choi, W. Y.; Termin, A.; Hoffmann, M. R., The role of metal-Ion dopants in quantum-sized TiO_2 - correlation between photoreactivity and charge-carrier recombination dynamics. *J. Phys. Chem.* **1994,** *98*, 13669-13679.
6. Li, W.; Wang, Y.; Lin, H.; Shah, S. I.; Huang, C. P.; Doren, D. J.; Rykov, S. A.; Chen, J. G.; Barteau, M. A., Band gap tailoring of Nd^{3+}-doped TiO_2 nanoparticles. *Appl. Phys. Lett.* **2003,** *83*, 4143-4145.
7. Bhattacharyya, K.; Varma, S.; Tripathi, A. K.; Bharadwaj, S. R.; Tyagi, A. K., Effect of vanadia doping and its oxidation state on the photocatalytic activity of TiO_2 for gas-phase oxidation of ethene. *J. Phys. Chem. C* **2008,** *112*, 19102-19112.
8. Li, W.; Frenkel, A. I.; Woicik, J. C.; Ni, C.; Shah, S. I., Dopant location identification in Nd^{3+}-doped TiO_2 nanoparticles. *Phys. Rev. B* **2005,** *72*, 155315-155316.
9. Mor, G. K.; Varghese, O. K.; Wilke, R. H. T.; Sharma, S.; Shankar, K.; Latempa, T. J.; Choi, K. S.; Grimes, C. A., p-Type Cu-Ti-O nanotube arrays and their use in self-biased heterojunction photoelectrochemical diodes for hydrogen generation. *Nano Lett.* **2008,** *8*, 3555-3555.
10. Arana, J.; Dona-Rodriguez, J. M.; Gonzalez-Diaz, O.; Rendon, E. T.; Melian, J. A. H.; Colon, G.; Navio, J. A.; Pena, J. P., Gas-phase ethanol photocatalytic degradation study with TiO_2 doped with Fe, Pd and Cu. *J. Mol. Catal. A: Chem.* **2004,** *215*, 153-160.
11. Park, H. S.; Kim, D. H.; Kim, S. J.; Lee, K. S., The photocatalytic activity of 2.5 wt% Cu-doped TiO_2 nano powders synthesized by mechanical alloying. *J. Alloys Compd.* **2006,** *415*, 51-55.
12. Xu, Y. H.; Liang, D. H.; Liu, M. L.; Liu, D. Z., Preparation and characterization of Cu_2O-TiO_2: Efficient photocatalytic degradation of methylene blue. *Mater. Res. Bull.* **2008,** *43*, 3474-3482.
13. Tseng, I. H.; Wu, J. C. S.; Chou, H. Y., Effects of sol-gel procedures on the photocatalysis of Cu/TiO_2 in CO_2 photoreduction. *J. Catal.* **2004,** *221*, 432-440.

14. Li, Y.; Wang, W. N.; Zhan, Z.; Woo, M. H.; Wu, C. Y.; Biswas, P., Photocatalytic reduction of CO_2 with H_2O on mesoporous silica supported Cu/TiO_2 catalysts. *Appl. Catal., B* **2010,** (In press).
15. Sakata, Y.; Yamamoto, T.; Okazaki, T.; Imamura, H.; Tsuchiya, S., Generation of visible light response on the photocatalyst of a copper ion containing TiO_2. *Chem. Lett.* **1998**, 1253-1254.
16. Teleki, A.; Bjelobrk, N.; Pratsinis, S. E., Flame-made Nb- and Cu-doped TiO_2 sensors for CO and ethanol. *Sens. Actuators, B* **2008,** *130*, 449-457.
17. Wu, B.; Huang, R.; Feng, X.; Biswas, P.; Tang, Y. J., Bacterial responses to Cu-doped TiO_2 nanoparticles. *Sci. Total Environ.* **2010,** *408*, 1755-1858.
18. Wang, Z. M.; Yang, G. X.; Biswas, P.; Bresser, W.; Boolchand, P., Processing of iron-doped titania powders in flame aerosol reactors. *Powder Technol.* **2001,** *114*, 197-204.
19. Nowotny, M. K.; Sheppard, L. R.; Bak, T.; Nowotny, J., Defect chemistry of titanium dioxide. application of defect engineering in processing of TiO_2-based photocatalysts. *J. Phys. Chem. C* **2008,** *112*, 5275-5300.
20. Thimsen, E.; Biswas, S.; Lo, C. S.; Biswas, P., Predicting the band Structure of mixed transition metal oxides: theory and experiment. *J. Phys. Chem. C* **2009,** *113*, 2014-2021.
21. McMillin, B. K.; Biswas, P.; Zachariah, M. R., In situ characterization of vapor phase growth of iron oxide-silica nanocomposites .1. 2-D planar laser-induced fluorescence and Mie imaging. *J. Mater. Res.* **1996,** *11*, 1552-1561.
22. Basak, S. Synthesis and characterization of magentic iron oxide for nanomaterial and nanosystem fabricatiom. Ph.D Dissertation, Washington University in St. Louis, Saint Louis, MO, USA, 2008.
23. Tiwari, V.; Jiang, J.; Sethi, V.; Biswas, P., One-step synthesis of noble metal-titanium dioxide nanocomposites in a flame aerosol reactor. *Appl. Catal., A* **2008,** *345*, 241-246.
24. Jiang, J.; Chen, D. R.; Biswas, P., Synthesis of nanoparticles in a flame aerosol reactor with independent and strict control of their size, crystal phase and morphology. *Nanotechnol.* **2007,** *18*, 285603.

25. Swihart, M. T., Vapor-phase synthesis of nanoparticles. *Curr. Opin. Colloid Interface Sci.* **2003,** *8*, 127-133.
26. Norris, D. J.; Efros, A. L.; Erwin, S. C., Doped nanocrystals. *Science* **2008,** *319*, 1776-1779.
27. Tsantilis, S.; Pratsinis, S. E., Soft- and hard-agglomerate aerosols made at high temperatures. *Langmuir* **2004,** *20*, 5933-5939.
28. Tsyganova, E. I.; Mazurenko, G. A.; Drobotenko, V. N.; Dyagileva, L. M.; Aleksandrov, Y. A., Kinetic principles of the thermolysis of yttrium, barium and copper acetylacetonates. *Zh. Obshch. Khim.* **1992,** *62*, 499-504.
29. Narayan, H.; Alemu, H.; Macheli, L.; Thakurdesai, M.; Rao, T. K. G., Synthesis and characterization of Y^{3+}-doped TiO_2 nanocomposites for photocatalytic applications. *Nanotechnol.* **2009,** *20*, 255601.
30. Thimsen, E.; Biswas, P., Nanostructured photoactive films synthesized by a flame aerosol reactor. *AlChE J.* **2007,** *53*, 1727-1735.
31. Francisco, M. S. P.; Mastelaro, V. R., Inhibition of the anatase-rutile phase transformation with addition of CeO_2 to CuO-TiO_2 system: Raman spectroscopy, X-ray diffraction, and textural studies. *Chem. Mater.* **2002,** *14*, 2514-2518.
32. Spurr, R. A.; Myers, H., Quantitative analysis of anatse-rutile mixtures with an X-Ray diffractometer. *Anal. Chem.* **1957,** *29* 760–762.
33. Colon, G.; Maicu, M.; Hidalgo, M. C.; Navio, J. A., Cu-doped TiO_2 systems with improved photocatalytic activity. *Appl. Catal., B* **2006,** *67*, 41-51.
34. Nair, J.; Nair, P.; Mizukami, F.; Oosawa, Y.; Okubo, T., Microstructure and phase transformation behavior of doped nanostructured titania. *Mater. Res. Bull.* **1999,** *34*, 1275-1290.
35. Yuan, S. B.; Meriaudeau, P.; Perrichon, V., Catalytic combustion of diesel soot particles on copper-catalysts supported on TiO_2 - effect of potassium promoter on the activity. *Appl. Catal., B* **1994,** *3*, 319-333.
36. Jiang, J.; Oberdorster, G.; Elder, A.; Gelein, R.; Mercer, P.; Biswas, P., Does nanoparticle activity depend upon size and crystal phase? *Nanotoxicology* **2008,** *2*, 33-42.

37. Suttiponparnit, K.; Jiang, J.; Sahu, M.; Suvachittanont, S.; Charinpanitkul, T.; Biswas, P., Role of surface area, primary particle size, and crystal phase on titanium dioxide nanoparticle dispersion properties. *Nanoscale Res. Lett.* **2010** (In press).
38. Jiang, J. K.; Oberdorster, G.; Biswas, P., Characterization of size, surface charge, and agglomeration state of nanoparticle dispersions for toxicological studies. *J. Nanopart. Res.* **2009,** *11*, 77-89.
39. Liu, G.; Sun, C. H.; Yan, X. X.; Cheng, L.; Chen, Z. G.; Wang, X. W.; Wang, L. Z.; Smith, S. C.; Lu, G. Q.; Cheng, H. M., Iodine doped anatase TiO_2 photocatalyst with ultra-long visible light response: correlation between geometric/electronic structures and mechanisms. *J. Mater. Chem.* **2009,** *19*, 2822-2829.
40. Braydich-Stolle, L. K.; Schaeublin, N. M.; Murdock, R. C.; Jiang, J.; Biswas, P.; Schlager, J. J.; Hussain, S. M., Crystal structure mediates mode of cell death in TiO_2 nanotoxicity. *J. Nanopart. Res.* **2009,** *11*, 1361-1374.
41. Zhao, Y. X.; Qiu, X. F.; Burda, C., The effects of sintering on the photocatalytic activity of N-doped TiO_2 nanoparticles. *Chemistry of Materials* **2008,** *20*, 2629-2636.
42. Xin, B. F.; Wang, P.; Ding, D. D.; Liu, J.; Ren, Z. Y.; Fu, H. G., Effect of surface species on Cu-TiO_2 photocatalytic activity. *Appl. Surf. Sci.* **2008,** *254*, 2569-2574.

Chapter 3:

In-Situ Charge Characterization of TiO_2 and Cu-doped TiO_2 Nanoparticles in a Flame Aerosol Reactor

The results presented here are adopted from a manuscript to be submitted to:

Sahu, M, J. Park, and P. Biswas, *In-Situ Charge Distribution Characterization of TiO_2 and Cu-doped TiO_2 Nanoparticles in a Flame Aerosol Reactor*, Journal of Nanoparticle Research, 2011.

3.1. Abstract

Charge distribution characteristics were investigated for nanoparticles synthesized in a diffusion flame aerosol reactor. The nanoparticles considered were pristine TiO_2 and Cu-TiO_2, with Cu dopant concentrations ranging from 1 to 5 wt%. *In-situ* measurements were conducted by integrating a tandem differential mobility analyzer (TDMA) experimental setup with the flame aerosol reactor. A charging model was used to identify the important parameters that govern the two charging mechanisms (diffusion and thermo-ionization) in the flame and their relative importance at different operating parameters. The results indicate that TiO_2 and Cu-TiO_2 nanoparticles carry single as well as double unit charges. The charged fraction depends strongly on particle size as well as on dopant concentration. The charged fraction increased with increasing particle size and decreased with copper dopant concentration. Measured charged fractions were similar for both the polarities at different mobility diameters. Based on the flame operating parameters, the calculations indicate that diffusion charging is dominant in the flame, which is consistent with the experimental results.

Keywords: Nanoparticles, Charge distribution, Flame synthesis, TiO_2, Dopant, Cu-TiO_2

3.2. Introduction

Application of nanomaterials in various fields requires the development of a low-cost synthesis process to produce large quantities of high purity materials. Flame aerosol synthesis is such a promising and scalable method. This process has been used to synthesize nanoparticles with controlled characteristics, such as composition, size, and crystal phase (Jiang et al., 2007a; Sahu and Biswas, 2011; Thimsen and Biswas, 2007; Tiwari et al., 2008). To control the physio-chemical properties of nanomaterials in these reactors, the process variables manipulated are precursor feed rate, time-temperature history, and quenching rate (Jiang et al., 2007a; Sahu and Biswas, 2011). Vemury and Pratsinis (1996) demonstrated that manipulating the charge on particles by employing an electrical field can slow the coagulation of particles and reduce particle size.

Studies reported that during the high temperature synthesis, particles are charged by diffusion as well as thermionic charging, by ions generated through the chemi-ionization process (Burtscher, 1992; Jiang et al., 2007b; Karasev et al., 2004; Kim et al., 2005; Sorokin and Arnold, 2004; Starik et al., 2008). Particle charging in flames may depend on many factors, such as temperature, structure, particle size, and material properties. For instance, particles synthesized in a premixed reactor are singly charged (Jiang, 2008; Sgro et al., 2010), whereas other studies have demonstrated that particles synthesized in diffusion flame reactors are singly as well as multiply charged (Ahn et al., 2001; Kim et al., 2005). Studies have reported that incorporation of dopant into TiO_2 structure alters the host material properties, such as size, crystal structure, light absorption, and dielectric constant (Mardare and Rusu, 2004; Sahu and Biswas, 2011; Wang et al., 2001; Xie et al., 2010). The altered material properties due to dopant

addition may lead to different charging behavior during flame synthesis, which has not been well understood. The relevance of the two important charging mechanisms in the flame, diffusion and thermo-ionization, has also not been studied in detail.

The charge on particles can affect growth dynamics during flame synthesis. It may also influence the morphology and aggregate restructuring to form different structures (Onischuk et al., 2003). Apart from influencing the properties, the charge on particles affects sampling, transport, and the deposition pattern in nanodevice fabrications (Kim et al., 2006; Modesto-Lopez et al., 2010). The charging behavior of particles has been utilized for aerosol instrumentation as well for effective particle capture (Chen et al., 1999; Kulkarni et al., 2002). A study by Sahu and Biswas (2010) found that nanoparticles' exposure potential during flame synthesis varies depending on operating scenarios. The charge on particles significantly affects inhaled particle deposition in the lungs (Vincent, 1985). In summary, there is a need to systematically study the charge distributions of flame synthesized nanoparticles and identify the important parameters that influence the charging characteristics. A detailed understanding of charge behavior will help to assess the role of charge in fabricating nano-devices, making aerosol measurements, and controlling particles in both fundamental and applied nanotechnology research.

Few studies have been conducted to understand the charging behavior. Ahn et al (2001) and Kim et al (2005) measured the charge distribution of SiO_2 and soot particles in a diffusion flame aerosol reactor. They reported that particles are singly as well as multiply charged. However, the charge characteristics of TiO_2 and doped TiO_2 nanoparticles synthesized in a diffusion flame have not been fully explored. TiO_2 based

nanoparticles have wide scale applications in energy, environmental, and other sectors (Almquist and Biswas, 2002; An et al., 2010; Asahi et al., 2001; Dhumal et al., 2009). Several techniques, such as differential mobility analysis (DMA) as well as tandem differential mobility analysis (TDMA) have been used to analyze the charge fraction of particles (Jiang, 2008; Kim et al., 2005).

In this study, in-situ charge distribution characteristics have been investigated for industrially relevant TiO_2 and Cu-doped TiO_2 nanoparticles synthesized in a diffusion flame aerosol reactor. To measure the charge distribution, a TDMA measurement system was integrated with the flame reactor. The effect of copper dopant concentration on nanoparticle charged fraction was investigated. Key parameters that govern the two charging mechanisms and calculation to illustrate the relative importance of each charging mechanisms at different flame operating conditions were identified and was determined in the flame.

3.3. Materials and Methods

3.3.1. Nanoparticle Synthesis

A schematic diagram of the experimental system used is shown in Figure 3-1. The system consisted of a diffusion flame reactor for nanoparticle synthesis integrated with a tandem differential mobility analyzer (TDMA) setup for *in-situ* charge characterization. The design details and description of the diffusion burner used for TiO_2 and Cu-doped TiO_2 synthesis are discussed in Sahu and Biswas (2011) and Jiang et al (2007a). Oxygen and methane were used to obtain the flame, and the flow rates were maintained at

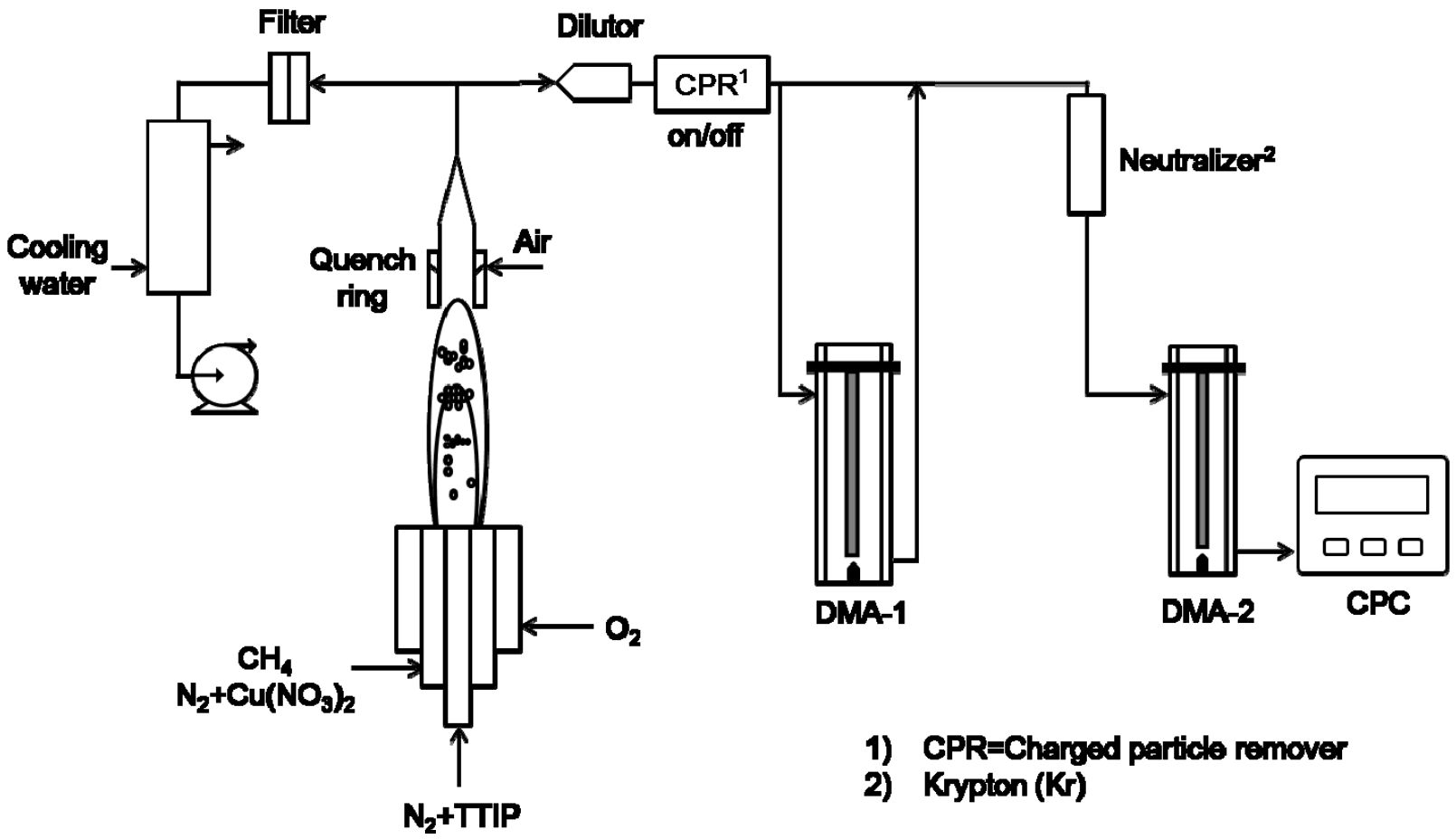

Figure 3- 1: Flame Aerosol synthesis syntem and tandem differential analyzer (TDMA) setup for charge distribution

1.8 lpm and 8 lpm. Titanium tetra-isopropoxide (TTIP, 97%, Aldrich) was the precursor for titanium dioxide and copper nitrate was the precursor for the copper dopant. The TTIP feed rate was maintained by passing 2 lpm of N_2 through a bubbler placed in an oil bath kept at 98^{o}C. Copper nitrate was dissolved in DI water, atomized by a stainless steel nebulizer, and was introduced to the high temperature flame in the form of fine droplets. Dopant concentration was varied from 1 to 5 wt% by changing the copper nitrate concentration in the aqueous solution. The dopant concentration was estimated based on the precursor feed rates to the flame. An air flow of 25 lpm was introduced through the quenching ring, which was fixed at a height of 10 cm. More detailed information on Cu-doped TiO_2 nanoparticle synthesis, including formation, growth, and characteristics, can be found in Sahu and Biswas (2011).

3.3.2. Charge Distribution Measurement

A schematic diagram of the TDMA setup integrated with the nanoparticle synthesis system is shown in Figure 3-1. The system consisted of two differential mobility analyzers (DMA) in series and a condensation particle counter (CPC) downstream to count the particles. Total particle concentrations were measured by a condensation particle counter (CPC) (TSI model 3022a). Size distributions were measured by a scanning mobility particle sizer (SMPS) (TSI Model 3080) coupled with a CPC (TSI model 3076). The system was operated at 6 lpm sheath flow and 0.3 lpm aerosol inlet flow. In the TDMA system, to classify particles of equivalent mobility, the central electrode of DMA-1 was operated at a fixed voltage. Then the particles classified by DMA-1 were passed through the neutralizer, which had a bi-polar radioactive ionizing

source. The particles were subsequently passed through DMA-2 and CPC, and scanned over different voltage ranges to give the particle size distributions. To remove the charged particles, a charged particle remover (CPR), operated at -2kV was placed in line before particles entered the DMA system. Nanoparticles were sampled through a sampling tube and diluted prior to measurements.

3.3.3. Experimental Plan

The experiments performed are listed in Table 3-1. First, the total particle concentration was measured using only the CPC, bypassing the DMA. Then the CPR was operated (-2 kV) to capture all the nascent charged particles. Based on the particle concentrations measured, the charged particle fractions were calculated (Test-1).

Table 3- 1: Experimental test plan

Test #	**Objective**	**System used/Procedure description**	**Parameters measured/ Experimental technique**
1	Study the overall charged fraction of particles in the flame	FLAR TTIP/N_2-2 lpm CH_4-1.8 lpm O_2-8 lpm $CuNO_3/N_2$ =2.3 lpm **Dopant Concentration** (wt%): 0 (TiO_2) 1 3 5	Particle concentration, size distribution, DMA, CPC
2	Examine the charged particle fraction corresponding to different sizes		
3	Examine the fraction of single as well multiple charges corresponding to different sizes		Particle concentration, Size distribution, TDMA, CPC

Abbreviations: FLAR: flame aerosol reactor; lpm: liter per minute; TTIP: Titanium tetra-isopropoxide; DMA: Differential mobility analyzer; CPC: Condensation particle counter; TDMA: Tandem differential mobility analyzer. All the particles were synthesized in a diffusion flame aerosol reactor (Jiang et al., 2007a; Sahu and Biswas, 2011; Tiwari et al., 2008).

The same experiment (Test-1) was repeated by passing the particles through the DMA followed by a CPC. The total particles sampled from the flame were passed through the neutralizer before entering the DMA and classified according to their electrical mobility to obtain the size distributions. Then the CPR was employed before the neutralizer to capture all charged particles. The uncharged particles were then passed through the neutralizer and subsequently through the DMA and CPC to measure the size distributions. The charged particle fraction as a function of mobility diameter was calculated. For a specific mobility diameter, the particle concentration with the CPR was compared to the concentration without the CPR before the DMA (Test-2). This ratio was then subtracted from 1 to obtain the charged particle fractions.

The TDMA system was employed to determine the fraction of singly as well as multiply charged particles (Test-3). To measure the fraction of positively charged particles, synthesized particles of both polarities were introduced into the DMA-1. Since the DMA-1 central electrode was operated at negative voltages, positively charged particles of equivalent mobility were classified at a fixed voltage. The classified particles having equivalent electrical mobility were a mixture of smaller sizes carrying single charges as well as larger sizes carrying multiple charges. Then the particles were irradiated with bipolar radioactive ions in the neutralizer to bring them into a steady charge distribution (where most of the particles carry either a single positive or negative charge or a zero charge). These particles were then passed through DMA-2 and CPC to measure the size distributions. Particles that were initially multiply charged were reduced to a single charge and classified in DMA-2. From the measured size distribution in DMA-2, the fraction of particles with a single positive charge was calculated by taking

the ratio of particle concentrations at that particular mobility with respect to the total concentration of particles measured at that mobility diameter in Test 2.

For determining the doubly charged particle fractions, the voltage on the DMA-1 central electrode was changed to select an electrical mobility corresponding to a doubly charged particle having same diameter. Then the particles were passed through the neutralizer and scanned through different voltages in DMA-2 to measure the size distributions. The concentration of doubly charged particles with that mobility diameter and fraction was evaluated as in the previous calculation. To determine the double charged fraction as a function of mobility diameter, the same experiments were repeated for different mobility diameters.

For determining the negatively charged particles, the voltage of the DMA-1central electrode was switched to positive, and negatively charged particle fractions were obtained in the manner already described. To determine the effect of doping on charged fractions, charge distribution was measured for both TiO_2 and Cu-doped TiO_2 particles (Test-4).

3.4. Results and Discussion

The charge distribution measurements of the particles are presented first, followed by a discussion of the importance of the two charging mechanisms at different flame operating parameters.

3.4.1. Charge Distribution and Effect of Dopant

The total charged fraction by number of TiO_2 particles was (50±5) % (Test-1). A decreased charged fraction was observed with increasing copper dopant concentrations.

The size distributions of nanoparticles obtained for TiO_2 and Cu-doped TiO_2 are shown in Figure 3-2. The size distributions were similar for all the cases, with a geometric mean particle size of approximately ~ 43 nm. Similar size distributions were observed for all the cases because the dopant concentration was not high enough to cause much variation. However, with high dopant concentration (>10 wt%) the primary particle size was altered, and this may lead to changes in particle size distributions (Sahu and Biswas, 2011; Wang et al., 2001). The size distributions of uncharged particles are shown in Figure 3-2 (Test-2). The results indicate that charged particle fraction increased from 21% at 20 nm mobility diameter to 79% at 75 nm mobility diameter for pristine TiO_2. The same increased charged fraction was observed for Cu-TiO_2 particles with increasing size. However, the charged particle fractions of Cu-doped TiO_2 were lower than for pristine TiO_2. The increase in charged particle fraction with increasing size is mainly attributed to the higher surface area available for the ions and electrons to attach. This result is consistent with our theoretical calculations that the attachment co-efficient increased with increased particle size, and is also consistent with other studies (Jiang et al., 2007b; Kim et al., 2006).

To investigate the singly as well as multiply charged particle fractions, a TDMA experiment was conducted at different electrical mobility diameters as described earlier (Test-3). The TDMA measurement for 1 wt% Cu-TiO_2 is shown in Figure S-1. The mobility diameters selected in DMA-1 were 25 nm, 40 nm, 60 nm, and 75 nm. The results shown in Figure S-1 indicate that particles passing through DMA-1 and having

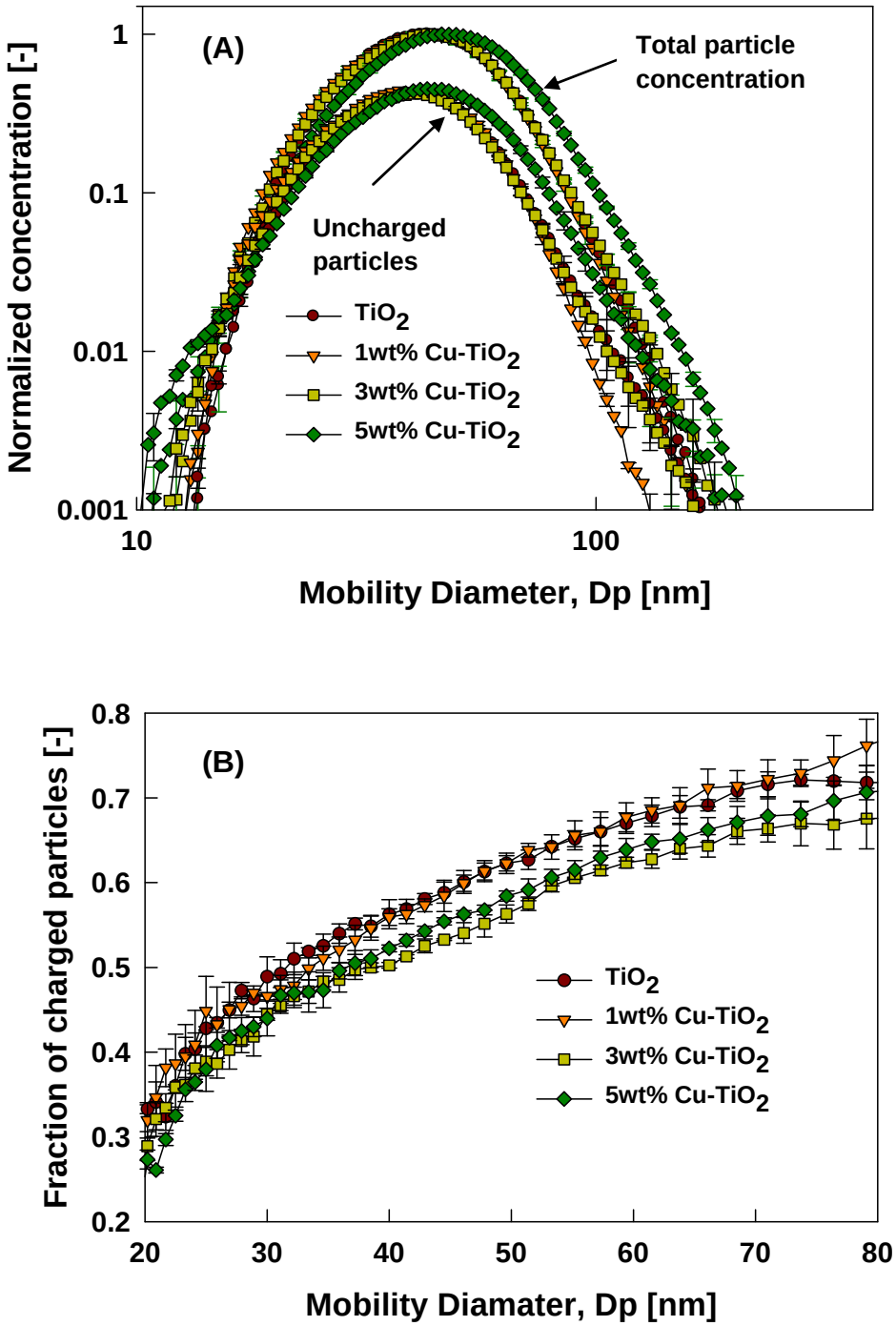

Figure 3- 2: (A) Size distributions of the total and uncharged particles from the flame (B) Fraction of charged TiO_2 and Cu-doped TiO_2 nanoparticles as a function of mobility diameter (Test-2).

same electrical mobility were classified as particles carrying a single unit of charge in the second DMA after effective neutralization. For instance, when the selected electrical mobility was fixed corresponding to a 40 nm particle size carrying +1 unit of charge (1.45E-07 m^2/volt.sec), both 40 nm particles carrying +1 unit of charge and 58 nm particles carrying +2 units of charge were separated in DMA-1 as their electrical nobilities were the same**.** After passing these particles through the neutralizer, most of the particles were classified in DMA-2 as having only a single unit of charge. The results shown in Figure S-2 confirm that particles synthesized from a diffusion flame carry single as well as multiple charges.

The fractions of +1 and +2 charges corresponding to different mobility diameters are shown in Figure 3-3. As shown in Figure3-3, the charging fraction of +1 as well as +2 charges increased with increasing mobility diameter. However, the fractions of +2 charges were relatively less compared to the fraction of +1 charges, which is consistent with reported studies for other materials (Ahn et al., 2001; Kim et al., 2005). The attachment co-efficient of ions leading to particles carrying +1 charges is higher than for particles carrying multiple charges, which verifies that most of the particles will likely be singly charged in the flame. The results indicate that Cu-TiO_2 particle fractions carrying both +1 and+2 charges were comparatively less than for TiO_2 and decreased with increasing dopant concentration. The change in charge fraction is attributed to the dielectric constant change of the TiO_2 nanoparticles by the incorporation of the copper dopant into TiO_2 structure. The dielectric properties strongly depend on the state of the

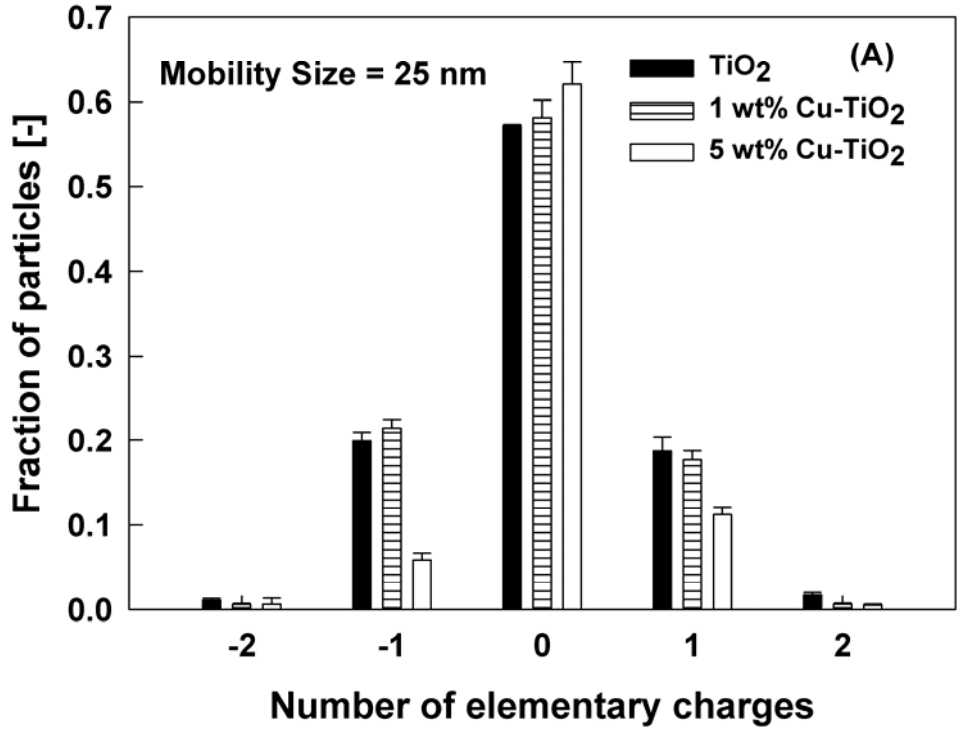
Mobility Size = 25 nm
(A)
TiO2
1 wt% Cu-TiO2
5 wt% Cu-TiO2
Fraction of particles [-]
0.0
0.1
0.2
0.3
0.4
0.5
0.6
0.7
-2
-1
0
1
2
Number of elementary charges

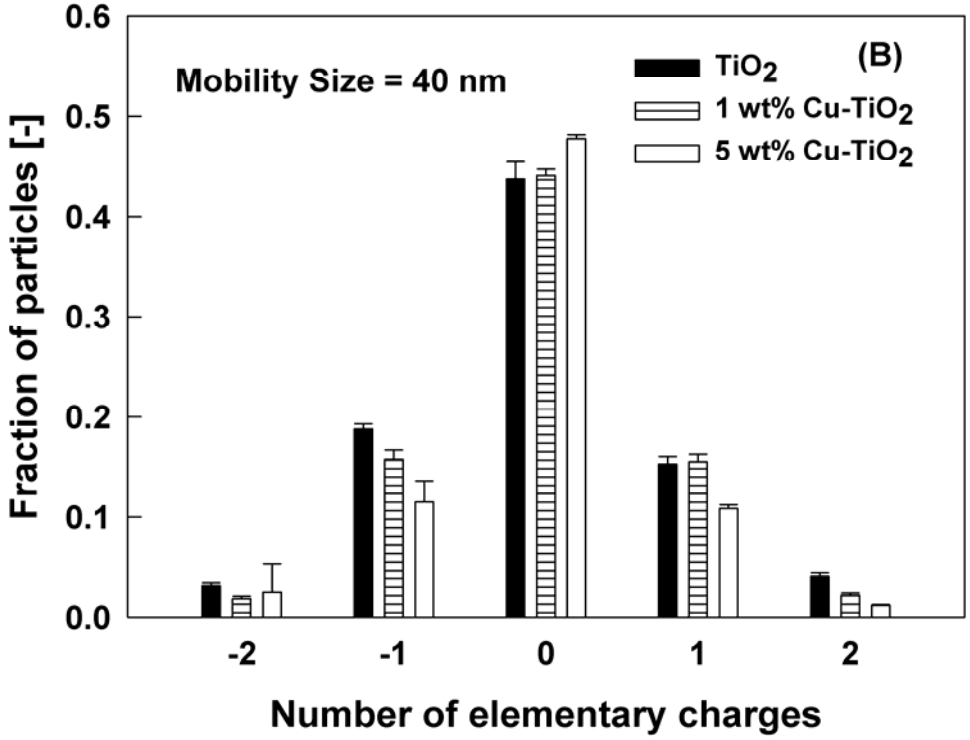
Mobility Size = 40 nm
(B)
TiO2
1 wt% Cu-TiO2
5 wt% Cu-TiO2
Fraction of particles [-]
0.0
0.1
0.2
0.3
0.4
0.5
0.6
-2
-1
0
1
2
Number of elementary charges

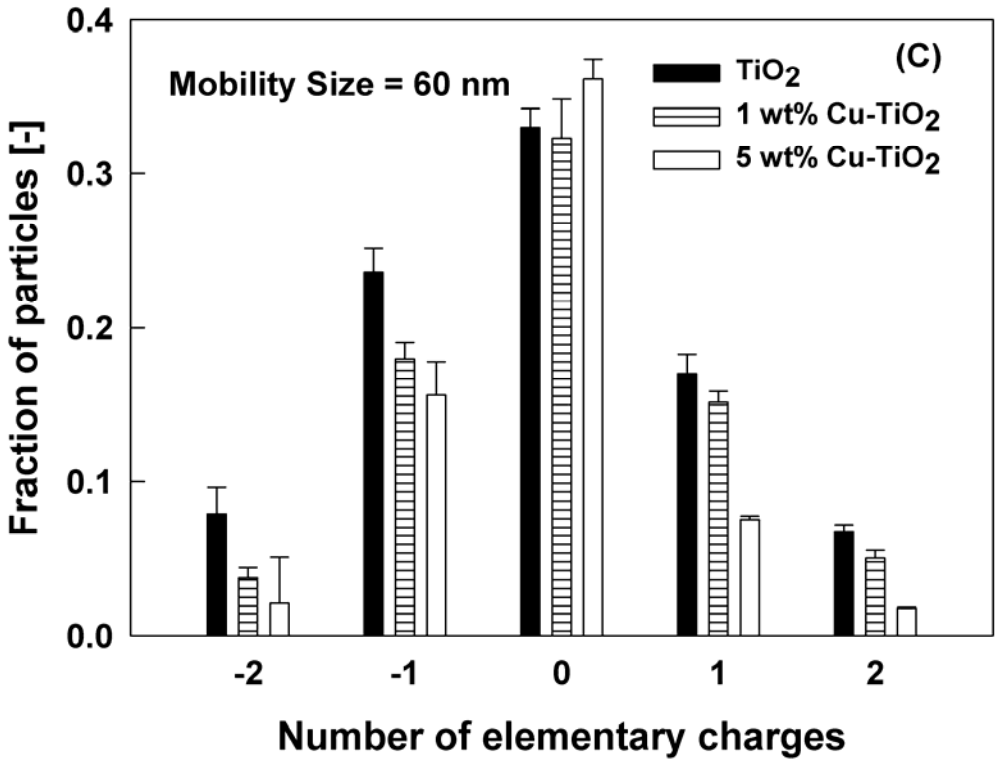

Figure 3- 3: Fraction of elementary charges carried by TiO_2 and Cu-doped TiO_2 nanoparticles for different mobility diameters (A) 25 nm (B) 40 nm (C) 60 nm (Test-2-3).

atoms in the crystal structure, as well as on crystal defects (Jian-Bo and Xiao-Peng, 2001). Sahu and Biswas (2011) demonstrated that with the addition of copper dopant to TiO_2, the defects generated promoted anatase to rutile crystal phase transition. They also observed distortion in the crystal structure, which shifted the diffraction peak of TiO_2. Mardare and Rusu (2004) and Xie et al (2010) demonstrated that doping increases the dielectric constant of TiO_2, due to structural differences. In the study reported here, the dielectric constant of Cu-TiO_2 particles most likely increased with increasing dopant concentration, which resulted in increasing bipolar coagulation that reduced the charged fraction. Bi-polar coagulation in a high temperature flame can be understood by

understanding its characteristic time, given by (Eliasson and Egli, 1991; Kim et al., 2006),

$$\tau_c = k_{ij}^{-1} n_p^{-1}, \quad (1)$$

$$k_{ij} = \frac{8\pi\pi_0}{3\mu}(p_r E)^2 (r_i r_j)(r_i + r_j), \quad (2)$$

$$p_r = \frac{3\varepsilon_r}{(\varepsilon_r + 2)}, \quad (3)$$

where k_{ij} is the collision co-efficient, E is the electric field strength of a particle, r_i and r_j are particle radii, and ε_r is the relative dielectric constant. The equation indicates that increasing dielectric constant (ε_r) enhances the bipolar coagulation rate by reducing τ_c. Therefore the increased dielectric constant due to copper doping may have reduced the charged particle fraction. The reduction in the charged fraction can be attributed to neutralization of particles as a result of both ion/electron impact and bipolar coagulation mechanisms. However, a more detailed understanding of the dielectric constant change with copper dopant is essential for a more quantitative explanation of the increasing bipolar collision rate, which is beyond the scope of this study.

The same experiments were repeated for determining the negatively charged particle fraction by changing the central electrode potential of DMA-1 to positive. The measured negatively charged -1 and -2 fractions are shown in Figure 3-3. The fraction of negatively charged particles increases with increasing particle diameter, and fewer particles carry -2 charges than -1 charge. This charging behavior is similar to that of positively charged particles. Comparing the fraction of positively charged and negatively charged particles, no significant difference is observed. However, in both the cases a

decreased charged fraction was observed for Cu-doped TiO_2 nanoparticles, which was attributed to the increased dielectric constant of the copper doped nanoparticles.

The results indicate that diffusion flame synthesized nanoparticles may carry single as well as multiple charges, and the fraction of charges can vary depending on the material properties and other operating parameters in the flame, such as temperature and concentration of ions.

3.4.2. Charging Parameters and Identification of Charging Mechanism

Nanoparticles in a high temperature flame can be charged by both diffusion charging and thermo-ionization charging (Jiang et al., 2007b; Kim et al., 2005; Sorokin and Arnold, 2004; Starik et al., 2008). In diffusion charging, particles are charged by Brownian collision with the positive as well as negative ions generated in the lower part of the flame. Charging depends on the number concentration of ions ($N_{ion}^{\pm}$) and the probability that ions attach to the particle, represented as the ion attachment coefficient, $\beta^{+}(v,q)$ The attachment co-efficient of ions $\beta^{+}(v,q)$ to the particle with a volume v and charge q is given by (Jiang et al., 2007b)

$$\beta^{+}(v,q) = \frac{\pi\theta c_{ion}^{\pm}\delta^{2}\exp(-U(\delta)/k_{B}T)}{1+\exp(-U(\delta)/k_{B}T)\dfrac{\theta c_{ion}^{\pm}\delta^{2}}{4D_{ion}^{\pm}}\displaystyle\int_{0}^{a/\delta}\exp(-U(a/y)/k_{B}T)dy} \quad (4)$$

$$U(r) = \frac{e^{2}}{4\pi\varepsilon_{0}}\left[\frac{q}{r}-\frac{(\varepsilon_{p}-1)}{(\varepsilon_{p}+1)}\frac{a^{3}}{2r^{2}(r^{2}-a^{2})}\right], \quad (5)$$

where $U(r)$ is the potential energy at distance r from the particle with radius a, v is the particle volume, q is the number of charges carried by the particle, $c_{ion}^{\pm}$ are the thermal velocities of positive and negative ions, $D_{ion}^{\pm}$ are the diffusion coefficients of positive and

negative ions, k_B is Boltzmann's constant, T is the temperature of the system, and y is a dimensionless integration variable ranging from 0 to a/δ. δ is the limiting sphere radius and is given by (Fuchs, 1963; Jiang et al., 2007b; Liu and Pui, 1977)

$$\delta = \frac{\mathrm{a}^3}{(\lambda_{ion}^{\pm})^2}\left[\frac{(1+\lambda_{ion}^{\pm}/a)^5}{5} - \frac{(1+(\lambda_{ion}^{\pm}/a)^2)(1+\lambda_{ion}^{\pm}/a)^3}{3} + \frac{2}{15}(1+(1+\lambda_{ion}^{\pm}/a)^{\frac{5}{2}})\right], \quad (6)$$

Thermo-ionization charging depends on thermal radiation and the work function of the material synthesized in the flame. When thermal radiation exceeds the work function of a material, electrons are emitted, a phenomena which strongly depends on material properties as well as temperature. The thermo-ionization yield co-efficient, based on the flow of electrons from the heated surface, is given by the Richardson and Dushman equation (Dushman, 1923) for a particle of volume v, carrying a charge q, as

$$\gamma^{+}(v,q) = AT^2 \exp\left(-\frac{\phi(v,q)}{k_B T}\right)\frac{4\pi a^2}{e}, \quad (7)$$

where $\phi(v,q)$ is the work function of the material, T is the temperature, A is a material dependent constant, and a is the particle diameter. The work function that must be overcome for an electron to escape is given by,

$$\phi(v,q) = \phi_{\infty} + \frac{e^2(q+1)}{4\pi\varepsilon_0 a} - \frac{5}{8}\left(\frac{e^2}{4\pi\varepsilon_0 a}\right), \quad (8)$$

where ϕ_{∞} is the work function for the plane surface of the material.

The relative importance of the two charging mechanisms can be examined by two important parameters, the attachment coefficients for diffusion charging and the thermo-ionization yield coefficients for different ion concentrations ($N_{ion}^{\pm}$)at different

temperatures. Using the parameters for TiO_2 nanoparticles listed in Table 3-2, the attachment co-efficient and the thermo-ionization yield co-efficient were calculated.

Table 3- 2: Parameters used for modeling

Parameters	**Values**
Temperature (T)	2000 K
Elementary Charge (e)	1.602×10^{-19} C
Permittivity of air (ε_0)	8.854×10^{-12} $C^2/N/m^2$
Positive ion mobility ($Z_{ion}^{\pm}$)	1.1×10^{-12} $m^2/V/s$
Positive ion mass ($m_{ion}^{\pm}$)	150 amu (1amu=1.661×10^{-27} kg)
Dielectric constant for TiO_2 (ε_p)	88
Work function for TiO_2 (Φ_p)	6.7 eV (8.20×10^{-19} J)
Empirical constant (A)	120 amp/cm^2deg^2

Figure 3-4 illustrates the variation of both coefficients with particle diameter. For diffusion charging, the attachment coefficient increases with particle diameter as more surface area is available for the attachment of ions. Particles less than 10 nm in size cannot be multiply charged by diffusion charging, as the attachment co-efficient of particles carrying multiple charges is zero. Particles smaller than 7 nm will not carry any charge, as the attachment coefficient is zero. Experimental charge measurements also confirmed that particles less than 7 nm carry no charge. Due to the electrostatic repulsive force between particles and ions, the attachment co-efficient decreases with particles carrying +1 and +2 charges compared to particles carrying zero charge, which is consistent with the reported values (Jiang et al., 2007b). Figure 3-4 (B) illustrates the

thermo-ionic yield coefficient variation with particle size at a temperature of 2200 K, which is the usual temperature in our flame system. As shown particles smaller than 20 nm cannot be charged by thermo-ionization in the flame, whereas particles smaller than

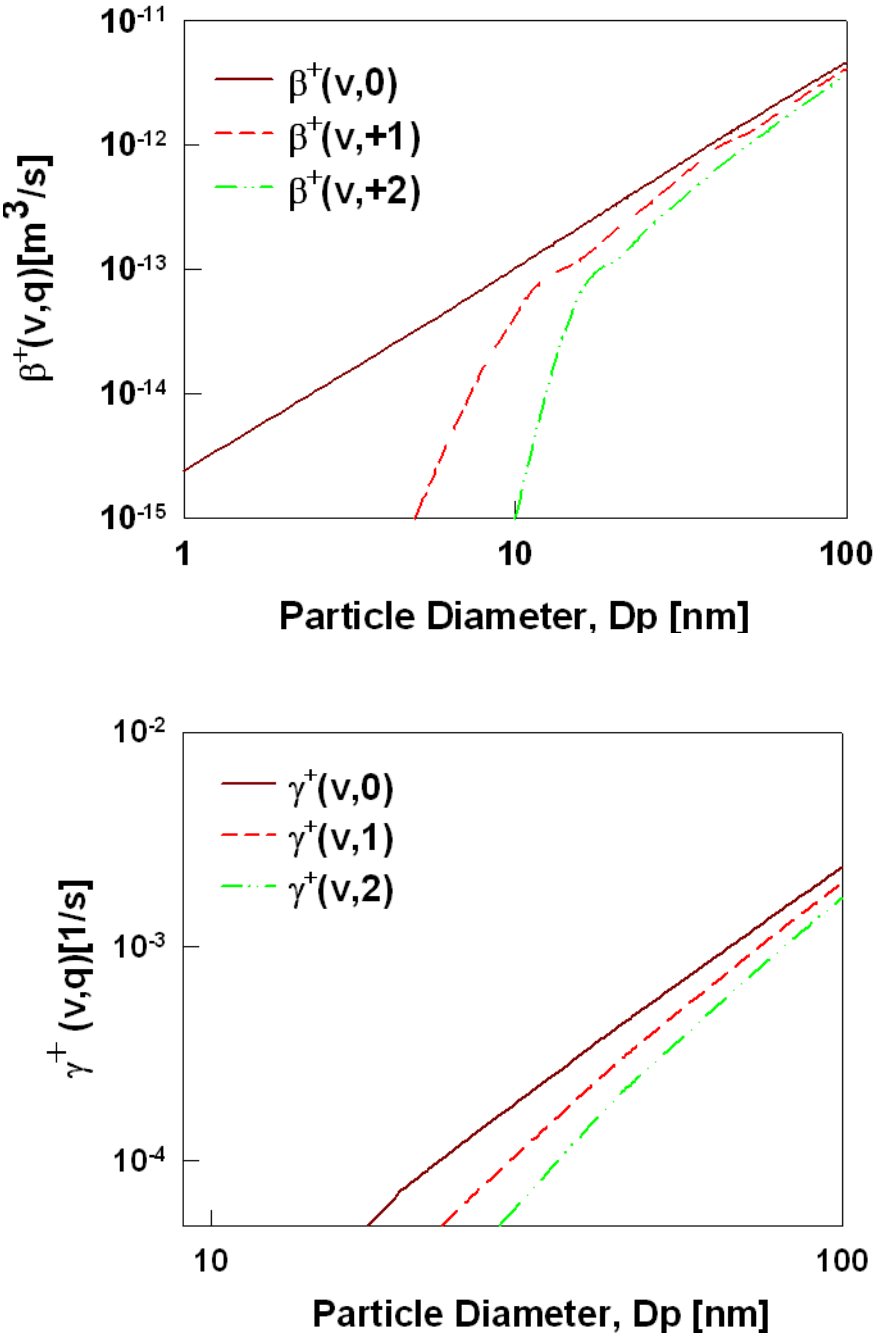

Figure 3- 4: (A) Diffusion charging co-efficient and (B) Thermionic yield co- efficient as function of particle size

25 nm cannot be multiply charged. However, the yield coefficient increases monotonically with size. It is important to note that the yield coefficient is strongly dependent on the work function of the material and the thermo-ionization constant, which was assumed to have a value of 120 amp/cm^{2}deg^2 (Dushman, 1923). A few studies have reported that these parameters may change for different materials (Hensley, 1961; Koeck et al., 2009). Dushman (1923) value was used for the calculation in this study as no values are available for TiO_2 nanomaterials in the literature.

The relative importance of the two chargin mechanisms (diffusion and thermo-ionization) was determined by the dimensionless ratio of both parameters (the ion attachment co-efficient and thermo-ionic yield coefficient) at different flame operating conditions. The concentration of positive ions considered in this analysis was 10^{12} ions/cm^3, the range of ion concentration in a flame (Kim et al., 2005). The thermo-ionization yield co-efficient was calculated for a range of temperatures (1700 to 2500 K). The dimensionless ratio is illustrated in Figure 3-5 for different particle sizes. The results indicate that above 2500 K thermo-ionization charging is dominant for particle sizes above 10 nm. However, below 10 nm, particles are charged only by diffusion charging, as the thermo-ionization yield co-efficient is zero in this size range. For temperatures below 2500 K, diffusion charging is the dominant mechanism. The experimental results suggest that the fractions of positive and negative charged particles are similar, which is consistent with our calculation. The result suggests that by controlling the important

process parameters (temperatures, ion concentrations) the charging mechanism can be manipulated.

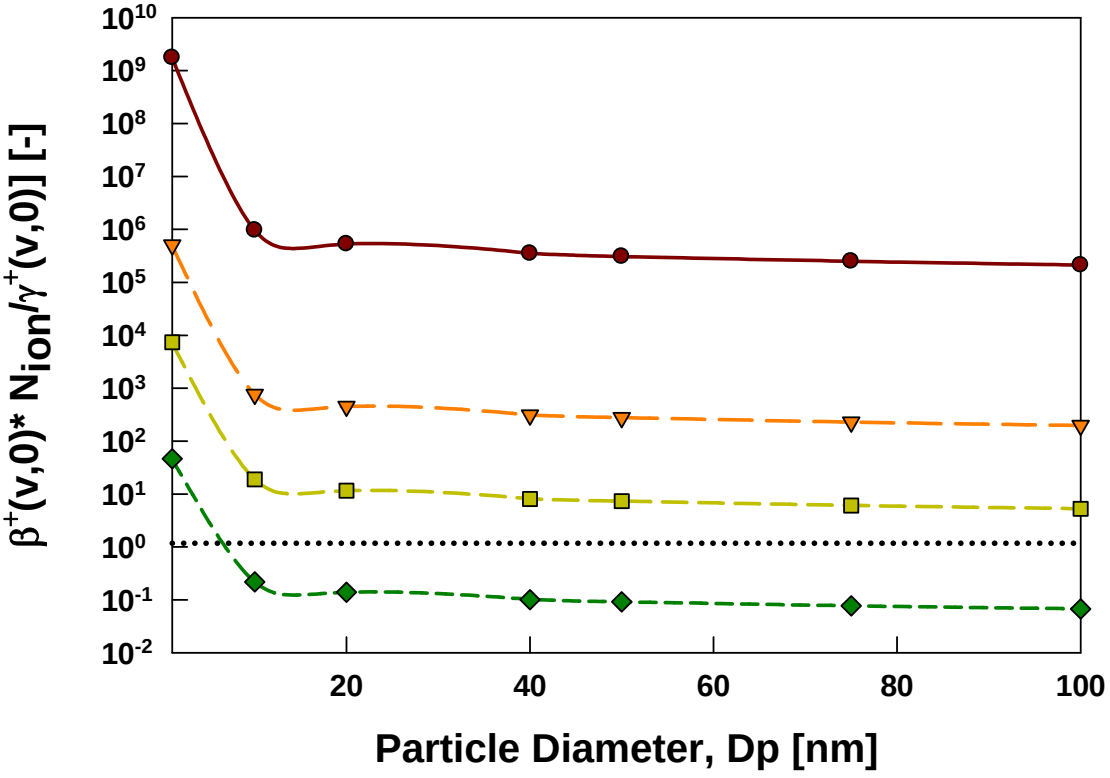

Figure 3-5: Identification of dominant regimes for diffusion charging and thermionic charging in the flame synthesis of nanoparticles (Region above the dotted line is diffusion charging dominant, below it is thermionic charging dominant).

3.5. Conclusions

In-situ charge distribution for TiO_2 and Cu-doped TiO_2 nanoparticles was measured using a TDMA system integrated with a flame synthesis system. The results indicate that particles synthesized by a diffusion flame reactor carry single as well as multiple charges. The charge distribution depends on the mobility diameter and material properties: Cu-

doped TiO_2 had a smaller charged fraction than TiO_2 particles. Fractions of positive as well as negatively charged particles were similar, suggesting that diffusion charging is the dominant mechanism in the diffusion flame reactor. A theoretical calculation based on the attachment co-efficient of ions to particles and on the thermo-ionization yield co-efficient suggests that particles smaller than 10 nm are mostly charged by diffusion charging. The thermo-ionization mechanism is dominant for flame temperatures over 2500 K. In our flame reactor (~2200 K) for synthesis of TiO_2 and Cu-TiO_2, diffusion is the dominant charging process. This detailed understanding of the charging behavior during synthesis can be helpful for effective sampling and capture, and can help in controlling material properties during the synthesis process.

3.6. References

Ahn KH, Sohn SH, Jung CH, Choi M. In situ measurement of nano particle size distribution and charge characteristics in H-2/O-2/TEOS diffusion flame. Scripta Materialia 2001; 44: 1889-1892.

Almquist CB, Biswas P. Role of synthesis method and particle size of nanostructured TiO2 on its photoactivity. Journal of Catalysis 2002; 212: 145-156.

An WJ, Thimsen E, Biswas P. Aerosol-chemical vapor deposition method for synthesis of nanostructured metal oxide thin films with controlled morphology. Journal of Physical Chemistry Letters 2010; 1: 249-253.

Asahi R, Morikawa T, Ohwaki T, Aoki K, Taga Y. Visible-light photocatalysis in nitrogen-doped titanium oxides. Science 2001; 293: 269-271.

Burtscher H. Measurement and characteristics of combustion aerosols with special consideration of photoelectric charging and charging by flame ions. Journal of Aerosol Science 1992; 23: 549.

Chen DR, Pui DYH, Mulholland GW, Fernandez M. Design and testing of an aerosol sheath inlet for high resolution measurements with a DMA. Journal of Aerosol Science 1999; 30: 983-999.

Dhumal SY, Daulton TL, Jiang J, Khomami B, Biswas P. Synthesis of visible light-active nanostructured TiOx (x < 2) photocatalysts in a flame aerosol reactor. Applied Catalysis B-Environmental 2009; 86: 145-151.

Dushman S. Electron emission from metals as a function of temperature. Physical Review 1923; 21: 623–636.

Eliasson B, Egli W. Bipolar coagulation modeling and applications. Journal of Aerosol Science 1991; 22: 429-440.

Fuchs NA. On the stationary charge distribution on aerosol particles in a bipolar ionic atmosphere. Pure and Applied Geophysics 1963; 56: 185-193.

Hensley EB. The effective work function is given by the Richardson equation when an "A" value of 120 amp/cm2 is assumed. Journal of Applied Physics 1961; 32: 301.

Jian-Bo Y, Xiao-Peng Z. Electrorheological effects of cerium-doped TiO2. China Physics Letter 2001; 18: 1144.

Jiang J. Studies of nanoparticle synthesis and charging in the gas phase: Appications in environemntal nanotechnology and nanotoxicology. Energy, Environemntal and Chemical Engineering. PhD Thesis. Washington University in St. Louis, St Louis, 2008, pp. 221.

Jiang J, Chen DR, Biswas P. Synthesis of nanoparticles in a flame aerosol reactor with independent and strict control of their size, crystal phase and morphology. Nanotechnology 2007a; 18: 285603.

Jiang J, Lee MH, Biswas P. Model for nanoparticle charging by diffusion, direct photoionization, and thermionization mechanisms. Journal of Electrostatics 2007b; 65: 209-220.

Karasev VV, Ivanova NA, Sadykova AR, Kukhareva N, Baklanov AM, Onischuk AA, et al. Formation of charged soot aggregates by combustion and pyrolysis: charge distribution and photophoresis. Journal of Aerosol Science 2004; 35: 363-381.

Kim H, Kim J, Yang HJ, Suh J, Kim T, Han BW, et al. Parallel patterning of nanoparticles via electrodynamic focusing of charged aerosols. Nature Nanotechnology 2006; 1: 117-121.

Kim SH, Woo KS, Liu BYH, Zachariah MR. Method of measuring charge distribution of nanosized aerosols. Journal of Colloid and Interface Science 2005; 282: 46-57.

Koeck FAM, Nemanich RJ, Lazea A, Haenen K. Thermionic electron emission from low work-function phosphorus doped diamond films. Diamonds and Related Materials 2009; 19: 789-791.

Kulkarni P, Namiki N, Otani Y, Biswas P. Charging of particles in unipolar coronas irradiated by in-situ soft X-rays: enhancement of capture efficiency of ultrafine particles. Journal of Aerosol Science 2002; 33: 1279-1296.

Liu BYH, Pui DYH. On the unipolar diffusion charging of aerosol particles in the continuum regime. Journal of Colloid and Interface Science 1977; 58: 142-149.

Mardare D, Rusu GI. Comparision of the dielectric properties for doped and undoped TiO2 thin films. Journal of Optoelectronics and Advanced Materials 2004; 6: 333 - 336.

Modesto-Lopez LB, Thimsen EJ, Collins AM, Blankenship RE, Biswas P. Electrospray-assisted characterization and deposition of chlorosomes to fabricate a biomimetic light-harvesting device. Energy & Environmental Science 2010; 3: 216-222.

Onischuk AA, di Stasio S, Karasev VV, Baklanov AM, Makhov GA, Vlasenko AL, et al. Evolution of structure and charge of soot aggregates during and after formation in a propane/air diffusion flame. Journal of Aerosol Science 2003; 34: 383-403.

Sahu M, Biswas P. Size distributions of aerosols in an indoor environment with engineered nanoparticle synthesis reactors operating under different scenarios. Journal of Nanoparticle Research 2010; 12: 1055-1064.

Sahu M, Biswas P. Single-step processing of copper-doped titania nanomaterials in a flame aerosol reactor. Nanoscale Research Letters 2011; In review.

Sgro LA, D'Anna A, Minutolo P. Charge distribution of incipient flame-generated particles. Aerosol Science and Technology 2010; 44: 651-662.

Sorokin A, Arnold F. Electrically charged small soot particles in the exhaust of an aircraft gas-turbine engine combustor: comparison of model and experiment. Atmospheric Environment 2004; 38: 2611-2618.

Starik AM, Savel'ev AM, Titova NS. Formation of charged nanoparticles in hydrocarbon flames: principal mechanisms. Plasma Sources Science & Technology 2008; 17: -.

Thimsen E, Biswas P. Nanostructured photoactive films synthesized by a flame aerosol reactor. AIChe Journal 2007; 53: 1727-1735.

Tiwari V, Jiang J, Sethi V, Biswas P. One-step synthesis of noble metal-titanium dioxide nanocomposites in a flame aerosol reactor. Applied Catalysis a-General 2008; 345: 241-246.

Vemury S, Pratsinis SE. Charging and coagulation during flame synthesis of silica. Journal of Aerosol Science 1996; 27: 951-966.

Vincent JH. On the practical signicance of electrostatic lung deposition of isomeric and 9brous aerosols. Journal of Aerosol Science 1985; 16: 511–51.

Wang ZM, Yang GX, Biswas P, Bresser W, Boolchand P. Processing of iron-doped titania powders in flame aerosol reactors. Powder Technology 2001; 114: 197-204.

Xie Y, Yin S, Hashimoto T, Tokano Y, Sasaki A, Sato T. A comparative study of different solvothermal methods for the synthesis of Sn2+-doped BaTiO3 powders and their dielectric properties Journal of Material Science 2010; 45: 725-732.

3.7. Supporting Information

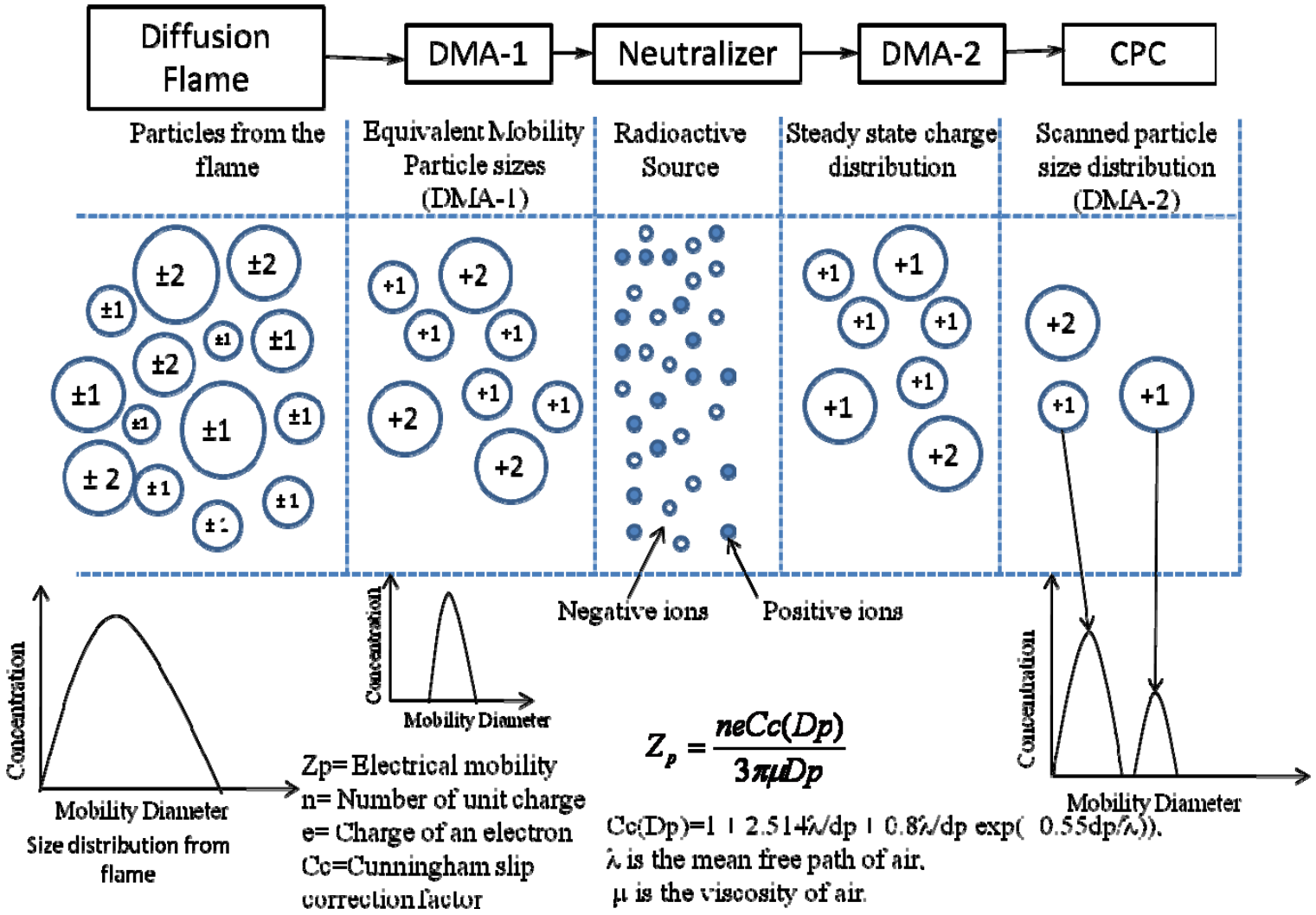

Figure S-1. Conceptual description of charge distribution characterization by TDMA size distribution measurement (Modified from Kim et al., 2005)

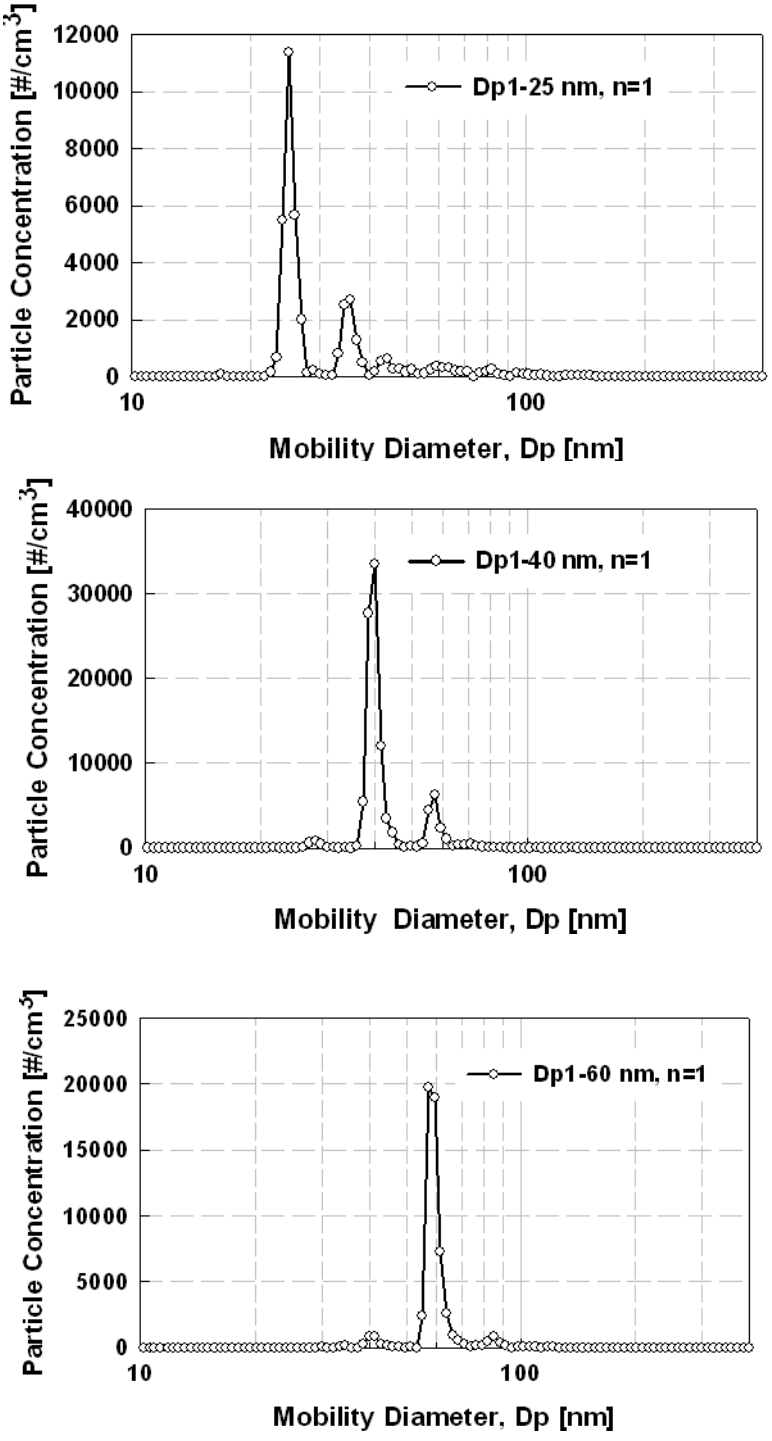

Figure S-2. Size distribution measurement from the flame aerosol reactor by TDMA at different mobility diameters (A) 25 nm (B) 40 nm (C) 60 nm (Test-2-3).

Chapter 4:

Size Distributions of Aerosols in an Indoor Environment with Engineered Nanoparticle Synthesis Reactors Operating Under Different Scenarios

The results presented here were published in:

Sahu, M and P. Biswas, *Concentration and Size Distribution of Nanoparticles in a Research Laboratory Working Environment with Nanomaterial Synthesis Reactors*. Journal of Nanoparticle Research, 2010, 12 (3): p 1055-1064.

4.1. Abstract

Size distributions of nanoparticles in the vicinity of synthesis reactors will provide guidelines for safe operation and protection of workers. Nanoparticle concentrations and size distributions were measured in a research academic laboratory environment with two different types of gas phase synthesis reactors under a variety of operating conditions. The variation of total particle number concentration and size distributions on the distance from the reactor, off design state of the fume hood, powder handling during recovery and maintenance of reactors are established. Significant increases in number concentrations were observed at all the locations during off design conditions (i.e. failure of the exhaust system). Clearance of nanoparticles from the work environment was longer under off design conditions (20 minutes) compared to that under normal hood operating conditions (4 to 6 minutes). While lower particle number concentrations are observed during operation of furnace aerosol reactors in comparison to flame aerosol reactors, the handling, processing and maintenance operations result in elevated concentrations in the work area.

Key words: Nanoparticles, exposure, gas phase synthesis, size distribution, particle concentration

4.2. Introduction

Engineered nanoparticles are building blocks for nanotechnology applications and are finding use in a variety of sectors such as electronics, medicine, energy, environment and many consumer products. Production of engineered nanomaterials with controlled sizes and structures are expected to increase due to their wide scale applicability (Maynard and Kuempel 2005). A recent database of nanotechnology products maintained by the Woodrow Wilson International Center for Scholars established that there are more than 600 consumer products that have nanomaterial constituents (Clarence 2008). Hence, there is significant interest in ensuring that nanomaterials are safe, and do not have any adverse consequences to the environment and human health (DOE 2007; NIOSH 2002; 2007). Many studies to establish the toxicity of nanoparticles are being conducted (Limbach et al., 2007; Nel et al., 2006; Oberdorster et al., 2005; Sayes et al., 2007, Jiang et al., 2008). For exposure measurement biologically relevant dose metrics such as number concentration, mass concentration, and surface area concentration should be considered for personal exposure to workers (Jiang, et al. 2008). To holistically ensure the environmental health and safety of nanomaterials, several steps as illustrated in Figure 4-1 have to be evaluated. The issue of safe nanotechnology requires a very comprehensive study ranging from exposure assessment, determination of metrics, toxicological and epidemiological studies, and life cycle analysis.

As outlined in Figure 4-1, exposure to nanoparticles can occur in a variety of different steps in the life cycle. An important aspect is the assessment of potential exposure to nanoparticles in the occupational environment where they are produced, and the adoption of control technologies and risk management practices. Unlike other

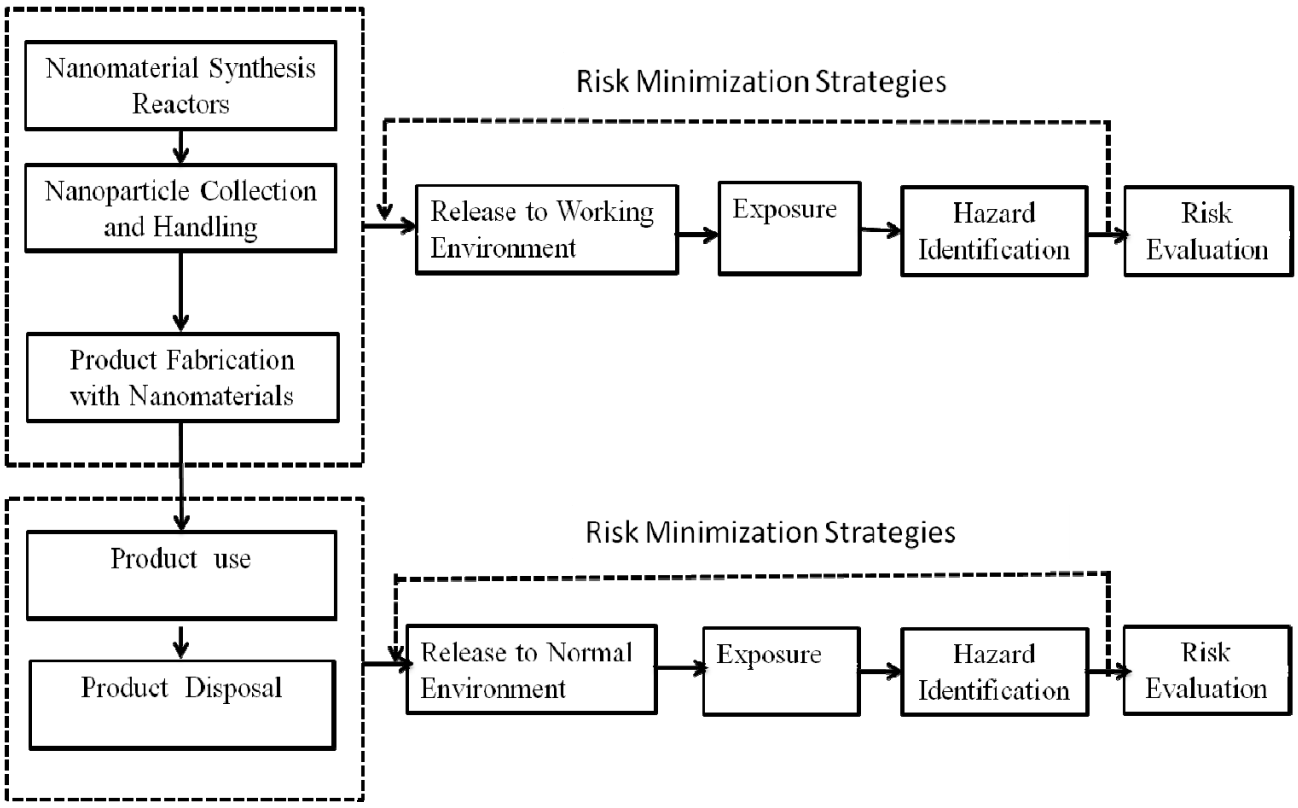

Figure 4- 1: Exposure pathway to naoparticles during the product lifecycle

occupational environments, only a limited set of guidelines have been proposed and are available (e.g., NIOSH 2007). While there have been several studies to examine workplace aerosol concentrations in welding and other high temperature operations (Biswas and Wu 2005; Iyiegbuniwe et al., 2007; Lee et al., 2007; Vincent and Clement 2000), very limited information is available in workplaces where engineered nanomaterials are synthesized, especially of any potential risks to health which might arise during their manufacture, use and disposal. Maynard et al. (2004) investigated the exposure and nature of aerosols in a laboratory and a field study during handling of unrefined single walled carbon nanotube (SWCNT) material. In their laboratory study

they found that fine particles were released into the environment when agitated, whereas in the field study airborne particle concentrations observed were not high. Tsai et al. (2009) studied the airborne exposure associated with the manual handling of nanoalumina and nanosilver in different fume hoods. Their study showed that the extent of exposure to nanoparticles during manual handling of nanomaterials depended on the quantity, type, handling methods and the different conditions in the fume hood. In another study Tsai et al. (2008) also studied the exposure during production of nanocomposites by compounding of the nanoparticles and polymer in a twin screw extruder. They demonstrated that quantity of nanoparticles release into air depends on the loading condition of the alumina and the polymer in the feeding system and the phases of operation of the twin screw feeder during the compounding process. The NIOSH guidelines report indicates that the development of a well designed exposure assessment study is needed for better understanding of the health effects caused due to exposure to nanoparticles, and to determine cost effective control measures to reduce exposure and improving baseline data for occupational settings.

Due to the continued development of new nanomaterials with different functionalities, these materials are being synthesized in a number of smaller scale research laboratories or small businesses, in lower volume production amounts compared to the large powder manufacturing industry. Academic research laboratories are an ideal first step to conduct evaluation studies as much of the early work producing nanoparticles is done therein. Changes in operating scenarios in academic laboratories under controlled conditions could also be readily done to evaluate the impacts on exposure. There are a few reports of laboratory studies on potential exposure on handling of nanomaterials

(Tsai et al., 2009; Maynard et al., 2004) and fewer on resulting size distributions during synthesis (Park et al., 2009; Demou et al., 2008) . A careful examination of the distribution of nanoparticle aerosols in the vicinity of gas-phase particle synthesis reactors has not been conducted. The Flame Aerosol Reactor (FLAR) and Furnace Aerosol Reactor (FUAR) are two commonly used aerosol synthesis methods for nanomaterials (Basak et al., 2007; Namiki et al., 2005, Jiang et al., 2007; Thimsen and Biswas 2007). In this paper, the results of a study of nanoparticle concentrations and size distributions under different scenarios in an academic research laboratory where multiple synthesis reactors are operational are reported. The emphasis is on the use of gas phase reactors, as they are scalable processes that are commonly used in industry. The size distributions and total concentrations of nanoparticles in the laboratory working environment measured by real time aerosol instruments under different operating scenarios of synthesis, product handling, recovery and maintenance are reported. Different scenarios to mimic potential off design operating conditions of the fume hoods were considered to establish the exposure levels. The morphology and chemical composition of the collected aerosols during synthesis are also presented.

4.3. Experimental

An academic research laboratory with several gas phase nanoparticle synthesis reactors was selected for this study. While the reactors are all placed in hoods and extreme precautionary principles are adopted, the setting offers a test site for study and evaluation, especially under off-design conditions.

4.3.1. Test Site

Two gas phase synthesis processes for nanomaterials, a FLAR and FUAR were examined in this study in a typical research laboratory environment. These reactors are located in a 120 m^2 (12 m ×10 m) research laboratory, with three laboratory fume hoods of dimension 1.5m L × 0.9m W × 2.28m H with hood face velocity of 0.5 m/sec. The layout of the laboratory test site with the gas phase reactors is shown in the Figure 4-2 (A). Such an environment is reflective of a small business with reactors that are used for production of nanomaterials during initial phases of development. The description of the two gas phase synthesis processes and characterization techniques of the particles are described in detail in the following sections.

4.3.2. Gas Phase Reactors

High temperature processes are used in gas phase reactors wherein precursors are oxidized to produce the desired product vapor, followed by their nucleation to form nanoparticles. The nanoparticles further grow by simultaneous condensation and coagulation mechanisms

4.3.2.1. Flame aerosol reactor (FLAR) synthesis process

In the flame synthesis process, nanoparticles are generated by high temperature decomposition of precursors. In this study, the FLAR system was used to produce nanoparticles and deposit them to create nanostructured films for different solar energy applications (Thimsen and Biswas 2007). Titanium tetra-isopropoxide (TTIP, Aldrich, 97% purity) was used as the precursor for the production of the nanoparticles in a methane-oxygen flame by thermal oxidation. The temperature of the bubbler was

maintained at 37 ^{o} C. The methane flow rate was 0.9 lpm (liters per minute at STP) and the oxygen flow rate was fixed at 2.7 lpm; with a resultant flame temperature of 2200 ^{0}C. The FLAR was operated at two different feed rates of the TTIP precursor, keeping all other parameters constant though out the operation.

4.3.2.2. Furnace aerosol reactor (FUAR) synthesis process

Titanium dioxide nanoparticles to be used for environmental applications were produced by thermal oxidation of TTIP precursor in the furnace aerosol reactor (Namiki et al., 2005) . The precursor vapor was carried by N_2 gas into the FUAR and was decomposed at different temperatures (500-1200 ^{o} C) to obtain the desired characteristics of particles. The exhaust gases from the reactor were cooled to room temperature and an electrostatic precipitator (ESP) operated at + 10 kV was used to collect the synthesized particles. Additional details of the experimental setup and the synthesis process is given in Namiki et al. (2005) and Basak et al. (2007).

4.3.3. Particle measurement and characterization

Total particle concentrations were measured by Condensation Particle Counters (CPC) (TSI model 3022a and 3025). Size distributions were measured by two Scanning Mobility Particle Sizer (SMPS) systems consisting of an electrostatic classifier (TSI Model 3080) with a differential mobility analyzer (LDMA; TSI 3081) coupled with condensation particle counters (TSI model 3022a and 3025). The system was operated at 6 lpm of sheath flow rate and 0.3 lpm of aerosol inlet flow rate.

Particles were collected on electron microscope grids using a vacuum pump (100 lpm capacity) during the synthesis process in the FLAR inside the hood under the same operating conditions that were used for the particle concentration and size distribution characterization. The collected particles were analyzed by Scanning Electron Microscopy (SEM, Model Hitachi S4500) coupled with energy dispersive X-ray (EDX) for size, shape, morphology and elemental composition.

4.3.4. Test plan

The total particle number concentrations and size distributions were independently measured in the laboratory environment under different operating scenarios (reactor type, distance from reactor, hood fan ON and OFF, hood door OPEN and CLOSED, precursor feed rates). The experimental plan and test conditions are summarized in Table 4-1.

Table 4-1: Summary of test plan for the study

Reactor	**Measurement Location**	**Operating Conditions**			**Test #**
		Hood Fan	**Hood Door**	**Precursor Feed Rate**	
FLAR	L1, L2, L3 (Figure 2) L1- Inside the hood L2- Breathing zone L3- 2m away from the hood	ON	OPEN	Normal	1
				Low	
		ON	CLOSED	Normal	2
		OFF	OPEN	Normal	3
	L2 (at various times upto 30 min; followed by turning fan ON to determine clearance time)	OFF	OPEN	Normal	4
FUAR	P1, P2, P3 (Figure 2) P1-Precursor feed location P2- Middle of the reactor P3-ESP location	Maintenance/ setup of the rector, product recovery and handling			5

Test 1 establishes the influence of distance (L1: inside the hood at 0.6 m from the flame and 0.3 m height from base of fume hood; L2: breathing zone; just outside the hood near the mouth and nostrils of a typical worker at a height where most likely inhalation exposure would occur; and L3: outside the hood at a distance of 2 m away from the flame and 1 m height from the floor of the laboratory; see Figure 4-2) from the nanoparticle source on concentration and size distribution characteristics, for a normal operating condition (Hood fan ON, Hood Door OPEN). The measurements are taken for two different precursor feed rates (normal – 2 lpm flow rate through bubbler; low – 0.3 lpm flow rate through bubbler), reflecting different nanoparticle production rates. Test 2 is similar to Test 1, except that the hood door is in the CLOSED position. Test 3 represents an off design condition (hood fan OFF - turned off inadvertently or due to a failure), and measurements are conducted at the three locations for a normal feed rate condition. Test 4 represents a temporal variation of the size distribution characteristics at the breathing zone (location L2). Also, reported are estimations of clearance time representative of time required for concentrations to return to background levels.

There maybe potential risks of exposure during handling of synthesized nanoparticles during recovery and processing or packing, and maintenance or cleaning of the gas phase reactors. Product recovery involves mechanical removal of particles from collecting substrates. The level of exposure to nanoparticles during reactor

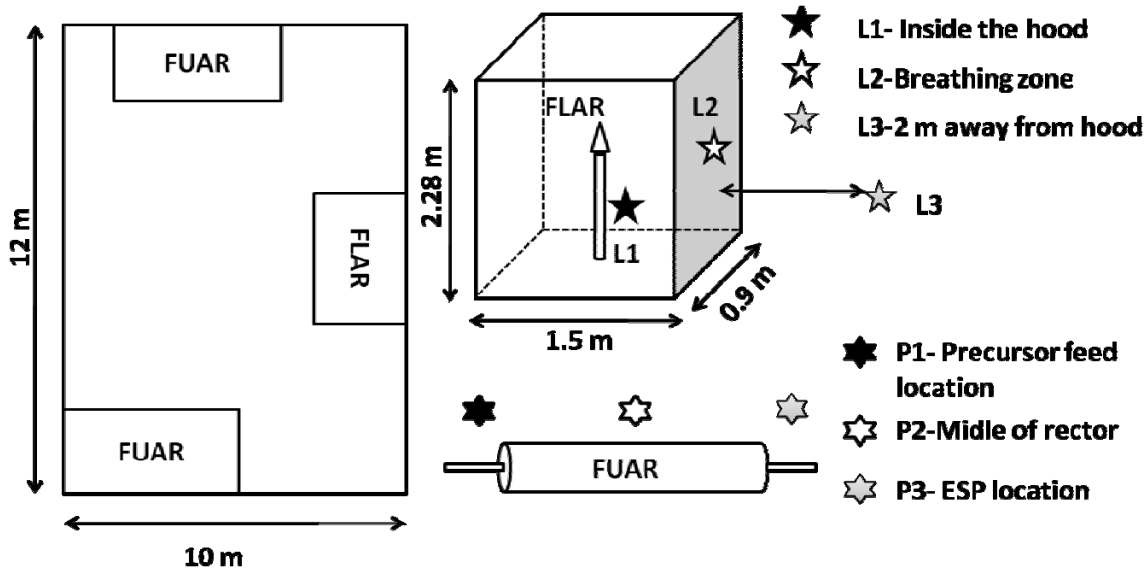

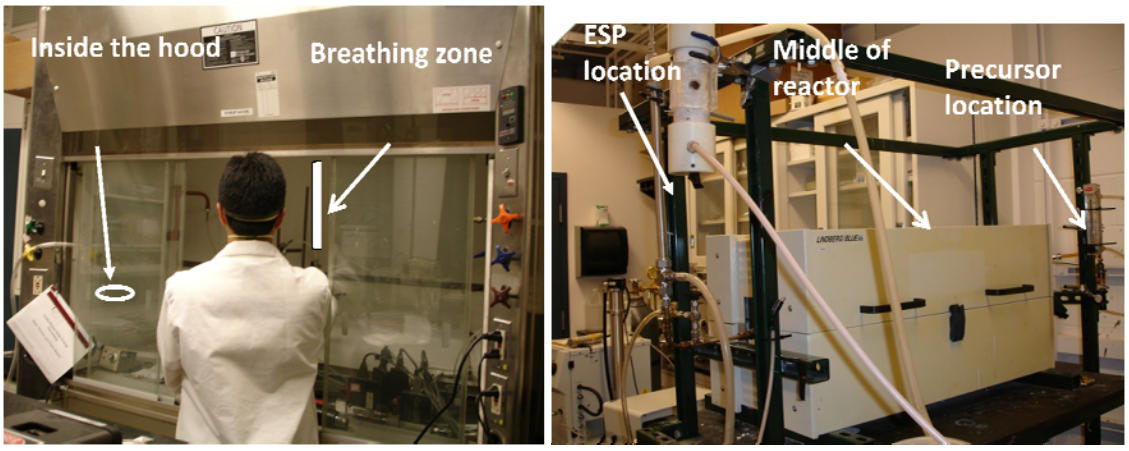

Figure 4- 2: Illustration of the sampling site and sampling locations for the gas phase reactors in the research laboratory with FLAR and FUAR, (B) Photographs of the synthesis system with sampling locations FLAR (Left) and FUAR (Right) (The third sampling location is 2m away from the hood in FLAR system and is not shown)

maintenance/setup, product handling and recovery were measured (Test 5). Background measurements were taken before the start of the synthesis process and other operations to determine the nanoparticle concentration level in the laboratory under normal conditions.

4.4. Results and Discussion

The measurement results during the synthesis process in both the reactors for different operational conditions are discussed first followed by maintenance/setup and product handling and recovery.

4.4.1. Particle concentration and size distribution during FLAR synthesis

4.4.1.1. FLAR system with hood operational

The nanoparticle size distributions during the synthesis process at different distances from the source of generation with the hood fan ON and door open condition (Test 1, Table 4-1) is shown in Figure 4-3. The total number concentration of the particles at L1 inside the hood was 4.03×10^5 particles cm^{-3} with a mean size of 32 nm; whereas the background concentration was 3.33×10^3 particles cm^{-3} with mean size of 48 nm. The concentration at the breathing zone (L2) was 1.06×10^4 particles cm^{-3} with a mean size of 30.8 nm. The operational hood (fan ON) is effective in reducing the concentration at the breathing zone even though the hood door is OPEN. However, the mean size is closer to that measured near the flame reactor and the number concentration is slightly higher than the background; indicating that a few particles are being transported from the flame reactor to near the breathing zone. Tsai et al. (2009) have showed that a complicated turbulent flow pattern exists around the bottom edge of the sash door sill where

contamination leakage is highest in a conventional hood. It is evident that nanoparticle release from the hood must be dependent on the vertical eddy, external cross draft, position of the sash and worker activities. The concentration observed at 2 m away from

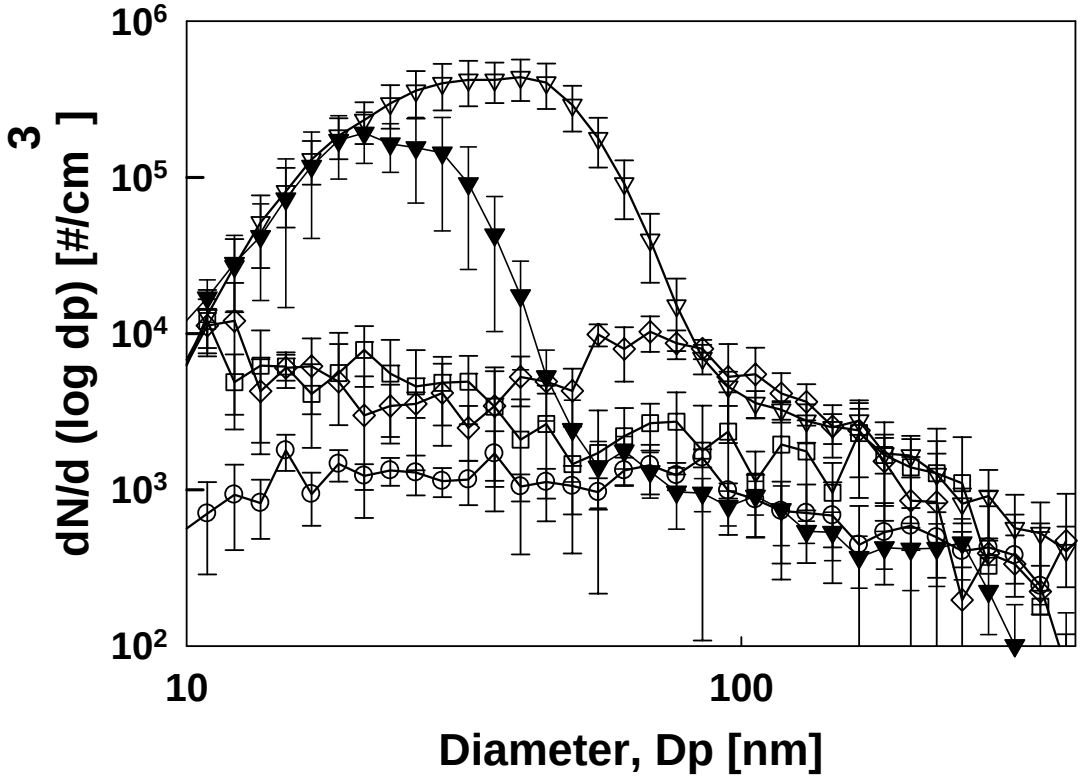

Figure 4- 3: Particle size distributions measured at different distances from the flame in a FLAR system for hood fan ON with door OPEN conditions (Test-1): ○-Background, ▽-Inside the hood (L1), □-Breathing zone (L2), ◇-2m away(L3) (Also shown is the size distribution inside the hood (L1) for a lower precursor feed rate: ▼- 0.3 lpm flow rate through the bubbler).

the synthesis zone (location L3) was 6.77×10^3 particles cm^{-3} with a mean size of ~54 nm (closer to background values). The change in concentration and mean size with distance away from the synthesis zone is due to growth by coagulation and dilution due to the

complex flow patterns. The observed result is consistent with those observed by Lee et al. (2007) in a welding aerosol study that the concentration decreases away from the zone of production with an increase in mean size. Also shown in Figure 4-3 is the size distribution inside the hood (location L1) for a lower precursor feed rate (flow rate through the precursor bubbler of 0.3 lpm, compared to a baseline value of 2 lpm) keeping all other operating conditions in the reactor the same. As expected, the lower precursor feed rate resulted in a lower total particle concentration in the hood. The mean size was lower due to the reduced growth rates (due to lower number concentrations) by collisional mechanisms.

Size distribution measurements were also done with the hood door CLOSED (Test 2), with other conditions similar as Test 1. The results at location L1 inside the hood were identical to the Test 1 conditions with the hood door OPEN. However, the measurements in the breathing zone (L2) and 2m away (L3) were identical to background values, indicating the hood was not leaking. While the hood door CLOSED maybe a preferred mode of operation, it should be noted that the operator has to often leave the hood door OPEN for attending to the FLAR system. Our results indicate that the workers near an operating flame reactor inside an operational hood should wear respiratory protection as a precautionary principle.

4.4.1.2. FLAR system under off design hood condition

The measurements under off design conditions (Test 3 and 4) correspond to a hood fan OFF condition which may happen advertently (turned off by the worker) or inadvertently (due to a failure). Figure 4-4 shows the particle size distributions during off design

conditions of the hood at different distances during synthesis process. The concentration observed during synthesis process at all the three locations (L1, L2 and L3) were identical at ~1.5×10^5 particles cm^{-3}, much higher than the background condition. The

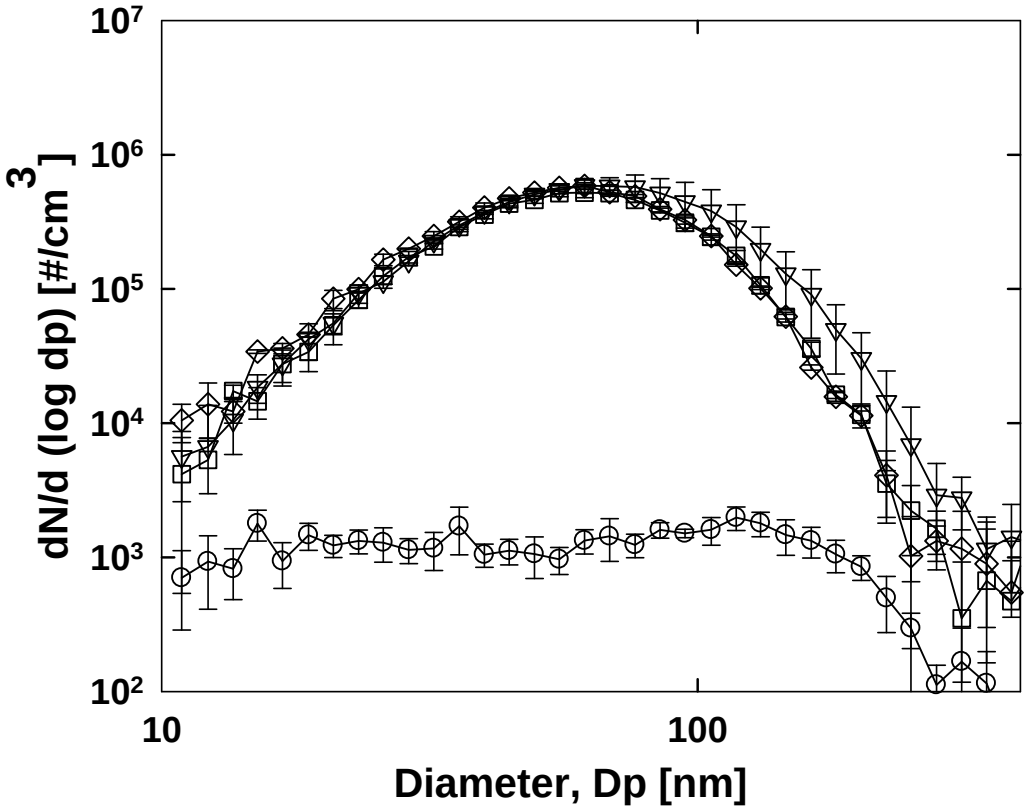

Figure 4- 4: Particle size distributions measured at different distances from the flame in a FLAR system for hood fan OFF with door OPEN conditions (Test-3): ○- Background, ▽- Inside the hood (L1), □- Breathing zone (L2), ◇-2m away (L3).

mean particle sizes were 62 nm, 56 nm and 55 nm inside the hood, breathing zone, and 2 m away from the hood, respectively. The mean size is higher as the particles are not being cleared off, and continue growing by coagulation in the confined space of the hood. The particles also disperse in regions of the vicinity of the hood. It clearly indicates that

without a proper exhaust system the nanoparticles spread throughout the working environment, and potential for exposure to the worker is significant.

An important aspect in nanomaterial production facilities is the clearance time. Under normal operating conditions (as in Test 1), this is important as the worker has to access the collected nanomaterials inside the hood. Similarly, under off-design conditions (Test 3), strategies to clear the work environment of nanoparticles have to be established. The size distributions and particle concentrations after the conclusion of the synthesis process under exhaust fan OFF conditions are shown in Figure 4-5. With the hood fan OFF, there is no significant change in the size distribution, with only a very slight shift to larger sizes. The total number concentration also decreases very slightly up to 30 minutes after the synthesis process was stopped. Under the hood fan OFF conditions, the slight decrease in total particle number concentration and increase in mean size can be attributed to a slow coagulation process. The characteristic time for coagulation of titanium dioxide particles with a diameter of 60 nm and particle concentration of $\sim 1.5 \times 10^5$ is on the order of 10^6 hours.

Convective currents in the laboratory are not sufficiently large to clear the nanoparticles from the breathing zone over a 30 minute period. On turning on the hood fan (at time = 30 min, Figure 4-5b), the total number concentrations start decreasing and reach background levels 20 minutes after the fan was turned ON. Though the breathing zone is just outside the hood, on turning the hood fan ON, it generates convective currents that help clear out the aerosols from the breathing zone. Workers should therefore not turn the hood fan OFF after synthesis is completed, but leave the fan ON during powder collection and system maintenance.

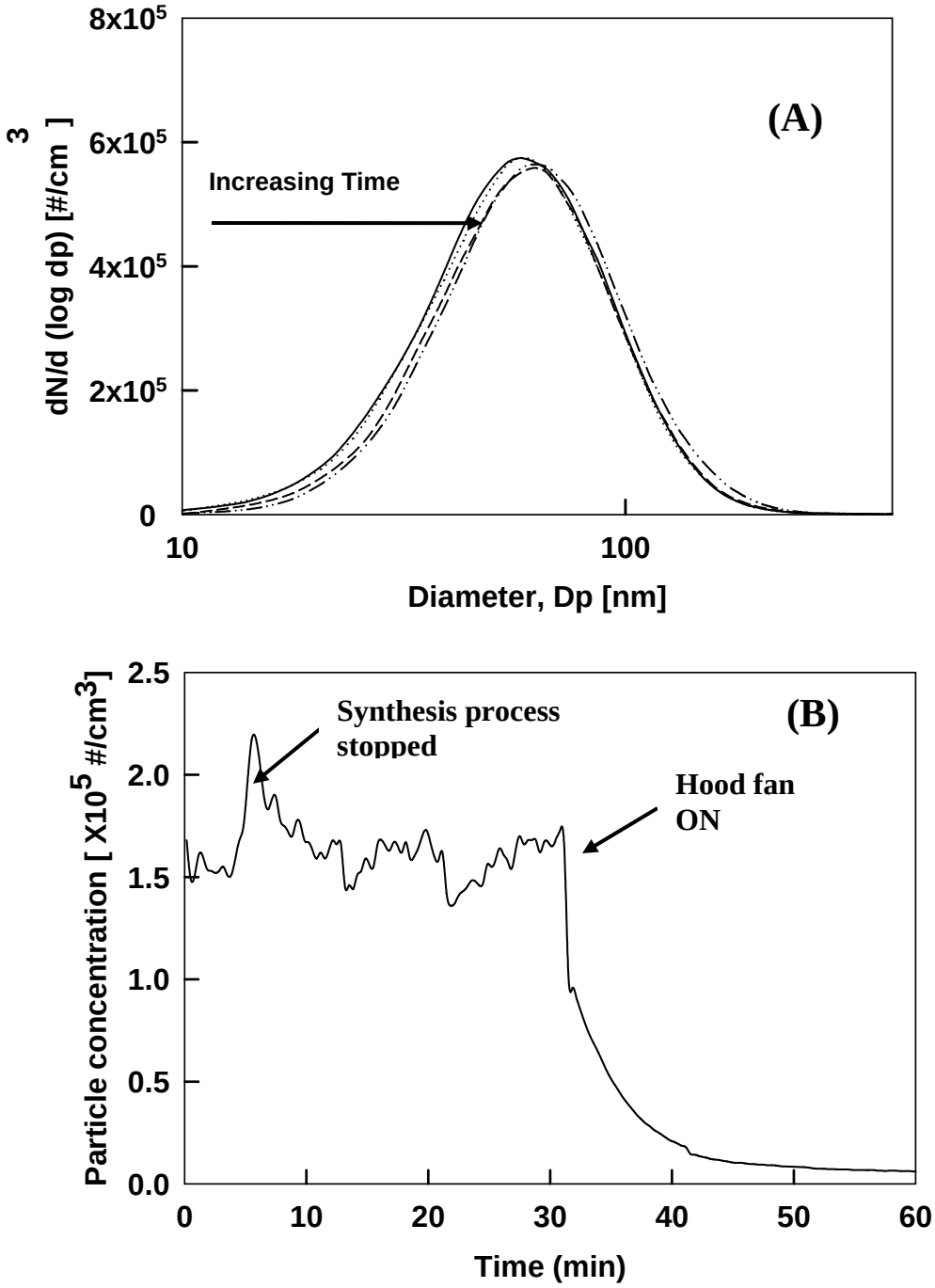

Figure 4- 5: (A) Measured particle size distributions in breathing zone (L2) at four different times after the conclusion of the FLAR synthesis process with hood fan OFF with door OPEN conditions (—10 min ·····15 min - - 25 min —· 30 min) (B) Total particle number concentration variation in breathing zone (L2) after the conclusion of the FLAR synthesis process with hood fan off with door open conditions.

It is interesting to also note that for the same operating conditions of the reactor in a hood operational condition (fan ON), the particle concentration reached the background level in a shorter duration of 4 to 6 minutes after the end of the synthesis process in FLAR. If the hood fan is ON during the synthesis process, the nanoparticle concentrations reach elevated levels only near the source (at L1, but not high at other locations as observed earlier in Figure 4-3, due to continued clearance during operation). Thus, on conclusion of the synthesis process, the clearance time in the hood with the fan ON is a much shorter duration.

4.4.2. Morphology and composition of the nanoparticles

Health effects associated with nanoparticle are dependent on the specific particle, its morphology, surface, composition and size. For example, a study by Oberodorster et al. (1994) showed that TiO_2 particles of the same aerodynamic size, but one made up on agglomerates of smaller primary particles in comparison to another made of larger TiO_2 particles will have a greater biological response. Figure 4-6 shows the size, shape and morphology of the particles collected inside the hood during the FLAR synthesis process at 2 lpm flow rate through the bubbler. The SEM image indicates that particles are spherical in shape with primary particle size less than 40 nm, which is consistent with the mean particle size measured with the SMPS. Some chain-like structures were also observed indicating that some of the particles were agglomerated, probably due to the high concentrations in the collection zone. The energy dispersive X-ray (EDX) analysis coupled with the SEM indicated that the major composition is Ti, which confirms that the particles measured are from the flame synthesis process.

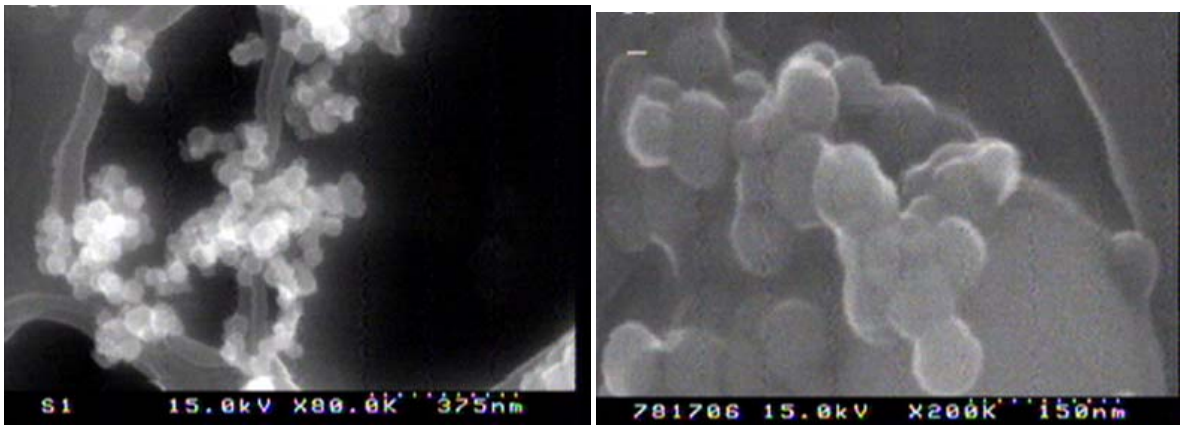

Figure 4- 6: SEM images of particles collected on electron microscope grids during FLAR synthesis

4.4.3. FUAR System: Various Operations

The FUAR is a closed system, and during the synthesis process the particle size distributions were similar at all the locations as the background. The concentrations and size distributions characteristics observed during the synthesis suggest that the chances of exposure to nanoparticles are lower unless there is a leak from the furnace system. In the furnace reactor system, the aerosol formation occurred inside the tubular system enclosed in a closed electrical furnace. The particles were collected with an online ESP (also a closed system), thus minimizing potential exposure.

Though FUAR systems are closed, and do not result in elevated concentrations during synthesis, there could be potential exposure to nanoparticles during handling in recovery operations, and during maintenance of the reactors (Test 5). Figure 4-7 (A) shows the particle size distribution measured during maintenance/set up (i.e. replacing and cleaning of the tubes used for the systems, changing of precursor, cleaning of the ESP) of the FUAR.

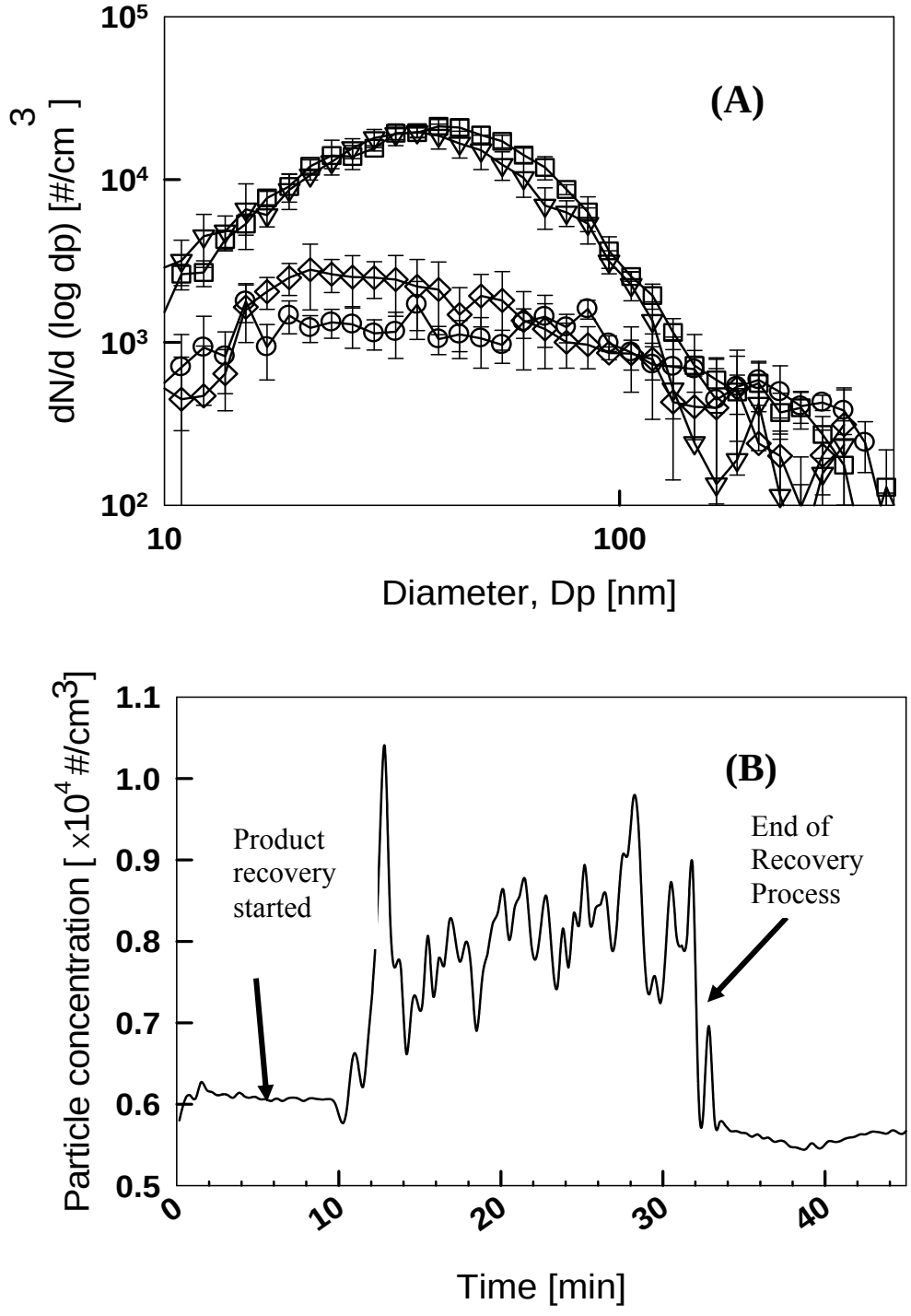

Figure 4-7: (A) Particle size distributions measured at different locations in a FUAR system during maintenance (Test-5): ○- Background, ▽-Precursor feed location (P1), □ - Middle of reactor (P2), ◇-ESP location (P3). (B) Particle concentration variation measured during product handling and recovery.

The concentration of particles was ~1.3×10^6 particles cm^{-3} and ~1×10^6 particles cm^{-3} near the precursor feed location (P1) and middle of the reactor (P2) respectively, compared to 4.5×10^3 particles cm^{-3} in ESP location. The mean particle sizes observed were 34.5 nm, 38.1 nm, 36.7 nm at the precursor feed location, middle of the reactor, and ESP location respectively. A possible reason for the higher particle concentration near precursor feed location and middle of the reactor could be due to the volatile nature of the precursor used for the synthesis in FUAR, some of which escapes into the environment during clean up operations, followed by reaction in the ambient environment to form nanoparticles. The particle number concentration decreased after the precursor was removed and other maintenance processes were finished (Figure 4-7 b). The spatial variation during the cleanup process is also a function of the convective patterns in the laboratory environment, and thus specific to the system for which the measurements were done.

After the nanoparticles are synthesized in gas phase reactors, particles are recovered mechanically from the collecting filters or ESP. Particle concentrations and size distributions were measured during product recovery, handling and weighing of the nanoparticles (Test-5). No significant concentration increase and size distribution change was observed at the breathing zone when 2 gm of nanomaterials were handled. To simulate handling of a large quantity of nanomaterial, a similar experiment was conducted with 25 gm of 25nm titanium dioxide. Increased particle concentration (1.04×10^4 particle cm^{-3} compared to background average concentration of 3.02×10^3 particles cm^{-3}) at the breathing zone was observed during product recovery and during transferring of nanomaterials with a spatula from the ESP to a plastic container box.

From the size distribution measurement, mean size of the particle observed was 29 nm during this product handling and recovery process, which is similar to the size of the particle collected from the ESP. After 10 minutes of conclusion of the recovery process, the concentration reached background levels. While the results in this study indicated that chances of exposure increase if larger amounts are handled; Tsai et al. (2009) found that manual handling of 15 gm of nano alumina in the conventional hood did not increase the particle concentration at the breathing zone significantly compared to handling of 100 gm of nano alumina particles. Thus, systems should be designed appropriately for convective clearance depending on the amounts of nanomaterials being handled.

4.5. Conclusions

The study established size distributions of aerosols in the vicinity of flame and furnace aerosol reactors producing nanomaterials under a variety of operational conditions. Caution has to be exercised with flame aerosol reactors, and hood conditions have to be carefully maintained. Concentrations inside the hood near the flame reactor are significantly higher during the synthesis process even under normal hood operational conditions. If the door of the hood is open with it fully operational, slightly elevated concentrations were measured near the breathing zone. It is therefore recommended that workers wear appropriate respiratory protection devices when operating flame aerosol reactors even if they are inside fully functional fume hoods. After the synthesis process was stopped, it took about 4 to 6 minutes to clear the nanoparticles from the work environment in the vicinity of the hood, and bring it down to background levels.

If the hood is not operational with the fan OFF, the potential for exposure is significantly higher. The concentration outside the hood also increases to levels observed near the flame reactor inside the hood. The nanoparticle aerosol occupies a larger volume of space, and do not clear out readily as there are no strong convective currents in the vicinity of the hood in the fan OFF condition. Furthermore, even on turning on the fan after synthesis is stopped, the clearance time is significantly greater (~ 20 minutes) as a larger volume of air is at the higher concentrations (in contrast to when the hood fan was ON).

Furnace reactors are closed systems, and if designed and operated correctly have a lower chance of worker exposure. However, caution has to be exercised during collection and handlings of the powder as the resultant concentrations are higher than of background levels.

While general guidelines and quantitative observations (size distributions, clearance times) have been reported in the study, they are specific to the system studied. A more generalized estimation and applicability to nanoparticle production facilities would require a more detailed representation of flow patterns and other operational conditions.

4.6. References

Basak, S; Chen, DR; Biswas, P, **2007,** Electrospray of ionic precursor solutions to synthesize iron oxide nanoparticles: Modified scaling law. *Chem. Eng. Sci. 62*, (4), 1263-1268.

Biswas, P; Wu, CY, **2005,** Critical Review: Nanoparticles and the environment. *J. Air Waste Manage. Assoc. 55*, (6), 708-746.

Clarence, DJ, **2008,** *Managing the effects of nanotechnology, Washington D.C Project on Emerging Nanotechnologies*.

Demou, E; Peter, P; Hellweg, S, **2008,** Exposure to Manufactiured Nanostructured Particles in an Industrial Pilot Plant. *Ann. Occup. Hyg. 10.1093/annhyg/men058*, 1-12.

DOE, **2007,** *Approach to Nanomaterial ES&H Department of Energy Nanoscale Science Research Centers, NSRC Revision 2. 6/15/07*.

Iyiegbuniwe, EA; Iyiegbuniwe, AO; Chekuri, L, **2007,** Nanomaterials and health: a critical review of occupational exposure assessment and control strategies. *Int. J. Nanomanuf. 1*, (5), 574-591.

Jiang, J; Chen, DR; Biswas, P, **2007,** Synthesis of nanoparticles in a flame aerosol reactor with independent and strict control of their size, crystal phase and morphology. *Nanotechnology 18*, (28).

Jiang, J; Oberdorster, G; Elder, A; Gelein, R; Mercer, P; Biswas, P, **2008,** Does nanoparticle activity depend upon size and crystal phase? *Nanotoxicology 2*, (1), 33-42.

Lee, MH; McClellan, WJ; Candela, J; Andrews, D; Biswas, P, **2007,** Reduction of nanoparticle exposure to welding aerosols by modification of the ventilation system in a workplace. *J. Nanopart. Res. 9*, (1), 127-136.

Limbach, LK; Wick, P; Manser, P; Grass, RN; Bruinink, A; Stark, WJ, **2007,** Exposure of engineered nanoparticles to human lung epithelial cells: Influence of chemical composition and catalytic activity on oxidative stress. *Environ. Sci. Technol. 41*, (11), 4158-4163.

Maynard, AD; Kuempel, ED, **2005,** Airborne nanostructured particles and occupational health. *J. Nanopart. Res. 7*, (6), 587-614.

Namiki, N; Cho, K; Fraundorf, P; Biswas, P, **2005,** Tubular reactor synthesis of doped nanostructured titanium dioxide and its enhanced activation by coronas and soft X-rays. *Ind. Eng. Chem. Res. 44*, (14), 5213-5220.

Nel, A; Xia, T; Madler, L; Li, N, **2006,** Toxic potential of materials at the nanolevel. *Science 311*, (5761), 622-627.

NIOSH, **2002,** *Exposure assessment methods: Research needs and priorities : NIOSH Report*.

NIOSH, **2007,** *Progress towards safe nanotechnology in the work place: A report from NIOSH nanotechnology Research Center*.

Oberdorster, G; Ferin, J; Lehnert, BE, **1994,** Correlation between Particle-Size, in-Vivo Particle Persistence, and Lung Injury. *Environ. Health Perspect. 102*, 173-179.

Oberdorster, G; Oberdorster, E; Jon, JG, **2005,** Nanotoxicology: An Emerging Discipline Evolving from Studies of Ultrafine Particles. *Environ. Health Perspect. 113*, (7), 823-839.

Park, J; Kwak, BK; Bae, E; Lee, J; Kim, Y; Choi, K; Yi, J, **2009,** Characterization of exposure to silver nanoparticles in a manufacturing facility. *J. Nanopart. Res. DOI 10.1007/s11051-009-9725-8*

Sayes, CM; Reed, KL; Warheit, DB, **2007,** Assessing toxicity of fine and nanoparticles: Comparing in vitro measurements to in vivo pulmonary toxicity profiles. *Toxicol. Sci. 97*, (1), 163-180.

Thimsen, E; Biswas, P, **2007,** Nanostructured photoactive films synthesized by a flame aerosol reactor. *AIChe 53*, (7), 1727-1735.

Tsai, S; Ashter, A; Ada, E; Mead, JL; Barry, CF; Ellenbecker, MJ, **2008,** Airborne Nanoparticle Release Associated with the Compounding of Nanocomposite Nanoalumina as Fillers. *Aerosol and Air Quality Research 8*, (2), 160-177.

Tsai, SJ; Ada, E; Isaacs, JA; Ellenbecker, MJ, **2009,** Airborne nanoparticle exposures associated with the manual handling of nanoalumina and nanosilver in fume hoods. *J. Nanopart. Res. 11*, (1), 147-161.

Vincent, JH; Clement, CF, **2000,** Ultrafine particles in workplace atmospheres. *Philos. Trans. R. Soc. London, Ser. A 358*, (1775), 2673-2682.

Chapter 5:

Characterization of Doped TiO_2 Nanoparticle Dispersions

The results presented here were published in:

Sahu, M, K. Suttiponparnit, S. Suvachittanont, T. Charinpanitku, and P. Biswas, *Characterization of Doped TiO_2 Nanoparticle Dispersions*, Chemical Engineering Science, 2011, 66 (15): p 3482-3490.

5.1. Abstract

Nanomaterial suspensions with different dopant types and compositions were investigated to examine their effects on agglomeration through the measurement of hydrodynamic diameter (HD), surface charge, and isoelectric point (IEP). Four different types of nanoparticles, all synthesized by a flame aerosol reactor, were considered for the analysis. The nanoparticles considered were pristine TiO_2, Cu-TiO_2, V-TiO_2, and Pt-TiO_2 with dopant concentrations ranging from 1 to 6 wt%. Measurements were conducted over a broad range of pH (3-11) and ionic strengths (0.001-0.1M) to understand the roles of pH and ionic strength (IS) on dispersion characteristics. Calculations were made using the classical DLVO theory to explain the agglomeration behavior. The results indicate that dopant addition can change surface charge, hydrodynamic diameter, and shift the IEP to higher or lower pH than pristine TiO_2, depending on the type of dopant and composition. Vanadium and platinum doping shifted the IEP to lower pH values, whereas copper doping shifted it to higher pH values. For each of the nanoparticles considered, pH and IS were found to have significant effects on the surface charge and HD, which were also verified by calculation from DLVO theory.

Keywords: Doped nanoparticle, Surface charge, Hydrodynamic diameter, Isoelectric point, DLVO theory.

5.2. Introduction

Engineered nanoparticles are building blocks for nanotechnology applications, and are widely used in electronics, medicine, energy and environmental applications, and in a variety of consumer products (Clarence, 2008). Applications of these nanomaterials are expected to expand beyond the current use and have also prompted concern about the potential adverse impact on human health and environmental systems (Grassian et al., 2007; Maynard et al., 2006; Nel et al., 2006). TiO_2 is a promising nanomaterial used extensively in variety of applications (Almquist and Biswas, 2002; An et al., 2010; Asahi and Morikawa, 2007; Hoffmann et al., 1995; Tiwari et al., 2008), and many functional doped nanomaterials are also under development (Asahi et al., 2001). As these materials continue to develop and become used extensively, their impacts on human health and the environment are yet to be fully explored. Many toxicological studies are underway to evaluate the toxic potentials of both pristine and doped TiO_2 nanomaterials. A few studies have already reported that TiO_2 nanoparticles can cause potential adverse impact on human health and biological systems (Oberdorster et al., 2005; Wu et al., 2010). However, their applications and potential adverse impact depend on their physical and chemical properties such as size, shape, crystal phase, doping species, and concentration of dopant (Jiang et al., 2008; Nel et al., 2006; Tiwari et al., 2008).

Most nanomaterial applications and toxicity studies require nanoparticles to be dispersed in different aqueous media. There is a tendency for such nanoparticles to form large agglomerates with altered surface charges depending on a number of factors such as size, shape, crystal structure, functionalization of the nanoparticle, and environmental parameters such as pH, and ionic strength (Grassian et al., 2007; Jiang et al., 2009;

Mukherjee and Weaver, 2010; Suttiponparnit et al., 2010). In addition to the above mentioned factors, the addition of dopants may influence the suspension properties such as agglomeration behavior of particles as their addition will alter the net surface charge on the particle. Addition of dopant changes the structure of TiO_2 and increases the absorption in the visible spectrum and also, the activity by decreasing the electron and hole pair recombination in case of photo-catalysis reactions. According to the model proposed by Tanabe et al (1974) charge imbalance created on the host material depends on each individual bond to the dopant cation. The model assumes, when the dopant oxide's cation such as Cu^{2+} in case of CuO enters the lattice of its host oxide and retains its original coordination number. As the dopant is bonded to the oxygen atoms with a new coordination, a charge imbalance is created (Tanabe et al., 1974). Brönsted sites (extra protons) are expected to form when the charge imbalance is negative and Lewis sites are expected to form when the charge is positive. The stability of the nanoparticles in suspension will thus depend on types of dopant and dopant concentration. Sahu and Biswas (2010) found that addition of copper dopant to TiO_2 structure increases the nanoparticle stability compared to pristine TiO_2 particles and attributed to charge imbalance created due to replacement of Ti atoms by copper atoms in the TiO_2 structure. The modification in the properties of TiO_2 nanoparticles in the aqueous suspension influences the fate and transport in the environmental system, catalytic reactivity and contamination treatment efficiency (Gilbert et al., 2009; Gun'ko et al., 2001; Guzman et al., 2006; Mukherjee and Weaver, 2010; Waychunas et al., 2005; Zeng et al., 2009). Several studies have demonstrated effective bacterial inactivation potential of nano sized TiO_2 suspensions for *E-coli* bacteria and found that concentration and size of the particles

in the suspensions are very important parameters (Byrne et al., 2011; Liu and Yang, 2003; Zhang et al., 2010). The form of TiO_2 nanoparticles to which microorganisms are exposed also influences their toxicity and also is a determining factor for the response of cells (Long et al., 2006; Wu et al., 2010). In summary, a detailed characterization of nanoparticles dispersed in aqueous suspension and the factors affecting the dispersion behavior is critical in understanding their toxicological and environmental fate and behavior. Few studies have reported the dispersion behavior of TiO_2 nanoparticles and found that particle size, crystal phase, surface area, and sonication time affect the dispersion properties (Jiang et al., 2009; Suttiponparnit et al., 2010). Suttiponparnit et al (2010) found that the isoelectric point (IEP) depends on primary particle size but is insensitive to crystal structure variation. However, the dispersion behavior of metal doped TiO_2 nanoparticles and the effect of dopants on the surface charge and isoelectric point has not been well investigated and understood.

In this study, the influence of dopant type and concentration on TiO_2 dispersion behavior has been investigated. The dispersion behavior was studied by measuring the agglomerate size and zeta potential under various environmental conditions. Three different dopants considered for this study were copper, vanadium, and platinum. The concentration of the dopant was varied (1-6 wt %) keeping the primary particle size and crystal structure similar. All particles were synthesized in a diffusion flame aerosol reactor. Pristine TiO_2 of similar size and crystal structure were also investigated for comparison. The effect of ionic strength was investigated for copper doped TiO_2 particles. DLVO theory was used to calculate the potential energy of interaction to verify the agglomeration behavior of the nanoparticles.

5.3. Materials and Methods

5.3.1. Doped TiO_2 Nanoparticle Synthesis and Characterization

A flame aerosol reactor with a three port co-flow diffusion burner was used to synthesize pristine and doped TiO_2 nanoparticles. The design details of the diffusion flame reactor used for synthesizing the nanoparticles can be found in Jiang et al (2007). Titanium tetra-isopropoxide (TTIP, 97%, Aldrich) was used as the precursor for titanium dioxide synthesis. Copper (II) 2-ethyl-hexanoate (Aldrich), vanadyl tri-isopropoxide (95-98%, Alfa Aesar) and platinum acetyl acetonate ($Pt(acac)_2$, 97%, Aldrich) were used as the precursors for copper, vanadium, and platinum doping, respectively. The $Pt(acac)_2$ precursor was dissolved in xylene and acetonitrile in a volume ratio of 2:1, whereas the copper precursor was dissolved in xylene alone. The dopant precursor solution was atomized by a stainless steel nebulizer and introduced in the form of fine droplets to the high temperature flame through the second port of the diffusion burner. Vanadium precursor vapor was introduced through the central port along with the TTIP vapor for V-TiO_2 nanoparticle synthesis. Nanoparticles with different dopant loading concentrations were synthesized by changing the molar feed ratio of precursors. For platinum and copper doping, the dopant precursor salt concentration was varied in the solvent to control the doping level; whereas the temperature of the bubbler (where the vanadium dopant precursor was placed) was controlled to vary the feed rate of vanadium precursor. Nitrogen gas at 2 lpm (liters per minute) was bubbled through TTIP in a bubbler maintained at 98 °C. Oxygen and methane flow rates were maintained at 7 and 1.6 lpm, respectively to set up the flame. Nanoparticle properties such as size, crystallinity, and morphology were controlled by controlling the residence and temperature time history in

the combustion zone. Further details about these doped nanoparticle synthesis can be found in Tiwari et al (2008) and Sahu and Biswas (2010).

Particle sizes and morphology were characterized by scanning and transmission electron microscopes (SEM: JEOL 7001LVF, Japan; TEM: JEOL 2100F, Japan). SEM coupled with energy dispersive spectroscopy (EDS) was used to analyze the presence of dopant in the nanoparticles. Crystal structures of the synthesized materials were verified using an X-ray diffractometer (XRD, Rigaku D-MAX/A9, Japan). Table 4-1 lists the characteristics of the nanomaterials synthesized and used in this study.

5.3.2. Dynamic Light Scattering (DLS) Characterization

A ZetaSizer Nano ZS (Malvern Instruments) dynamic light scattering instrument was used to measure the hydrodynamic diameter and zeta potential of the nanoparticle suspensions. The fluctuations in the light intensity due to Brownian motion of the nanoparticles in the liquid suspensions were used to determine the intensity weighted average translational diffusion coefficients. The average hydrodynamic diameter is estimated from the diffusion coefficient using the Stokes-Einstein equation $HD = k_B T / 6\pi 6\pi$, where k_B is the Boltzmann constant ($J \cdot K^{-1}$), T is the absolute temperature (K), and μ is the viscosity of the medium ($kg \cdot m^{-1} \cdot s^{-1}$). This instrument could measure nanoparticle aggregation sizes over a wide range (2 nm to 6 μm).

The electrophoretic mobility of the nanoparticle in the liquid suspension was measured and zeta potential was determined from the electrophoretic mobility by using the Smoluchowski equation $\zeta = \mu U/\varepsilon$, where ε is the electric permittivity of the medium ($C^2 \cdot N^{-1} \cdot m^{-2}$). All the measurements were conducted at a temperature of 25°C, which was

automatically controlled by the instrument. To check the reproducibility of the results, five measurements were taken for each sample and average values of the measurements are reported here.

5.3.3. DLVO Prediction of Nanoparticle Agglomeration

The agglomeration behavior of the nanoparticle suspensions can be understood by estimating the potential energy of interaction between particles. The two important forces which govern the agglomeration in the suspensions are the van der Waals attractive force and the electrostatic repulsive force. The interaction potential energy due to the van der Waals attraction force is given by the expression:

$$Va = \frac{-A}{6}\left[\frac{2a^2}{s(s+4a)} + \frac{2a^2}{s(s+2a)^2} + \ln\frac{s(s+4a)}{s(s+2a)^2}\right], \qquad (1)$$

where A is the Hamaker constant, a is the particle radius and s is the separation distance between the particle surfaces (Garcia-Garcia et al., 2006). The Hamaker constant indicates the strength of mutual attraction between two colloidal particles and depends on material properties, and was 4×10^{-20} J for TiO_2 (Zhang, 2006). The equation used for calculating potential energy between particles due to electrical repulsion ($ka > 10$) was:

$$Vr = 2\pi\varepsilon_0\varepsilon_r a\zeta^2 \ln(1+e^{-ks}), \qquad (2)$$

where $\varepsilon_0\varepsilon$ is the dielectric permittivity of the medium, ζ is the potential at the surface of the particle and k is the Debye length and is evaluated as:

$$k = \left(\frac{1000e^2 Na}{\varepsilon_0\varepsilon_r k_B T}\sum z_i^2 Mi\right)^{1/2}, \qquad (3)$$

where k_B is Boltzmann constant, *Na* is Avogadro's constant, ε_0 is the permittivity of vacuum, ε is the dielectric constant, and *Mi* is the molarity. The total potential energy is calculated as $Vt = Va + Vr$. The limitation associated with calculating the potential energy using this above expression is that other forces, such as hydration and Born forces, are not taken into account (Garcia-Garcia et al., 2006). The particle considered for calculation was of single size and equal to the primary mean particle size. Due to these assumptions, this DLVO calculation was used to qualitatively compare the effect of pH and ionic strength on dispersion behavior of the nanoparticles.

5.3.4. Experimental Test Plan

Table 5-1 outlines the experiments performed in this study. Doped TiO_2 nanoparticles of spherical shape, with controlled properties such as primary particle size (~40±10 nm) and crystalline phase (anatase) were synthesized in a flame aerosol reactor by controlling the key process parameters such as molar feed ratios of precursors, temperature, and time history in the flame (Test-1). For zeta potential and hydrodynamic size measurements, nanoparticles were dispersed in solution at a concentration of 50 μg/ml for all the cases considered and sonicated for 20 minutes using a bath sonicator (40 W, 50 kHz, 5 Fisher Scientific, Fairlawn, New Jersey) before all measurements. The aggregation behavior of the doped nanomaterials dispersed in de-ionized water (DI) was studied first without adjusting the ionic strength and pH of the solutions. Since pH influences the surface charge and nanoparticle aggregation properties (Jiang et al., 2009), its effect was

Table 5-1: Summary of experiments performed in this study

Test #	Objective	Samples	System used/ Procedure description	Parameter values/ Experimental technique
1	Synthesis and characterization of nanoparticles	Pristine TiO_2 1-3 wt% Cu-TiO_2 1-6 wt% V-TiO_2 1-3 wt% Pt-TiO_2 Size=40±10 nm Phase-Anatase	FLAR TTIP/N_2-2 lpm CH_4-1.6 lpm O_2-7 lpm Pt, Cu, V dopant Concentration-1-6 wt %	Characterization: TEM; SEM/EDS; XRD.
2	pH effect on doped nanoparticle dispersion characteristics	Dopant types: Cu, V, Pt Dopant Concentration range 1-6 wt %	Concentration: 50 µg/ml pH values was changed from 2 -11 by adding HCl or NaOH; IS-0.001M	Zeta potential, Hydrodynamic diameter
3	Dopant type and concentration effect on dispersion characteristics			Zeta potential, Hydrodynamic diameter, IEP
4	Influence of ionic strength on dispersion characteristics	1-3 wt% Cu-TiO_2	Concentration: 50 µg/ml Ionic strength was varied from 0.001 M to 0.1 M. pH maintained at 4.	Zeta potential, Hydrodynamic diameter

*Abbreviations: FLAR: flame aerosol reactor; lpm: liter per minute; TTIP: Titanium tetra-isopropoxide; TEM: Transmission electronic microscope; SEM: scanning electronic microscope; EDS: energy dispersive spectroscope; XRD: X-ray diffraction;

investigated by adjusting the pH from 3 to 11 by addition of HCl and NaOH (Test-2). The ionic strength was kept constant at 0.001M by addition of NaCl. The pH effect was studied for all the doped nanoparticles considered in this study, along with pristine TiO_2 for comparison. The influence of different dopant types and dopant concentrations on nanoparticle agglomeration size and surface charge was investigated using Pt-TiO_2, Cu-

TiO_2, and V-TiO_2 nanoparticles by varying the dopant concentrations (Test-3). The dopant concentration was varied from 1 to 3 wt% for Cu- and Pt- TiO_2 and from 1 to 6 wt% for V-TiO_2 nanoparticles. Ionic strength is a function of number of potential determining ions (PDI) present in the solutions, which suppresses the electrostatic diffuse layer and affects the agglomeration behavior of the nanoparticle suspensions. The effect of ionic strength was examined for Cu-doped TiO_2 nanoparticles by varying the ionic strength from 0.001 to 0.1 M, while keeping the pH constant at 4 (Test-4) and the agglomeration behavior is described by DLVO calculation.

5.4. Results and Discussion

Metal doping changes the physicochemical properties such as crystal structure, particle size, morphology and specific surface area of TiO_2, all of which are important factors for toxicity investigation and photocatalytic activity of TiO_2 and also affect the state of dispersion. The doped nanomaterial synthesis characterization results are presented first followed by dispersion characterization in the liquid suspension under various environmental conditions.

5.4.1. Doped TiO_2 Nanomaterial Synthesis

The XRD spectra of the flame synthesized doped TiO_2 nanomaterials are shown in Figure 5-1. The nanomaterials prepared were primarily of anatase crystalline phase, as evident from the anatase (101) and rutile (101) peaks that were used for calculating the crystal phase composition. This phase was achieved by manipulating the process parameters in the flame aerosol reactor. The dopant level used for this study was varied from 1 to 3

wt% for copper and platinum dopants, and from 1 to 6 wt% for vanadium dopant. However, with increasing dopant concentrations, a small amount of phase transition from anatase to rutile phase was observed for copper and vanadium doped TiO_2, whereas little phase transformation from rutile to anatase was observed for platinum doping. The phase composition was altered (less than 10 % change) for all the cases based on the crystal phase composition calculation from XRD diffraction pattern. No characteristic peaks attributed to oxides of the dopant metal were found in the XRD patterns, implying that either Cu or V ions were incorporated into the crystal lattice of TiO_2. The similarity in the Cu, V and Ti ionic radius (0.73 Å for Cu (Hsiang and Liu, 2009), 0.68 Å for V (Cho and Biswas, 2006) and 0.68 Å for Ti) allows the interstitial incorporation of the dopant into the titania network. The effect of dopant concentration on TiO_2 crystal structure is described further elsewhere (Sahu and Biswas, 2010; Tiwari et al., 2008; Wang et al., 2001). The details about Pt-TiO_2 particles are discussed in Tiwari et al (2008). TEM micrographs of the doped nanoparticles used for this study are shown in Figure 5-2. The average particle size of all the doped TiO_2 particles was calculated to be 40±10 nm. The particles synthesized were very similar in size as the doping concentration was low enough that it did not change the primary particle size significantly. However, increased doping concentration can change the particle size, depending on the type and concentration of dopant (Sahu and Biswas, 2010). (Suttiponparnit et al., 2010) demonstrated that the agglomeration behavior and surface potential change with a change in primary particle size. In this work, the particles sizes were kept similar to avoid interference due to variation in particle size and also to directly compare with the pristine TiO_2.

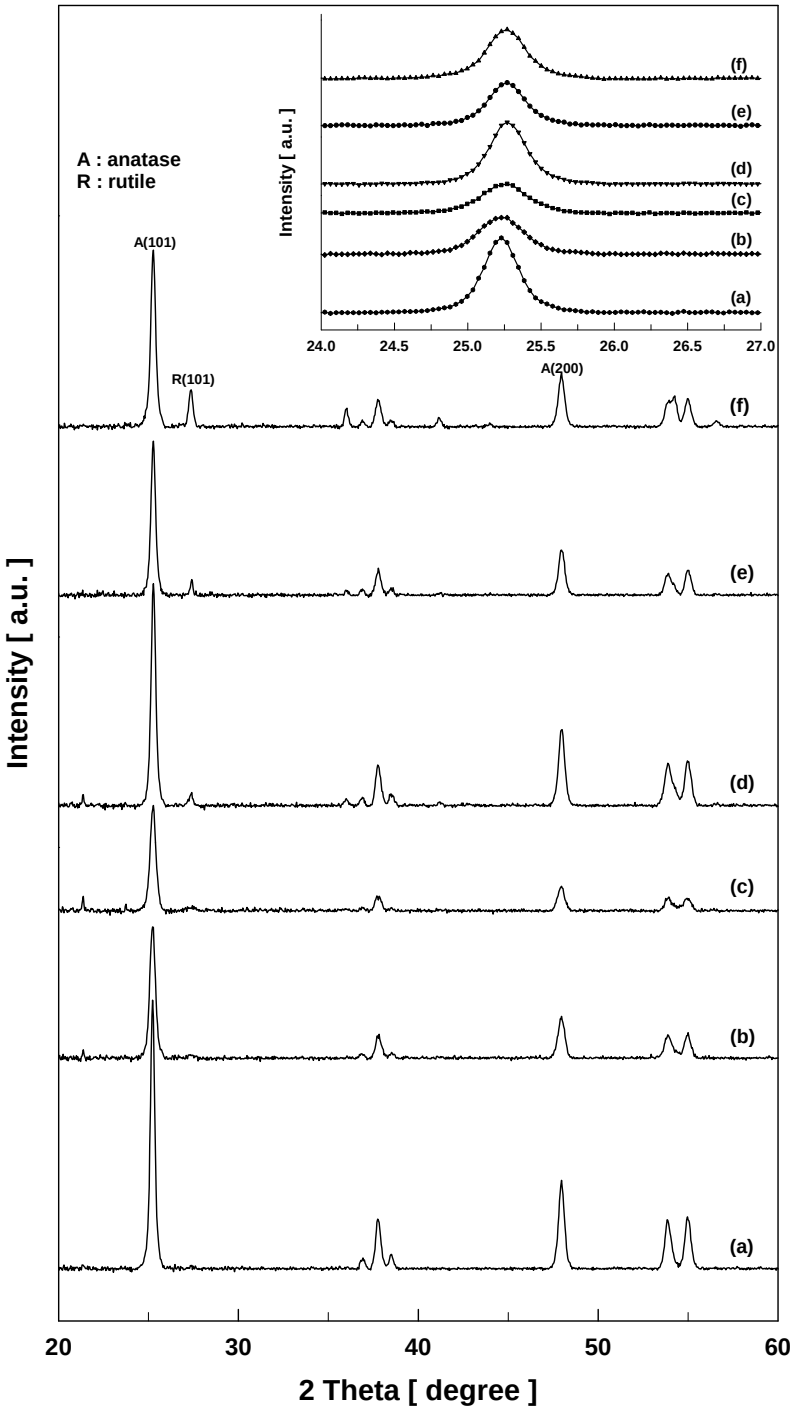

Figure 5-1: XRD patterns of synthesized nanoparticles used in this study (a) TiO_2, (b) 1wt% Cu-TiO_2, (c) 3wt% Cu-TiO_2, (d) 1wt% Ṽ-TiO_2, (e) 3 wt% Ṽ-TiO2, and (f) 6 wt% Ṽ-TiO_2. The inset is an enlargement of the anatase (1 0 1) peaks for these samples. Details about the diffraction pattern of Pt-TiO_2 is discussed in the previous publication [9])

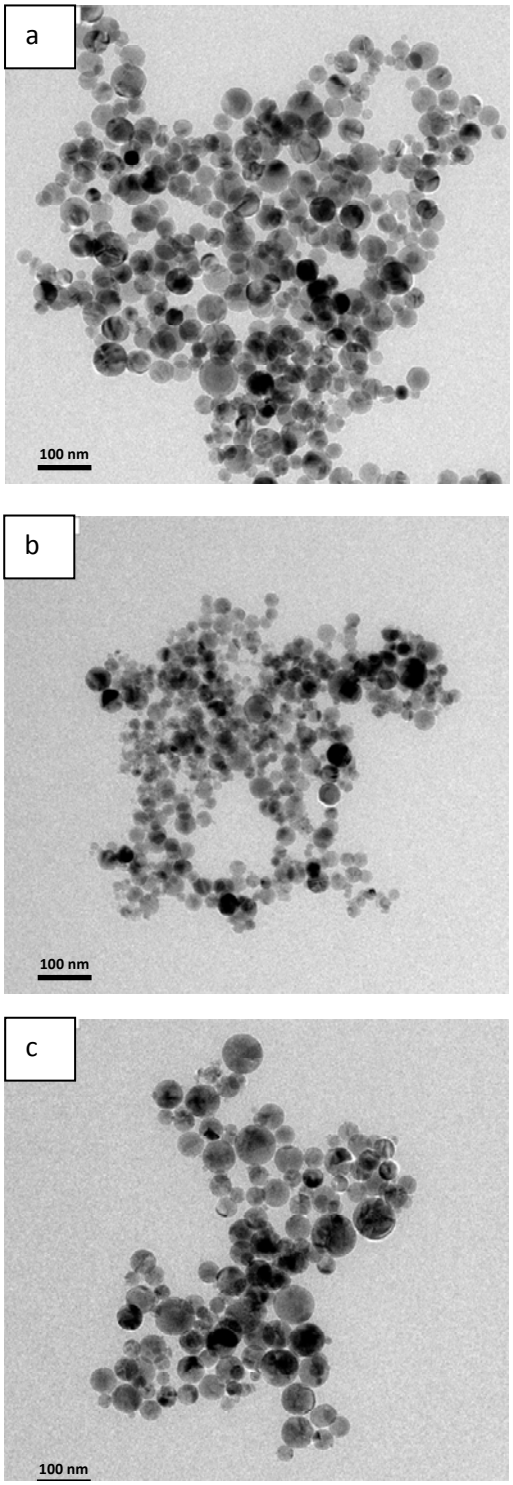

Figure 5- 2: Transmission electron micrographs (TEM) of representative samples (a) TiO_2 (b) Cu-TiO_2 (c) V-TiO_2 (Details about the Pt-TiO_2 size is discussed in Tiwari et al [9])

5.4.2. Dispersion Characterization

Nanoparticles dispersion behavior is characterized based on the zeta potential and hydrodynamic size in the suspension. These two important parameters in liquid suspensions are interrelated and significantly influence the nanoparticle aggregation and transport behavior in environmental systems (Jiang et al., 2009). Surface potential is mainly developed by surface ionization on the metal oxide surface and adsorption of ions from the electrolyte on the particle surface. When metal oxide nanoparticles are dispersed in water , because of the reactivity of the defective surface structure, the OH^- ion is attached to the oxygen vacancies present in the crystal structure, and the H^+ ion is attached to the lattice O^- ion to form OH^- ion on the metal oxide surface (Nowotny et al., 2006). Apart from the potential determining ions (PDI) present in the solutions (H^+, OH^- in metal oxides), the concentration and type of electrolyte also affects the potential developed at the particle surface and the agglomeration size (Jiang et al., 2009; Suttiponparnit et al., 2010).

5.4.2.1. Effect of pH on Surface Charge and Hydrodynamic Size

When TiO_2 is dispersed in water, the first step is the hydration of the TiO_2 surface followed by protonation and deprotonation of the surface groups from the metal oxide surface (Carre et al., 1992; Gun'ko et al., 1998).

$$TiO_2 + H_2O \rightarrow Ti^{IV}\text{-}OH + H^+ \quad (4)$$

$$Ti^{IV}\text{-}OH + H^+ \rightarrow TiOH_2^+ \quad (pH < pH\ (IEP) \quad (5)$$

Ti^{IV}-OH $\rightarrow$ Ti-O^- + H^+ (pH > pH (IEP)) (6)

When doped TiO_2 is dispersed in water the hydration reaction can be written in the similar fashion to the reaction demonstrated by (Gun'ko et al., 1998) for mixed oxides.

Ti-O-M_2 + $H_2O \rightarrow$ Ti-OH-O(H)-M_2 (M_2 = Cu, V, Pt) (7)

Ti-O(H)-M_2 $\rightarrow$ Ti-O^--M_2 + H^+ (pH > pH (IEP)) (8)

Ti-O(H)-M_2 $\rightarrow$ Ti-OH_2^+-M_2 + H^+ (pH < pH (IEP)) (9)

The equation indicates that when water molecules are adsorbed on metal oxide surface, one terminal Ti-OH group and one bridging group Ti-O(H)-M_2 can be formed, which depends on the type of dopant, defects on the surface, and other phases in the matrix of the complex oxide (Gun'ko et al., 1999). The pH value at which surface charge is equal to zero is called the iso-electric point.

The effect of pH on dispersion characteristics is shown in Figure (5-3 to 5-5) for both pristine and doped TiO_2 nanoparticles at an ionic strength (IS) of 0.001M. The IEP for pristine anatase TiO_2 was found to be 5.1, which is consistent with the value reported by (Suttiponparnit et al., 2010). However, the IEP of TiO_2 nanoparticles was altered by adding different dopants. The IEP was found to be 5.9 and 6.6 for 1 and 3 wt% Cu-TiO_2 particles, 3.6 and 2.2 for 1 and 3 wt% V-TiO_2 particles, and varied from 4.4 to 3.5 when Pt dopant concentration increased from 1 to 3 wt%. The change in IEP with dopant type and concentration will be discussed in the following section. All the particles considered in this study initially had a negative charge surface (as found from the zeta potential measurements), except for the Cu-TiO_2, which carried positive charge on the surface of the particles when dispersed in DI water. The pH decreased in all metal doped TiO_2 nanoparticles compared to that of TiO_2. The pH was slightly decreased to 5.4–5.5 for

Cu-TiO_2 compared to that of TiO_2 (pH = 6.0). However, for V-TiO_2 and Pt-TiO_2 addition increased the acidity having pH range about 5.5–4.8 and 5-4.4. These results suggested that the surfaces of Cu–TiO_2, which included the metals of lower oxidation state than Ti^{4+}, slightly attracted the OH^- ions, while the surfaces of V–TiO_2 and Pt-TiO_2 , which included the metals of higher oxidation state than Ti^{4+}, more strongly attracted the OH^- ions in water. In general, for all cases as the pH values became lower than the IEP of the nanoparticles, the magnitude of the zeta potential became more positive, and at increasingly higher pH values the observed zeta potentials became more negative.

The measurements show that pH has a significant influence on the surface charge of the particles, which affects their agglomeration behavior. As discussed earlier, agglomeration is mainly influenced by the van der Waals force and the electrostatic repulsive force due to surface charging. The zeta potential value on the particle surface is an indication of the magnitude of the electrostatic forces. The hydrodynamic diameter estimated from the DLS measurements indicates that HD increased from ~200 nm at a pH of 3 to ~1928 nm at a pH of 5.1, which is close to the IEP of pristine TiO_2 in this study (5.1), and decreased as it move further from the IEP in either direction. The increased HD close to IEP (surface charge zero) shows that the van der Waals attraction force is dominant at this pH, compared to the electrostatic repulsion force. From the DLVO prediction of total potential energy (Figures 5-3-5-5) at different pH, the net repulsive energy barrier near the IEP is much less, and therefore promotes fast agglomeration and results in larger HD for all the cases, which is consistent with other studies (Jiang et al., 2009; Suttiponparnit et al., 2010). However at lower and higher pH beyond the IEP, the net increase in the electrostatic repulsive barrier prevents the

agglomeration. The same phenomenon of larger HD was observed for copper, vanadium, and platinum doped TiO_2 nanoparticles at pH values close to their respective IEP. The experimental result and DLVO calculations suggest that the stability and agglomeration of nanoparticles in suspension is related to the magnitude of the repulsive electrostatic energy.

5.4.2.2. Effect of Dopant Types on IEP

When a dopant is added, the crystal structure of the TiO_2 changes depending on the dopant type and concentration (Li et al., 2003; Sahu and Biswas, 2010). The addition of dopant forms incompletely O-coordinated Ti atoms and incompletely O-coordinated dopant atoms, and thus causes distortion in the crystal structure. Doping changes the structural features on the surface of TiO_2 and causes the surface acidity and surface charge variation on mixed oxide surfaces when dispersed in water as described in equation (7) and (8).

The zeta potential measurements suggested that the surface charge of Cu-TiO_2 was positive due to more H^+ ions on the surface compared to pristine TiO_2. The IEP shifted to higher pH values of 5.9 and 6.6 at 1 and 3 wt% copper doping (Figure 5-3). A similar shift in IEP trend was observed by Ko et al (2005) for an Al-TiO_2 nanoparticle dispersion. The IEP shift is attributed to surface modification caused by copper doping into TiO_2 crystal structure, which promotes rutile phase transformation from anatase and distorts the structure. When Cu^{2+} replaces some of the Ti^{4+} atoms in the TiO_2 nanoparticles, anion vacancies are created and the surface of the particles becomes more negatively charged. The charge imbalance was calculated following the procedure

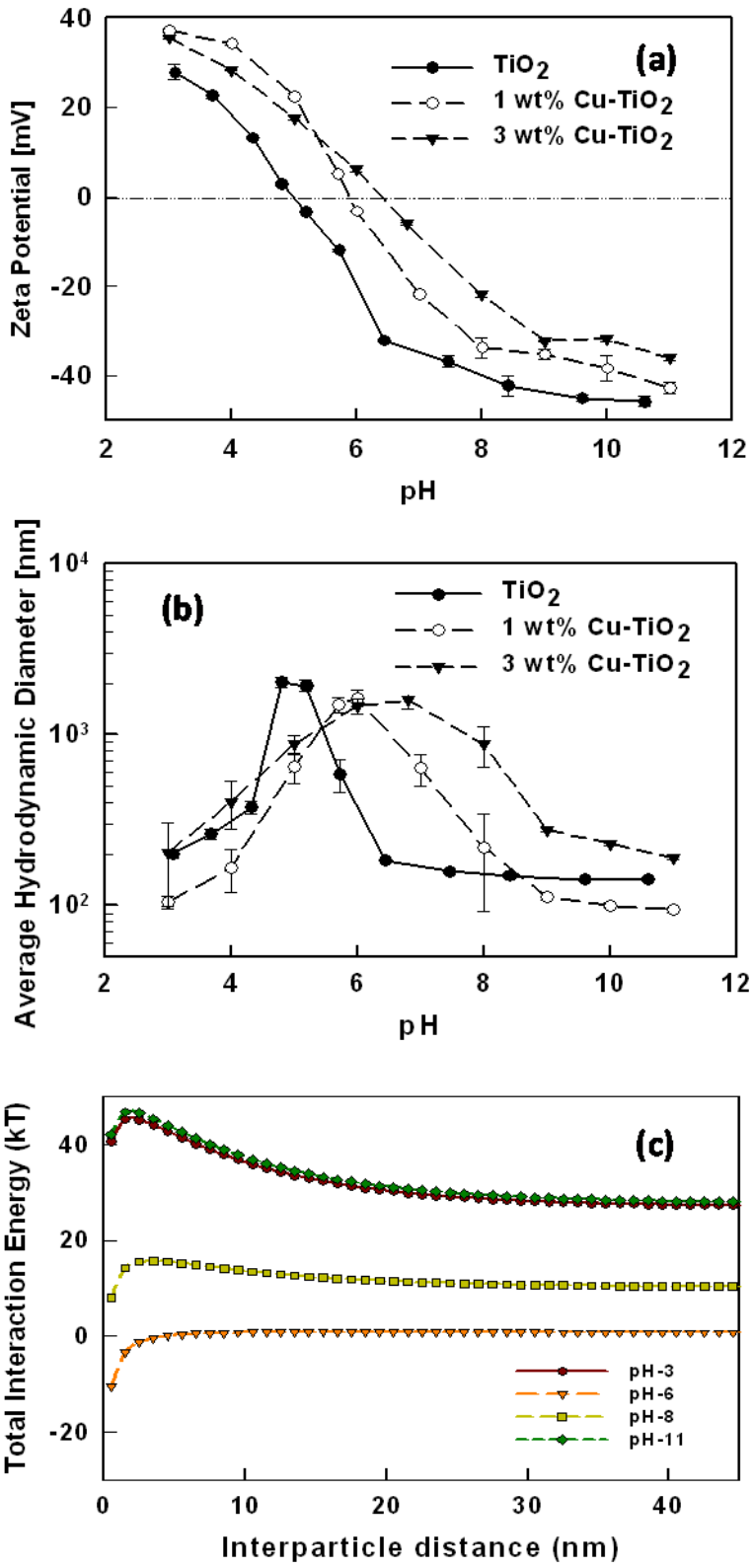

Figure 5- 3: pH and Cu-dopant effects on TiO_2 nanoparticles (a) Zeta potential and (b) Average hydrodynamic diameter (Ionic strength=0.001 M NaCl) (c) DLVO prediction of pH (IS-0.001M) effect on 1wt % Cu-TiO_2 nanoparticle interaction potential.

adopted by Tanabe et al (1974). Copper is 4−fold coordinated (Aniya and Shimojo, 2006) with each oxygen atom bonded to two copper atoms. Titania is octahedrally coordinated with each oxygen bonded to three titanium atoms. coordinated with each oxygen bonded to three titanium atoms. Since the Cu^{2+} ions (ionic radius is 0.73 Å) similar radius with Ti^{4+} (ionic radius is 0.68 Å), the Ti^{4+} could be substituted by Cu^{2+} and Ti–O–Cu bonds could be formed.

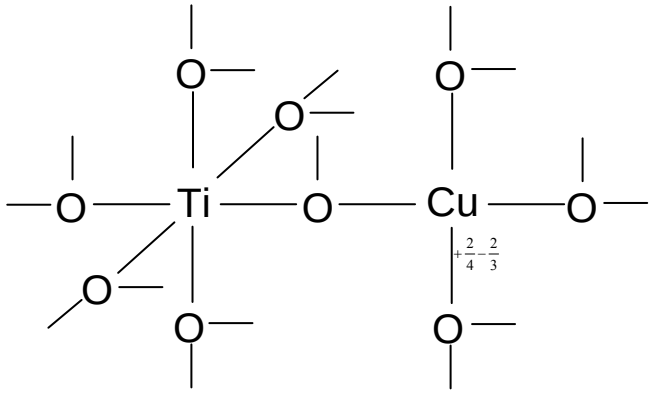

Charge difference: $4 \times \left(+\frac{2}{4}-\frac{2}{3}\right)=-\frac{2}{3}$

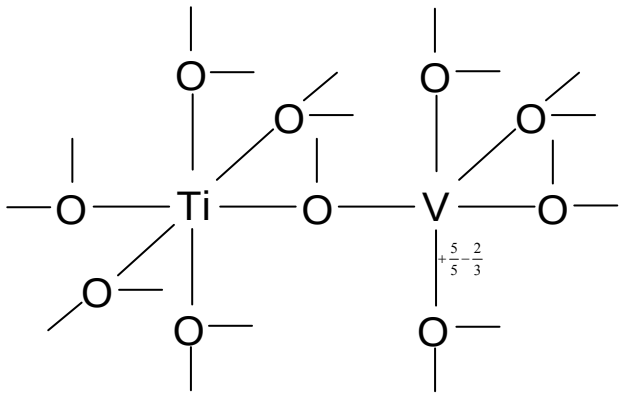

Charge difference: $4 \times \left(+\frac{5}{5}-\frac{2}{3}\right)=+\frac{4}{3}$

Figure 5- 4: Illustration of model structure and charge balance calculation by using Tanabe's model (Tanabe et al., 1974) to describe the surface acidity behavior of binary metal oxides (a) copper doped TiO_2 and (b) vanadium doped TiO_2.

When a copper atom enters a titanium lattice, the two valence electrons on Copper atom (two positive charges) are distributed to four bonds, while the two negative charges of oxygen atom are distributed to three bonds. The difference in charge for one bond is $+1/2 - 2/3 = -1/6$, and for all the bonds the valence unit imbalance of $-1/6 \times 4 = -2/3$. In this case the imbalance is negative, the Brönsted acidity is assumed to appear. The fact that adding more the copper created Brönsted sites may be attributed to explain the IEP of Cu−doped TiO_2 nanoparticles is higher than the TiO_2.

In the case of V-TiO_2 nanoparticles, vanadium substitution decreased the IEP (Figure 5-4). The values of the IEP were 3.6 and 2.2 for 1 and 3 wt% V-TiO_2 particles. The zeta potential and shift in IEP indicate more hydroxyl groups are absorbed to the TiO_2 surface. The observed trend is consistent with reported values for V-TiO_2 and for W-TiO_2 (Sene et al., 2003). Vanadium is 5−fold coordinated (Giuli et al., 2004) with each oxygen atom bonded to five vanadium atoms. Since the V^{5+} ions (ionic radius is 0.68 Å) are similar radius with Ti^{4+} (ionic radius is 0.68 Å), the Ti^{4+} could be substituted to V^{5+} and Ti–O–V bonds could be formed. For vanadium atom enters a titanium lattice, the five positive charges of the vanadium atom are distributed to five bonds, while the two negative charges of oxygen atom are distributed to three bonds. The charge difference for each bond is $+1 - 2/3 = +1/3$, and for all the bonds the valence unit imbalance of $+1/3 \times 4 = +4/3$. In this case, the Lewis acidity is assumed to appear upon the presence of an excess of positive charge on the vanadium doped TiO_2 which is consistent with the measured data and with those reported in other studies (Gervasini et al., 2004) .

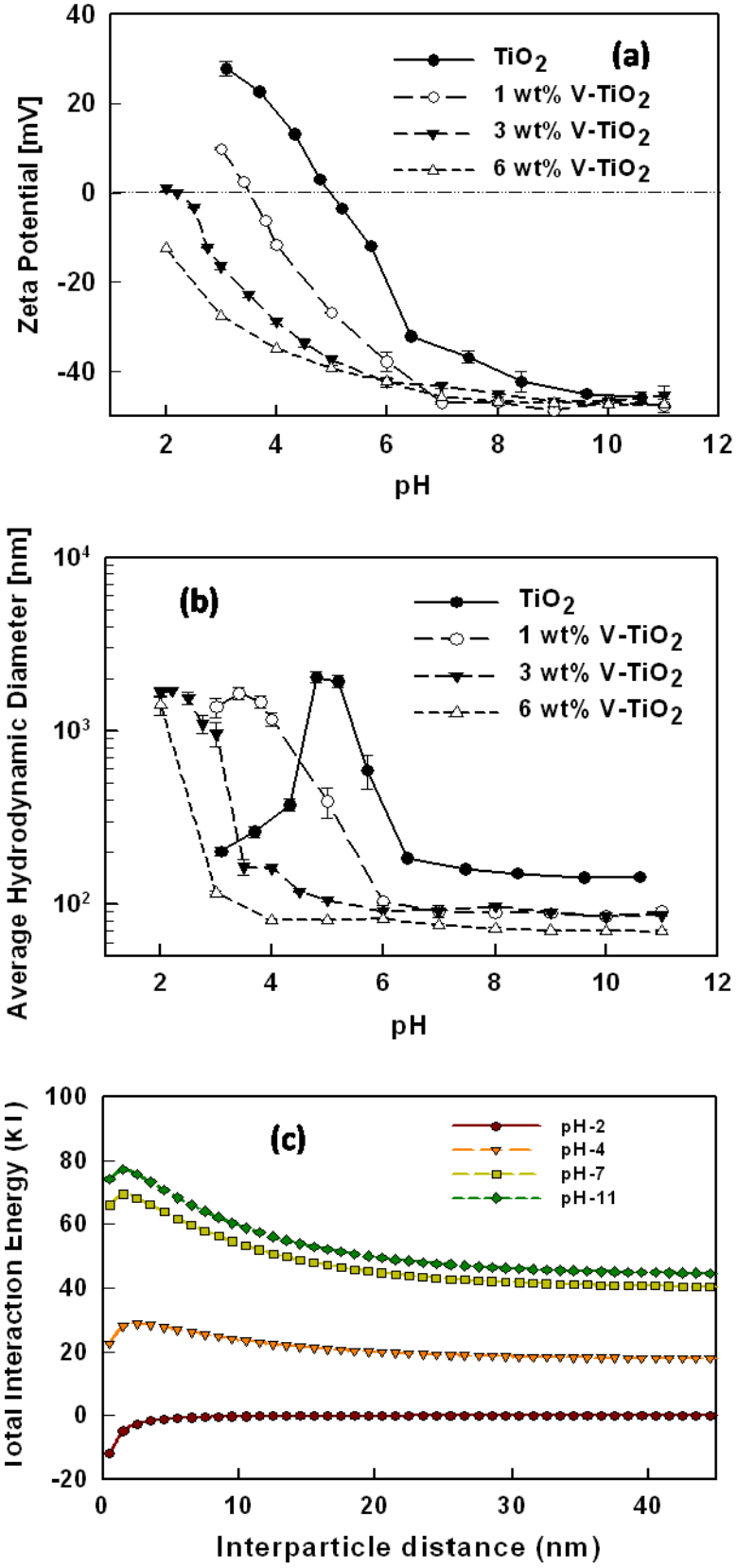

Figure 5- 5: pH and V-dopant effects on TiO_2 nanoparticles (a) Zeta potential and (b) Average hydrodynamic diameter (Ionic strength=0.001 M NaCl)) (c) DLVO prediction of pH (IS-0.001M) effect on 1wt % V-TiO_2 nanoparticle interaction potential.

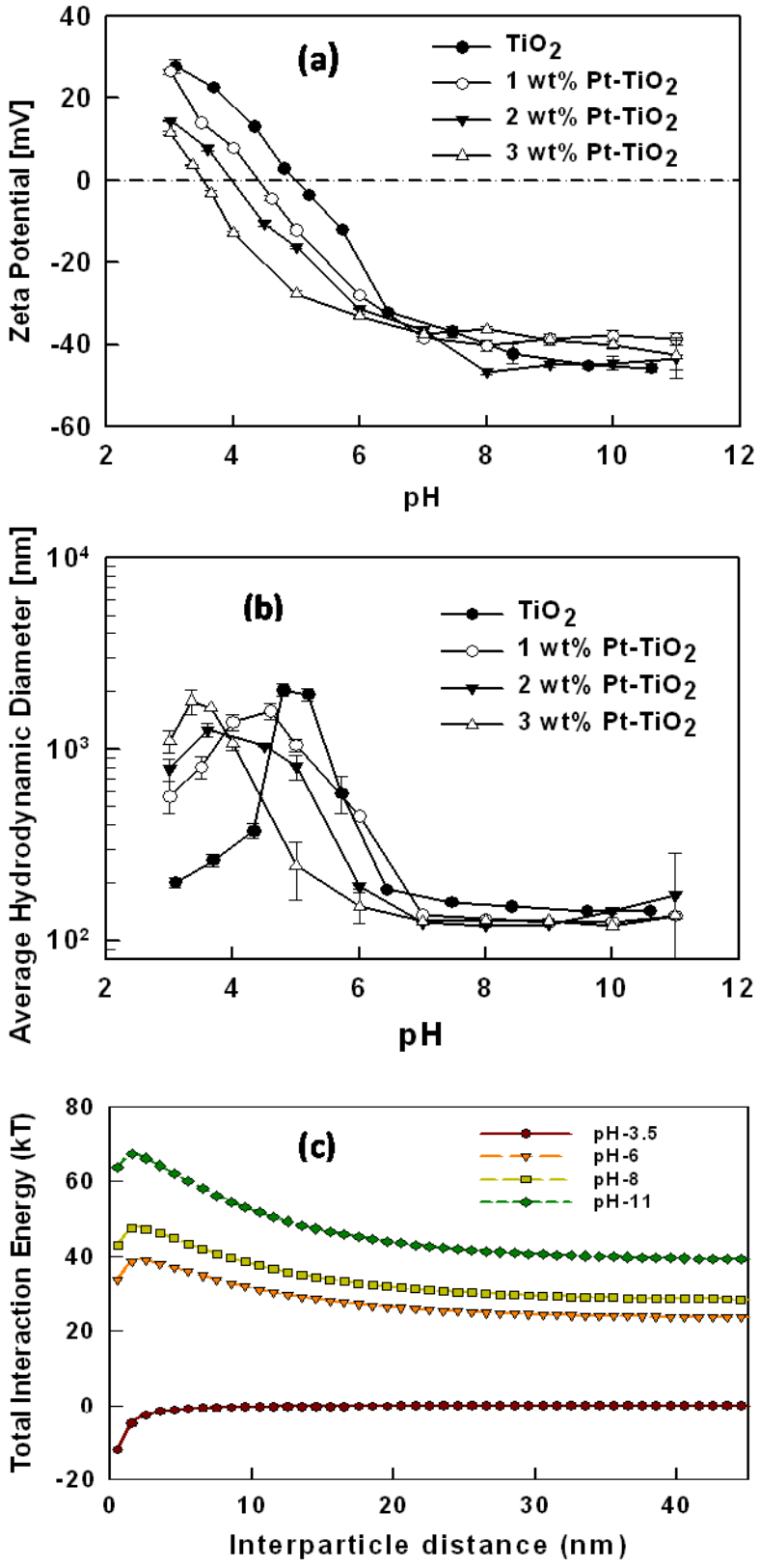

Figure 5- 6: pH and Pt-dopant effects on TiO_2 nanoparticles (a) Zeta potential and (b) Average hydrodynamic diameter (Ionic strength=0.001 M NaCl)) (c) DLVO prediction of pH (IS-0.001M) effect on 1wt % Pt-TiO_2 nanoparticle interaction

The effect of Pt doping on zeta potential, IEP and HD is shown in Figure 5. The IEP decreased from 4.4 to 3.5 when the Pt doping concentration increased from 1 to 3 wt%. The variation in IEP is due to the change in crystal structure and surface properties. However, the coordination number of platinum is not available in the literature and the charge balance could not be calculated. However, the change in IEP of Pt-TiO_2 is due to the higher oxidation state of Pt compared to Ti. Therefore more positive surface charge exists on Pt-TiO_2 and caused more Lewis acidity sites similar to the case of V-TiO_2 particles and changed the IEP.

The variation in IEP is due to the change in crystal structure and surface. In other words, pH controls particle' surface charge and controls the HD through electrostatic repulsive forces. At IEP, the HD size observed for Cu-TiO_2 particles was lower compared to vanadium and platinum doped TiO_2 particles. DLVO calculation predicted that more energy is needed to overcome the electrostatic repulsive barrier for Cu-TiO_2 particles compared to the other two doped cases, which is consistent with our experimental results (Figures 5-3-5-5). Additionally, change in Hamakar constant (mutual attraction between two colloidal particles) due to addition of dopants may have caused different HD for different dopants. As pH increased, the charge built up on the surface of the particle, and the repulsive force became strong enough to reduce the HD. There is one remaining consideration, which, however, is beyond the scope of this study, some metallic ions may dissolve into the solution, which would increase the surface charge density and may change the double layer thickness and interaction between the nanoparticles. This possibility needs further investigation. The results indicate that

depending on the dopant types, dopant oxidation state, and concentrations, the surface charge can be altered and can affect the dispersion behavior of the doped nanomaterials.

4.2.3. Effect of Ionic Strength

The effect of ionic strength on zeta potential and HD size is shown in Figure 5-6 for Cu-TiO_2 particles.

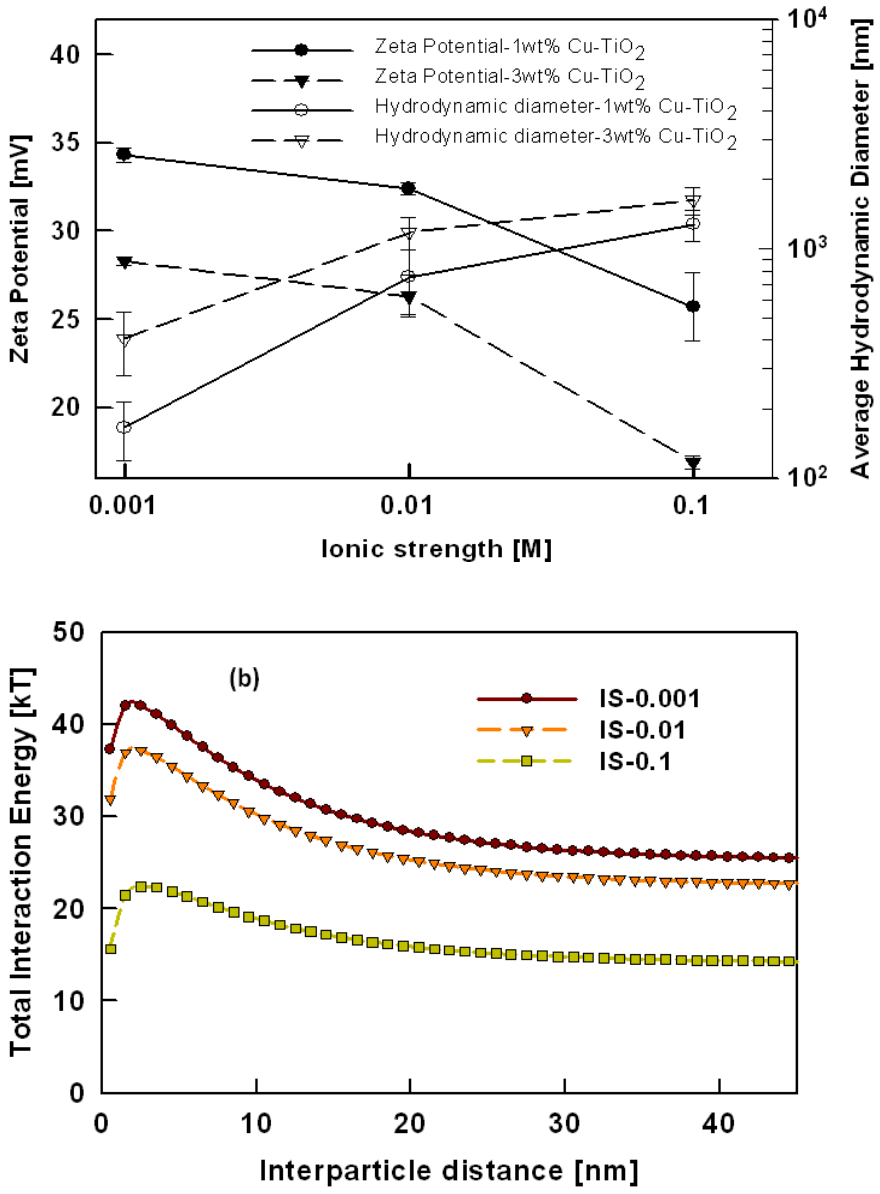

Figure 5- 7: (a) Ionic strength effect on Cu-TiO_2 nanoparticles zeta potential and hydrodynamic diameter (pH=4.0) (b) DLVO prediction of IS effect on Cu-TiO_2 nanoparticle interaction potential.

The zeta potential decreased from 34.3 to 25.7 mV for 1 wt% Cu-TiO_2 and from 28.3 to 16.9 mV for 3 wt% Cu-TiO_2 respectively, when ionic strength increased from 0.001M to 0.1M. As discussed earlier, the HD related to the zeta potential, the HD increased with decreased in zeta potential. However, there was no straightforward relationship between zeta potential and HD. The results are consistent with the observed increased in HD with increasing IS with other reported study (Jiang et al., 2009; Suttiponparnit et al., 2010). The decreased zeta potential and increased HD with increasing ionic strength can be explained by the change in Debye length (*1/k*), which affects the electrostatic repulsive force. The calculated Debye length from equation (3) increased from 0.104 to 1.04 nm by changing the IS from 0.001 M to 0.1 M. The increase in Debye length (i.e. decreasing double layer thickness) and decreased zeta potential at higher IS increased the HD. The total potential energy calculated from classical DLVO theory is shown in Figure 5-6(b) at different ionic strengths. Calculations indicate that the potential energy barrier for agglomeration decreased as the ionic strength increased from 0.001 M to 0.1 M, which further explains the higher HD observed at higher IS.

5.5. Conclusions

The dispersion behavior of doped TiO_2 nanoparticles in water was investigated by using different types of dopants (Cu, V, and Pt). Dopant type and concentration affected the zeta potential and shifted the IEP by changing the surface actives sites, which is mainly attributed to the dopant oxidation state, distortion caused in the crystal structure and charge imbalance created by the incorporating dopant onto host TiO_2 nanoparticles. This study indicated that dopant with oxidation state above that of Ti shift the IEP of TiO_2 to

lower pH values and, where as for dopant with oxidation state below shifted the IEP to higher pH value. The agglomeration behavior of nanoparticles in the suspension was found to vary depending on solution pH, ionic strength and dopant types. Potential energy calculation from DLVO theory was consistent with the experimental results and supported the findings. The study results have important implications for studies on toxicity and contamination treatment, nanoparticles transport in the environment, as potential toxicity and transport behavior depends strongly on whether nanoparticles are in aggregated or dispersed state and factors that control the aggregation behavior of nanoparticles. The state of dispersion including physicochemical properties of nanoparticles, pH and ionic strength should be carefully studied before application of doped nanomaterials.

5.6. Nomenclature

Rh	Average hydrodynamic diameter (nm)
IEP	Iso-electric point
HD	Hydrodynamic diameter (nm)
D	Diffusion coefficient(m^2s^{-1})
k_B	Boltzmann constant ($J.K^{-1}$)
μ	Viscosity of medium ($kg.m^{-1}.s^{-1}$)
ζ	Zeta potential (mV)
U	Electophoretic mobility($m^2V^{-1}s^{-1}$)
T	Temperature (K)
E	Electrical permittivity of medium ($C^2.N^{-1}.m^{-2}$)
A	Hamakar constant (J)
Na	Avogadro's constant
Mi	Molarity (M)
A	Particle radius (nm)
S	Separation distance between particle surfaces (nm)
Va	Potential energy due to van der Waals attraction force
Vr	Potential energy between particles due to electrical repulsion

5.7. References

Almquist, C. B., Biswas P. (2002). Role of synthesis method and particle size of nanostructured TiO_2 on its photoactivity. Journal of Catalysis 212, 145-156.

An, W. J., Thimsen E., Biswas P. (2010). Aerosol-chemical vapor deposition method for synthesis of nanostructured metal oxide thin films with controlled morphology. Journal of Physical Chemistry Letter 1, 249-253.

Aniya, M., Shimojo F. (2006). Atomic structure and bonding properties in amorphous Cu-x(As2S3)(1-x) by ab initio molecular-dynamics simulations. Journal of Non-Crystalline Solids 352, 1510-1513.

Asahi, R., Morikawa T. (2007). Nitrogen complex species and its chemical nature in TiO2 for visible-light sensitized photocatalysis. Chemical Physics 339, 57-63.

Asahi, R., Morikawa T., Ohwaki T., Aoki K., Taga Y. (2001). Visible-light photocatalysis in nitrogen-doped titanium oxides. Science 293, 269-271.

Byrne, J. A., Fernandez-Iba˜nez P. A., Dunlop P. S. M., Alrousan D. M. A., Hamilton J. W. J. (2011). Photocatalytic enhancement for solar disinfection of water: a review. International Journal of Photoenergy 2011, 1-12.

Carre, A., Roger F., Varinot C. (1992). Study of acid-base properties of oxide, oxide glass, and glass-ceramic surfaces. Journal of Colloid and Interface Science 154, 174-183.

Cho, K., Biswas P. (2006). Sintering rates for pristine and doped titanium dioxide determined using a tandem differential mobility analyzer system. Aerosol Science and Technology 40, 309-319.

Clarence, D. J. Managing the effects of nanotechnology, Washington D.C Project on Emerging Nanotechnologies. Woodrow Wilson International Center for Scholars 2008.

Garcia-Garcia, S., Jonsson M., Wold S. (2006). Temperature effect on the stability of bentonite colloids in water. Journal of Colloid and Interface Science 298, 694-705.

Gervasini, A., Carniti P., Keranen J., Niinisto L., Auroux A. (2004). Surface characteristics and activity in selective oxidation of o-xylene of supported V_2O_5 catalysts prepared by standard impregnation and atomic layer deposition. Catalysis Today 96, 187-194.

Gilbert, B., Ono R. K., Ching K. A., Kim C. S. (2009). The effects of nanoparticle aggregation processes on aggregate structure and metal uptake. Journal of Colloid and Interface Science 339, 285-295.

Giuli, G., Paris E., Mungall J., Romano C., Dingwell D. (2004). V oxidation state and coordination number in silicate glasses by XAS. American Mineralogist 89, 1640-1646.

Grassian, V. H., O'Shaughnessy P. T., Adamcakova-Dodd A., Pettibone J. M., Thorne P. S. (2007). Inhalation exposure study of titanium dioxide nanoparticles with a primary particle size of 2 to 5 nm. Environmental Health Perspectives 115, 397-402.

Gun'ko, V. M., Zarko V. I., Leboda R., Chibowski E. (2001). Aqueous suspension of fumed oxides: particle size distribution and zeta potential. Advances in Colloid and Interface Science 91, 1-112.

Gun'ko, V. M., Zarko V. I., Turov V. V., Leboda R., Chibowski E., Holysz L., et al. (1998). CVD-titania on fumed silica substrate. Journal of Colloid and Interface Science 198, 141-156.

Gun'ko, V. M., Zarko V. I., Turov V. V., Leboda R., Chibowski E., Pakhlov E. M., et al. (1999). Characterization of fumed alumina/silica/titania in the gas phase and in aqueous suspension. Journal of Colloid and Interface Science 220, 302-323.

Guzman, K. A. D., Finnegan M. P., Banfield J. F. (2006). Influence of surface potential on aggregation and transport of titania nanoparticles. Environmental Science & Technology 40, 7688-7693.

Hoffmann, M. R., Martin S. T., Choi W. Y., Bahnemann D. W. (1995). Environmental applications of semiconductor photocatalysis. Chemical Reviews 95, 69-96.

Hsiang, H. I., Liu Y. L. (2009). Electrical properties of copper and titanium-codoped zinc ferrites. Journal of Alloys and Compounds 472, 516-520.

Jiang, J., Chen D. R., Biswas P. (2007). Synthesis of nanoparticles in a flame aerosol reactor with independent and strict control of their size, crystal phase and morphology. Nanotechnol. 18, 285603.

Jiang, J., Oberdorster G., Elder A., Gelein R., Mercer P., Biswas P. (2008). Does nanoparticle activity depend upon size and crystal phase? Nanotoxicology 2, 33-42.

Jiang, J. K., Oberdorster G., Biswas P. (2009). Characterization of size, surface charge, and agglomeration state of nanoparticle dispersions for toxicological studies. Journal of Nanoparticle Research 11, 77-89.

Ko, K. H., Lee Y. C., Jung Y. J. (2005). Enhanced efficiency of dye-sensitized TiO_2 solar cells (DSSC) by doping of metal ions. Journal of Colloid and Interface Science 283, 482-487.

Li, W., Wang Y., Lin H., Shah S. I., Huang C. P., Doren D. J., et al. (2003). Band gap tailoring of Nd^3-doped TiO_2 nanoparticles. Applied Physics Letters 83, 4143-4145.

Liu, H. L., Yang T. C. K. (2003). Photocatalytic inactivation of Escherichia coli and Lactobacillus helveticus by ZnO and TiO_2 activated with ultraviolet light. Process Biochemistry 39, 475-481.

Long, T. C., Saleh N., Tilton R. D., Lowry G. V., Veronesi B. (2006). Titanium dioxide (P25) produces reactive oxygen species in immortalized brain microglia (BV2): Implications for nanoparticle neurotoxicity. Environmental Science & Technology 40, 4346-4352.

Maynard, A. D., Aitken R. J., Butz T., Colvin V., Donaldson K., Oberdorster G., et al. (2006). Safe handling of nanotechnology. Nature 444, 267-269.

Mukherjee, B., Weaver J. W. (2010). Aggregation and charge behavior of metallic and nonmetallic nanoparticles in the presence of competing similarly-charged inorganic ions. Environmental Science & Technology 44, 3332-3338.

Nel, A., Xia T., Madler L., Li N. (2006). Toxic potential of materials at the nanolevel. Science 311, 622-627.

Nowotny, J., Bak T., Nowotny M. K., Sheppard L. R. (2006). Chemical diffusion in metal oxides. example of TiO2. Ionics 12, 227-243.

Oberdorster, G., Oberdorster E., Jon J. G. (2005). Nanotoxicology: an emerging discipline evolving from studies of ultrafine particles. Environmetal Health Perspectives 113, 823-839.

Sahu, M., Biswas P. (2010). Single-step processing of copper-doped titania nanomaterials in a flame aerosol reactor. Nanoscale Research Letters Under review.

Sene, J. J., Zeltner W. A., Anderson M. A. (2003). Fundamental photoelectrocatalytic and electrophoretic mobility studies of TiO2 and v-doped TiO_2 thin-film electrode materials. Journal of Physical Chemistry B 107, 1597-1603.

Suttiponparnit, K., Jiang J., Sahu M., Suvachittanont S., Charinpanitkul T., Biswas P. (2010). Role of surface area, primary particle size, and crystal phase on titanium dioxide nanoparticle dispersion properties. . Nanoscale Research Letters DOI: 10.1007/s11671-010-9772-1,2010.

Tanabe, K., Sumiyosh.T, Shibata K., Kiyoura T., Kitagawa J. (1974). New hypothesis regarding surface acidity of binary metal-oxides. Bulletin of the Chemical Society of Japan 47, 1064-1066.

Tiwari, V., Jiang J., Sethi V., Biswas P. (2008). One-step synthesis of noble metal-titanium dioxide nanocomposites in a flame aerosol reactor. Applied Catalysis a-General 345, 241-246.

Wang, Z. M., Yang G. X., Biswas P., Bresser W., Boolchand P. (2001). Processing of iron-doped titania powders in flame aerosol reactors. Powder Technology 114, 197-204.

Waychunas, G. A., Kim C. S., Banfield J. F. (2005). Nanoparticulate iron oxide minerals in soils and sediments: unique properties and contaminant scavenging mechanisms. Journal of Nanoparticle Research 7, 409-433.

Wu, B., Huang R., Feng X., Biswas P., Tang Y. J. (2010). Bacterial responses to Cu-doped TiO_2 nanoparticles. Sci. Total Environ. 408, 1755-1858.

Zeng, H., Singh A., Basak S., Ulrich K. U., Sahu M., Biswas P., et al. (2009). Nanoscale size effects on uranium(VI) adsorption to hematite. Environmental Science & Technology 43, 1373-1378.

Zhang, D. Q., Li G. S., Yu J. C. (2010). Inorganic materials for photocatalytic water disinfection. Journal of Materials Chemistry 20, 4529-4536.

Zhang, J. Surface forces between silica surfaces in CnTACl solutions and surface free energy characterization of talc. Mining and Minerals Engineering. PhD. Virginia Polytechnic Institute and State University (Virginia Tech), Blacksburg, VA, 2006.

Chapter 6:

Bacterial Responses to Cu-doped TiO_2 Nanoparticles

The results presented here were published in:

Wu, B, R. Huang, M. Sahu, X. Feng, P. Biswas, and Y. J. Tang, *Bacterial Responses to Cu-doped TiO_2 Nanoparticles,* Science of the Total Environment*,* 2010*,* 408 (7): p 1755-1758.

6.1. Abstract

The toxicity of Cu-doped TiO_2 nanoparticles (NPs) of 40 nm size, synthesized by a flame aerosol reactor, on *Mycobacterium smegmatis* (pathogenic bacteria) and *Shewanella oneidensis* MR-1 (environmental bacteria) has been studied. Pristine TiO_2 NPs did not affect the growth of the two species, while Cu-doped TiO_2 NPs significantly reduced *Mycobacterium smegmatis* growth. The Cu-doped TiO_2 NPs was also able to suppress certain key enzyme functions (such as NADPH production). The Cu-doped TiO_2 NPs were found not to penetrate into the cell or physically damage the cellular structure. Their toxicity was mainly mediated by released ionic copper from the NPs. The dissolved copper (ionic copper) was associated (or concentrated) on negatively charged NP surface and thus its cellular toxicity was significantly enhanced. The inhibitory effect from ionic copper on NPs was removed in the presence of EDTA in the culture medium. On the other hand, *S. oneidensis* MR-1 was able to reduce ionic copper and absorb Cu-doped TiO_2 NPs on the cell surface, thus remediating toxic NPs from the culture medium during its growth.

Key words: *Mycobacterium smegmatis, Shewanella oneidensis* MR-1, EDTA, ionic copper, NADPH, remediate

6.2. Introduction

Due to the significant potential of nanotechnology and wide scale applications, there is now an understanding that nanomaterials should have minimal environmental and toxic side effects. An upfront evaluation of nanomaterials in this regard will not only help ensure safety of nanotechnological applications, but also help design materials that have minimal adverse effects, and retain their functionality.[1, 2] Agencies have also evaluated and proposed strategies for research in this area.[3] Titanium dioxide (TiO_2) is considered to be an inert material and has therefore been widely used in many industrial applications as a pigmentary material.[4] In recent years, it has also been used as a photocatalyst, and many applications have been proposed especially for the anatase crystal phase nanomaterial.[5, 6, 7, 8] To evaluate if nanostructured titanium dioxide would have enhanced adverse biological impacts, many researchers have conducted studies with these materials.[9, 10, 11] The reports in the literature are conflicting in the trends, however, it is apparent that titanium dioxide is a low toxicity material. Jiang et al. performed very detailed studies using a range of nanometer sized titanium dioxide particles and found a clear set of trends and metrics that were important.[12] They reported that the reactive oxygen species (ROS) production followed a S-shaped curve dependence on particle size. They also used their samples to establish effects of crystal phase.

To enhance the functional properties and applicability of titanium dioxide, doped versions of the materials are being synthesized. Enhanced light activation by visible frequencies and increased catalytic activity have been demonstrated.[13, 14, 15] Cu-doped TiO_2 is also being considered for light harvesting applications and has potential for wide scale use in the solar energy sector.[16, 17] On the other hand, Karlsson and co-researchers

pointed out that CuO NPs were most potent regarding cytotoxicity and DNA damage of human lung epithelial cell when comparing with other metal oxides and carbon nanotubes.[18] Meng et al. found that high reactivity of nano-copper particles resulted in specific nanotoxicity to living organisms by culminating the metabolic alkalosis.[19] Results reported by Chen et al. also indicated that nano-copper particles could induce gravely toxicological effects and injuries on kidney, liver and spleen of experimental mice.[20] However, up to now, the toxicity of copper doped TiO_2 NPs to different microbial systems is still poorly understood, and very few methods have been proposed to remediate toxic metal NPs from the environment.[21] While functional property enhancement studies have been extensively conducted, there are few to none on the eventually toxicity of doped materials. Such studies are important as they would help develop insights to mechanistic effects of toxicity, by comparing the biological effects of pristine to doped titanium dioxide nanomaterials.

Exposure of nanomaterials to microorganisms can provide preliminary answers on their potential toxicity. Mahapatra and Karak studied the antibacterial activity of silver NPs against *Bacillus subtilis* and *Staphylococcus aureus* bacteria and found toxicity increased with increasing concentration of the nanoparticles.[22] Sanpui and his colleagues used *Escherichia coli* as a model bacteria to test the bactericidal efficacy of chitosan-siliver NPs.[23] Using microorganisms as a model to test the toxicity is a simple and fast approach; and response mechanisms could be understood readily. In addition, some environmental microorganisms can bioremediate NPs, which may further be considered as a potential methodology for countering the toxicity of such materials in the environment.[24]

In this paper, aerosol reactors are used to carefully synthesize Cu-doped titanium dioxide nanomaterials. The well characterized nanomaterials are then used to evaluate the toxicity by examining the effects on two model bacterial species: *Mycobacterium smegmatis,* a gram-positive bacterium and a model pathogenic strain for study of *Tuberculosis*; *Shewanella oneidensis* MR-1, a gram-negative environmental bacterium found in sediments. This microorganism has a versatile metabolic system that can reduce many kinds of metal ions, including Fe (III), Cu(II), Cu(I), and Cr(VI) [25, 26, 27]. The growth rates of the two microbial species in the presence of the various nanomaterials are studied. To develop a mechanistic understanding, the impact of dissolved copper (ionic forms) and doped nanoparticles on cellular enzymatic functions (using NADPH production as a model example) is established.

6.3. Materials and Methods

6.3.1. Synthesis of nanoparticles

A flame aerosol reactor (FLAR) with a three-port co-flow diffusion burner was used to synthesize 40 nm Cu-doped TiO_2 and pristine TiO_2 nanoparticles. The FLAR has been used previously to synthesize nanoparticles with independent control over the size, shape, crystal phase, and morphology, and details are provided in earlier publications.[12] Titanium tetra-ispopropoxide (TTIP, 97%, Aldrich, USA) and copper (II) ethyl hexanoate (Aldrich, USA) were used as the precursors for the synthesis of the various nanomaterials. Copper (II) ethyl hexanoate was dissolved in the xylene and atomized by a stainless steel nebulizer to the high temperature zone. Nitrogen gas at 1.5 lpm (liter per minute) was bubbled through TTIP in a bubbler maintained at 88 °C. Doping percentages

Table 6- 1: Summary of experiments performed in this study.

	Objectives	Sample	System used/ Procedure description	Parameter values/ Experimental technique
1	Synthesis and characterization of nanoparticles	A 1.8% Cu-TiO_2 (40 nm) Zeta P. = -7.73 $\pm$0.59	FLAR Temperature: 88°C; Gas flowrate: 1.5 lpm (N_2/TTIP); 7 lpm (O_2); 1.6 lpm (CH_4)	Characterization: SEM/EDS; XRD; ICP-MS
		B 0.6% Cu-TiO_2 (40 nm) Zeta P. = -9.30 $\pm$0.85		
		C Pristine TiO_2 (40 nm) Zeta P. = -9.79 $\pm$0.49		
		D Pristine CuO (< 50 nm) Zeta P. = -7.96 $\pm$0.40	Commercial product from Sigma	
		E Dissolved $CuCl_2$ and CuCl (Ionic form)	Commercial product	
2	*In vivo* microbial nano-toxicity	*Shewanella oneidensis*	NPs concentrations of 0.005 and 0.02 g/L	Cell density measurements on exposure to NPs
		Mycobacterium smegmatis	NPs concentrations of 0.005 and 0.02 g/L	
3	*In vitro* enzymatic inhibition	Glucose assay kit	Hexokinase (HK) and glucose-6-phophate dehydrogenase	NADPH production under NPs stress
4	Control of NPs toxicity	*Mycobacterium smegmatis*	Increase of cell density; Addition of nutrient; Addition of EDTA; Addition of $CuCl_2$	Cell density measurements on exposure to NPs or ionic copper

*Abbreviations: FLAR: flame aerosol reactor; lpm: liter per minute; TTIP: Titanium tetra-isopropoxide; SEM: scanning electronic microscope; EDS: energy dispersive spectroscope; XRD: X-ray diffraction; ICP-MS: Inductively coupled plasma mass spectrometry; Zeta P.: Zeta potential (in modified Sauton liquid medium, pH=6.65)

were varied by feeding different molar ratios of the precursors to the high temperature combustion zone of the diffusion flame. Oxygen and methane at 7 lpm, and 1.6 lpm, respectively, were introduced into the FLAR system. The temperature and residence time history of the nanoparticles in the combustion zone were controlled to obtain the desired size and composition of the nanoparticles. Sizes of the nanoparticles were characterized

by scanning or transmission electron micrographs (SEM: JEOL 7001LVF, Japan; TEM: JEOL 2100F, Japan). SEM coupled with energy dispersive spectroscopy (EDS) was used to confirm the presence of copper in the nanoparticles. Cu content was further verified by Inductively Coupled Plasma Mass Spectrometry (ICP-MS, Agilent, USA) analysis. Crystal phases of the materials were determined using X-ray diffraction (XRD, Rigaku D-MAX/A9, Japan). Copper oxide (CuO) nanoparticles size < 50 nm (Aldrich, USA) were also used to aid in the mechanistic understanding. Table 6-1 lists the characteristics of the nanomaterials used in the biological experiments.

6.3.2. Preparation of Nanoparticles (NPs) suspension for biological experiments

Four types of NPs (1.8% Cu-doped TiO_2, 0.6% Cu-doped TiO_2, pristine TiO_2, CuO) were tested in this study. The NPs were added to sterilized DI water to make the stock solution (1 g/L). After ultrasonic treatment (MISONIX, USA), the NP stock was directly added into cell cultures for toxicity studies. The zeta potential of the NP suspensions was measured by Zeta-sizer (Nanoseries ZS, Malvern, UK).

6.3.3. *In vivo* microbial growth experiments

M. smegmatis and *S. oneidensis* MR-1 strains were stored at -80°C prior to use. *M. smegmatis* was grown in Middlebrook 7H9 medium at 37 °C and *S. oneidensis* MR-1 was grown in Luria-Bertani (LB) medium at 30 °C overnight (supplementary Table S1), respectively. The bacteria were then inoculated into minimal medium with an inoculation rate of 5%. The compositions of the minimal media (supplementary Table S-1) were:

modified Sauton liquid medium (for *M. smegmatis*) and MR-1 medium (for *S. oneidensis* MR-1). When *M. smegmatis* or *S. oneidensis* MR-1 growth in the minimal medium reached middle log phase (optical density at 600 nm (OD_{600}) about 1.0), a second subculture was performed by transferring the cell culture (5% inoculation ratio) into 5 ml fresh minimal medium for toxicity experiments. NPs were added to the subculture solutions usually when cell density was equal to OD_{600}~0.1 (e.g., early exponential phases). The cell cultures in 50 mL falcon tubes were then shaken at a speed of 200 rpm (each experiment has duplicates). Cell density was monitored by a UV spectrometer (Genesys, Thermo Scientific, USA) at a wavelength of 600 nm. The NPs also have certain absorbance at OD_{600}, so the actual cell density was obtained based on the equation (1) below:

$$OD_{600,\ actual} = OD_{600,\ measured\ with\ NPs\ and\ cells} - OD_{600,\ measured\ with\ NPs\ in\ cell\ free\ solution} \quad (1)$$

6.3.4. Copper concentration measurement by ICP-MS

In order to determine free ionic copper concentrations in the aqueous culture solutions, Cu-TiO_2 NPs were removed from the culture by high speed centrifugation (20,000 g) for 20 minutes, after which the supernatant was collected and filtered (0.22 μm, Nylon, Millipore, USA). The ionic copper (Cu^{2+}) concentrations in the supernatant were determined by Inductively Coupled Plasma Mass Spectrometry (ICP-MS, Agilent, USA). *S. oneidensis* MR-1 is able to reduce metal ions and absorb NPs.[27] To monitor microbial remediation of total Cu-TiO_2 NPs, the bacteria (treated with Cu-TiO_2 NPs for three hours or six hours) were filtered out using 0.22 μm membrane filter (Nylon, Millipore, USA). The solution was further pretreated with 2% HNO_3 and 0.5 % HCl before estimating the

total copper (including both Cu^{2+} and Cu-doped NPs) remaining in the cell-free solution by ICP-MS. Since the bacterial size is >1μm, NPs or metal copper absorbed on bacterial surface could be removed together with bacteria by micro-filtration, while free Cu-TiO_2 NPs or ionic copper would pass through the filter and remained in the cell-free solution. Due to the agglomeration of the NPs, some of them may not pass through the microfilter and deposit on the filter membrane, and this was observed by comparing the initial total copper added in cell free medium to that measured with a filtration run (Table 6-2).

Table 6- 2: Total copper in the culture solutions

. Strain			*M. smegmatis*	*S. oneidensis* MR-1
A: 1.8% Cu - TiO_2 NPs (20 mg/L)	Total copper in cell free medium with NP A (μg/L)			360.5±18.0
	Micro-filtration of cell free NP A solution, total copper remained in the medium (μg/L)			326.4±16.3
	0 hr	OD_{600}	ND*	0.193±0.001
		[copper](μg/L)	ND	316.5±16.1
	3 hrs	OD_{600}	ND	0.273±0.010
		[copper](μg/L)	ND	267.5±3.4
	6 hrs	OD_{600}	ND	0.349±0.025
		[copper](μg/L)	ND	210.8±13.8
	copper reduction rate from 3 hrs to 6 hrs	Δ [copper] / ($OD_{600\ ave}$× time) =((μg/L)/Abs×hr)	ND	60.8
B: 0.6% Cu - TiO_2 NPs (20 mg/L)	Total copper in cell free medium with NP B (μg/L)		~125	~130
	3 hrs	OD_{600}	0.213±0.001	0.261±0.008
		[copper](μg/L)	117.9±2.1	122.0 ±0.6
	6 hrs	OD_{600}	0.397±0.006	0.359±0.015
		[copper](μg/L)	120.9±1.4	97.6±9.8
	Copper reduction rate from 3 hrs to 6 hrs	Δ [copper]/ ($OD_{600\ ave}$× time) =((μg/L)/Abs×hr)	~0	26.2

*NP A strongly inhibited mycobacterium cellular function, so the copper microbial reduction by mycobacterium in NP A medium was not discussed.

$OD_{600\ ave}$ is the average cell density between 3 and 6 hours culture.

6.3.5. *In vitro* study on NPs and ionic Cu toxicity via enzymatic assay kit

The effect of NPs and ionic Cu on enzyme functions was analyzed using a D-glucose enzymatic assay kit (R-Biopharm, Germany). The test is based on NADPH production rates from glucose in the presence of enzyme hexokinase (HK) and glucose-6-phosphate dehydrogenase. The two enzymes convert sugar, ATP, and cofactor NADP to gluconate-6-phosphate, ADP, and NADPH. This enzymatic reaction is present in most biological systems and thus it was used as a standard test for *in vitro* NPs toxicity. In our experiment, samples with known amount of NPs or ionic copper (e.g., $CuCl_2$) was added to the cell-free assay solutions (containing standard amount of NADP, ATP, the two enzymes, and 0.5 g/L glucose standards). The reaction was carried out in 2 mL cuvettes and the NADPH production rate was monitored by the UV absorbance at a wavelength of 340 nm using a spectrometer (Genesys, Thermo Scientific, USA). If any enzyme (HK or glucose-6-phophate dehydrogenase) is inhibited, the production of NADPH from D-glucose will be reduced in comparison to the control experiments (without addition of any stresses such as NPs). Since reactants (e.g., ATP) and the products (e.g., NADPH) in the enzymatic reactions are essential to cellular energy metabolism for all living species, this *in vitro* test provides a simple and fast approach to study NPs biochemical toxicity at enzyme level.

6.3.6. SEM/TEM protocols

Cellular scanning electron microscope (SEM) and transmission electron microscope (TEM) images were taken for the samples as described briefly. *Mycobacteria smegmatis* and *Shewanella oneidensis* cultures were treated with 0.02 g/L of 1.8% Cu-doped TiO_2

NPs for one hour. The NPs mixed with the bacterial culture solution was removed from the culturing tube by centrifugation and fixed in 4% Paraformaldehyde/ 2.5% Gluteraldehyde in 0.1M cacodylate buffer (pH 7.2) overnight. Samples were post fixed with Osmium Tetroxide and then dehydrated in ethanol. TEM samples were embedded in Pelco Eponate 12 resin (Ted Pella Inc., Redding, USA). Sections were cut on an Ultramicrotome (Leica, Germany) and viewed in a TEM (H7500, Hitachi, Japan) at 80 kV using the HR mode and photographed using a digital camera (Hamamatsu, Japan). SEM samples were dried using a critical-point drier and coated with gold/palladium by a sputter gun. Samples were viewed and photographed using a SEM (3000H, Hitachi, Japan). The overall test plan in this study is described in Table 6-1.

6.4. Results

The overall objective of the tests was to examine the toxicity of Cu-doped TiO_2 to microgansims. To better elucidate the mechanisms, tests were also conducted with pristine TiO_2 and CuO NPs. These were done by performing both i*n vivo* and *in vitro* tests. The *in vivo* tests using the two species can reveal the tolerance of the microorganisms to NPs. *In vitro* enzymatic tests provided a simple and fast method to study the interaction of NPs with key enzymes excreted by the bacteria.

6.4.1. The effect of NPs on microbial growth

When the bacterial density reached 0.1 (OD_{600}), a series of tests were conducted with all the four different NPs (1.8% Cu-TiO_2, 0.6% Cu-TiO_2 ,TiO_2 and CuO) by adding them to a *M. smegmatis* or *S. oneidensis* MR-1 culture. When low concentration of NPs (0.005

g/L) are added, the three types (A, B, C in Table 6-1) have no apparent effect on microbial growth (see supplemental Figure S-1).

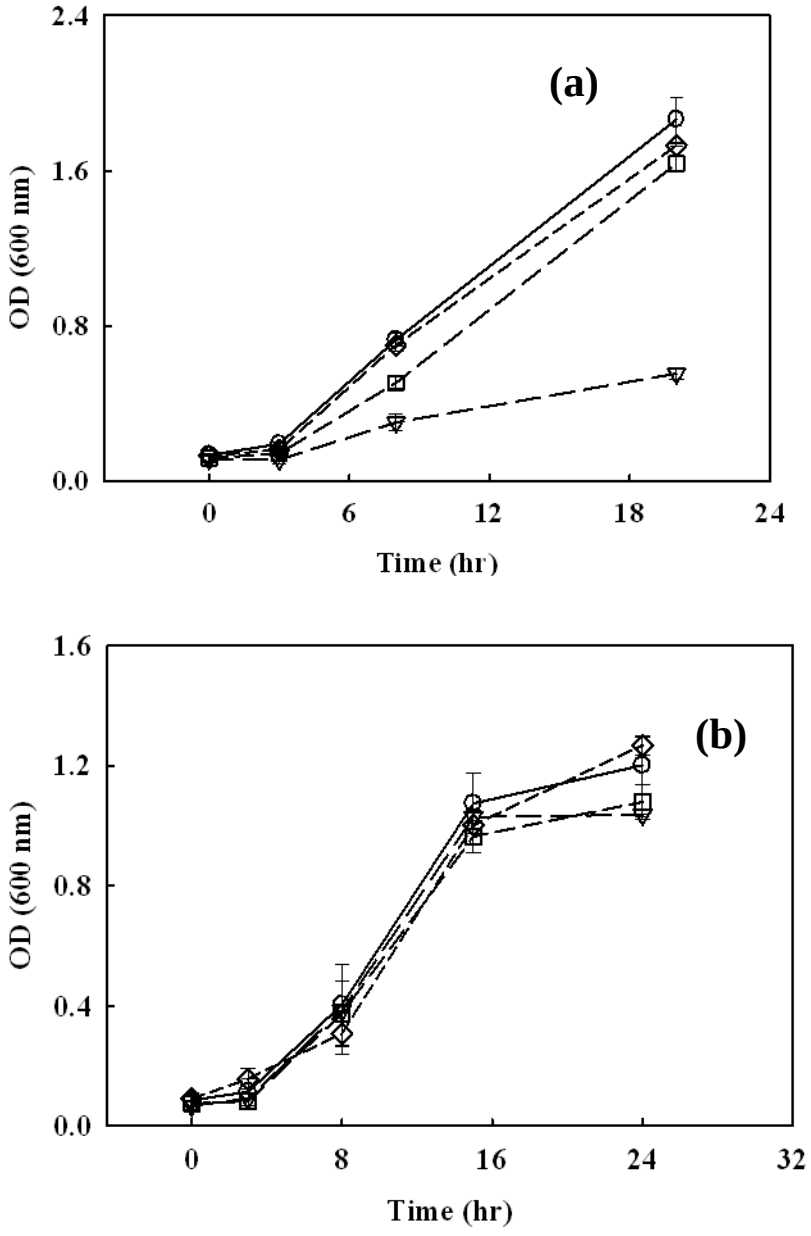

Figure 6- 1: Nanoparticles toxicity (0.02 g/L) on M. smegmatis (a) and S. oneidensis MR-1 (b); (○) Control; (▽) 1.8% Cu-TiO_2 NPs; (□) 0.6% Cu-TiO_2 NPs; (◊) TiO_2 NPs.

On addition of high concentration NPs (0.02 g/L), the growth of *M. smegmatis* was completely inhibited by 1.8% Cu-TiO_2 NPs (A, Table 1; 0.02 g/L, contains about 0.36 mg/L total copper), and moderately negative-affected by 0.6% Cu-TiO_2 NPs (B, Table 6-1; 0.02 g/L, contains about 0.11 mg/L total copper) (Figure 1). Pristine TiO_2 (C, Table 6-1) did not show any effect on *M. smegmatis* (or *S. oneidensis* MR-1) growth even at higher concentrations (0.02 g / L). On the other hand, *S. oneidensis* MR-1 growth was only slightly affected by 1.8 and 0.6% Cu-TiO_2 NPs at high concentrations (0.02 g/L), i.e., final cell density was reduced by at most 10~20%. Since no growth stress was detected when *M. smegmatis* and *S. oneidensis* MR-1 were exposed to pristine TiO_2 NPs, Cu-TiO_2 NPs toxicity is apparently associated with copper and the toxicity increases with NPs copper content. This was verified by tests in which the same concentration of pristine CuO NPs (D, Table 6-1; 0.02 g/L, contains 12.9 mg/L total copper) to test its toxicity to *M. smegmatis* and *S. oneidensis* MR-1 in order to further confirm this conclusion. The results (supplementary Figure S-2) indicated that *M. smegmatis* growth was completely inhibited by pristine CuO NPs, while *S. oneidensis* MR-1 still displayed significant growth.

6.4.2. *In vitro* enzymatic test on ionic copper and NPs toxicity

Copper is an essential nutrient for cell growth, but high concentrations of ionic Cu can produce reactive radicals and interfere with protein functions.[28, 29, 30] To quickly test the toxicity of NPs, a simple enzymatic assay was used to investigate the enzyme activity under the effects of NPs. Hexokinase and glucose-6-phosphate dehydrogenase are common enzymes involved in the glycolysis and pentose phosphate pathway, which

regulate energy (NADPH) metabolism. The enzyme activity assay can be used as a model test to explain NPs effect on enzyme or cofactor functions. Figure 6-2 demonstrates that NADPH production decreased by more than 22 % in the presence of 1.8 and 0.6% Cu-TiO_2 NPs, even at low concentrations (0.005 g/L), while pristine TiO_2 NPs did not have any influence on the enzyme activity.

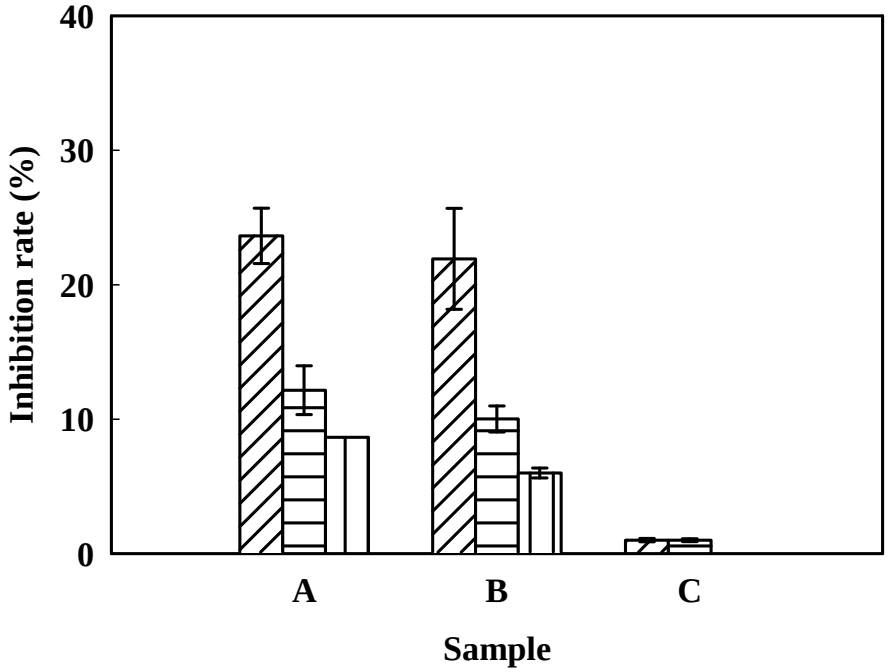

Figure 6- 2: Nanoparticle toxicity in vitro test using enzyme kit; A: 1.8% Cu-TiO_2 NPs; B: 0.6% Cu-TiO_2 NPs; C: TiO_2 NPs; (Diagonal line column) NPs concentration (0.02 g/L); (Horizontal line column) NPs concentration (0.005 g/L); (Vertical line column) NPs concentration (0.02 g/L, with EDTA).

$$\text{The inhibition rate} = [1 - \frac{NADPH \text{ production (with NPs)}}{NADPH \text{ production (control)}}] \times 100\%$$

6.4.3. Specification of copper associated toxicity

The copper in Cu-TiO_2 NPs can be dissolved and releases free copper ions into the aqueous solution because of the large specific surface area of the NPs. After addition of 1.8 % Cu-TiO_2 NPs (A, Table 6-1) into *Mycobacterium* or *Shewanella* cultures, the NPs were precipitated from the well mixed culture by high-speed centrifugation (20,000 g for 20 minutes). The free ionic copper in supernatant was measured by ICP-MS. Up to 18 μg/L ionic copper was present in solution (~5 % wt of the total copper in Cu-TiO_2 NPs). In order to investigate free ionic copper stresses to bacterial strains, *M. smegmatis* and *S. oneidensis* MR-1 were both exposed to Cu^{2+} ($CuCl_2$) or Cu^{+} (CuCl) using similar cell culture conditions. Figure 6-3 indicates that the growth inhibition of *M. smegmatis* was not obvious when Cu^{2+} concentration was 93 μg/L, while complete inhibition of growth occurred at a Cu^{2+} concentration of 1.9 mg/L. *S. oneidensis* had even higher tolerance to copper ions in the MR-1 medium. Furthermore, the growth profiles of *M. smegmatis* and *S. oneidensis* MR-1 in presence of CuCl (total copper concentration ranged from 14 μg/L to 1.9 mg/L) did not differ from the controls (Supplementary Figure S-3), possibly because CuCl has very low solubility. Such results indicate that *Mycobacterium* can grow with higher ionic copper concentrations if NPs are not present. Thus, the inhibitory effect from Cu-TiO_2 NPs to cells was probably due to an increased localized concentration of Cu^{2+} near the surface of the NPs.

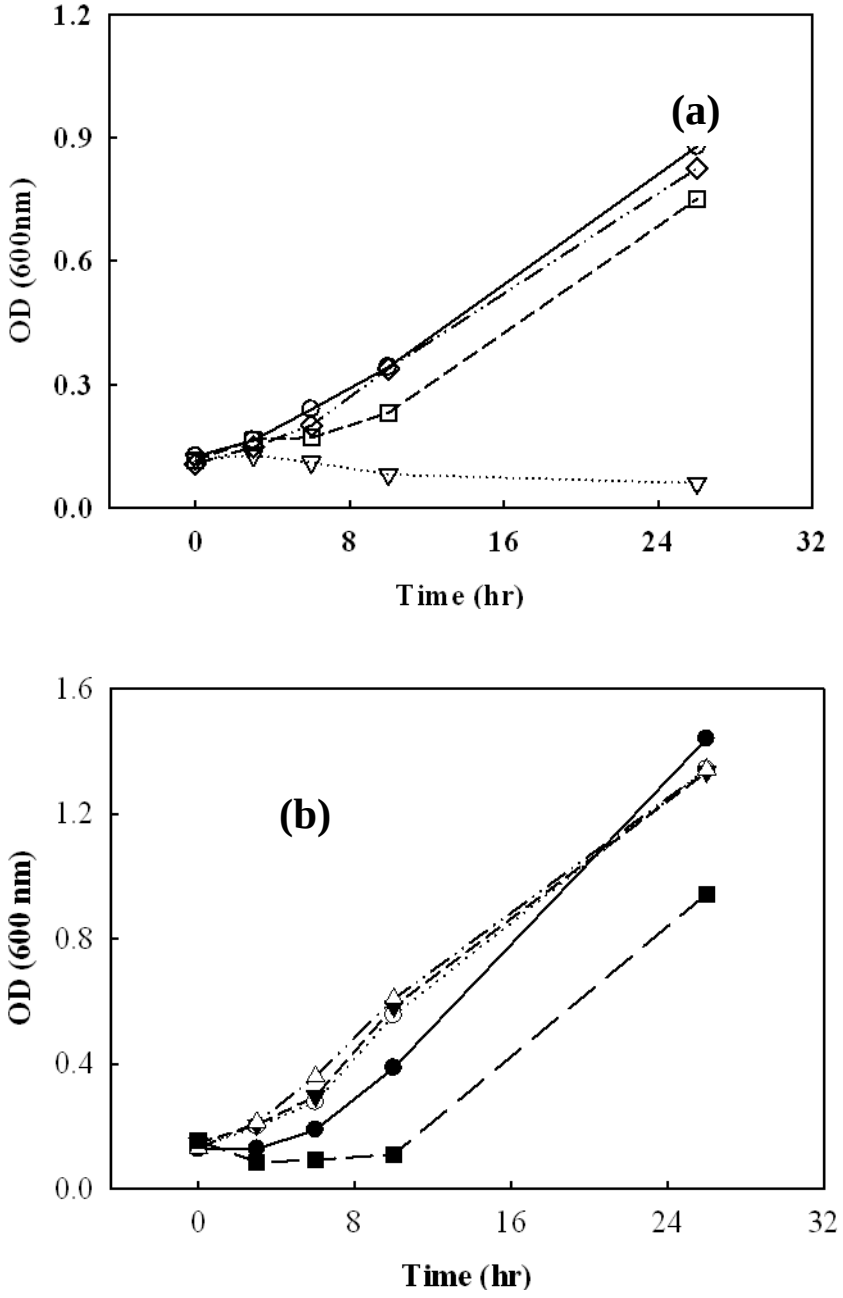

Figure 6- 3: The effect of [Cu (II)] on the growth of M. smegmatis (a) and S. oneidensis MR-1 (b); (○) Control; (Δ) 18.7 mg/L; (□) 1.9 mg/L; (□) 93 µg/L; (◊) 14 µg/L.

6.5. Discussion

Previous studies [31, 32, 33] on mechanisms of NP toxicity have pointed out two hypotheses: (1) Very small NPs can enter the cell and change cellular structure integrity; (2) NPs release toxic ions and interfere with cellular metabolism rather than penetrating into the cell. The SEM and TEM results (Figure 6-4 and 6-5) show that NPs were not inside the *M. smegmatis* or *S. oneidensis* MR-1 cells and there was no apparent physical damage to cellular structures. SEM pictures (Figure 6-4) showed that large numbers of NPs resided on the *S. oneidensis* MR-1 cell surface, but did not lyse the cells. Such observations confirm that 1.8 % Cu-TiO_2 NPs (A, Table 6-1) mediated its toxicity mainly through ionic copper. In the culture medium (i.e., modified Sauton liquid medium, pH 6.65, 20 mg/L pristine TiO_2 and 1.8% Cu-TiO_2 NPs have zeta potential values of -9.79 $\pm$0.49 and -7.73 $\pm$0.59 mV respectively. Less negative zeta potential of Cu-TiO_2 NPs explains that they tend to aggregate more (also illustrated by Figure 6-5). [12, 34] The agglomeration of the NPs increases the particle sizes (small fraction of NPs can't pass through 0.22μm micro filtration due to agglomeration, Table 6-2) and may reduce its ability to mechanically damage cellular structure. TiO_2 based NPs are negatively charged (based on zeta potential) and its surface appeared to be able to absorb/re-absorb positive charged ionic Cu. The copper in the Cu-TiO_2 NPs are dissolved slowly and therefore form a more concentrated layer around the agglomerate structure[32, 34] , i.e., Cu-TiO_2 NPs serve as a dissolved ionic copper carrier/concentrator (e.g., 20 mg Cu-TiO_2 NPs A contains around 360 μg total copper). Thus, the Cu-TiO_2 NPs more efficiently suppress cellular functions via locally concentrated ionic copper zone when they contact cells (illustrated by Figure

6-6). Furthermore, *M. smegmatis* was cultured with $CuCl_2$ solution (Cu^{2+} = 360 µg/L) and the same $CuCl_2$ solution with pristine TiO_2 NPs (20 mg/L) respectively.

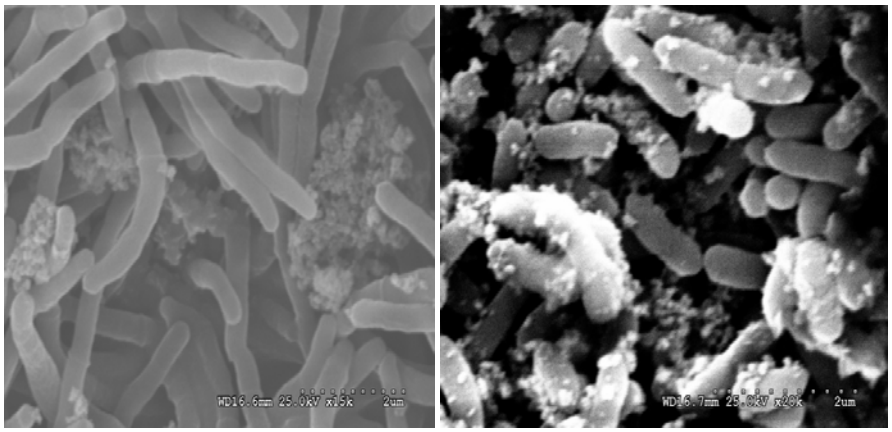

Figure 6- 4: SEM images of M. smegmatis with 1.8% Cu-TiO_2 NPs (a) and S. oneidensis MR-1 with 1.8% Cu-TiO_2 NPs (b).

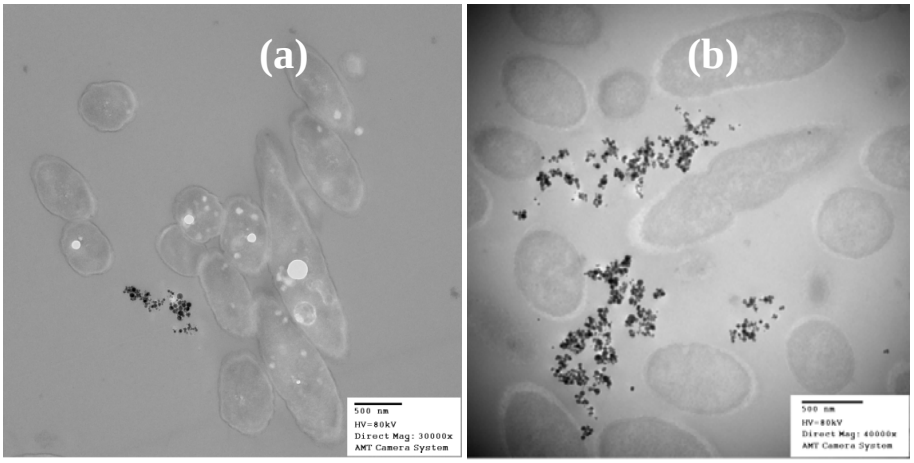

Figure 6-5: TEM images of *M. smegmatis* with 1.8% Cu-TiO_2 NPs (a) and *S. oneidensis* MR-1 with 1.8% Cu-TiO_2 NPs (b).

Supplementary Figure S-4 indicated that presence of none-toxic TiO_2 (C, Table 6-1) would also enhance $CuCl_2$ inhibition to *M. smegmatis* to some extent. With same amount of total copper content, the observed toxicity is in the following order: 20 mg/L 1.8% Cu-TiO_2 NPs (A, Table 6-1) > 360 μg/L Cu^{2+} + pristine TiO_2 NPs (20 mg/L) > 360 μg/L Cu^{2+} (Supplementary Figure S-4). This also indicates the combined effect from NPs and toxic ions may produce higher cytotoxicity to microorganisms.

Cu-TiO_2 NPs toxicity level can be influenced by cell density, addition of nutrients, and presence of chelating agents in the system. First, increased bacterial density could reduce the degree of Cu-TiO_2 NPs toxicity. For example, by comparing the final cell density obtained from Cu-TiO_2 NPs stressed cultures (0.02 g/L) to that of the control cultures (without NPs stresses), the stress on microbial growth was significantly alleviated if *M. smegmatis* was stressed by Cu-TiO_2 NPs at higher OD_{600} (Table 6-3). This is because high cell density reduces the average amount of NPs interacting with each cell, resulting in lower localized ionic copper concentrations. Addition of rich nutrients (Middlebrook 7H9 nutrients, Table S-1) into a minimal medium promoted bacterial growth and also reduced the inhibition effect of NPs on the growth of *M. smegmatis* (Figure 6-7). EDTA is a chelating agent which is able to sequester di- and trivalent metal ions to reduce metal toxicity of ions such as Mn^{2+}, Cu^{2+}, Fe^{3+}, Pb^{2+} and Co^{3+}.[35] EDTA may be also absorbed onto the Cu-TiO_2 NPs surface to form Ti-(OH)EDTA-Cu complex and prevent its dissolution.[36]

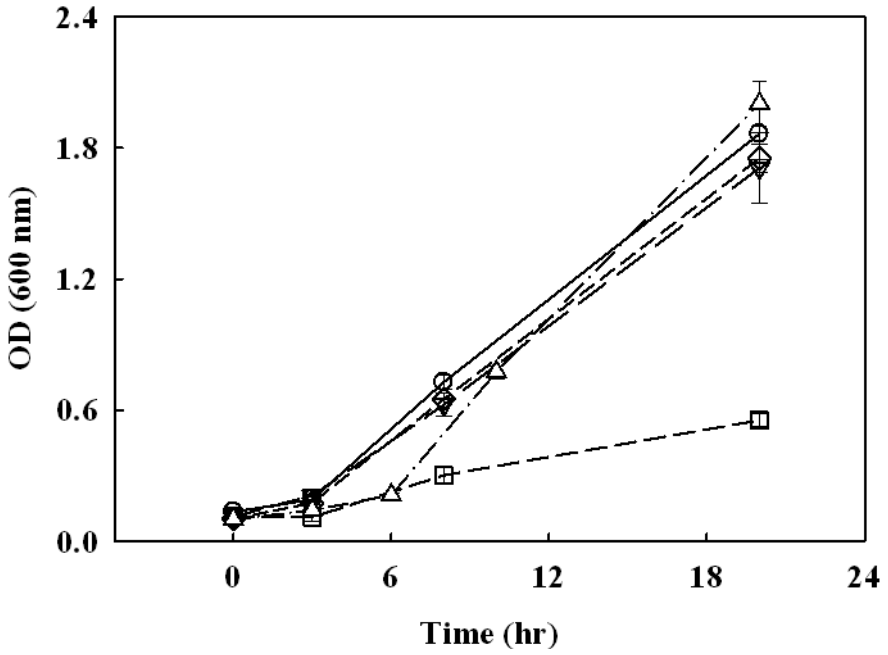

Figure 6- 6: The effect of EDTA and nutrients addition on nanoparticle toxicity (M. smegmatis); (○) Control; (□) Control with EDTA; (□) 1.8% Cu-TiO_2 NPs (0.02 g/L); (◊) 1.8% Cu-TiO_2 NPs (0.02 g/L with EDTA); (Δ) 1.8% Cu-TiO_2 NPs (0.02 g/L with Middlebrook 7H9 nutrients).

After addition of 0.02 g/L EDTA to a *M. smegmatis* culture solution, cells were able to maintain normal growth under 0.02 g/L 1.8% Cu-TiO_2 NP stress (Figure 6-7). *In vitro* enzymatic assay tests also showed that EDTA significantly reduced the inhibitory effect of Cu-TiO_2 NPs on NADPH production (Figure 6-3).

S. oneidensis MR-1 was able to absorb Cu-TiO_2 NPs during its growth (illustrated by Figure 6-4-b). *M. smegmatis* or *S. oneidensis* MR-1 grew with 0.02 g/L Cu-TiO_2 NPs A or B. The total copper (including free copper ions and copper with TiO_2 particles) in the aqueous phase (e. g., not absorbed by cells) was measured by ICP-MS after removing the cells using a 0.22 μm membrane-filter. The total copper concentration in the aqueous

phase in the *M. smegmatis* culture did not change significantly when it grew with Cu-TiO_2 NPs B. However, the total copper concentration in the aqueous phase in the *S. oneidensis* MR-1 culture significantly decreased when it grew with Cu-TiO_2 NPs A or B, most likely by reducing copper to metal copper and immobilizing the NPs or metal copper on cell surfaces (Figure 6-4-b and Table 6-2). Because *S. oneidensis* MR-1 has unique Cu^{2+} reducing enzymatic systems on its outer membrane, it is able to tolerate higher concentration of metal ions and remediate soluble or insoluble copper ions.[26, 27, 29] Therefore, *S. oneidensis* MR-1 may be a potential candidate to remediate the toxic metal NPs in the environment.

6.6. Conclusions

Results from both *in vivo* (*S. oneidensis* MR-1 and *M. smegmatis* growth) and *in vitro* (enzymatic test) experiments have demonstrated that TiO_2 NPs themselves may not be toxic to microorganisms (at the sizes and concentrations tested). However, NPs can enhance the cytotoxicity of metal compounds (i.e., Cu^{2+}) possibly by creating more efficient interactions between metal ions and cells by forming a locally concentrated ionic zone near the surface of NPs. While there are clear impacts on the environment, this observation may help in the design of new NPs based drugs to limit pathogen activities (such as *Mycobacterium* species). Hence, the composition of NPs (i.e., toxic ionic copper) is an important consideration for NPs toxicity. Meanwhile, high cell density, nutrient supplement or addition of EDTA, reduces the associated cellular stress by metal-doped NPs. Metal reducer bacterium, *S. oneidensis* MR-1, can reduce the toxic metals

via their versatile metabolisms, as well as the capability of immobilizing NPs on cellular surfaces.

6.7. References

[1] M. R. Wiesner, G. V. Lowry, P. Alvarez, D. Dionysiou, P. Biswas, *Environ. Sci. Technol.* **2006**, *40*, 4336–4345.

[2] P. Biswas, C. Y. Wu, *J. Air Waste Manag. Assoc*. **2005**, *55*, 708-746.

[3] National Research Council, *Review of Federal Strategy for Nanotechnology-Related Environmental, Health, and Safety Research*, **2008**

[5] M. R. Hoffmann, S. T. Martin, W. Choi, D. W. Bahnemann, *Chem. Rev.* **1995**, *95*, 69-96.

[6] A. Fujishima, K. Honda, *Nature* **1972**, *238,* 37.

[7] E. Sahle-Demessie, M. A. Gonzalez, J. Enriquez, Q. Zhao, *Ind. Eng. Chem. Res*., **2000**, *39*, 48-58.

[8] P. Biswas, C. Y. Wu, *J. Air Waste Manag. Assoc.* **1998**, *48 (2)*, 113-127.

[9] G. Oberdörster, E. Oberdörster, J. Oberdörster, *Environ. Health Persp.* **2005**, *113*, 823-839.

[10] D. B. Warheit, T. R. Webb, K. L. Reed, S. Frerichs, C. M. Sayes, *Toxicology* **2007**, *230*, 90-104.

[11] C. M. Sayes, R. Wahi, P. A. Kurian, Y. P. Liu, J. L. West, K. D. Ausman, *Toxicol. Sci.* **2006**, *92*, 174-185.

[12] J. Jiang, G. Oberdörster, P. Biswas, *J. Nanopat. Res.* **2009**, *In press*.

[13] Z. M. Wang, G. Yang, P. Biswas, W. Bresser, P. Boolchand, *Powder Technol.* **2001**, *114 (1-3)*, 197-204.

[14] G. M. M. Colón, M. C. Hidalgo, J. A. Navío, *Appl. Cata. B: Environ.* **2006**, *67*, 41-51.

[15] N. Namiki, K. Cho, P. Fraundorf, P. Biswas, *Ind. Engr. Chem. Res.* **2005**, *44(14)*, 5213-5220.

[16] C. A. Grimes, *J. Mater. Chem.* **2007**, *17*, 1451-1457.

[17] W. Choi, A. Termin, M. R. Hoffmann, *J. Phys.Chem.* **1994**, *98(51)*, 13669-13679.

[18] H. L. Karlsson, P. Cronholm, J. Gustafsson, L. Möller, *Chem. Res. Toxicol.* **2008**, *21*, 1726-1732.

[19] H. Meng, Z. Chen, G. Xing, H. Yuan, C. Chen, F. Zhao, C. Zhang, Y. Zhao, *Toxicol. Lett.* **2007**, *175*, 102-110.

[20] Z. Chen, H. Meng, G. Xing, C. Chen, Y. Zhao, G. Jia, T. Wang, H. Yuan, C. Ye, F. Zhao, Z. Chai, C. Zhu, X. Fang, B. Ma, L. Wan, *Toxicol. Lett.* **2006**, *163*, 109-120.

[21] N. Lewinski, V. Colvin, R. Drezek, *Small* **2008**, *4(1)*, 26-49.

[22] S. S. Mahapatra, N. Karak, *Mater. Chem. Phy.* **2009**, *In press*.

[23] P. Sanpui, A. Murugadoss, P. V. D. Prasad, S. S. Ghosh, A. Chattopadhyay, *Int. J. Food Microbiol.* **2008**, *124*, 142-146.

[24] Y. J. Tang, A. L. Meadows, J. D. Keasling, *Biotech. Bioeng.* **2007**, *96(1)*, 125-133.

[25] J. M. Tiedje, *Nature Biotech.* **2002**, *20*, 1093-1094.

[26] Y. A. Gorby, S. Yanina, J. S. Malean, K. M. Rosso, D. Moyles, A. Dohnalkova, T. J. Beveridge, I. S. Chang, B. H. Kim, K. S. Kim, D. E. Culley, E. A. Hill, L. Shi, D. S. Elias, D. W. Kennedy, G. Pinchuk, K. Watanabe, S. Ishii, B. Logan, K. H. Nealson, J. K. Fredrickson, *PNAS* **2006**, *103 (30)*, 11358-11363.

[27] Y. J. Tang, M. Ashcroft, D. Chen, G. Min, C. Kim, B. Murkhejee, C. Larabell, J. D. Keasling, F. F. Chen, *Nano Lett.* **2007**, *7(3)*, 754-760.

[28] A. Manceau, K. L. Nagy, M. A. Marcus, M. Lanson, N. Geoffroy, T. Jacquet, T. Kirpichtchikova, *Environ. Sci. Technol.* **2008**, *42*, 1766-1772.

[29] A. C. M. Toes, M. H. Daleke, J. G. Kuenen, G. Muyzer, *Microbiology* **2008**, *154*, 2709-2718.

[30] A. Turner, N. Singh, L. Millard, *Environ. Sci. Technol.* **2008**, *42 (23)*, 8740-8746.

[31] N. Lubick, *Environ. Sci. Technol.* **2008**, *42*, 8617–8617.

[32] E. Navarro, F. Piccapietra, B. Wagner, F. Marconi, R. Kaegi, N. Odzak, L. Sigg, R. Behra, *Environ. Sci. Technol.* **2008**, *42*, 8959-8964.

[33] M. Yamanaka, K. Hara, J. Kudo, *Appl. Environ. Microbiol.* **2005**, *71(11)*, 7589-7593.

[34] M. Lundqvist, J. Stigler, G. Elia, I. Lynch, T. Cedervall, K. A. Dawson, *PNAS* **2008,** *105 (38)*, 14265-14270.

[35] M. Iijima, N. Sato, M. Tsukada, H. Kamiya, *J. Am. Ceram. Soc.* **2007**, *90 (9)*, 2741-2746.

[36] J. K. Yang, A. P. Davis, *J. Coll. Interface Sci.* **1999**, *216(1)*, 77-85.

6.9. Supporting Information

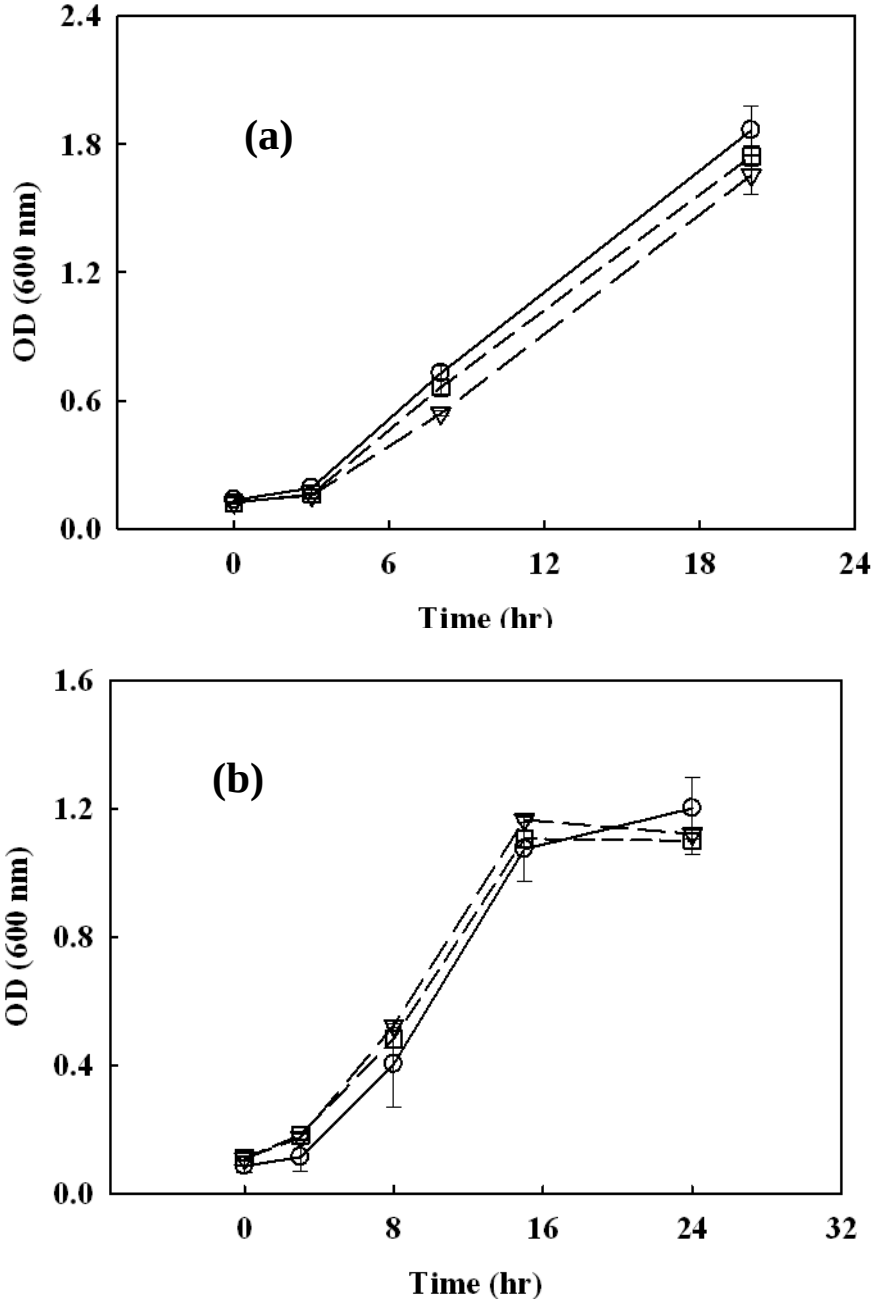

Figure 6-S1. Cu-TiO_2 nanoparticles toxicity (0.005 g/L) on *M. smegmatis* (a) and *S. oneidensis* MR-1 (b); (○) Control; (▽) 1.8% Cu-TiO_2 NPs; (□) 0.6% Cu-TiO_2 NPs.

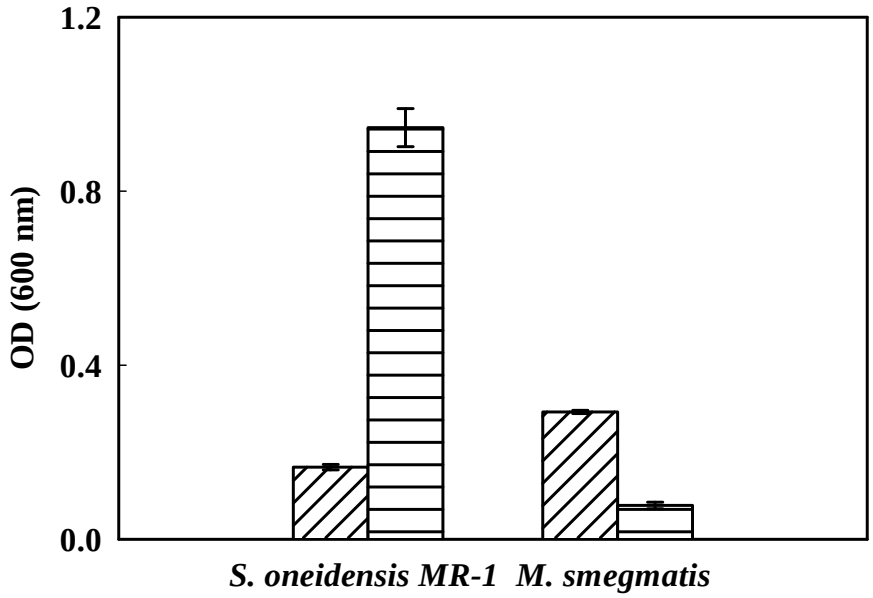

Figure 6-S2: Effect of CuO nanoparticles (0.02 g/L) on *M. smegmatis* and *S. oneidensis* MR-1 growth; (Diagonal line column) OD_{600} at 0 hr; (Horizontal line column) OD_{600} at 24 hrs.

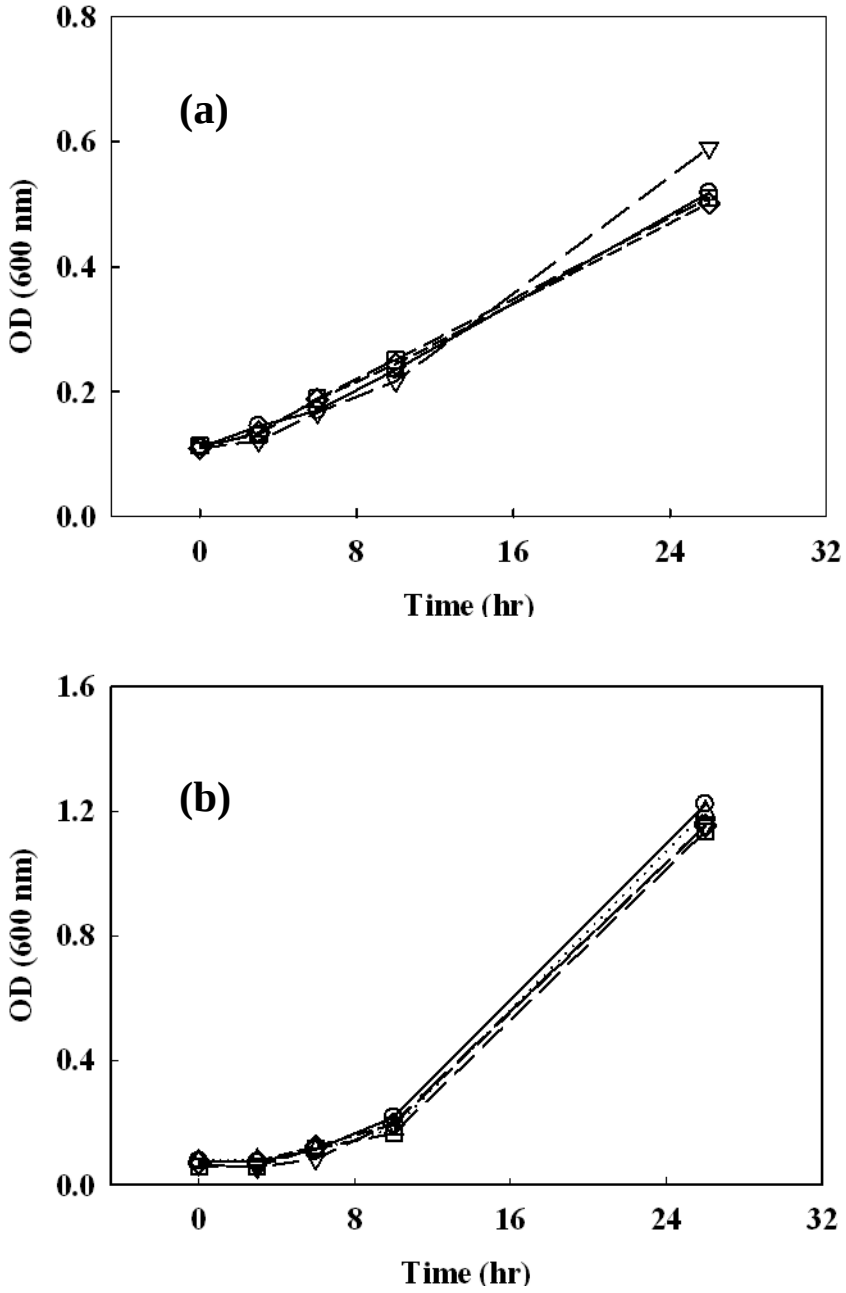

Figure 6-S3: The effect of [Cu (I)] on the growth of *M. smegmatis* (a) and *S. oneidensis* MR-1 (b); (○) Control; (■) 18.7 mg/L; (▽) 1.9 mg/L; (□) 93 µg/L; (◊) 14 µg/L.

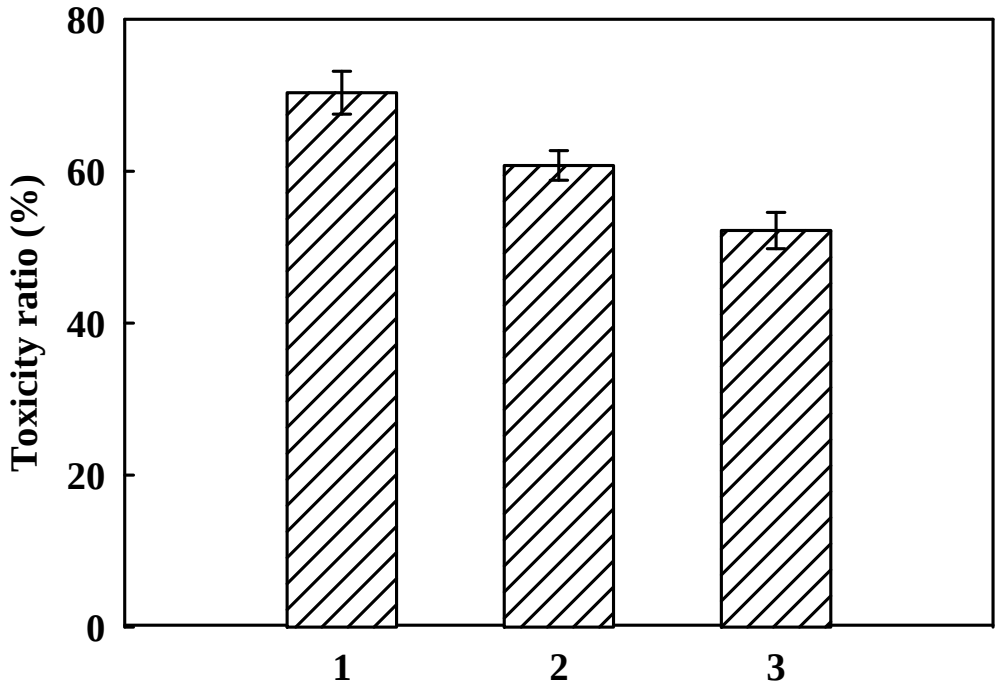

Figure 6-S4: Toxicity comparison of 1.8% Cu-TiO_2 NPs, $CuCl_2$ solution with TiO_2 NPs and $CuCl_2$ solution on the growth of *M. smegmatis;* 1: 1.8% Cu-TiO_2 NPs (20 mg/L) 2: TiO_2 (20 mg/L) + Cu (II) (360 µg/L) 3: Cu (II) (360 µg/L).

Chapter 7:

Role of Dopant Concentration, Crystal Phase, and Particle Size on Microbial Inactivation of Cu-Doped TiO_2 Nanomaterials

The results presented here were published in:

Sahu, M, B. Wu, L. Zhu, C. Jacobson, W. N. Wang, K. Jones,Y. Goyal, Y. J. Tang, and P. Biswas, *Role of Chemical Composition, Crystal Phase, and Particle Size on Microbial Inactivation of Cu-Doped TiO_2 Nanoparticles,* Nanotechnology, 2011 (In press).

7.1. Abstract

The properties of Cu-doped TiO_2 nanoparticles (NPs) were independently controlled in a flame aerosol reactor by varying the molar feed ratios of the precursors, and by optimizing temperature and time history in the flame. The effect of the physico-chemical properties (dopant concentration, crystal phase, and particle size) of Cu-doped TiO_2 nanomaterials on inactivation of *Mycobacterium smegmatis* (a model pathogenic bacterium) was investigated under three light conditions (complete dark, fluorescent light, and UV light). The survival rate of *M. smegmatis* (in a minimal salt medium for 2 hr) exposed to the NPs varied depending on the light irradiation conditions as well as the dopant concentrations.

In dark conditions, pristine TiO_2 showed insignificant microbial inactivation, but inactivation increased with increasing dopant concentration. Under fluorescent light illumination, no significant effect was observed for TiO_2. However, when TiO_2 was doped with copper, inactivation increased with dopant concentration, reaching more than 90% (>3 wt% dopant). Enhanced microbial inactivation by TiO_2 NPs was observed only under UV light. When TiO_2 NPs were doped with copper, their inactivation potential was promoted, and the UV-resistant cells were reduced by over 99%. In addition, the microbial inactivation potential of NPs was also crystal phase- and size-dependent under all three light conditions. A lower ratio of anatase phase and smaller sizes of Cu-doped TiO_2 NPs resulted in decreased bacterial survival. The increased inactivation potential of doped TiO_2 NPs is possibly due to both enhanced photo-catalytic reactions and leached copper ions.

Key words: *Mycobacterium smegmatis*; anatase phase ratios; particle size; UV light; chemical composition.

7.2. Introduction

Adverse health impacts stemming from waterborne particles and microbial agents remain an important public health concern. Numerous control methods are employed for water purification including disinfection through chlorination, ozonation, and UV-irradiation [1, 2]. Among these strategies, UV-irradiation is a widely used method that yields no byproducts; it is effective against most microorganisms [3], and is integrated into various applications such as heating, ventilation, and air conditioning systems (HVAC) [4] as well as sterilization and medical applications. Recent studies indicate that some species of *Mycobacteria* and viruses are resistant to UV-irradiation [1, 5]. As an alternative, recent advancements in nanoparticle technology have enabled the production of several antibacterial nanomaterials that have demonstrated powerful photo-catalytic inactivation of various microorganisms [5-8]. The advantages of this nanomaterial photo-catalysis approach include its high inactivation potential for most pathogenic microorganisms (due to formation of oxidizing reactive radicals), oxidation potential for organic wastes, and minimal formation of disinfection byproducts [5]. Additionally, there is no consumption of oxidizing agents, and as an added benefit, the nanomaterials can be recycled.

The photo-catalytic inactivation potential of nanomaterial primarily depends on the generation of reactive oxygen species (ROS) (OH, O_2^- , and H_2O_2) upon irradiation and direct contact with the microorganisms [6-9]. The reactivity of nanomaterials is a function of their physico-chemical properties, such as size, surface characteristics, crystal

phase, dopant types and concentrations, agglomeration behavior, and suspension stability [10-13]. Of the various nanomaterials, TiO_2 is one of the most promising and widely used due to its low cost, chemical stability in aqueous environments and strong oxidizing power against microorganisms. However, one disadvantage of using TiO_2 is that it absorbs light only in the UV region for photo-catalysis reactions. To shift the absorption range to the visible spectrum, numerous approaches have been pursued in effort to alter the structure of TiO_2, however, doping is considered to be very promising [14-16]. Although several doped TiO_2 materials have been developed and applied for microbial inactivation [6, 17], processing of stable doped nanomaterials with well-controlled properties that can effectively harvest visible light remains a challenge.

In recent investigations, Cu-doped TiO_2 has proven to be stable, has shown enhanced photo-catalytic degradation [18, 19], and has improved CO_2 photo-reduction [20, 21]. A few studies indicate that compared to TiO_2, Cu-doped TiO_2 enhances microbial inactivation potential when treated in aqueous media under dark [22], weak UV, and visible light irradiation [7, 9, 23]. Other studies indicate that incorporating copper dopant into the TiO_2 lattice structure alters the properties such as size and crystal phase, and shifts the absorption spectra to the visible spectrum by replacing Ti in the substitutional sites or in the interstitial sites. Cu-doping also alters the stability in suspensions [15, 24]. The altered physico-chemical properties due to dopant incorporation may result in different concentrations of active and defect sites that might affect overall performance. However, the role of the different physico-chemical properties of Cu-doped TiO_2 (such as composition, crystal phase, and particle size) on its inactivation potential under different light irradiation conditions has not been

demonstrated and is not well understood. To develop a better understanding and correlation of different material properties with inactivation potential, doped nanomaterial properties need to be independently controlled.

Recent advancements in understanding the effects of process parameters in the flame aerosol reactor (FLAR) allow for the production of nanomaterials with strictly controlled properties [15, 25], and FLAR is the preferred synthesis route to manufacture commercial quantities. Sahu and Biswas [15] studied in detail the synthesis of Cu-doped TiO_2 nanomaterial in a flame aerosol reactor. In this paper, the study is extended to control the nanomaterial properties independently for microbial inactivation evaluation. For example, to clearly correlate the inactivation potential with the crystal phase of the nanoparticles, the crystal phase of the particles was varied while maintaining the same size.

Mycobacteria are widespread in the environment and also colonize their hosts. For example, billions of people around the world are infected by *M. tuberculosis*. All mycobacterium species have thick and waxy cell walls, which make them naturally resistant to a number of antibiotics (e.g., penicillin) and harmful chemicals (acids, alkalis, detergents, etc.) [26]. Besides, *Mycobacteria* were found to have 2–10 times more resistance to UV than other bacteria, such as *E. coli* [1]. Some mycobacterial species have extremely long growth periods, making laboratory culturing a slow process. However, *M. smegmatis* is a fast-growing and non-pathogenic species which is often used as a model species for Tuberculosis studies [27]. In this study, *M. smegmatis* was an ideal species for analysis of the general properties of *Mycobacteria.*

The goals of this study are twofold. First, the synthesis of Cu-doped TiO_2 nanomaterials with controlled physico-chemical properties is demonstrated. By controlling the process parameters, nanomaterials with different dopant compositions maintaining a similar primary particle size and crystal phase were synthesized. Crystal phase and primary particle size were independently varied at a fixed dopant concentration. Second, the effect of copper-doped TiO_2 nanoparticles (with specified physico-chemical properties) on the survival rates of *M. smegmatis* was investigated. In addition, the potential interaction mechanisms of the doped nanoparticles (NPs) with the bacteria have been illustrated. The study of the interaction between Cu-doped TiO_2 NPs and bacteria under various irradiation conditions (dark, UV-light, fluorescent light) was conducted to demonstrate the potential application of NPs for controlling infectious disease (e.g., tuberculosis).

7.3. Materials and Methods

7.3.1. Nanomaterial synthesis and characterization

TiO_2 and Cu-doped TiO_2 NPs were synthesized in a diffusion flame aerosol reactor. The design details and description of the diffusion burner used for the synthesis of Cu-doped TiO_2 are discussed in detail in Jiang et al [25]. Oxygen and methane were used to set up the flame and the flow rates were varied based on the final material properties desired. Titanium tetra-isopropoxide (TTIP, 97%, Aldrich) was used as the TiO_2 precursor and copper nitrate was the precursor for the dopant. The TTIP feed rate was controlled by varying the carrier gas flow rate through the bubbler. Copper nitrate was dissolved in DI water and atomized by a stainless steel nebulizer before being introduced to the high

temperature flame in the form of fine droplets. Doping concentration was varied by changing the concentration of copper nitrate in the aqueous solution. All the particles were synthesized by the diffusion flame aerosol reactor, except for the pristine CuO (used for comparison with TiO_2 and doped TiO_2) which was commercially obtained from Sigma-Aldrich.

Particle size and morphology were characterized by scanning and transmission electron microscopy (SEM: JEOL 7001LVF, Japan; TEM: JEOL 2100F, Japan). SEM coupled with energy dispersive spectroscopy was used to analyze the dopant in the NPs. Crystal phase of the synthesized materials was verified using an X-ray diffractometer (XRD, Rigaku D-MAX/A9, Japan). The crystal phase composition was determined according to the method described by Spurr and Meyer [28].

7.3.2. M. smegmatis cultivation and its survival under NP stress

M. smegmatis was grown in a Sautons' liquid medium at 37°C at a shaking speed of 150 rpm [29]. NPs (with different properties) were suspended in sterilized distilled water to make the stock solutions (1 g/L). Before use, the NP suspension was sonicated for 1 min (to break up any large agglomerates). When the growth of *M. smegmatis* approached the stationary phase (OD_{600} ~1.0), cells were diluted with 5 ml Sautons' salt medium (no carbon sources) to a concentration of 10^6 ~10^7 CFU/ml before mixing with sonicated NP stock solution or Cu^{2+} ions. The bacterial culture was exposed to dark, fluorescent light (intensity-505 $\mu w/cm^2$), UV light (intensity-3.07 $\mu w/cm^2$) with NPs (20 mg/L) or Cu^{2+} ions for 2 hr. Then 100 μL of sample was extracted, diluted, and spread onto the agar plates (Sautons' liquid medium with 1.5% agar). The total number of viable cells was estimated based on colony-forming units (CFU) after 1~2 days' incubation at 37°C. The

reported averaged CFU and standard deviations are based on multiple tests (n=4). To determine the dissolution of Cu^{2+} from the NPs under different conditions, Cu-doped TiO_2 NPs with cells were removed from the cultures by high speed centrifugation (19,000 ×g) for 20 min, after which the supernatant was collected and filtered (0.22 μm, Nylon, Millipore, USA) and then analyzed by inductively coupled plasma mass spectrometry (ICP-MS, Agilent, USA) [22].

7.3.3. Experimental plan

Table 7-1 summarizes the experiments conducted in this study. In the first set of experiments, the molar feed ratios of the precursor were varied (0.25 to 7 wt%) to synthesize nanomaterials with different dopant concentrations (Test-1(B-F)). Nitrogen gas at 2 lpm (liters per minute) was bubbled through TTIP in a bubbler maintained at 98 °C. Oxygen and methane at 8 and 1.8 lpm respectively were introduced into the FLAR system. TiO_2 was synthesized under the same conditions to compare with the doped TiO_2 nanoparticles (Test 1 (A)). The dopant concentration was kept below 10 wt% so that the dopant would not have a significant effect on the material properties.

The second set of experiments was aimed at varying the crystal phase composition while maintaining similar primary particle size, as crystal phase of the nanomaterials affects the microbial inactivation potential and agglomeration behavior in the suspension [10, 30]. The methane flow rates were varied from 0.8 to 1.8 lpm to control the crystal phase of the material while maintaining the particle size to be the same (Test 2(A-F)). The dopant concentration was kept constant at 3 wt%, and primary particle size was approximately ~35 nm.

Table 7-1: Summary of investigated Cu-doped TiO_2 NPs

Test #	Dopant Concentration (wt %)	Crystal Phase	Particle size (nm)	Light Condition	Objective
1 A B C D E F G H	0 0.25 0.5 1 3 5 7 100 (commercial)	~100 % anatase	~35	Dark, Fluorescent light, UV-light	Study the influence of nanoparticle composition on inactivation potential
2 A B C D	3	39% anatase 50% anatase 79% anatase 95% anatase	~35	Dark, Fluorescent light, UV-light	Crystal phase effect on inactivation potential
3 A B C D	3	~100 % anatase	<20 33 59 69	Dark, Fluorescent light, UV-light	Examine the effect of particle size on inactivation potential
4 A B C	TiO_2 Cu^{2+} (145 µg/L) 3 wt% Cu-TiO_2	100% anatase	~35	UV-light	Examine the effect of copper ions and nanoparticles with time on inactivation potential

In the third set of experiments, to study the effect of particle size on microbial inactivation potential, particle size was varied while maintaining similar crystal phase. The TTIP precursor feed rate was varied from 1 to 5.5 lpm, and the residence time was controlled at 3 wt% dopant concentration (Test 3).

Microbial inactivation was investigated under dark, fluorescent (intensity-505 $\mu W/cm^2$) and UV-light (intensity-3.07 $\mu W/cm^2$) conditions at a dose of 20 mg/L of NPs for 2 hours (Test (1-3)). The light emission spectra of the UV- and fluorescent light used for this study are shown in Figure 7-1. The UV-light was mainly in the UV-C region,

with the emission peak at 253 m, and the fluorescent light had an emission spectrum ranging from 400 to 800 nm, with the highest peak at 611 nm.

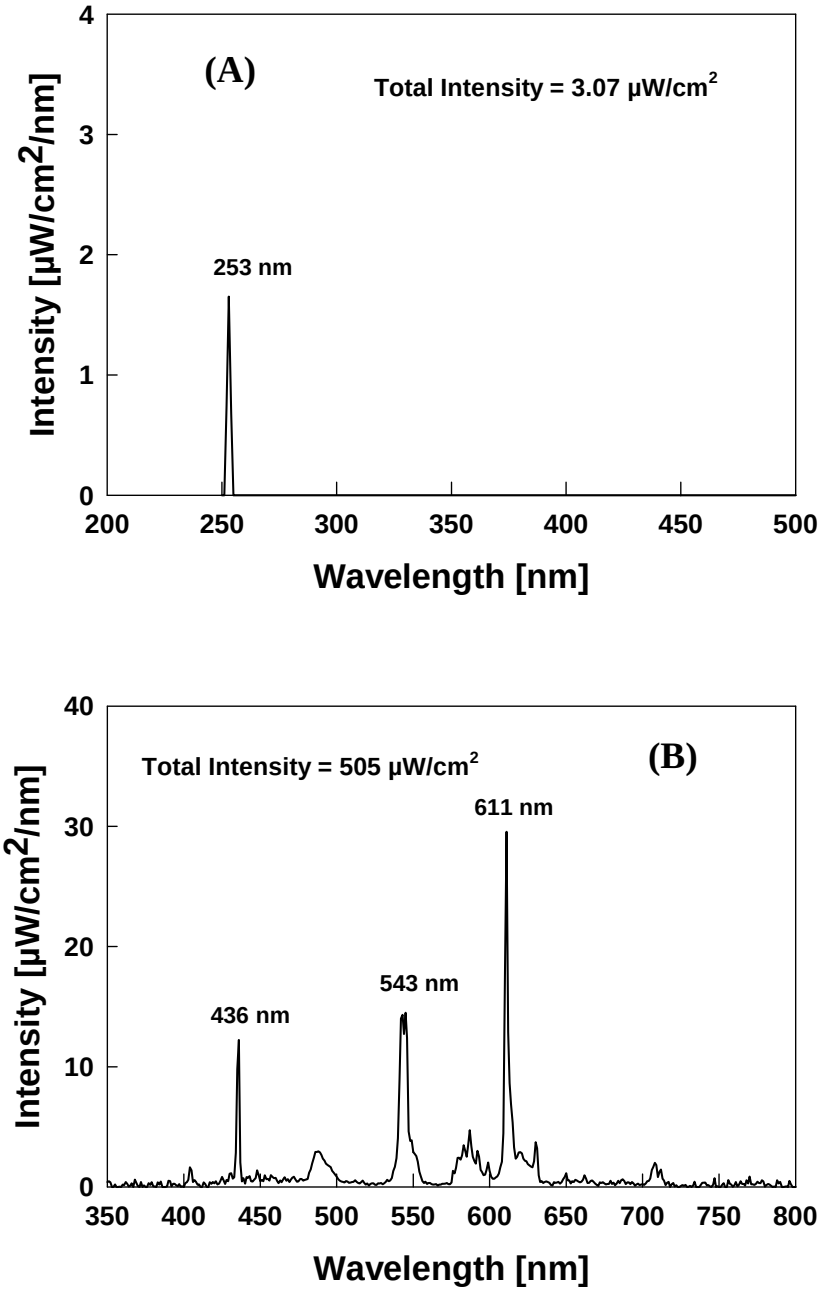

Figure 7- 1: Light emission spectra of the (A) UV light, and (B) Florescent light used for this study

Finally, to understand the potential inactivation mechanisms, the microbial inactivation was compared among TiO_2, Cu^{2+} ions, and 3 wt% Cu-doped TiO_2 materials under UV light as a function of time (Test-4).

7.4. Results and Discussion

Nanoparticles' physico-chemical properties influence their inactivation potential for microbes. To establish the dependence of NP properties on inactivation potential, there is a need to synthesize materials with strict control of characteristics. The synthesis of doped nanomaterials is discussed first, followed by details of their microbial inactivation potential against *M. smegmatis.*

7.4.1. Cu-doped TiO_2 nanomaterial with controlled dopant concentration, crystal phase, and size

7.4.1.1. Dopant Concentration

Nanomaterial reactivity depends on dopant types and concentrations. Limbach et al (2007) illustrated that dopant concentration is the most important factor that determines ROS generation by NPs. They found optimum generation of reactive radicals for intermediate iron dopant concentrations in SiO_2. Based on the composition of the nanomaterials, the active sites may vary and generate different amounts of reactive species. In this study, the effect of dopant concentration of Cu-doped TiO_2 nanomaterial on microbial inactivation potential was investigated by varying the concentration from 0.25 to 7 wt% (Test-1). The dopant concentration was varied while ensuring no major

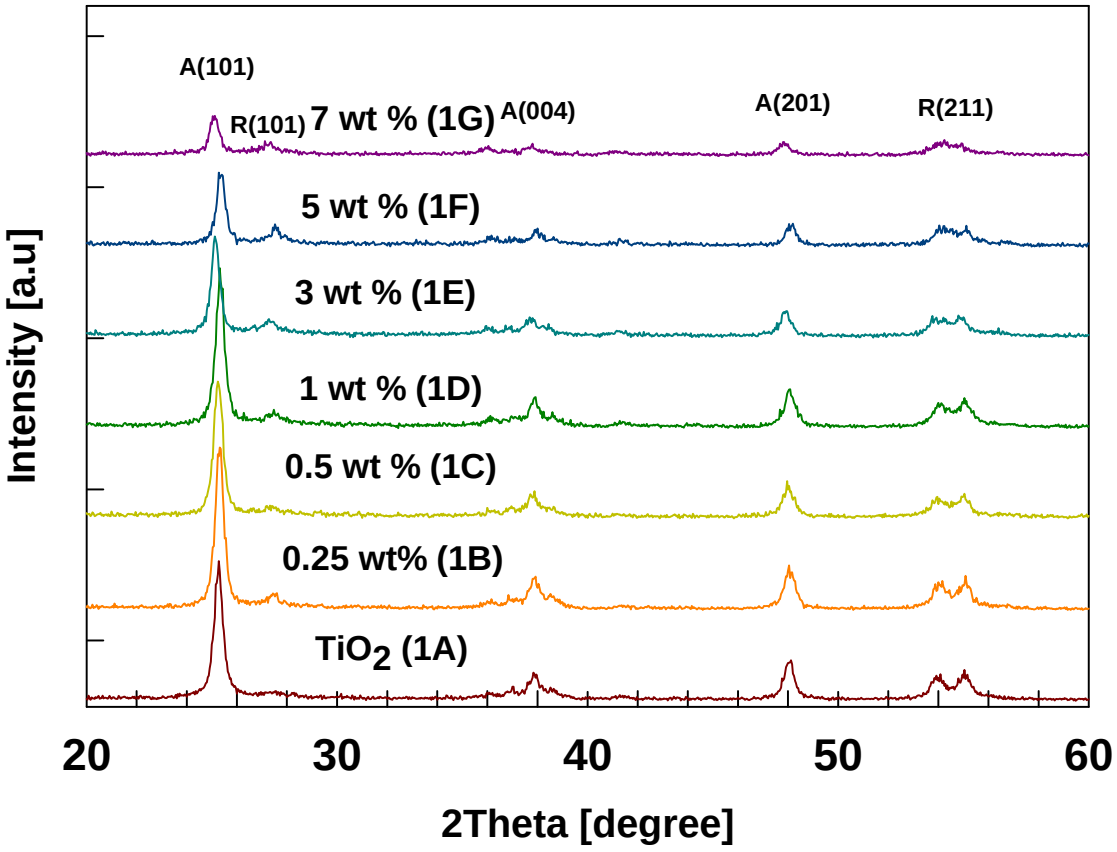

Figure 7- 2: XRD spectra of as prepared pristine TiO_2 and Cu-doped TiO_2 NPs with different dopant concentrations (A-anatase, R-rutile, particle size ~35nm) (Numbers in the parenthesis refer to Test # in Table 1)

change in particle size and crystal phase. The XRD diffraction patterns of the Cu-doped TiO_2 nanoparticles prepared at different dopant concentrations are shown in Figure 7-2. All the particles prepared were mostly of anatase phase, as seen from the figure. However, the results indicate that with increasing dopant concentration, anatase to rutile phase transition occurred. The phase transition from anatase to rutile is attributed to oxygen vacancies created due to the replacement of Ti atoms by Cu^{2+} ions in the crystal structure [15, 31]. The results are consistent with our previous study [15], where a detailed explanation was provided. Other studies have reported that dopant addition to host material may change the crystal phase, which is also consistent with this study [16]. Representative TEM micrographs of TiO_2 and Cu-doped TiO_2 nanomaterials are shown

in Figure 7-3. The mean primary particle size measured by counting 200 nanoparticles from the TEM micrographs is approximately ~35 nm for all the cases. TEM micrographs indicate that particles are loosely agglomerated and spherical. To ensure that the crystal phase of TiO_2 was primarily anatase, the copper dopant concentration was kept less than 10 wt%. The results indicate that the particle composition can be varied (maintaining similar size and crystal phase) by better understanding of the synthesis process and dopant effects on material properties.

7.4.1.2. Crystal phase

The crystal phase of NPs plays an important role in photo-catalytic applications as well as in microbial inactivation [10, 13, 30]. For instance, the anatase phase of TiO_2 is mostly preferred for photo-catalytic applications [13]. Jiang et al [10] demonstrated that ROS generation is crystal phase composition dependent; amorphous is more active than anatase, followed by an anatase and rutile mixture. The different crystal phase compositions lead to different arrangements of atoms in the structure and may generate different ROS that will affect the microbial inactivation potential. In the second set of experiments (Test-2), the crystal phase of the doped NPs was controlled by varying the temperature and time history in the flame. The methane flow rates were changed, while the dopant concentration was maintained at 3 wt%. By changing the methane flow rates from 0.8 to 1.8 lpm, anatase crystal phase compositions were varied from 39 to 95%, whereas particles remained spherical and similar in size. The control of crystal phase composition is attributed to the temperature and residence time balance at different

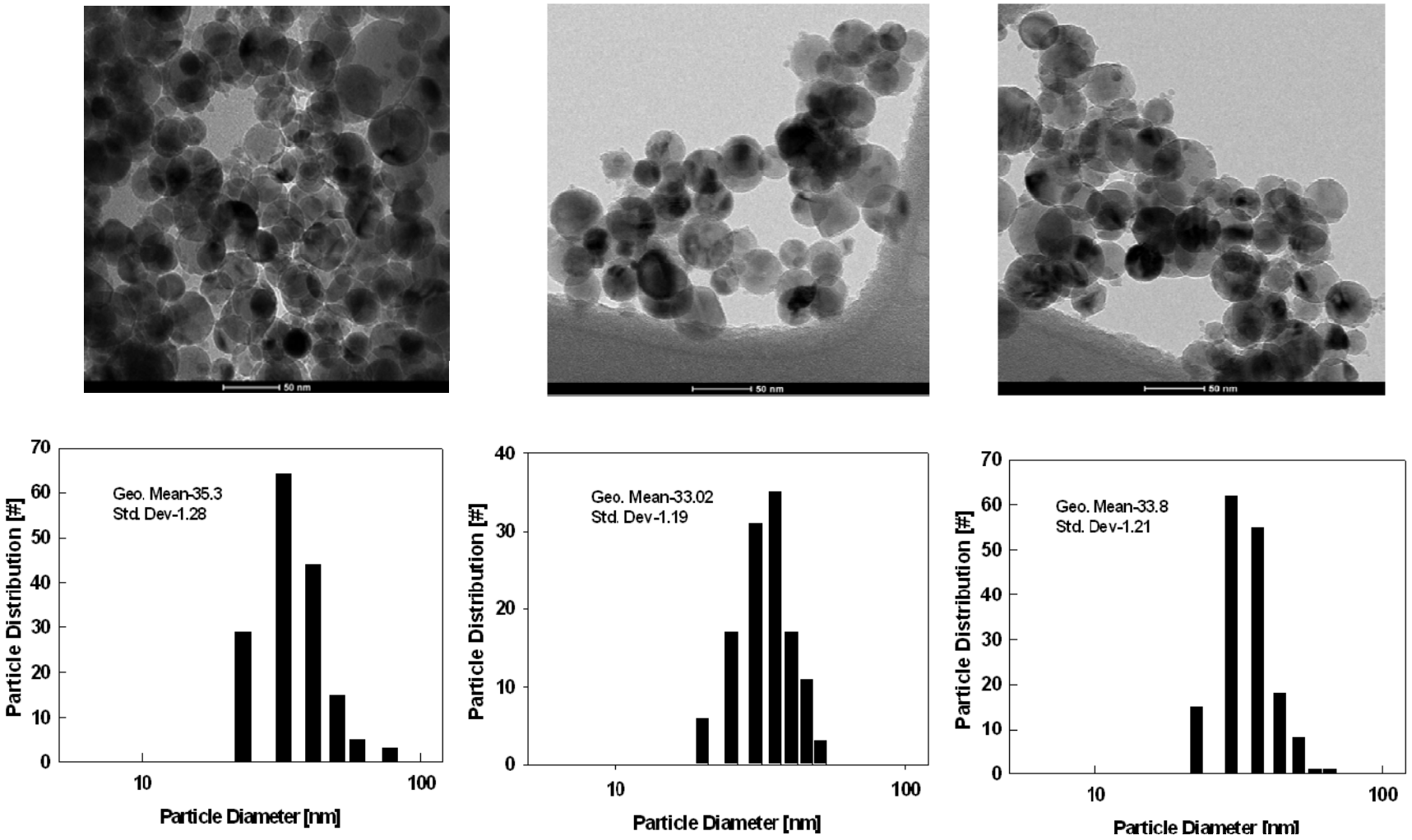

Figure 7- 3: TEM micrographs and particle size distribution of representative pristine TiO_2 and Cu-dopedTiO_2 NPs with different dopant composition (Test-1) (A) Pure TiO_2 (1A) (B) 1 wt% Cu-TiO_2 (1D) (C) 3 wt% Cu-TiO_2 (1E)

methane flow rates [15, 25]. The same observation was made by Jiang et al [25], who synthesized TiO_2 NPs under different methane flow rates in a diffusion flame reactor.

7.4.1.3. Particle size

Various studies have reported that particle size is an important parameter that affects the catalytic activity of the materials; however no study has reported microbial inactivation potential of Cu-doped TiO_2 nanomaterials. The size and mobility of the nanoparticles will influence the microbial inactivation. Earlier studies have demonstrated that partially soluble materials may be taken up into the cell by a Trojan-horse type mechanism (i.e. the nanoparticle is transported into the cell and then releases ions) and may enhance the damaging action [12]. To study the particle size effect, particles of different sizes were prepared at 3 wt% dopant concentration. Particle size was controlled by varying the precursor feed rate as well as the residence time in the flame. However, synthesizing different particle sizes with the same crystal phase is challenging. The feed rate of TTIP was varied from 0.5 to 5.5 lpm (Test-3). A corresponding amount of copper nitrate was dissolved in the solution to maintain the 3 wt% copper dopant concentration. The particle size was varied from < 20 to 69 nm. The XRD spectra of different size particles are shown in Figure 7-4. TEM micrographs (Figure 7-5) show that all particles were of the same anatase crystal phase but with differing particle size. With increasing feed rates and residence time in the high temperature flame, more number of particles was generated, and enhanced collisonal growth resulted in larger sized particles. Studies show that the crystal phase of a material can be dictated by controlling both temperature

and the cooling rate. The anatase phase was stabilized by a high quenching rate. The results indicate that these control measures can be extended to other doped nanomaterials.

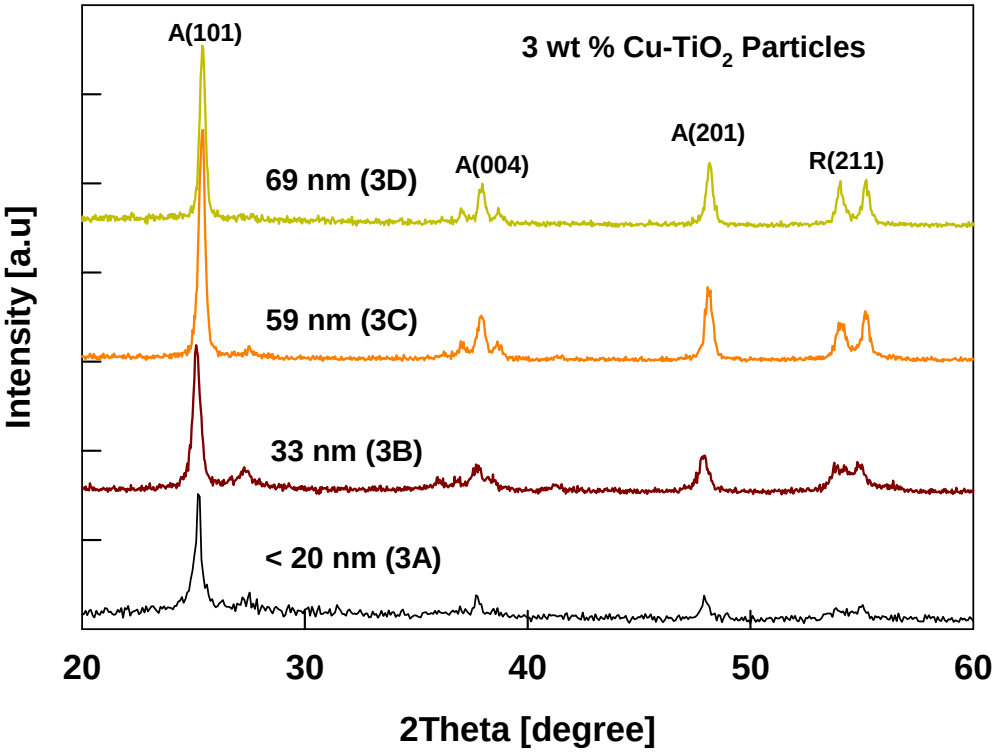

Figure 7- 4: spectra of as prepared pristine TiO_2 and Cu-doped TiO_2 NPs with different dopant composition (A-Anatase, R-Rutile, Particle size ~35nm) (Test-1)

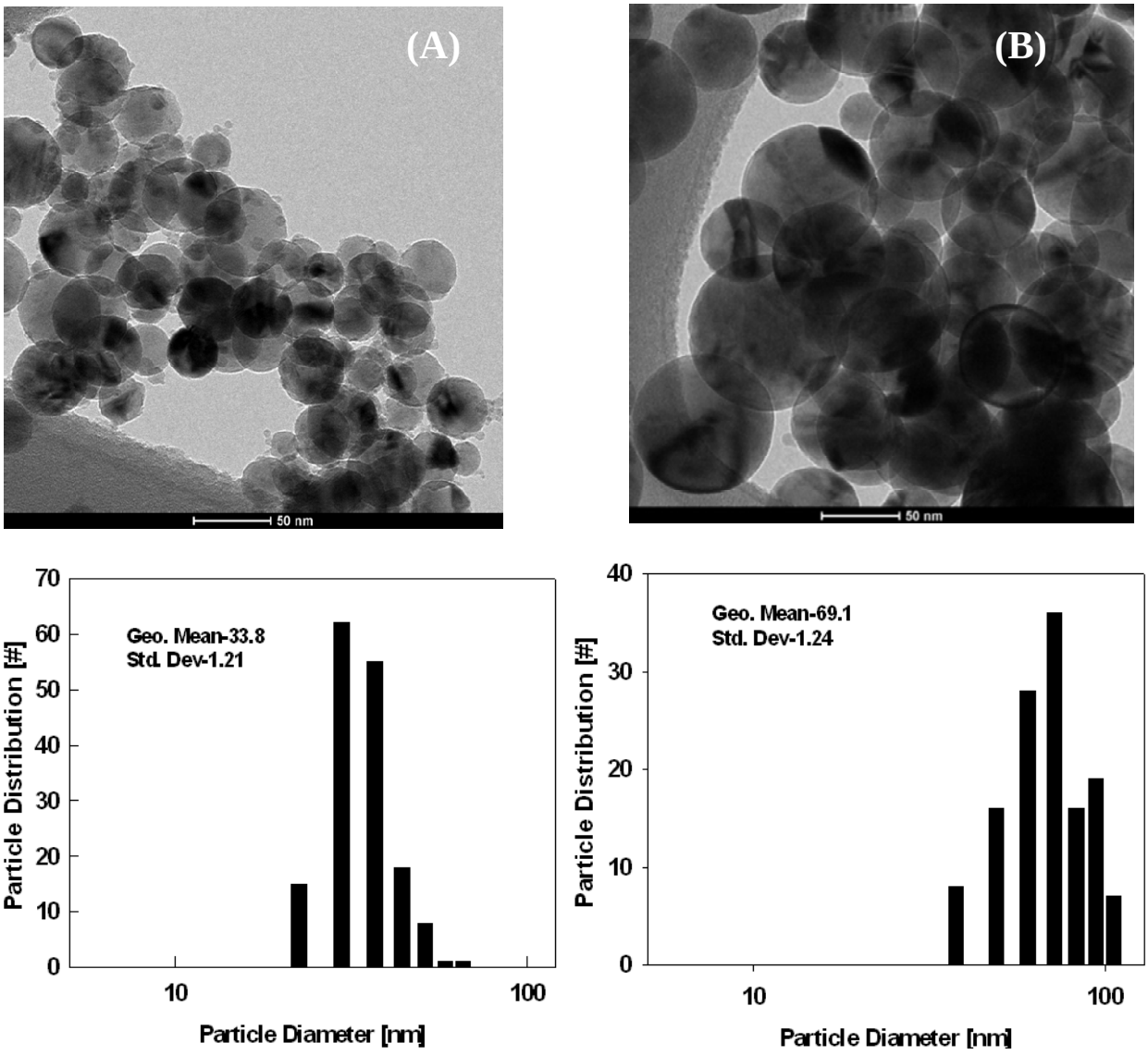

Figure 7- 5: TEM micrographs and particle size distribution of representative 3 wt% Cu-doped TiO_2 NPs with different size (Test-3) (A) 33 nm (3A) (B) 69 nm (3D)

7.4.2. Viability of *M. smegamatis* in the presence of Cu-doped TiO_2 NPs under different light conditions

7.4.2.1. Effect of dopant concentration on M. smegamatis inactivation

The response of *M. smegamatis* to Cu-doped TiO_2 NPs under different light conditions is shown in Figure 7-6 (Test-1). Under dark conditions (2 hr of exposure time), pristine TiO_2 NPs had very little effect on the cell viability compared to the control samples without any NPs (*P*-values > 0.05, Students *t*-test). However, the survival of *M. smegamatis* decreased with increasing dopant concentration, indicating that Cu-doped TiO_2 NPs have microbial inactivation potential under dark conditions. The CFU based survival decreased by 90% for 7 wt% Cu-doped NPs, and the highest microbial inactivation potential was observed for pure CuO NPs (>95%). The higher microbial inactivation potential of CuO was most likely due to release of copper ions and/or the high surface reactivity when NPs physically interacted with the cells [32]. Karlsson et al [33] have shown that release of Cu ions in the cell medium may not be the only mechanism for introducing toxic effects. The toxic effects were attributed to both NP physical interaction with cells and the release of copper ions from NPs. Limbach et al [12] proposed that nanoparticles may enter the cytoplasm of the cell by a Trojan-horse mechanism and that the inactivation capability of NPs was enhanced due to an increased uptake of ions into the cell structure, disturbing its function [12]. However, Cu-doped TiO_2 NPs tend to agglomerate in the aqueous solution, and their effective sizes were not much smaller than the bacteria itself [22]. Also, mycobacteria have a very thick and waxy cell wall. Therefore, the Trojan horse mechanism discussed earlier may not play an important role here [12]. Instead, the leached Cu^{2+} ion, which electro-statically interacts

with the negatively charged cell membrane, forms a concentrated ionic zone of copper enhancing the microbial effects as illustrated in Figure 7-8.

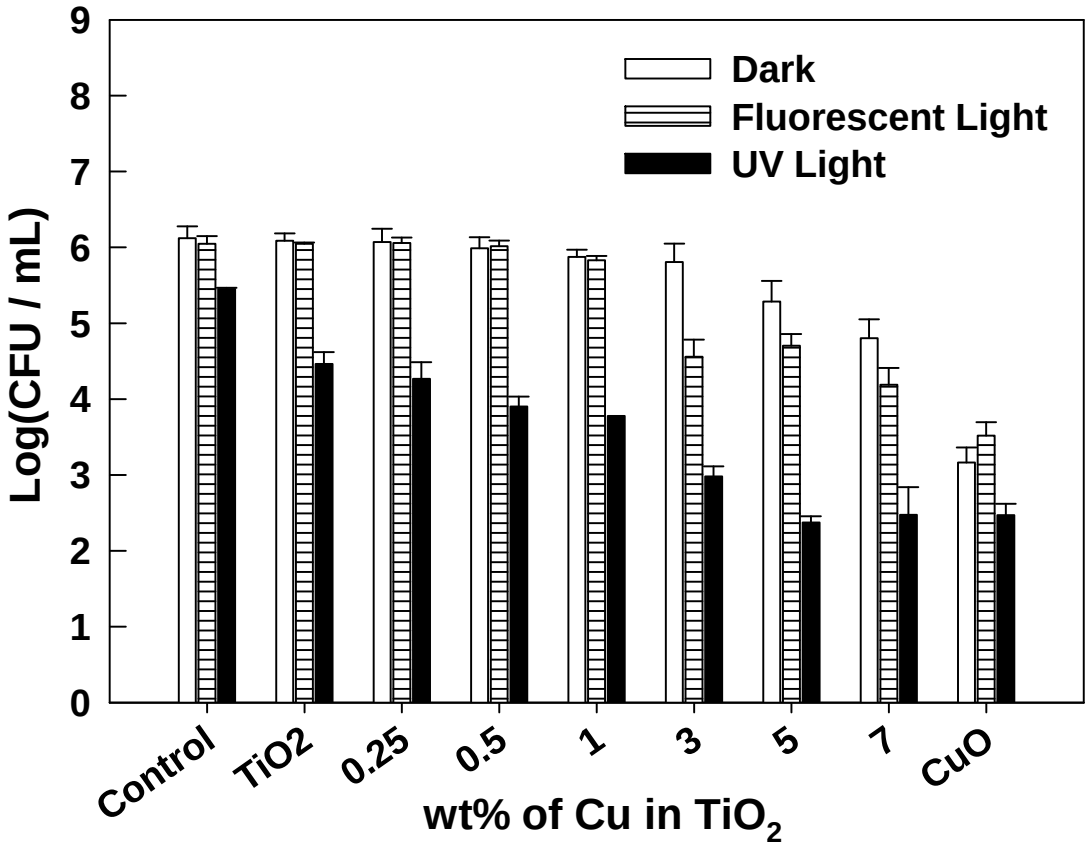

Figure 7- 6: Response of M. smegamatis to Cu-doped TiO_2 NPs with different dopant composition under different light conditions (Dose: 20 mg/L, Particle size: ~35 nm, Crystal Phase-~100 % Anatase, UV-light Intensity-3.07 µW/cm2, Fluorescent Light Intensity-505µW/cm^2)

Under fluorescent light, TiO_2 had no statistically significant effect on the survival rate when the dopant concentration was below 3wt%. However, above 3 wt% dopant concentration the NPs microbial inactivation potential was enhanced above 90% (*P*-values < 0.05) (Figure 7-6) and was higher than for the dark condition at the same dopant

concentration. The enhanced microbial inactivation potential above 3 wt% dopant indicates increased visible light photo-catalysisc reaction due to more absorption of fluorescent light. Sahu and Biswas [15] demonstrated that the absorption is increased in the visible spectrum when copper dopant is incorporated into the TiO_2 structure. The absorption spectra of the Cu-doped TiO_2 nanomaterials indicate that the absorption in the visible wavelength range (400-800 nm) increased with increased dopant concentration leading to increased microbial inactivation potential. In addition, the leached copper ions may enhance OH radical generation, which contributes to higher inactivation potential as discussed below.

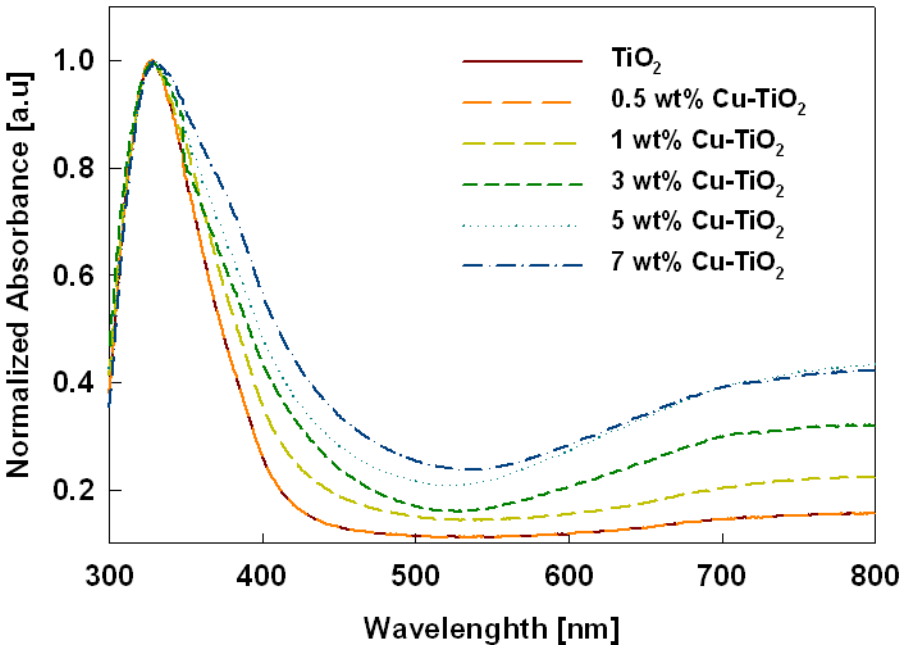

Figure 7- 7: UV-vis absorption spectrum of the Cu-doped TiO_2 nanomaterial used for the study

Under UV-light illumination, *M. smegamatis* could tolerate UV stress (only about 1.5-magnitude decrease in viable cells) due to its unique thick cell wall structure [26]. The cell wall plays an important role in photo-catalytic cell inactivation efficiency, since the cell wall is the first barrier of the inactivation process. Egerton et al [34] demonstrated that increased UV resistance of gram positive bacteria is attributed to a stronger cell envelope compared to gram negative bacteria. In a similar study, Cho et al [35] demonstrated that differences in cell size and surface structure may lead to different inactivation behaviors. Interestingly, copper doping in the TiO_2 NPs reduced the viability of *M. smegamatis* under UV by over 99%. In addition, it was observed that the survival rate of *M. Smegmatis* also depended on the Cu-doping amount: ~5 wt% Cu-doped NPs produced the highest inactivation under UV light. Sato and Taya [9] observed similar enhanced microbial inactivation for *E-coli* in the presence of Cu-TiO_2, compared to TiO_2 nanostructured films. Under light irradiation, photo-catalysis reactions generate ROS (H_2O_2, OH, O_2^-), which in turn react with the cell surface and disturb the structural integrity of the cell, leading to enhanced inactivation compared to dark conditions [7, 9, 13]. However, the increased photo-catalytic microbial inactivation of doped NPs, compared to pristine TiO_2 may be attributed to three factors. First, the dopant enhances the photo-catalytic reaction process by reducing the electron-hole pair recombination rate: the interfacial charge transfer caused by the copper dopant attracts the conduction band electrons and thus generates more reactive radicals [20, 36]. Erkan et al [37] and Egerton et al [34] found similar improved bacterial inactivation, when they tested the effect of UV irradiated Pd-TiO_2 and Fe-TiO_2 nanomaterials on *E-coli*. Second, Cu^{2+} ions that leached out of the doped materials had deleterious effects on bacterial functions, as

indicated in the experiments under dark conditions (Figure 7-8 indicates that the copper on the particle surface was released into the aqueous solution very quickly, in one minute). Third, Cu^{2+} may undergo a reduction reaction with the electron generated from the photoreaction thereby forming Cu^{1+} ion, which subsequently react with H_2O_2 to generate more harmful OH radicals, as shown in Figure 7-8 [7, 9]. Cho et al [35] demonstrated a linear correlation between photo-irradiation generated OH radicals and

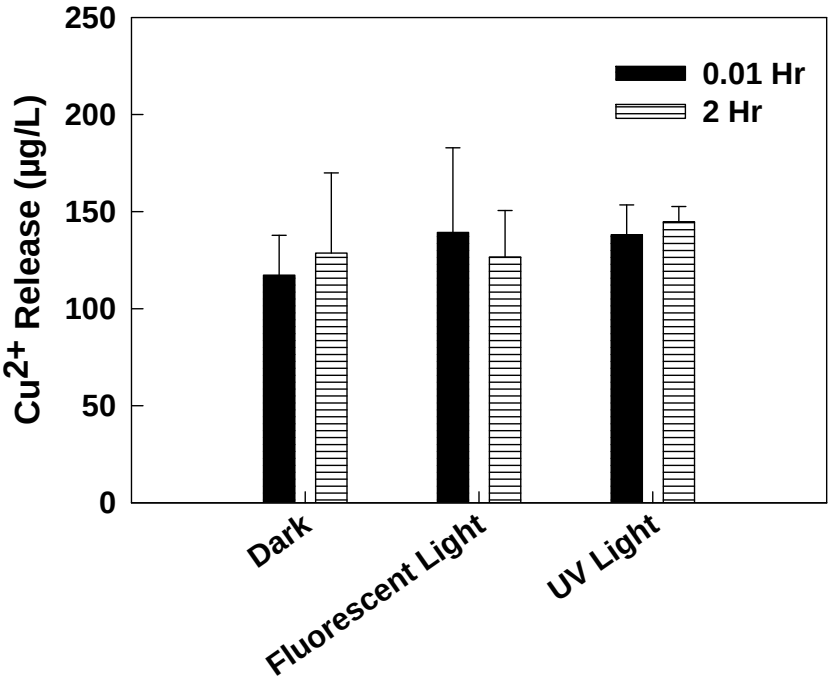

Figure 7- 8: Amount of copper leached from the 3 wt% Cu-doped TiO_2 NP after introduced in the solution under different conditions (Dose-20 mg/L)

E. coli microbial inactivation. Therefore, increased OH radical formation enhances oxidative stress on *M. smegamatis.* Sjogren et al [38] demonstrated that adding Fe^{3+} ions to the photo-catalytic process of TiO_2 enhanced microbial inactivation of MS2 virus due

to the generation of OH radicals from the Fenton reaction. Similarly, the presence of a copper component in NPs eventually increased OH radical generation in aqueous solution and led to enhanced microbial inactivation. The change in surface defects characteristics and dynamic change in property that may arise due to disoulution of dopant has not been considered in this study and beyond the scope of this work.

To test of our hypothesis and gain a detailed mechanistic understanding of the role of Cu^{2+} ions and nanoparticles, *M. smegamatis* was treated with 3 wt% Cu-doped TiO_2 NPs, TiO_2 NPs, or Cu^{2+} ions for different exposure times under UV-light (Test-4). Figure 7-9 shows the microbial inactivation potential normalized with the leached copper ions. Under UV light, Cu-doped TiO_2 NPs killed more viable cells than TiO_2 NPs / Cu^{2+}

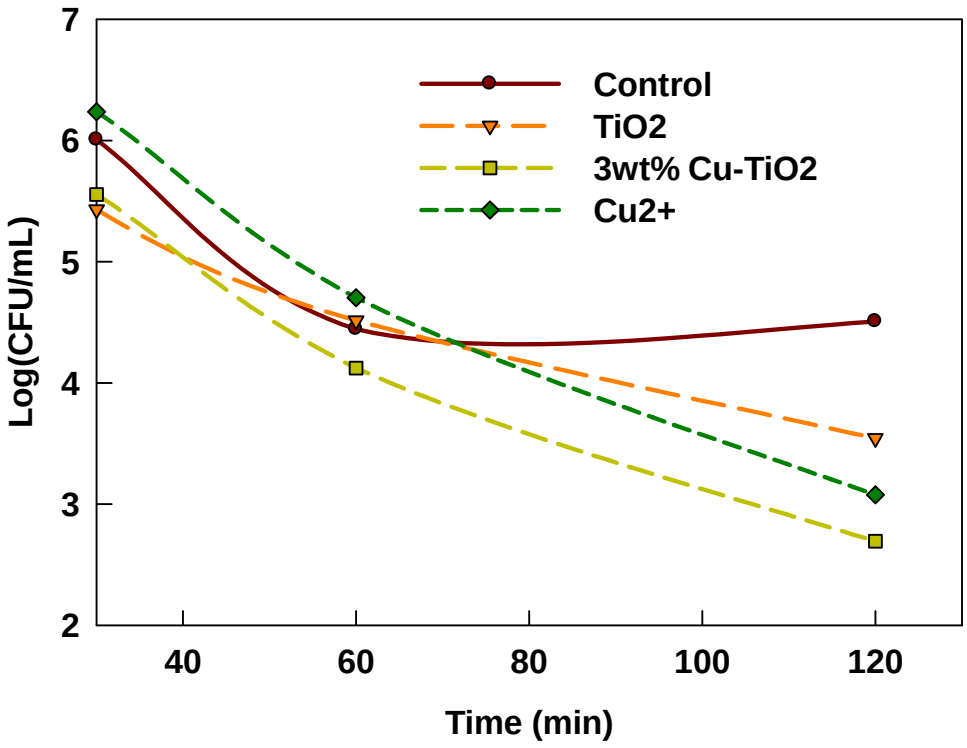

Figure 7- 9: Response of *M. smegamatis* with time under UV-light irradiation for TiO_2, 3wt% Cu-TiO_2 and Cu^{2+} ions (145 µg/L) (Test-4)

ions. Sato and Taya [9] demonstrated that the co-existence of Cu^{2+} ions and H_2O_2 enhances the inactivation potential for *E. coli* by producing more reactive OH radicals. Similarly, the increased microbial inactivation of Cu-doped TiO_2 also suggested the combined effect of Cu^{2+} ions, NPs surface reactions, and UV light, as shown in Figure 7-10.

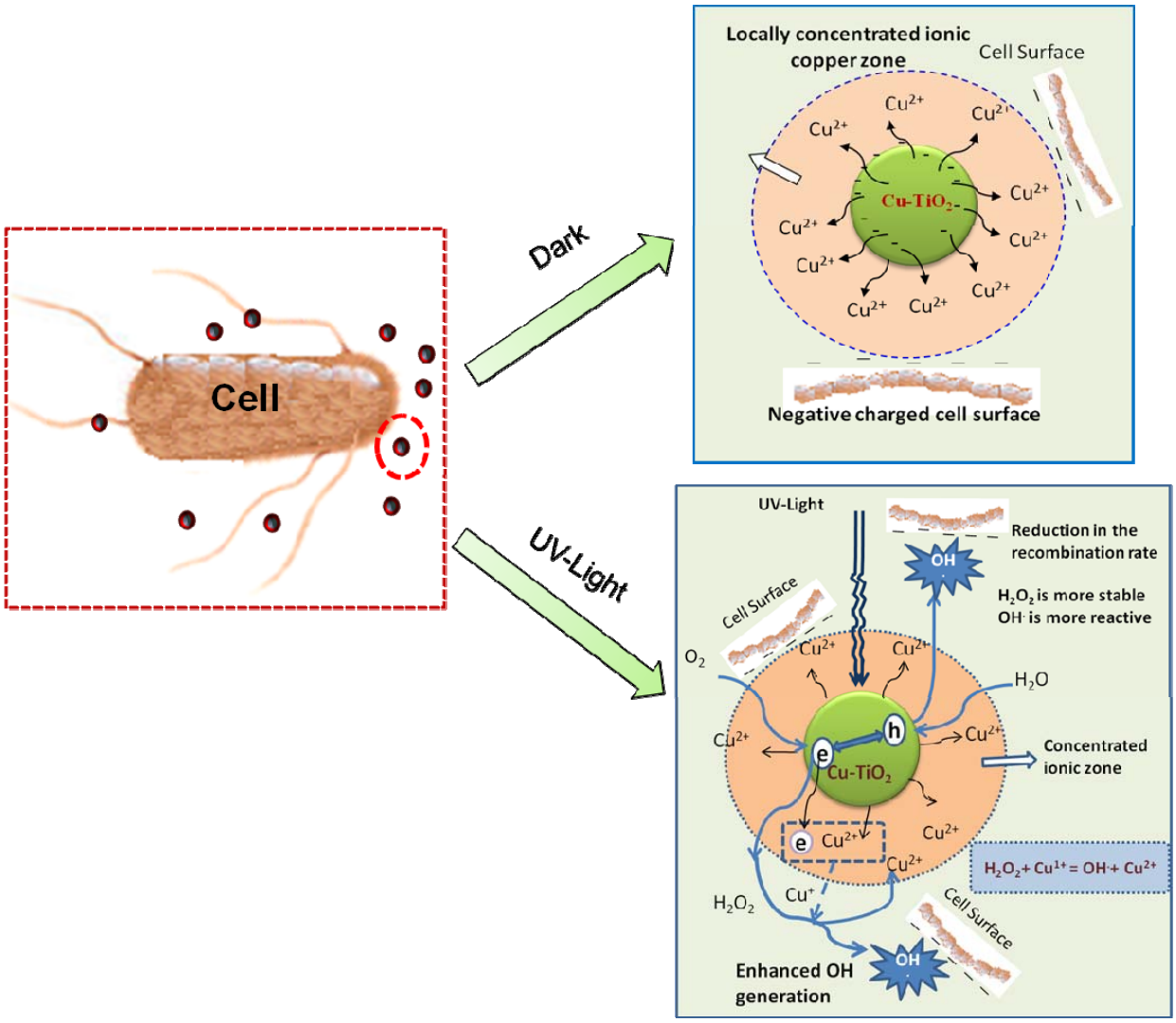

Figure 7- 10: A schematic illustration of M. smegamatis interaction mechanism with Cu-doped TiO_2 NPs under dark and UV-light conditions

This current study indicates that inactivation under light conditions is attributed to the combined effect of three factors: (1) interaction of the cell with ionic copper, (2) enhanced formation of OH radicals, and (3) improved photo-catalytic reactions due to reduced electron-hole pair recombination. The results suggest that the Cu-doped TiO_2 system is much more effective for inactivation, and the photo-catalysis reaction pathway can be adopted for inactivation for various bacteria. These results clearly indicate that bioavailable copper and exposed nanoparticle concentration have to be considered for ecological risk assessments, which may be different for reallife exposure scenarios.

7.4.2.2. Crystal phase and particle size effects on M. smegamatis inactivation

The reactive oxygen species generation potential of nanomaterials depends on size, crystal phase, and agglomeration behavior in the suspension [10, 30]. Discontinuous crystal planes or defects in the crystal structures of nanomaterials can influence reactive oxygen species generation and hence nanoparticle activity [39]. A high number of surface defects can result in more activity. Higher activity has been observed for anatase phase TiO_2 compared to the rutile phase in many studies [10]. Almquist and Biswas [13] found that 25-40 nm anatase TiO_2 is more active than the rutile material. Gurr et al [40] demonstrated that photo-catalytic oxidative damage for TiO_2 is greater for an anatase-rutile mixture than for a pure anatase or rutile phase. In addition, the dispersion behavior of the nanoparticles in the solution can significantly influence the photo-catalytic efficiency [24, 40]. The effects of crystal phase composition and size of Cu-doped TiO_2 NPs on the viability of *M. smegamatis* are illustrated in Figure 7-11. When the anatase

phase ratio of Cu-doped TiO_2 NPs was decreased from 95 to 70% (i.e., reduced agglomeration of particles), the survival of *M. smegamatis* dropped considerably

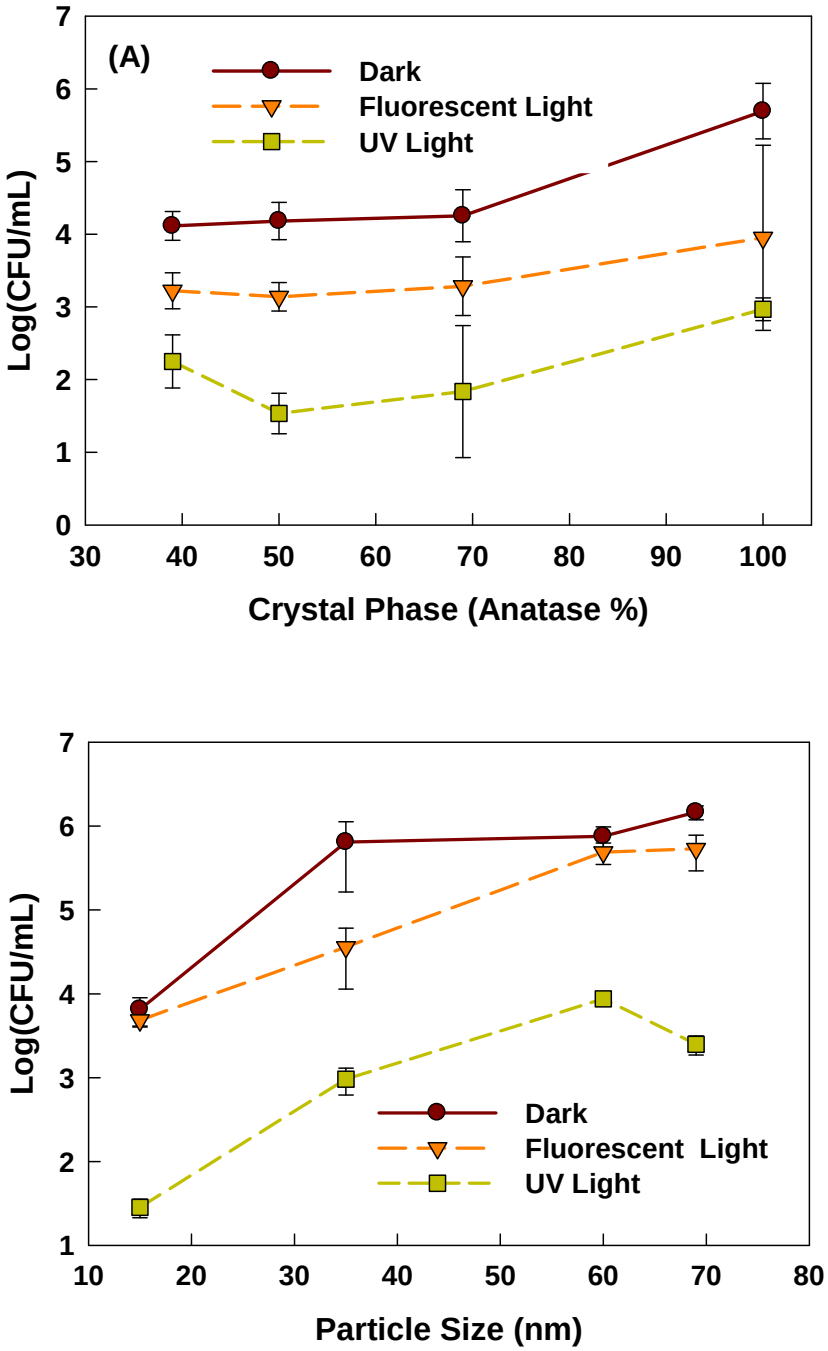

Figure 7- 11: Response of M. smegamatis to 3wt % Cu-doped TiO_2 NPs under different light conditions with different (A) Anatase crystal phase composition (Particle size ~35nm) (Test-2) (B) Particle size (Crystal phase-100% anatase)

under all three light conditions. Further decreasing the anatase phase ratio reduced the inactivation potential even more, because the agglomeration of the nanoparticles in the suspension reduced the available surface area Particle agglomeration depends on the iso-electric point (IEP) of the nanomaterial [24, 30, 41]. Recently, Sahu et al [24] reported that the IEP of 3 wt% Cu-doped TiO_2 is around a pH of 6.6. They also demonstrated that the IEP of Cu-doped TiO_2 is greater than TiO_2 alone, due to replacement of Ti^{4+} ions by Cu^{2+} ions in the crystal lattice. Particles having more rutile phase structures have a lower IEP [30]. For all crystal phase compositions in this study, the pH of NP solutions was 6.5 under all light conditions. As the anatase phase composition increased to 95% (pH 6.5 close to the IEP), agglomeration was promoted. Enhanced agglomeration resulted in less surface contact between the particles with the bacterial cells, and thus reduced inactivation potential. Furthermore, photo-induced reactions take place at the surface of the nanoparticles. A reduction in particle size provides a larger surface area enhancing the photo-catalytic reactions. The effect of particle size on survival of *M. smegmatis* is illustrated in Figure 7-11. Microbial inactivation potential of *M. smegamatis* by NPs became less effective when the particle size was increased from <20 to 69 nm. A similar phenomenon was observed in other studies [10]. The smaller size particles have more surface defect sites [10], which can induce more inactivation compared to larger size particles. As the particle size decreases, the number of surface atoms/molecules increases, changing the particle's electronic structure, surface defect density, and surface sorption sites and enhancing the particle reactivity [42]. Studies have demonstrated that surface area of the nanoparticles may be a better dose metric for evaluating toxic effects.

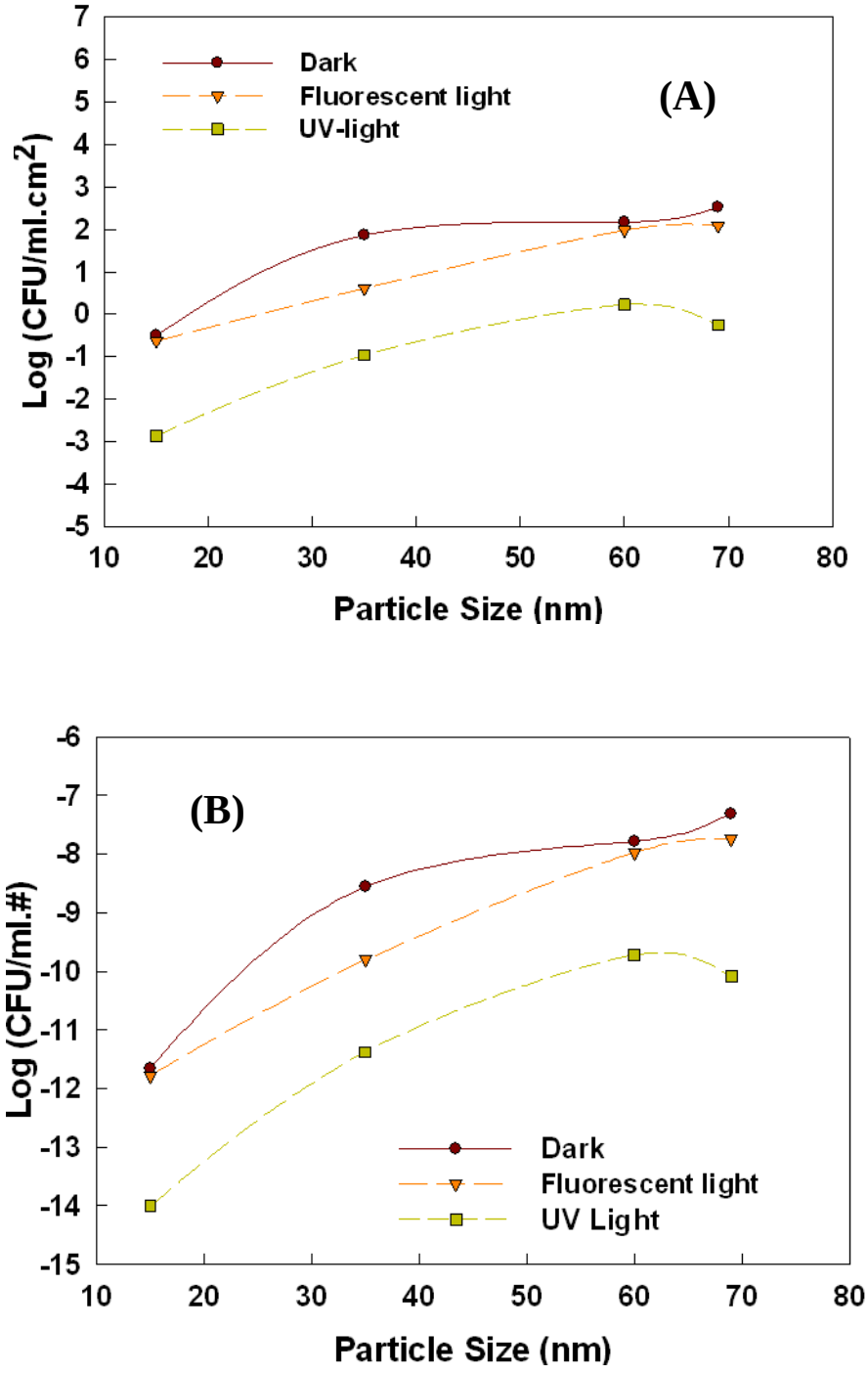

Figure 7- 12: Response of M. smegamatis to 3 wt % Cu-doped TiO_2 NPs under different light conditions normalized with different dose metrics (A) particle surface area concentration (B) Particle number concentration

The size effect based on surface area concentration and number concentrations are shown in Figure 7-12. The same increasing bacterial survival was observed when expressed in surface area and number concentrationdose parameters. Previous studies indicate that ROS generation is correlated with particle surface area in dark conditions for TiO_2 nanoparticles [10]. In this study ROS generation was not measured. The genartion of ROS may be different due to different light irradiation conditions. In addition, the mechanisms of potential toxic effects are very different from pristine TiO_2 as discussed before. More detailed investigation on ROS measurement under different light conditions may provide better correlation with particle size, which is beyond the scope of this study.

7.5. Conclusions

Cu-doped TiO_2 nanoparticles' physico-chemical properties (dopant concentration, crystal phase, and particle size) were well controlled by manipulating the synthesis process parameters (i.e. the molar feed ratios of precursors, temperature, and time history) and their microbial inactivation potentials were evaluated. The microbial inactivation potential increased with increasing dopant concentration under both dark and light conditions. Under light conditions, the increased microbial inactivation potential for Cu-TiO_2 NPs is attributed to enhanced photoreactions and generation of more harmful OH radicals due to the leached copper from the surfaces of the particles. Crystal phase composition affects particle agglomeration (the anatase phase promoted agglomeration), and thus anatase phase was found to have a lower microbial inactivation potential compared to the rutile phase. Due to their larger surface area, smaller size particles exhibited higher microbial inactivation than larger size particles. This study clearly

indicates that microbial inactivation potential of Cu-doped TiO_2 can be enhanced after proper physical-chemical modifications, and is more efficient than conventional TiO_2 with UV and fluorescent light illumination. These light-activated NPs may lead to novel photo-induced antimicrobial reagents for environmental and medical applications.

7.6. References

[1] Lee E S, Yoon T H, Lee M Y, Han S H and Ka J O 2010 *Water Res.* **44** 1329-34

[2] Li Q, Mahendra S, Lyon D Y, Brunet L, Liga M V, Li D and Alvarez P J J 2008 *Water Res.* **42** 4591-602

[3] Hijnen W A M, Beerendonk E F and Medema G J 2006 *Water Res.* **40** 3-22

[4] Griffiths W D, Bennett A, Speight S and Parks S 2005 *J. Hosp. Infection* **61** 242-7

[5] Zhang D, Li G and Yu J C 2010 *J. Mater. Chem.* **20** 4529-36

[6] Hamal D B, Haggstrom J A, Marchin G L, Ikenberry M A, Hohn K and Klabunde K J 2010 *Langmuir* **26** 2805-10

[7] Sunada K, Watanabe T and Hashimoto K 2003 *Environ. Sci. Technol.* **37** 4785-9

[8] Liu H L and Yang T C K 2003 *Process Biochem.* **39** 475-81

[9] Sato T and Taya M 2006 *Biochem. Eng. J.* **30** 199-204

[10] Jiang J, Oberdorster G, Elder A, Gelein R, Mercer P and Biswas P 2008 *Nanotoxicology* **2** 33-42

[11] Jin X, Li M, Wang J, Marambio-jones C, Peng F, Huang X, Damoiseaux R and Hoek E M V 2010 *Environ. Sci. Technol.* **44** 7321-8

[12] Limbach L K, Wick P, Manser P, Grass R N, Bruinink A and Stark W J 2007 *Environ. Sci. Technol.* **41** 4158-63

[13] Almquist C B and Biswas P 2002 *J. Catal.* **212** 145-56

[14] Asahi R, Morikawa T, Ohwaki T, Aoki K and Taga Y 2001 *Science* **293** 269-71

[15] Sahu M and Biswas P 2011 *Nanoscale Res. Lett.* (**In press)**

[16] Wang Z M, Yang G X, Biswas P, Bresser W and Boolchand P 2001 *Powder Technol.* **114** 197-204

[17] Wong M, Chu W, Sun D, Huang H, Chen J, Tsai P, Lin N, Yu M, Hsu S, Wang S and Chang H 2006 *Appl. Environ. Microbiol.* **72** 6111–6

[18] Arana J, Dona-Rodriguez J M, Gonzalez-Diaz O, Rendon E T, Melian J A H, Colon G, Navio J A and Pena J P 2004 *J. Mol. Catal. A: Chem.* **215** 153-60

[19] Park H S, Kim D H, Kim S J and Lee K S 2006 *J. Alloys Compd.* **415** 51-5

[20] Li Y, Wang W N, Zhan Z, Woo M H, Wu C Y and Biswas P 2011 *Appl. Catal., B* **100** 386-92

[21] Tseng I H, Wu J C S and Chou H Y 2004 *J. Catal.* **221** 432-40

[22] Wu B, Huang R, Sahu M, Feng X Y, Biswas P and Tang Y J 2010 *Sci. Total Environ.* **408** 1755-8

[23] Karunakaran C, Abiramasundari G, Gomathisankar P, Manikandan G and Anandi V 2010 *J. Colloid Interface Sci.* **352** 68-74

[24] Sahu M, Suttiponparnit K, Suvachittanont S, Charinpanitkul T and Biswas P 2011 *Chem. Eng. Sci.* DOI:10.1016/j.ces.2011.04.003.

[25] Jiang J, Chen D R and Biswas P 2007 *Nanotechnol.* **18** 285603

[26] Society A T 1997 *Am. J. Respir. Crit. Care Med.* **156** S1-S25

[27] Snapper S B, Melton R E, Mustafa S, Kieser T and Jacobs W R 1990 *Mol. Microbiol.* **4** 1911-9

[28] Spurr R A and Myers H 1957 *Anal. Chem.* **29** 760–2

[29] Tang Y J, Shui W Q, Myers S, Feng X Y, Bertozzi C and Keasling J D 2009 *Biotechnol. Lett.* **31** 1233-40

[30] Suttiponparnit K, Jiang J, Sahu M, Suvachittanont S, Charinpanitkul T and Biswas P 2010 *Nanoscale Res. Lett.* **6** 1-8

[31] Nair J, Nair P, Mizukami F, Oosawa Y and Okubo T 1999 *Mater. Res. Bull.* **34** 1275-90

[32] Karlsson H L, Gustafsson J, Cronholm P and Moller L 2009 *Toxicol. Lett.* **188** 112-8

[33] Karlsson H L, Holgersson A and Moller L 2008 *Chem. Res. Toxicol.* **21** 726-31

[34] Egerton T A, Kosa S A M and Christensen P A 2006 *Phys. Chem. Chem. Phys.* **8** 398-406

[35] Cho M, Chung H, Choi W and Yoon J 2004 *Water Res.* **38** 1069-77

[36] Xu J, Sun Y, Zhao Y M, Huang J J, Chen C M and Jiang Z Y 2007 *International Journal of Photoenergy* **2007** 1-7

[37] Erkan A, Bakir U and Karakas G 2006 *J. Photochem. Photobiol., A* **184** 313-21

[38] Sjogren J C and Sierka R A 1994 *Applied and Environmental Microbiology* **60** 344-7

[39] Arenz M, Mayrhofer K J J, Stamenkovic V, Blizanac B B, Tomoyuki T, Ross P N and Markovic N M 2005 *J. Am. Chem. Soc.* **127** 6819-29

[40] Gurr J R, Wang A S S, Chen C H and Jan K Y 2005 *Toxicol.* **213** 66-73

[41] Mukherjee B and Weaver J W 2010 *Environ. Sci. Technol.* **44** 3332-8

[42] Waychunas G A, Kim C S and Banfield J F 2005 *J. Nanopart. Res.* **7** 409-33

Chapter 8:

Summary and Future Directions

8.1. Summary

The research conducted for this dissertation addressed fundamental aspects of doped-nanomaterial synthesis in a high temperature gas phase process. It explored how particles are formed and how important parameters control nanomaterial properties. In addition, *in situ* nanoparticles' charge characterization, exposure characterization, and detailed post synthesis characterization was conducted at different stages to relate the material properties with their applications. Some of the major conclusions from this study are summarized below.

i. A single-step diffusion flame aerosol reactor system developed earlier was modified for the synthesis of doped-TiO_2 nanomaterials. The influences of important process parameters that control the doped nanomaterial properties were identified. The dopant and annealing conditions were found to have a strong effect on nanomaterial size, crystal phase, suspension stability, and absorption properties. This system can be used to synthesize nanomaterials with different compositions, crystal phases, and different sizes and morphologies. This continuous process can be extended for other doped nanomaterials and is scalable.

ii. The *in-situ* charging characteristics of TiO_2 and Cu-doped TiO_2 were measured by integrating a DMA and a TDMA measurement system with the nanoparticle synthesis process. It was found that nanoparticles synthesized in a diffusion flame carry single as well as double charges depending on the particle size and dopant concentration. Numerical calculation identified the charging mechanism at different flame operating parameters, and the diffusion charging mechanism was

found to be dominant of particles in the flame, which was consistent with the experimental results.

iii. A nanoparticle characterization methodology was developed to assess the exposure potential during different operating scenarios for the gas phase reactors. It was found that surrounding concentration levels are much higher during synthesis in a flame aerosol reactor than in an enclosed furnace aerosol reactor. Nanoparticle exposure levels also depend on product recovery and handling procedures, and maintenance of the reactor. Based on the exposure scenarios, appropriate personal protective equipment was recommended for workers operating flame aerosol reactors.

iv. The roles of dopant types and concentration on dispersion properties were studied. It was found that dopant with an oxidation state above that of Ti shifts the iso-electric point (IEP) of TiO_2 to lower pH values, whereas dopant with lower oxidation state shifted the IEP to higher pH values. The agglomeration and surface charge behavior of nanomaterials was found to depend on size, crystal phase, pH, and ionic strength. The results from this study demonstrate that the state of dispersion should be carefully considered, while evaluating the nanomaterial for toxicity, photo-catalytic action, and environmental fate and transport behavior.

v. Response of two environmental microorganisms; *Mycobacterial smegamitis* and *Shewanella Oneidensis* was investigated by exposing them to pristine TiO_2 and Cu-doped TiO_2. Doped nanomaterial was found to have more toxic effect than

pure TiO_2 on *M. Smegamitis*, although no significant effect was observed for *S. Oneidensisunder* under complete dark conditions. The study indicates that the agglomeration state of the suspended nanoparticles can have a significant effect on toxicity. The finding will help in evaluating the toxic potential effect of doped nanomaterials on environmental ecosystems hosting specific types of microorganisms.

vi. The role of dopant concentration, crystal phase, and size on microbial inactivation potential was evaluated under dark, fluorescent light, and UV light conditions. It was found that inactivation potential depends both on light conditions as well as on physio-chemical properties of the doped nanomaterials. The dopant concentration was found to have a remarkable effect on the inactivation potential: inactivation increased with increased copper dopant concentration under all three light conditions. Inactivation potential also seems to be crystal phase and size dependent, and particle agglomeration in the suspension reduces the effective inactivation potential.

vii. The microbial inactivation of *M. Smegamitis* when exposed to Cu-doped TiO_2 nanoparticles were found to combine the effect of leached copper ions and enhanced photo-catalytic reactions due to reduction in the electron and hole pair recombination under light conditions. The inactivation potential under fluorescent light above 3 wt% copper dopant indicates that these doped nanomaterials can be effectively used as antibacterial materials, which can act effectively under normal living light conditions.

8.2. Future directions

This work demonstrated the synthesis and characterization doped TiO_2 nanomaterials and their applications. However, as nanomaterial applications will grow; its environmental impacts need more attention. Some of the issues have been addressed in this dissertation but more exploration is required for making the nanotechnology applications viable and sustainable.

The work in this dissertation addresses doped TiO_2 nanomaterial synthesis in a laboratory scale gas phase reactor. However, for industrial scale application, the synthesis process needs to be scaled up. There are experimental evidences that nanomaterial property changes based on the different criteria used for scaling the reactor. There are two different approaches that can be adopted for scaling up the flame reactor. First, increasing the numbers of small scale laboratory reactors to increase the nanomaterial producion quantities. Due to many reactors, operation and maintennace of the individual reactors is essential. Second approach is scaling up burner dimension and other operating parameters to increase the production rate of materials. A detailed study is needed to identify the scale up parameters for producing large quantities while controlling the doped nanomaterial properties. Developing second generation new nanoscale materials in a single-step scalable process, as well as method to characterize and manipulate will advance the nanotechnology to broader applications in energy and the environment such as solar cells for energy harvesting and sensors to detect and clean environmental pollutants. In addition, a detail modeling approach is essential to predict the nanostructure and composition that give rise to desirable functional behavior.

Exposure to nanoparticles will potentially increase with enhanced nanotechnology applications. Few characterization techniques were adopted in this work to characterize nanoparticle exposure. Studies have already demonstrated that various dose metrics should be considered while evaluating the potential toxic effects. Other dose parameters such as surface area of the particles should be measured to gain a more understanding of the potential adverse impacts arise due to nanoparticle exposure. Nanoparticle exposure measurement in small occupational environments such as research laboratory is helpful; however, continuous exposure in industrial and pilot scale plants producing nanomaterial will provide a better assessment of exposure to nanotechnology workers. Research on developing portable exposure measurement instruments will bring new advancement in exposure characterization.

Detailed characterization of the nanomaterials at different stages is important to fundamentally understand the phenomena occurring at nanoscale. Surface defect characteristics and other intrinsic properties of TiO_2 material changes due to doping, which need to be studied. For example, addition of dopant modifies the dielectric properties of TiO_2, which affect the charge carried by the particles during the synthesis process. In addition, more surface characterization techniques are required to identify the surface defect sites that will help in correlating with the performance.

Although nanomaterials were applied for bacterial inactivation in this work, the detailed mechanisms of inactivation are still not clear. Experimental evidence indicates inactivation potential depends on the bacterial species. More investigation regarding bacterial cell structures and detailed microscopic changes in cell structure after exposed to nanomaterials will help in understanding the inactivation behavior. In addition, various

other doped and composite nanomaterials should be investigated for bacterial inactivation using different bacterial species. The inactivation mechanisms as well as potential inactivation may vary from species to species. In addition, the toxicity potential of these nanomaterials on mammalian cell should be investigated, as the nanomaterials will be exposed to mammalian animals through different exposure pathways.

Appendix-A:

Experimental setups

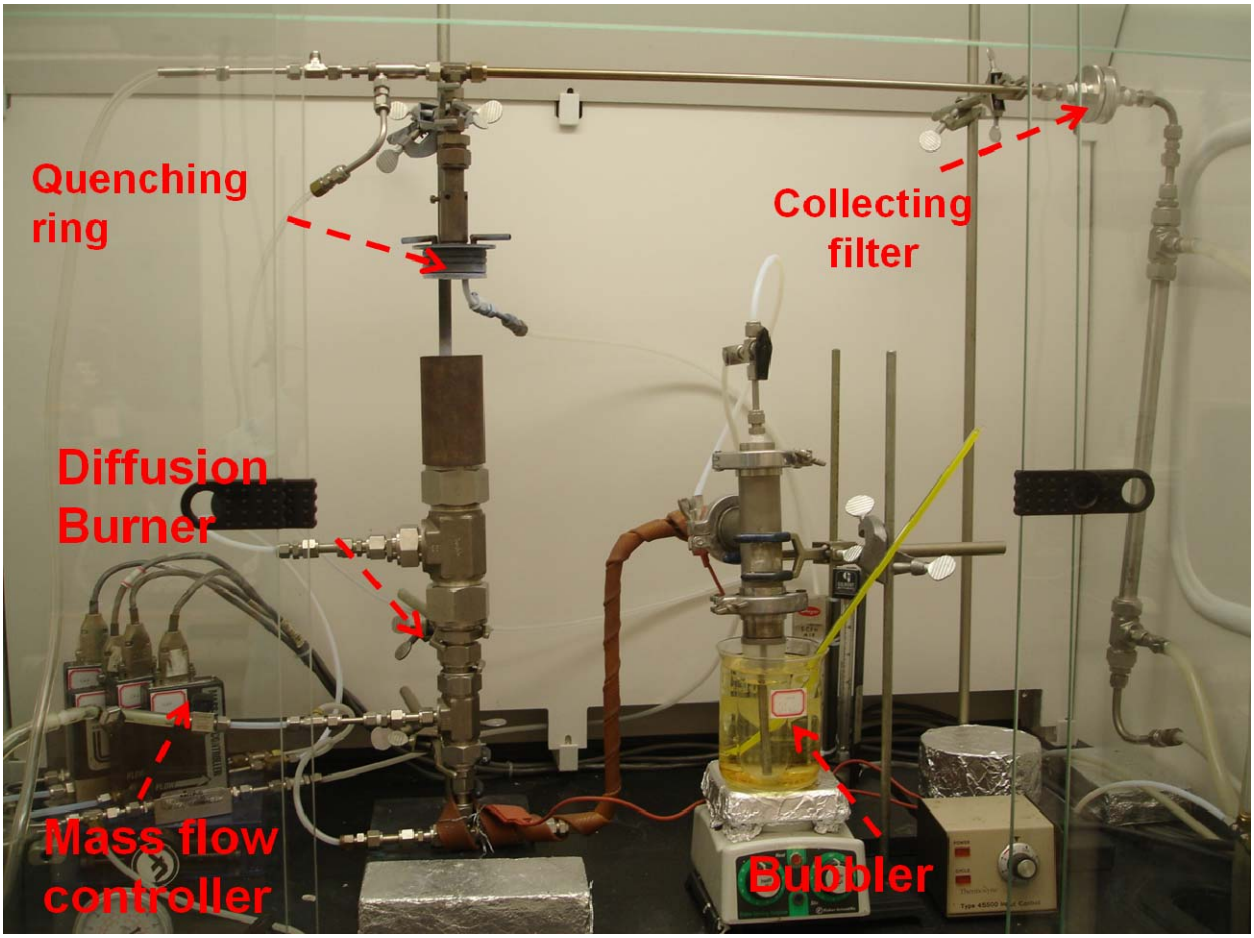

Figure A- 1: Digital image of the flame aerosol reactor system used for Cu-doped TiO_2 nanomaterial synthesis

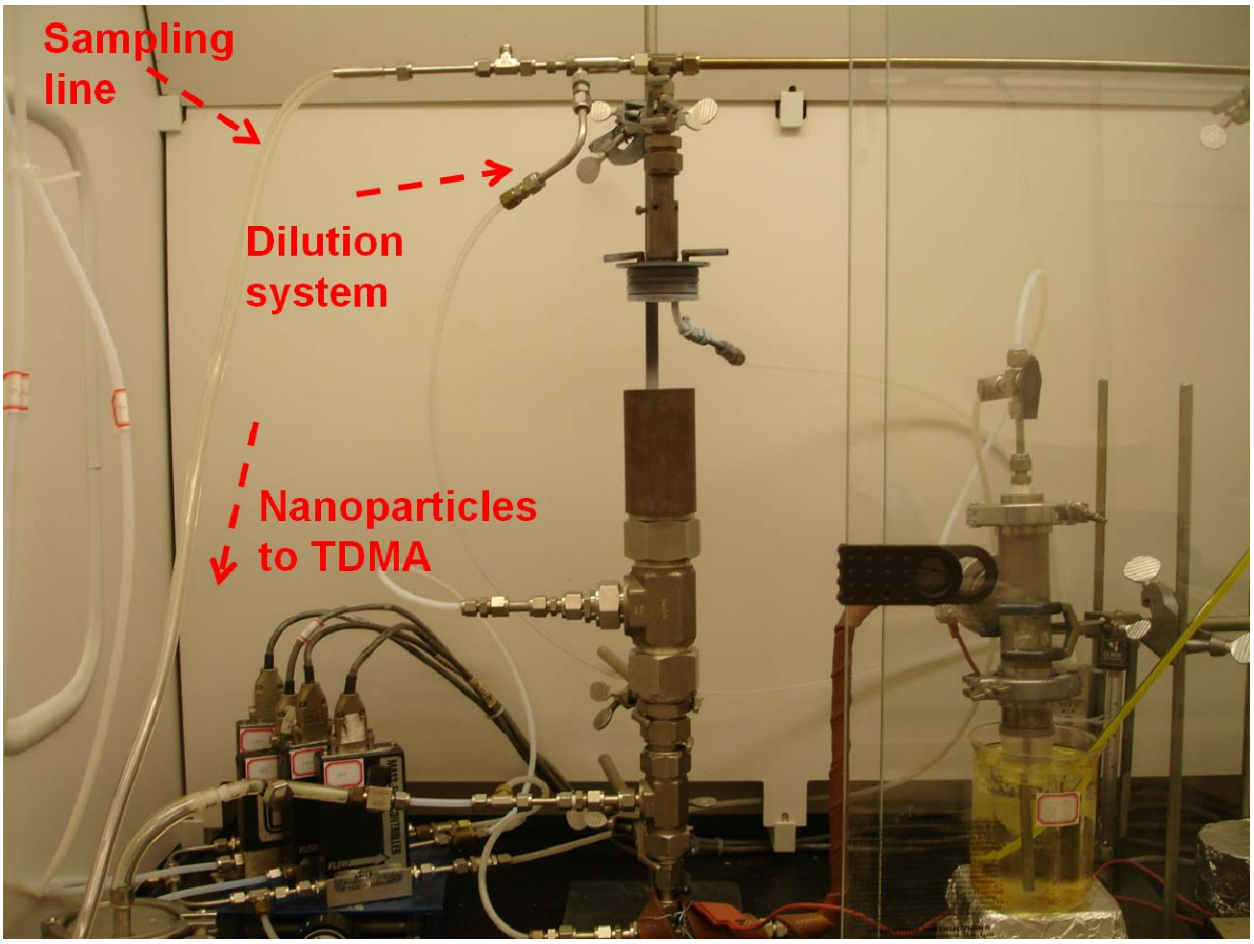

Figure A-2: Digital image of the sampling system from flame aerosol reactor to TDMA system

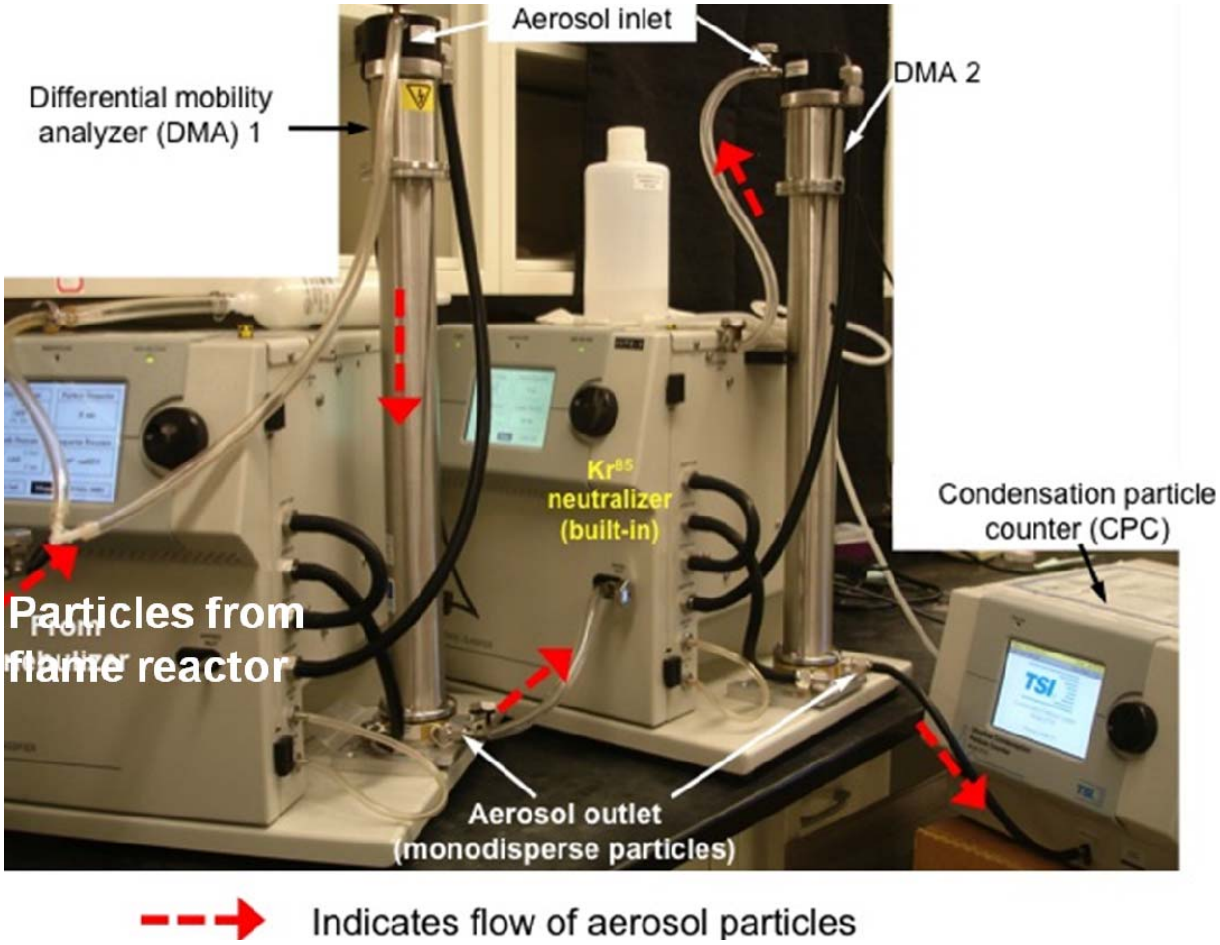

Figure A- 3: Tandem differential analyzer system used for charge distribution measurement study.

Figure A- 4: Dynamic light scattering instrument used for dipserison study

Appendix-B:

Cu-doped TiO_2 Nanoparticles Enhance Survival of *Shewanella oneidensis* MR-1 under Ultraviolet Light (UV) Exposure

The results presented here were published in:

Wu, B, W, Zhuang, M, Sahu, P, Biswas , and Y. J. Tang, *Cu-doped TiO_2 Nanoparticles Enhanced Survival of Shewanella oneidensis MR-1 during UV Exposure*, Science of the Total Environment, 2011(In press).

B.1. Abstract

It has been known that photocatalytic TiO_2 nanoparticles (NPs) can be used as an efficient anti-microbial agent under UV light due to generation of reactive oxygen species (ROS), while *Shewanella oneidensis* MR-1 is a metal-reducing bacterium highly susceptible to UV radiation. Interestingly, we found that the presence of Cu-doped TiO_2 NPs in the cultural medium dramatically increased the survival rates of strain MR-1 by over 10,000-fold (incubation without shaking) and ~200 fold (incubation with shaking) after a 2-hr exposure to UV light. Furthermore, we observed that the DNA repair gene *rec*A in MR-1 was significantly induced by UV exposure (indicating cellular damage under UV stress), but the influence of NPs on *rec*A expression was not statistically evident. Plausible explanations to NP attenuation of UV stresses are: 1. TiO_2 based NPs are capable of scattering and absorbing UV light and thus create shading effect to protect MR-1 from UV radiation; 2. more importantly, Cu-doped TiO_2 NPs can co-agglomerate with MR-1 to form large flocs that improves cells' survival against the environmental stresses. This study improves our understandings of NP ecological impacts and provides useful insights to application of photocatalytic-NPs for bacterial disinfection.

Key words: Absorb; agglomerate ; Disinfection; Flocs; *rec*A; Shaking

B.2. Introduction

The use of nanoparticles to destroy microorganisms is an effective method for water disinfection (Adams et al., 2006; Rawat et al., 2007). To increase NP antimicrobial efficiency, irradiation of photo-catalytic nanoparticles with UV light can be employed for photoelectrochemical oxidation of bacterial cells (Matsunaga and Okochi, 1995). For example, Titanium dioxide (TiO_2) NPs are widely used as photocatalysts. To enhance their photoactivity properties, transition metals (such as copper, silver, etc.) have been doped with TiO_2 NPs (Hamal et al. 2010; Namiki et al., 2005; Colón et al., 2006; Wu et al., 2010a). Metal doped TiO_2 NPs in the anatase crystalline form is a strong bactericidal agent when exposed to near-UV light (Hamal et al.; Marciano et al., 2009). This is due to the fact that metal doped TiO_2 NPs produce reactive oxygen species (ROS, such as $OH^{\bullet}$), which cause lipid peroxidation in membranes, DNA damage, and oxidation of amino acids and protein catalytic centers (Brunet et al., 2009). On the other hand, TiO_2 NPs can agglomerate in the aqueous medium and affect the interactions between NPs and microorganisms. The NP agglomeration may also affect NPs' antimicrobial activity (Jiang et al., 2009; Wu et al., 2010a).

Shewanella oneidensis MR-1 is an environmentally important bacterium which can use electrons from carbon substrates to reduce diverse heavy metals (e.g. Mn(III) and (IV), Fe(III), Cr(VI), U(VI)) (Heidelberg et al., 2002). Previous study has shown that MR-1 is highly sensitive to all wavelengths of UV radiation. In general, UV light damages cell nucleotide and the cell normal functions cannot recover without correct repair of DNA molecules. However, some nucleotide excision repair component genes (*uvrA*, *uvrB*, and *uvrD*) in MR-1 are not active under UV stress and thus cannot prevent

harmful mutations caused by UV-damaged DNA (Qiu et al., 2004; Qiu et al., 2005a; Qiu et al., 2005b). In addition, UV irradiation stimulates the release of Fe(II) from MR-1 proteins, leading to additional cellular damage by Fe(II)-dependent oxidative stress (Ghosal et al., 2005). In this study, we focus on the responses of MR-1 to Cu-doped TiO_2 NPs under UV light condition, which can provide insights into the ecological impact of photoactive nanoparticles under solar irradiations.

B.3. Materials and Methods

B.3.1. Preparation of TiO_2 NPs and humic acid-coated NP stock solutions.

A flame aerosol reactor (FLAR) with a three-port co-flow diffusion burner was used to synthesize TiO_2 NPs (35 nm) and Cu-doped TiO_2 NPs (15, 35 and 65 nm) (Jiang et al., 2009; Wu et al., 2010a). In brief, titanium tetra-ispopropoxide (TTIP, 97%, Aldrich-Sigma, USA) and copper (II) ethyl hexanoate (Aldrich-Sigma, USA) were used as the precursors to the Cu-doped TiO_2 NPs. Copper (II) ethyl hexanoate was dissolved in xylene and atomized by a stainless steel nebulizer in the high temperature zone. Doping percentages were varied by feeding different molar ratios of the precursors into the high temperature combustion zone. The temperature and residence time of the NPs in the combustion zone were controlled to obtain the desired size and composition of the NPs.

Furthermore, CuO NPs (40 nm) were purchased from Aldrich-Sigma (USA). Polystyrene NPs (~100 nm, served in the control experiments) were purchased from Duke Scientific Corporation (USA). TiO_2 NPs, Cu-doped TiO_2 NPs, CuO NPs, and polystyrene NPs were suspended in sterilized and distilled water to make a stock solution (1 g/L). The size distributions of NPs were measured by a dynamic light scattering

analyzer (Malvern, UK). The absorbance profiles of Cu-doped TiO_2 NPs after the UV exposure were investigated by a UV/Visible spectrometer (Olis DW2000, On-Line Instrument Systems, USA) using a cell-free medium as the blank.

Humic acid (HA) solution was obtained by dissolving solid HA (Sigma-Aldrich, USA) with 0.1 M NaOH and then adjusted to pH 5.0 by 0.1 M HCl. Humic acid-coated NP stock solution was prepared by mixing 20 mL NP stock solution (1 g/L) with 20 mL HA solution (0.4 g/L) in a sterilized glass vial. After shaking (150 rpm at 30°C) in the dark for 2 days, the humic acid-coated NP stock solutions were ready for the experiments (Yang et al., 2009; Zhang et al., 2009).

B.3.2. MR-1 survival under NP stresses.

S. oneidensis MR-1 was first grown in a minimal MR-1 medium (30 mM lactate as carbon source) at 30°C (Tang et al., 2007). When the MR-1 growth approached OD_{600} (~1.0), cells were diluted with 5 mL of minimal MR-1 medium (no carbon source) to ~ 4×10^7 CFU/mL. NP stock solution was sonicated for 1 min to break NP agglomerates before being added to the cell cultures (final NP concentration of 2 mg/L or 20 mg/L). The cell cultures with NPs were incubated in sterilized glass bottles for 2 hr without or with shaking (200 rpm). The incubation condition was under dark, florescence light (1324.2 $\mu w/cm^2$), or UV radiation (120.8 $\mu w/cm^2$). To count the survival cells, 100 μL cultures (two biological and two technical replicates) were serially diluted and spread on the LB agar (Difco, BD, USA) plates. The total number of viable cells was estimated by the colony-forming unit (CFU) after 24-hr incubation at 30°C.

B.3.3. Observation of NP and cell morphologies by transmission electron microscopy (TEM), scanning electron microscopy (SEM), and optical microscopy.

TEM was used to observe the agglomeration of the NPs after UV exposure. The samples were air dried and inspected with the TEM (H7500, Hitachi, Japan) at 80 kV using the HR mode and photographed by an attached digital camera (FEI, USA). SEM was used to observe cell morphologies. After UV exposure, the cells were deposited on a piece of silicon wafer and were fixed using 2% glutaraldehyde for 2 hrs. The samples were washed three times by soaking them in 0.1 M sodium cacodylate buffer (20 minutes each time). The fixed cells were dehydrated in a series of 10-minute soaks in 50%, 70%, 85%, 95%, and 100% ethanol and were subsequently dried in a freezing-drier (Labconco, USA). The dried cells were sputter gold-coated (SPI supplies, USA) and imaged using an SEM (FEI, USA) (Wu et al., 2010b). Besides, an optical microscope (Zeiss, USA) was used to directly observe the natural conformation of cell agglomeration, and pictures were taken by a built-in camera (Nikon, Japan).

B.3.4 Transcriptional analysis of key genes by quantitative reverse transcription-polymerase chain reaction (qRT-PCR).

After exposure of the MR-1 culture (OD_{600} ~0.1) to UV radiation (with or without Cu-doped TiO_2 NPs) for 30 min or 2 hrs (without shaking), the cultures were recovered at 30°C in MR-1 medium (shaking at 200 rpm). Subsequently, cell samples were taken after 20 and 60 min. Controls were treated the same but without UV exposure. The qRT-PCR was performed following a protocol previously reported (Wu et al., 2010c). In brief, total RNA was extracted from the cell pellets using an RNAwiz kit (Ambion, Japan) according

to the manufacturer's instruction. DNA contamination was further removed by DNase treatment using a RQ1 RNase-Free DNase kit (Promega, USA) in accordance with the manufacturer's protocol. The extracted RNA was then transcribed to cDNA using a Reverse Transcriptase kit (Applied Biosystems, USA) by following the manufacturer's protocol. The forward primer (5'-TGCCGAAGGTTTCGAGGTC-3') and reverse primer (5'-TGATTTTAGTGCCGCCCTTG-3') were employed to amplify the *ldh*A (internal control), and the forward primer (5'-CCTCAAGCAATCGAACACTCTG-3') and reverse primer (5'-CACCCGTTGTGGTTTCTGG-3') were used to amplify the *rec*A genes (inducible genes) (Qiu et al., 2004; Qiu et al., 2005a) in the cDNA by a GoTaq® qPCR Master Mix kit (Promega, USA) using a real-time PCR system (Applied Biosystems, USA). The relative quantification method (comparative C_T) was used to calculate the expression level of the UV-stressed cells compared to that of the unstressed cells. Three biological replications and three technical replications were conducted.

B.4. Results and Discussion

B.4.1. MR-1 survival under NPs and light conditions (incubation without shaking)

We incubated MR-1 with NPs for 2 hrs without shaking. Figure B-1A showed that neither TiO_2 NPs nor Cu-doped TiO_2 NPs reduced the viability of MR-1 compared to the controls under dark or fluorescent light conditions. These results confirmed that MR-1 tolerated the Cu-doped TiO_2 NP stress (Wu et al., 2010a). Three reasons explain resistance of MR-1 to NP stress. First, outer membrane of MR-1 (a gram-negative bacterium) contains lipopolysaccharides that protect the membrane from NP attack (note: lipopolysaccharides improve the structural integrity of cell membrane).

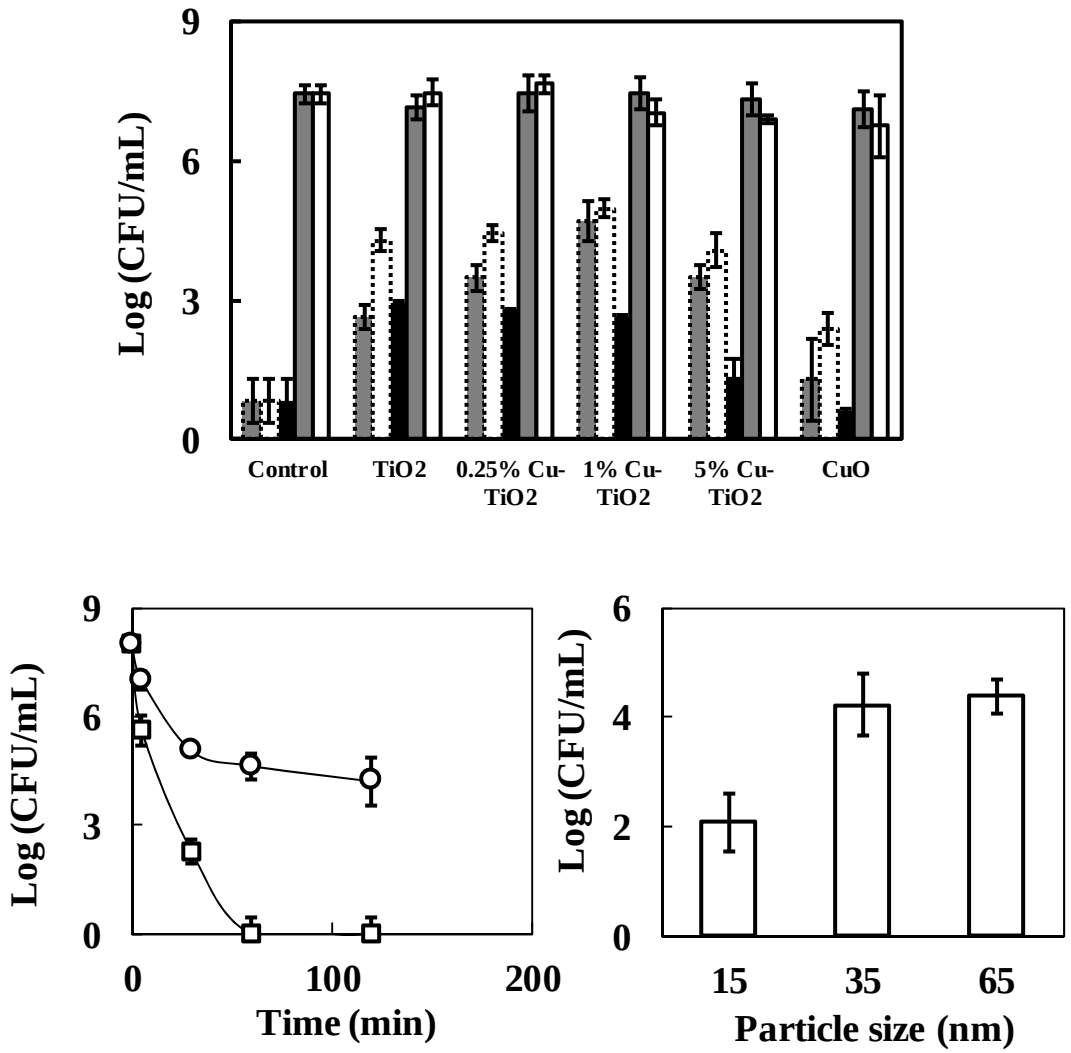

Figure B-1: *S. oneidensis* MR-1 survival (in the $\log_{10}$ scale) under NP and UV stresses.
(A) Responses of MR-1 to NPs (35 nm) under light conditions (2 hr light exposure). Grey column with dot line, under UV light (2 mg/L NPs); White column with dot line, under UV light (20 mg/L NPs); Black column, under UV light (20 mg/L NPs) with shaking (200 rpm); Grey column with solid line, in dark (20 mg/L NPs); White column with solid line, under fluorescent light (20 mg/L NPs).

(B): Time-dependent responses of MR-1 to 1% Cu-doped TiO_2 NPs (35 nm, 20 mg/L, incubation without shaking). (□) Cells survival after UV exposure (without NPs); (○) Cells survival after UV exposure (with NPs).

(C): Particle size effect on MR-1 survival after 2 hr UV exposure (3% Cu-doped TiO_2 NPs, 20 mg/L, incubation without shaking).

Figure B- 1: S. oneidensis MR-1 survival (in the log10 scale) under NP and UV stresses.

Second, MR-1 produces extracellular polymeric substances (e.g., extracellular proteins). Such biomaterials form physical barriers that prevent NP penetrations into cells (Suresh et al., 2010; Wu et al., 2010b). Third, the metal reducer MR-1 can transfer electrons from metabolism of organic sources to various electron acceptors and thus attenuates potential NP oxidative stress. For example, MR-1 enzymatically reduces the copper ions released from Cu-doped TiO_2 NPs (Wu et al., 2010a).

MR-1 is highly sensitive to UV light because of their unique physiology (Qiu et al., 2004; Qiu et al., 2005a). Although UV light killed most MR-1 cells in the culture (survival of 5~6 CFU/mL) after a 2 hr-exposure, the presence of small amount of Cu-doped TiO_2 NPs (2 mg/L) tended to significantly increase the survival rates of MR-1 by up to 1,000 fold (Figure B-1A). As the NP concentration increased from 2 mg/L to 20 mg/L, the cell survival rate further improved by 2~50 fold. This observation indicated a positive correspondence of the NP doses and MR-1 survival rates. Besides, SEM images (Figures B-2A and B-2B) revealed the cell morphology after UV exposure for 2 hrs: the surface structure of solitary cells was rough and lysed, while the agglomerated cells with NPs might maintain their normal shape.

Cell survival rate was associated with a doping amount of copper on TiO_2 NPs, UV exposure time, and NP sizes. First, Cu-doped TiO_2 NPs (i.e., 0.25% and 1% copper) showed significantly higher improvement of cell survival rates compared to the TiO_2 NPs. For example, after 2 hr-UV exposure, culture with 1% Cu-doped TiO_2 NPs (35 nm, 20 mg/L) had the highest viable cell amount (~9×10^4 CFU/mL) among our experiments. Such protection was reduced when doped copper was over 5% (Figure B-1A), and CuO NPs had minimal effectiveness to protect MR-1 against UV stress.

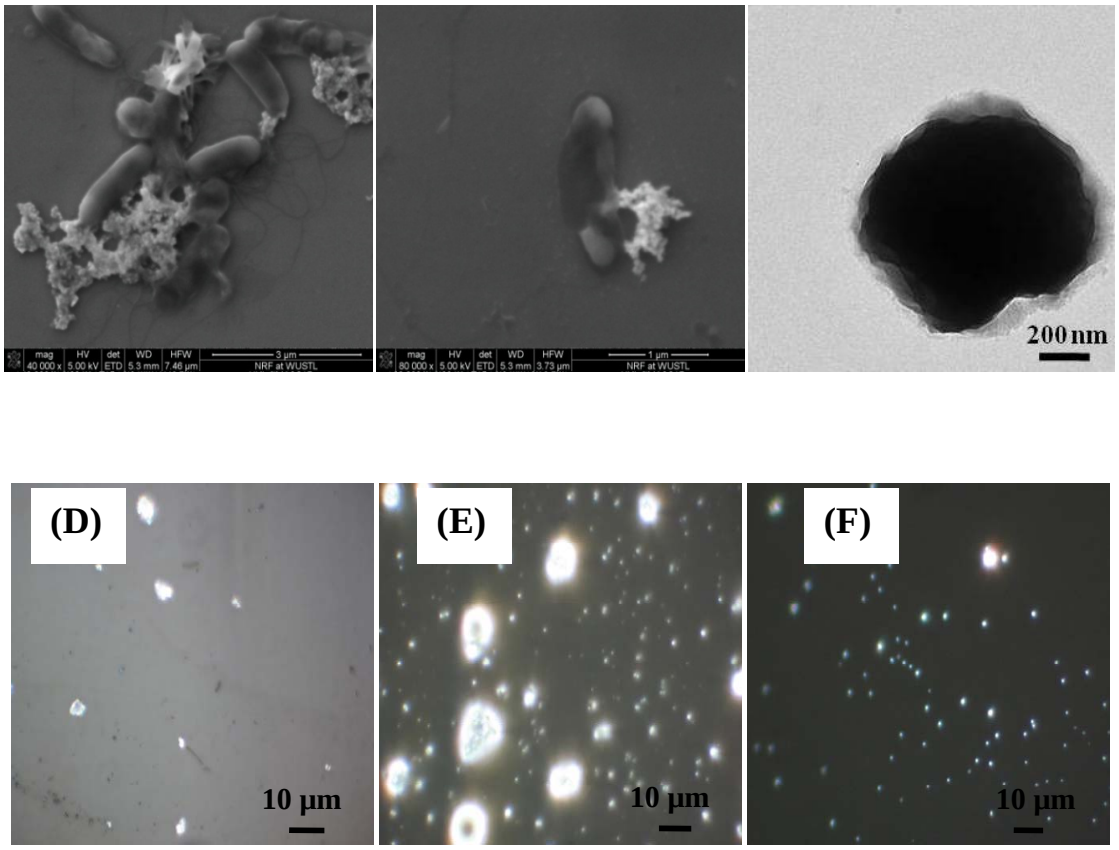

Figure B- 2: S. oneidensis MR-1 survival (in the log10 scale) under NP and UV stresses.

(A) SEM image of cell agglomerates in the presence of NPs;

(B) SEM image of solitary damaged cell in the presence of NPs;

(C) TEM image of agglomerated NPs (35 nm);

(D) Optical microscopy image of cells without NPs (incubation without shaking);

(E) Optical microscopy image of cells in the presence of NPs (incubation without shaking);

(F) Optical microscopy image of cells in the presence of NPs under shaking conditions (200 rpm).

Second, cell survival rate was a function of UV exposure time. In the cultures without any NPs, viable cell number dropped sharply from ~3×10^7 CFU/mL to ~180 CFU/mL after 30 minutes of UV-exposure (Figure B-1B). However, if the cultures were supplemented with 1% Cu-doped TiO_2 NPs (35 nm and 20 mg/L), viable MR-1 number was over 4×10^5 CFU/mL after 60 minutes of UV-exposure; further extending UV exposure time to 2 hrs, the live cell population was still high (~9×10^4 CFU/mL, Figure B-1B). Third, small size NPs were less effective in protecting cells from UV stress than the NPs with larger sizes (>35nm). For example, we had tested Cu-doped TiO_2 NPs with three different particle sizes (15nm, 35nm, and 65nm). We found that MR-1 survival rates were lowest in the culture with 15 nm ultrafine NPs (Figure B-1C).

B.4.2. MR-1 recA gene regulation under NP stresses and UV light

The *rec*A gene in MR-1 is involved in important cellular functions including cell division, DNA repair and maintenance, and mutagenesis (Qiu et al., 2005a). The expression levels of *rec*A gene in MR-1 after UV exposure in the absence of NPs was compared to those in the presence of NPs. Table B-1 demonstrates that UV exposure significantly induced average *rec*A gene expression (unit: n-fold) by 5.5-fold, indicating that the UV radiation caused apparent DNA damage. However, the induction of *rec*A gene expressions in the absence and presence of Cu-doped TiO_2 NPs was not significantly different (*P*-value >0.1) under light conditions (i.e., DNA damage was not induced by NPs). This result suggested that the presence of NPs did not significantly affect *rec*A gene expression in MR-1. Thus, the attenuation of UV stress to MR-1 was not due to the NP stimulation for the repair of cellular functions.

Table B- 1: Expression level (unit: n-fold) of S. oneidensis MR-1 after UV exposure.

	Cells	Cells with 1% Cu-doped TiO_2 NPs	*P*-value
Without UV exposure	1.0* (0.39 to 2.6)**	0.82 (0.55 to 1.2)	0.214
UV exposure for 30 min and recovery 20 min	2.4 (0.84 to 6.7)	2.4 (0.83 to 6.8)	0.998
UV exposure for 2 hr and recovery 1 hr	5.5 (1.7 to 17.7)	7.5 (1.3 to 43.3)	0.713

*** The data presented here was normalized using *ldh*A as internal control and was the mean of 6 data points from the three biological replicates and three technical replicates.**

**** The number in the parenthesis was the confidence intervals (95%).**

B.4.3. Agglomeration of NPs and MR-1 cells

Both TiO_2 and Cu-doped TiO_2 NPs (~35 nm) tended to spontaneously agglomerate in the aqueous environments because of NP high surface forces. The final formed bulk NP agglomerates had a mean particle size of ~700 to 900 nm in the aqueous medium (Figure B-2C), regardless of light conditions (data not shown). In addition, MR-1 (negatively charged cell surface) produced extracellular polymeric substances (EPS), which led to an co-agglomeration of cells with NPs (Wu et al., 2010a). Under non-agitation conditions, we found that MR-1 formed cell clusters in the medium suspension (Figure B-2D), while addition of NPs significantly promoted cell agglomeration, which led to the formation of much larger flocs ranging from a size of a few micrometers to ~20 micrometers (Figure B-2 E). Compared to solitary cells, the agglomerated cells usually have high survival ratios under environmental stresses (Monier and Lindow, 2003). Therefore, we

hypothesized that TiO_2 based particles served as the "platform" to facilitate the formation of large bacterial flocs that sheltered the viable cells within the matrix from UV radiations (Monier and Lindow, 2003), while detailed study of NP agglomeration has been reported in our earlier papers (Jiang et al., 2009; Wu et al., 2010a).

On the other hand, we conducted experiments using HA-coated 1% Cu-doped TiO_2 or polystyrene NPs to reduce the agglomeration of NPs in the liquid medium. The HA is natural organic matter that influences the stability and agglomeration state of particles (Xie et al., 2008; Yang et al., 2009; Zhang et al., 2009). In our study, HA-coating on 1% Cu-doped TiO_2 NPs led to an apparent decrease in a mean particle size of NP agglomerates from ~914 nm to ~ 380 nm (Figure B-3). In addition, the hydrophobic characteristics of polystyrene NPs (primary size of ~100 nm) (Habicht et al., 2008; Jiang et al., 2010) resulted in less agglomeration of the NPs in the aqueous solutions, where they had a mean particle size of ~ 230 nm (Figure B-3). Table B-2 shows that MR-1 survival rate dropped 1.5~3 orders of magnitude when HA-coated 1% Cu-doped TiO_2 or polystyrene NPs were mixed with MR-1 compared to that 1% Cu-doped TiO_2 NPs (without shaking). In addition, we shook the culture vigorously (shaking speed of 200 rpm) during the incubation under UV light. Continuous agitation could increase microbial exposure to UV light and reduce co- agglomeration of NPs and cells (i.e., decrease of floc size, Figure B-2F). As expected, shaking condition significantly reduced the viable cells under UV light. Under shaking conditions, cell survival rate was below 5 CFU/mL without any NPs, while up to 1000 CFU/mL was still observed in the presence of Cu-doped TiO_2 NPs (~200-fold improvement of cell survival rate).

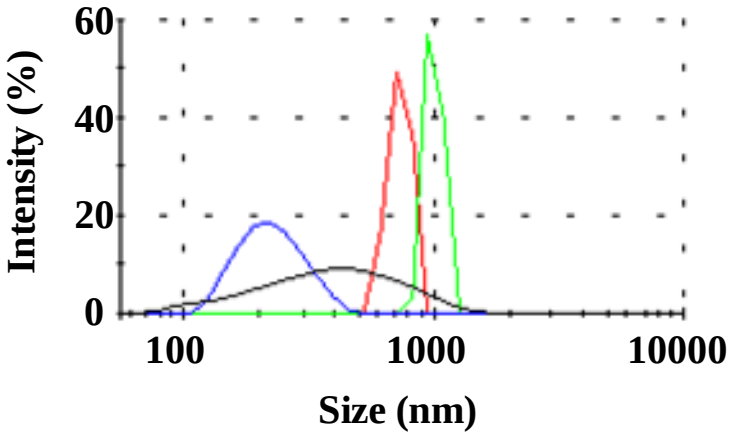

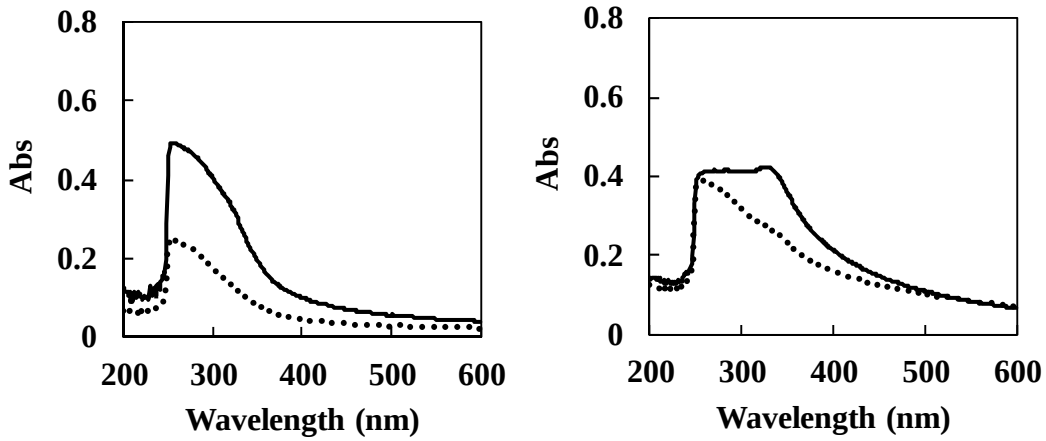

Figure B- 3: The hydrodynamic size distributions of NPs in the cell-free medium. Red line: TiO_2 NPs; Green line: 1.0% Cu-doped TiO_2 NPs (35 nm); Black line: HA-coated 1.0% Cu-doped TiO_2 NPs (35 nm); Blue line: Polystyrene NPs.

Figure B- 4: Absorbance profiles of NPs before and after UV exposure. (A) 1.0% Cu-doped TiO_2 (35 nm); (B) 3.0% Cu-doped TiO_2 (35 nm). Solid line: absorbance at the beginning of UV exposure; Dot line: absorbance after 2hr-UV exposure.

These results indicated that the protection of MR-1 by Cu-doped TiO_2 NPs was less effective if the cells and NPs agglomeration was minimized.

B.4.4. Cu-doped TiO_2 NPs absorbed UV light to reduce UV stress on MR-1

TiO_2 NPs can absorb the UV light or shift the absorption spectrum towards visible light spectrums (Wang et al., 2009). Previous study has proved that TiO_2 particles (at high concentrations) can reduce photochemical disinfection of *Escherichia coli* under UV light due to light absorption and scattering (Matsunaga and Okochi, 1995). For example, concentration of TiO_2 particles (2.5mg/L) can enhance UV light for disinfection of *Escherichia coli*. If the concentration of TiO_2 NP was raised to 100mg/L, the survived cell after UV-exposure increased significantly. This study found that CuO-TiO_2-based

Table B- 2: Viable cells in the presence of NPs (20 mg/L) after UV exposure for 2 hr.

	1.0% Cu-doped TiO_2 NPs		**HA-coated 1.0% Cu-doped TiO_2 NPs**		**Polystyrene NPs**	
	No shaking	**Shaking**	**No shaking**	**Shaking**	**No shaking**	**Shaking**
Log_{10} (CFU/mL)	4.96±0.19	2.65±0.04	3.21±0.72	1.69±0.08	1.87±0.01	~ 0

NP suspensions attenuated UV stress to MR-1 cells even at a very low concentration (2 mg/L). Figure B-4 showed that photocatalytic Cu-doped TiO_2 (with 1% or 3% copper) displayed strong UV absorbing capabilities (270~340 nm) and thus led to a decrease of light transmission in the culture medium. Even under shaking conditions, Cu-doped TiO_2 NPs still effectively attenuated UV radiation into cultures (Table B-2). Compared to HA-coated TiO_2 NPs and polystyrene NPs (NPs with lower photo-activities), shaking cultures with Cu-doped TiO_2 NPs had highest survival rate (450 CFU/mL) after 2hr-UV exposure (Table B-2).

B.5. Conclusions

In previous studies, it has been demonstrated that photo-catalytic NPs can promote the efficiency of UV disinfection of bacteria. Interestingly, Cu-doped TiO_2 NPs may mediate the UV stress to *Shewanella oneidensis* MR-1. NPs tend to form micrometer-sized agglomerates due to their special surface characteristics. During the self- agglomeration process, NPs may facilitate co- agglomeration with microbial cells to form larger flocs. Furthermore, Cu-doped TiO_2 NPs effectively absorb UV light and decrease UV transmission in the culture medium. This hints that the presence of NPs may be beneficial to some vulnerable environmentally relevant bacteria under exposure to harmful sun light. On the other hand, prevention of cell and NP agglomerations is important for effective disinfection of harmful bacteria by photo-catalytic NPs.

B.6. References

Adams LK, Lyon DY, McIntosh A, Alvarez PJ. Comparative toxicity of nano-scale TiO2, SiO2 and ZnO water suspensions. Water Sci Technol 2006; 54: 327-334.

Brunet L, Lyon DY, Hotze EM, Alvarez PJ, Wiesner MR. Comparative photoactivity and antibacterial properties of C_{60} fullerenes and titanium dioxide nanoparticles. Environ Sci Technol 2009; 43: 4355-4360.

Colón G, Maicu M, Hidalgo MC, Navio JA. Cu-doped TiO_2 systems with improved photocatalytic activity. Appl Catal B 2006; 67: 41-51.

Farré M, Gajda-Schrantz K, Kantiani L, Barcelo D. Ecotoxicity and analysis of nanomaterials in the aquatic environment. Anal Bioanal Chem 2009; 393: 81-95.

Ghosal D, Omelchenko MV, Gaidamakova EK, Matrosova VY, Vasilenko A, Venkateswaran A, Zhai M, Kostandarithes HM, Brim H, Makarova KS, Wackett LP, Fredrickson JK, Daly MJ. How radiation kills cells: survival of *Deinococcus*

radiodurans and *Shewanella oneidensis* under oxidative stress. FEMS Microbiol Rev 2005; 29: 361-375.

Habicht S, Nemanich RJ, Gruverman A. Physical adsorption on ferroelectric surfaces: photoinduced and thermal effects. Nanotechnology 2008; 19: 1-4.

Hamal DB, Haggstrom JA, Marchin GL, Ikenberry MA, Hohn K, Klabunde KJ. A multifunctional biocide/sporocide and photocatalyst based on titanium dioxide (TiO_2) codoped with silver, carbon, and sulfur. Langmuir 2010; 26: 2805-2810.

Handy RD, Owen R, Valsami-Jones E. The ecotoxicology of nanoparticles and nanomaterials: current status, knowledge gaps, challenges, and future needs. Ecotoxicology 2008a; 17: 315-325.

Handy RD, von der Kammer F, Lead JR., Hassellov M, Owen R, Crane M. The ecotoxicology and chemistry of manufactured nanoparticles. Ecotoxicology 2008b; 17: 287-314.

Heidelberg JF, Paulsen IT, Nelson KE, Gaidos EJ, Nelson WC, Read TD, Eisen JA, Seshadri R, Ward N, Methe B, Clayton RA, Meyer T, Tsapin A, Scott J, Beanan M, Brinkac L, Daugherty S, DeBoy RT, Dodson RJ, Durkin AS, Haft DH, Kolonay JF, Madupu R, Peterson JD, Umayam LA, White O, Wolf AM, Vamathevan J, Weidman J, Impraim M, Lee K, Berry K, Lee C, Mueller J, Khouri H, Gill J, Utterback TR, McDonald LA, Feldblyum TV, Smith HO, Venter JC, Nealson KH, Fraser, CM. Genome sequence of the dissimilatory metal ion-reducing bacterium *Shewanella oneidensis*. Nat Biotechnol 2002; 20: 1118-1123.

Jiang JK, Oberdorster G, Biswas P. Characterization of size, surface charge, and agglomeration state of nanoparticle dispersions for toxicological studies..J Nanopart Res 2009; 11: 77-89.

Jiang X, Dausend J, Hafner M, Musyanovych A, Rocker C, Landfester K, Mailander V, Nienhaus GU,. Specific effects of surface amines on polystyrene nanoparticles in their interactions with mesenchymal stem cells. Biomacromolecules 2010; 11:748-753.

Marciano FR, Lima-Oliveira DA, Da-Silva NS, Diniz AV, Corat EJ, Trava-Airoldi VJ. Antibacterial activity of DLC films containing TiO_2 nanoparticles. J Colloid Interface Sci 2009; 340: 87-92.

Matsunaga T, Okochi M. TiO_2-mediated photochemical disinfection of *Escherichia coli* using optical fibers. Environ Sci Technol 1995; 29: 501-505.

Monier JM, Lindow SE. Differential survival of solitary and aggregated bacterial cells promotes aggregate formation on leaf surfaces. Proc Natl Acad Sci USA 2003; 100: 15977-15982.

Namiki N, Cho K, Fraundorf P, Biswas P. Tubular Reactor Synthesis of Doped Nanostructured Titanium Dioxide and Its Enhanced Activation by Coronas and Soft X-rays. Ind Engr Chem Res 2005; 44: 5213-5220.

Qiu X, Sundin GW, Chai B, Tiedje JM. Survival of *Shewanella oneidensis* MR-1 after UV radiation exposure. Appl Environ Microbiol 2004; 70: 6435-6443.

Qiu X, Sundin GW, Wu L, Zhou J, Tiedje JM. Comparative analysis of differentially expressed genes in *Shewanella oneidensis* MR-1 following exposure to UVC, UVB, and UVA radiation. J Bacteriol 2005a; 187: 3556-3564.

Qiu X, Tiedje JM, Sundin GW. Genome-wide examination of the natural solar radiation response in *Shewanella oneidensis* MR-1. Photochem Photobiol 2005b; 81: 1559-1568.

Rawat J, Rana S, Srivastava R, Misra RDK. Antimicrobial activity of composite nanoparticles consisting of titania photocatalytic shell and nickel ferrite magnetic core. Mater Sci Eng C 2007; 27: 540-545.

Suresh AK, Pelletier DA, Wang W, Moon JW, Gu B, Mortensen NP, Allison DP, Joy DC, Phelps TJ, Doktycz MJ. Silver Nanocrystallites: Biofabrication using *Shewanella oneidensis*, and an Evaluation of Their Comparative Toxicity on Gram-negative and Gram-positive Bacteria. Environ Sci Technol 2010; 44: 5210-5215.

Tang YJ, Hwang JS, Wemmer DE, Keasling JD. *Shewanella oneidensis* MR-1 fluxome under various oxygen conditions. Appl Environ Microbiol 2007; 73: 718-729.

Wang J, Tafen de N, Lewis JP, Hong Z, Manivannan A, Zhi M, Li M, Wu N. Origin of photocatalytic activity of nitrogen-doped TiO_2 nanobelts. J Am Chem Soc 2009; 131: 12290-12297.

Wu B, Huang R, Sahu M, Feng X, Biswas P, Tang YJ. Bacterial responses to Cu-doped TiO_2 nanoparticles. Sci Total Environ 2010a; 408: 1755-1758.

Wu B, Wang Y, Lee Y-H, Horst A, Wang Z, Chen DR, Sureshkumar R, Tang YJ. Comparative Eco-toxicities of Nano-ZnO Particles under Aquatic and Aerosol Exposure Modes. Environ Sci.Technol 2010b; 44: 1484-1489.

Wu B, Zhang B, Feng X, Rubens JR, Huang R, Hicks LM, Pakrasi HB, Tang YJ. Alternative isoleucine synthesis pathway in cyanobacterial species. Microbiology 2010c; 156: 596-602.

Xie B, Xu Z, Guo W, Li Q. Impact of natural organic matter on the physicochemical properties of aqueous C_{60} nanoparticles. Environ Sci Technol 2008; 42: 2853-2859.

Yang K, Lin D, Xing B. Interactions of Humic Acid with Nanosized Inorganic Oxides. Langmuir 2009; 25 (6): 3571-3576.

Zhang Y, Chen Y, Westerhoff P, Crittenden J. Impact of natural organic matter and divalent cations on the stability of aqueous nanoparticles. Water Res 2009; 43: 4249-4257.

Appendix C:

Chemical Compositions and Source Identification of $PM_{2.5}$ Aerosols for Estimation of a Diesel Source Surrogate

The results presented here were published in:

Sahu, M, S. Hu, P. Ryan, G. LeMasters, S. Grinshpun, J. Chow, and P. Biswas, *Chemical Compositions and Source Identification of $PM_{2.5}$ Aerosols for Estimation of a Diesel Source Surrogate,* Science of the Total Environment, 2011, 409 (13): p 2642-2651.

C.1.Abstract

Exposure to traffic-related pollution during childhood has been associated with asthma exacerbation, and asthma incidence. The objective of the Cincinnati Childhood Allergy and Air Pollution Study (CCAAPS) is to determine if the development of allergic and respiratory disease is associated with exposure to diesel engine exhaust particles. A detailed receptor model analyses was undertaken by applying positive matrix factorization (PMF) and UNMIX receptor models to two $PM_{2.5}$ data sets: one consisting of two carbon fractions and the other of eight temperature-resolved carbon fractions. Based on the source profiles resolved from the analyses, markers of traffic related air pollution were estimated: the elemental carbon attributed to traffic (ECAT) and elemental carbon attributed to diesel vehicle emission (ECAD).

Application of UNMIX to the two data sets generated four source factors: combustion related sulfate, traffic, metal processing and soil/crustal. The PMF application generated six source factors derived from analyzing two carbon fractions and seven factors from temperature-resolved eight carbon fractions. The source factors (with source contribution estimates by mass concentrations in parentheses) are: combustion sulfate (46.8%), vegetative burning (15.8%), secondary sulfate (12.9%), diesel vehicle emission (10.9%), metal processing (7.5%), gasoline vehicle emission (5.6%) and soil/crustal (0.7%). Diesel and gasoline vehicle emission sources were separated using eight temperature-resolved organic and elemental carbon fractions. Application of PMF to both datasets also differentiated the sulfate rich source from the vegetative burning source, which are combined in a single factor by UNMIX modeling. Calculated ECAT and ECAD values at different locations indicated that traffic source impacts depend on factors such as

traffic volumes, meteorological parameters, and the mode of vehicle operation apart from the proximity of the sites to highways. The difference in ECAT and ECAD, however, was less than one standard deviation. Thus, a cost benefit consideration should be used when deciding on the benefits of an eight or two carbon approach.

Keywords: $PM_{2.5}$, Receptor modeling, Diesel exhaust, gasoline exhaust, elemental carbon, organic carbon.

C.2. Introduction

Exposure to traffic-related particles during childhood has been shown to exacerbate existing asthma including decreased lung function (Trenga et al., 2006), emergency department visits (Sun et al., 2005), wheezing in early infancy and childhood (Ryan et al. 2007, 2009) and medication use (Schildcrout et al., 2006). Recently, Jerrett et al. (2008) demonstrated an association between exposure to traffic-related pollution and the development of asthma. Traffic-related sources represented by vehicular exhaust, contribute a major fraction to total ambient PM (Chow et al., 2007; Shi et al., 1999; Watson et al., 2008) and are comprised of metals, organic polycyclic aromatic hydrocarbons (PAH), secondary sulfate and nitrate, and elemental and organic carbon (EC and OC, respectively) (Hetland et al., 2005; Wichmann, 2007). Particles arising from traffic sources are of particular interest because of size (primarily fine, $PM_{2.5}$, and ultrafine, $PM_{0.1}$), chemical composition, and shape (morphology). The characteristics of traffic-originated particles enable them to penetrate the upper and lower airways and translocate to other tissues including the brain (Kreyling et al., 2002). Approximately 92% of diesel engine exhaust particulates (DEP) by mass concentration are within the ultrafine size range resulting in high particle density concentrations that reach and deposit in the nasal and peripheral airways upon inhalation (EPA, 2002). Inhalation of DEP generates reactive oxygen species (ROS), inducing oxidative stress on nasal mucosal and bronchial epithelial cells leading to increased mucus production, disruption of the respiratory epithelial barrier and increased airway hyper responsiveness (Riedl and Diaz-Sanchez, 2005). DEP also possess immune adjuvant properties capable of enhancing local nasal production of allergic cytokines and specific IgE responses (e.g., IL-4) to

inhaled aeroallergens, particularly in the nasal airway (Pandya et al., 2002). Recently, studies have suggested that particles arising from gasoline combustion may demonstrate similar toxicity to DEP (Seagrave et al., 2002).

The objective of the Cincinnati Childhood Allergy and Air Pollution Study (CCAAPS), a longitudinal birth cohort study, is to determine if exposure to DEP during infancy and early childhood is associated with the development of allergic disease and asthma (Martuzevicius et al., 2004). In order to examine the relationship between exposure to traffic-related air pollutants and health effects in the CCAAPS cohort, a land-use regression (LUR) model was developed. This LUR model utilized a marker of traffic-related particles thought to be dominated by DEP (Ryan et al., 2007; Ryan et al., 2008), the fraction of elemental carbon attributable to traffic (ECAT). ECAT was derived by applying two commonly used receptor modeling techniques for source apportionment to ambient data, positive matrix factorization (PMF) and UNMIX (Henry, 2003; Kim and Hopke, 2004a; Lee et al., 2006; Lewis et al., 2003; Maykut et al., 2003; Polissar et al., 2001). Hu et al. (2006) applied UNMIX receptor modeling to $PM_{2.5}$ data collected at two CCAAPS sampling sites in order to identify four possible major polluting sources: 1) combustion related sulfate sources, 2) traffic related sources, 3) metal processing industries and 4) soil/crustal sources. In the CCAAPS cohort, exposure to increased levels of ECAT during infancy was associated with wheezing prior to age one (Ryan et al. 2007). Further, children exposed to high levels of ECAT and endotoxin in their home prior to age one had greater than a five-fold increased risk for persistent wheezing at age three when compared to children exposed to low levels of ECAT and endotoxin (Ryan et

al., 2009). Sucharew et al. (2010) reported that traffic exhaust exposure (quantified by ECAT) may be a risk factor for night cough in young children.

More recently, source sampling of diesel and gasoline vehicular emissions and subsequent analysis of the carbon fractions by the temperature resolved thermal optical method indicates that gasoline and diesel sources can be differentiated based on the abundance of individual carbon sub fractions (Cao et al., 2006; Chow et al., 2004; Watson et al., 1994). OC and EC fractions and the organic pyrolyzed organic carbon (OPTRC) are measured at different temperature steps. PMF receptor modeling analysis using temperature resolved eight carbon fractions for $PM_{2.5}$ data from Seattle, WA (Maykut et al., 2003), Atlanta, GA (Kim et al., 2004), Washington, DC (Kim and Hopke, 2004b), Georgia and Alabama (Liu et al., 2006), and St. Louis (Lee et al., 2006) illustrated that diesel and gasoline vehicle sources can be delineated.

The objective of this study was to improve the identification of source contributions by differentiating gasoline and diesel vehicle emissions using temperature resolved eight carbon fractions. In addition, the potential for combining the sampling data obtained at different sites into one dataset for source apportionment when the sampling sites are in close proximity was examined. UNMIX and PMF are applied to the same dataset containing only EC and OC carbon fractions estimated by the NIOSH method. In addition, UNMIX and PMF are applied to eight temperature resolved carbon fractions estimated by the IMPROVE protocol (Chow et al., 1993). The major sources identified by both modeling techniques are compared. The EC attributed to individual traffic sources (diesel and gasoline) is derived based on the resolved sources from the receptor modeling.

C.3. Materials and Methods

C.3.1. Ambient $PM_{2.5}$ sampling and chemical analysis methods

For the epidemiological study undertaken in the Greater Cincinnati area, sampling was conducted at 24 sites of the CCAAPS network (Figure C-1). Details regarding the monitoring sites can be found in previous publications (Hu, 2007; Hu et al., 2006). Ambient data obtained at eleven selected sites between 2002 and 2006 were utilized for this analysis. These extensive data base provides more representative source profiles and contributions than modeling conducted with a few datasets.

Twenty-four hour integrated ambient air sampling was conducted nominally from 0900 am to 0900 pm (+1 day). 37-mm Teflon-membrane filters (nominal pore size = 1 μm) (Pall Corporation) and 37-mm quartz-filters (Whatman Inc) with Harvard-type impactors (Air Diagnostics and Engineering Inc.) were used for collecting $PM_{2.5}$ samples. Teflon filters were conditioned at a temperature of 22-24^{o}C with a humidity of 30-40 % for at least 24 hours for temperature and humidity equilibration at Washington University in St. Louis (Hu et al, 2006). The difference in weight of the filter samples after sampling and before sampling were used to determine the $PM_{2.5}$ mass concentrations. X-ray fluorescence (XRF) technique was used to analyze the Teflon filters for ambient elemental concentrations (Chester Labnet). A total of 39 elements were analyzed and 15 chemical species (Al, Si, S, K, Ca, Ti, Cr, Mn, Fe, Ni, Cu, Zn, Se, Br, Pb) were consistently present in the analyzed samples (Hu et al., 2006). More details regarding the advantage of XRF elemental measurements, quality control, and comparison with other methods can be found in our previous studies (Reponen et al., 2003; Martuzevicius et al., 2004). The detailed sampling procedure and analytical methods adopted for the

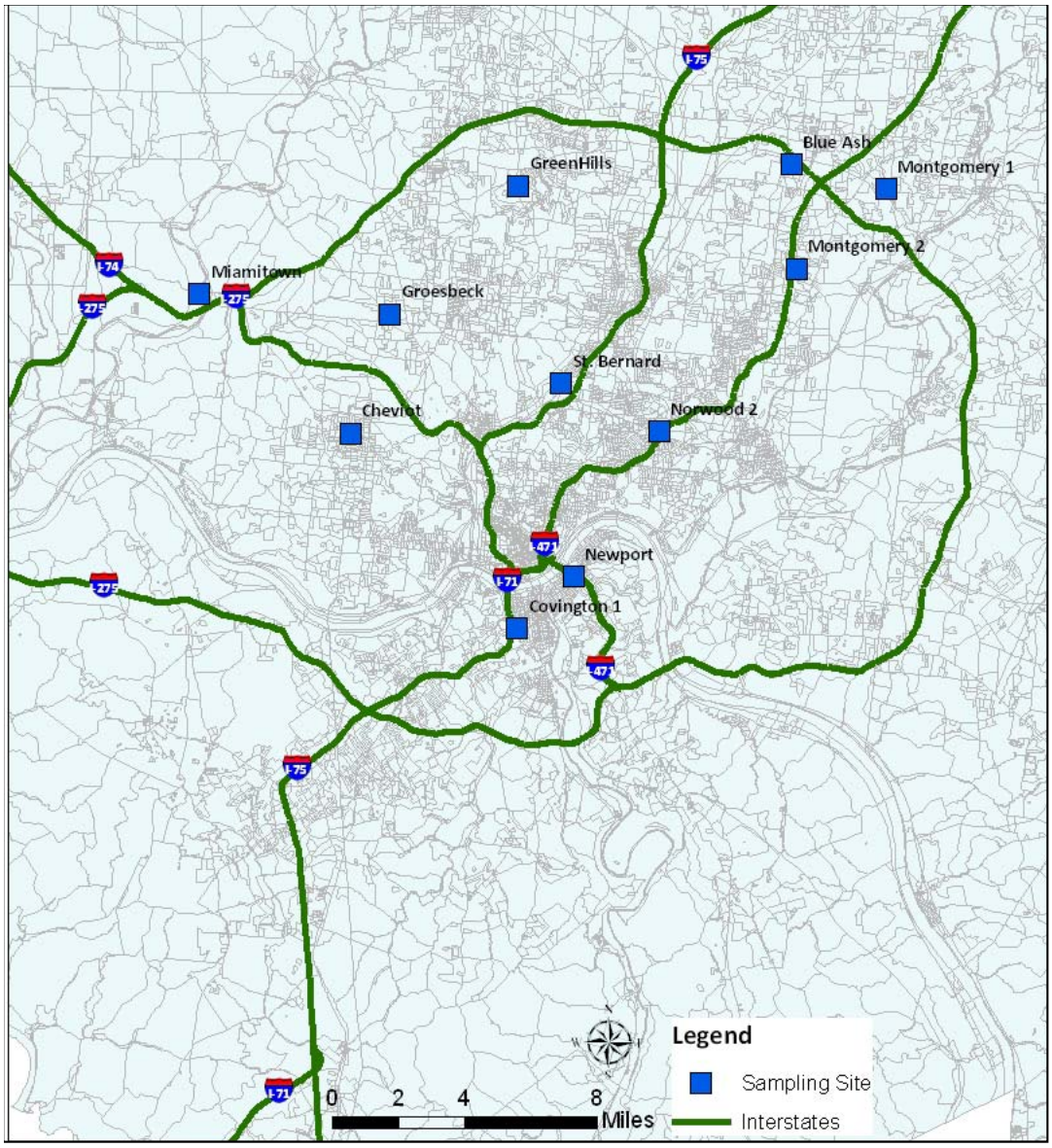

Figure C- 1: Schematic diagram of the sampling locations (11 Cincinnati Childhood Allergy and Air Pollution Study (CCAAPS) sampling sites). Abbreviation of the sampling locations is given below

. (Blue Ash (BLU), Brighton (BRI), Cheviot (CHE), Covington 1(COV1), Green Hills (GRE), Groesbeck (GRO), Montogomery 1(MON1), Montgomery 2(MON2), Newport (NEW), Norwood 2 (NOR2), St. Bernard (STB). CCAAPS network sampling sites are described elsewhere (Hu, 2007; Martuzevicius et al., 2004).

CCAAPS network sampling sites are described elsewhere (Hu, 2007; Martuzevicius et al., 2004).

The quartz filters were sectioned into two halves to measure the carbon fractions. The first half of the filters was analyzed by the thermal optical transmittance (TOT) technique using the NIOSH-5040 method (Birch and Cary, 1996) to determine EC and OC concentrations (Sunset Lab). The other half was frozen, preserved, and then analyzed by the Interagency Monitoring of Protected Visual Environments (IMPROVE) thermal optical reflectance (TOR) protocol (Chow et al., 1993) for eight temperature resolved carbon fractions (Desert Research Institute). According to this protocol, OC fractions are measured at four different temperature steps: O1TC at 120 °C, O2TC at 250 °C, O3TC at 450 °C, and O4TC at 550 °C in 100 % helium (He) atmosphere. The three EC fractions were measured in a mixture of 2% oxygen/98% He: E1TC at 550 °C, E2TC at 700 °C, and E3TC at 800 °C. Pyrolyzed carbon (OPTRC) was determined based on the laser response (laser reflectance is monitored until it returned to its initial value). In IMPROVE method, EC1 measurement includes OPTRC. In this study, OPTRC has been subtracted from the EC1 before using as an independent variable in the modeling. The detailed analysis procedure for the eight carbon fractions has been described in Chow et al. (2007) and Chow et al. (1993). The total carbon was estimated by this method as TC= OC (O1TC + O2TC + O3TC + O4TC + OPTRC) + EC (E1TC + E2TC + E3TC). In this study, 203 samples were used for which both the EC and OC concentration measurements and eight carbon fraction measurements were available. To directly compare the source estimates from the model, sampling data sets with samples having

both carbon fractions and temperature resolved eight carbon fraction measurements were used.

Data from all the sampling stations were combined to form large datasets, which is a step forward from the earlier receptor modeling study that relied on a few samples collected at the CCAAPS sampling sites (Hu et al., 2006). The CCAAPS sampling sites are very closely located within a dimension of 35 km × 40 km. The pollutants from any local source will have a fair chance to have potential impact on receptors anywhere within the CCAAPS sampling network, during the 24-h sampling period. The relative strength of the impact on an individual receptor is dependent on the proximity of that receptor to the source, but the source profiles will be the same for different receptors. However, combining the data from all the sites into one dataset may produce higher uncertainties in model predictions.

C.4. Model Description and Calculation

Receptor modeling assumes mass conservation to apportion different source categories for ambient particulate matter. It can be explained in general terms as the impact of N independent sources on the receptor site for all chemical species in a given sample:

$$x_{ij} = \sum_{k=1}^{N} g_{ik} f_{kj} + \varepsilon_{ij} \qquad (1)$$

where x_{ij} is the j^{th} species concentration measured in the i^{th} sample, g_{ik} is the particulate mass concentration from the k^{th} source contributing to the i^{th} sample. f_{kj} is the j^{th} species mass fraction in the k^{th} source and ε_{ij} is the error estimate.

UNMIX (Henry, 2003) and PMF (Maykut et al., 2003; Paatero, 1997; Polissar et al., 2001) provide solution to equation (1) based on two different mathematical approaches.

UNMIX determines the edges in the dataset. The number and direction of the edges depends on the number of species chosen for the UNMIX model. UNMIX incorporates the algorithm "NUMFACT" that estimates the number of factors in the data using principal component analysis on randomly sampled subsets of the original data (Henry, 2003). PMF derives a solution that minimizes an object function, *Q*, which is determined based on the uncertainties associated with individual measured data, subject to nonnegative constraints (Polissar et al., 2001). The objective function is defined as:

$$Q = \sum_{i}^{n} \sum_{k=1}^{m} \left[\frac{x_{ik} - \sum_{k=1}^{N} g_{ik} \times f_{kj}}{\sigma_{ij}} \right]^2 \qquad (2)$$

where σ_{ij} is an uncertainty estimate in the j^{th} species measured in the i^{th} sample. A PMF solution is not as sensitive as UNMIX to the choice of input species. The combined dataset has been analyzed by both UNMIX (EPA UNMIX 6.0) and PMF (EPA PMF 3.0) to identify the source profiles and contributions. Details about both UNMIX and PMF modeling techniques can be found in the literature (Henry, 2003; Paatero, 1997).

Some of the key aspects of the receptor modeling approach are post processing of the datasets, identifying the outliers in the datasets, and assigning uncertainty to the measured species, all of which influence the modeling results. For UNMIX modeling, species having a signal/noise ratio greater than 2 and a minimum R^2 of 0.8 were used to filter the sources. For initial runs, good edge species obtained by plotting the $PM_{2.5}$ mass versus species concentration were chosen to find minimum possible solution (Henry, 2003; Hu et al., 2006). Additional species were included to test the stability of the solution and determine if this measure could enhance the identification of sources with respect to the number and resolution. For datasets consisting of two carbon fractions, species chosen

for the model runs were, EC, OC, Al, Si, S, Fe, Cu, Zn, Ca, Se, Pb, Ti, and Ca. For datasets consisting of eight carbon fractions species chosen were O1TC, O2TC, O3TC, O4TC, OPTRC and E1TC in place of EC and OC fractions. However, with the addition of the E2TC and E3TC fractions, feasible solutions for source profiles could not be found. For the chosen four source factor solutions, the minimum R^2=0.82 and signal/noise ratio was 3.31 for the eight temperature resolved carbon fractions, and R^2=0.84 and signal/noise ratio equal to 2.73 for the two non-temperature resolved carbon fractions. When more species were added, five sources were resolved. Since many species concentrations were negative in one of the resolved profiles, a four-source solution was finally chosen for this study.

In PMF modeling, the number of factors is determined by experimenting and finding the optimal number based on the physical meaningful sources. The uncertainty values for the different species were chosen according to the values reported for the U.S EPA Speciation Trends Network (STN ; part of the Chemical Speciation Network [CSN]) (Kim et al., 2005). To minimize the influence of extreme values on the PMF solution, a robust mode was chosen in this study. Based on the signal/noise ratio of the species, values less than 1.5 were qualified as weak. For some of the species, O1TC, OPTRC and E1TC were assigned higher uncertainty because of the uncertainty associated with their measurements (Kim and Hopke, 2004b; Kim et al., 2004). The resulting PMF source profiles were derived based on trial and error evaluation of the solutions.

C.5. Results and Discussion

C.5.1.1. Ambient $PM_{2.5}$ concentration

The $PM_{2.5}$ and elemental concentrations differed between sampling sites. The locations near interstate highways, the main pathway for heavy diesel vehicles, showed higher levels of EC and traffic-related elements such as Fe, Cu, Mn, Pb, Al and Si. The average $PM_{2.5}$ concentration ranged from 12.6 ±5.1 $\mu g/m^3$ at Groesbeck to 24.2±19.5 $\mu g/m^3$ at Newport. The major reason for variation is the site location. The Newport site is located in the downtown area which is very close to I-471 while the Groesbeck site is in suburban area within 400 m from the Ronald Reagan highway. The average $PM_{2.5}$ concentrations as well as the concentrations of metals are presented in Table C-1 for all the sampling locations. Overall, a lower spatial variation in $PM_{2.5}$ (CV=21%) was observed throughout the sampling periods. Martuzevicius et al. (2004) measured the spatial and temporal variation of the $PM_{2.5}$ concentration and composition at 11 locations of CCAAPS during the field campaign from December 2001 to November 2002 and found very little variation in $PM_{2.5}$, which is consistent with the observations of this study. However, the temporal variations in $PM_{2.5}$ concentration observed at specific sites in this study were relatively high with the coefficient of variation ranging from 26% to 80%. The low overall variation in $PM_{2.5}$ concentration may be due to high temporal variation in $PM_{2.5}$, and indicates the contribution of regional sources and long range atmospheric transport of the fine particulate matter (Gehrig and Buchmann, 2003; Martuzevicius et al., 2004). The concentration was greater at city centers than in suburban and rural areas, which likely resulted from the merger of interstate highways and increased traffic near the city.

C. 5.1.2. Elemental composition of ambient PM2.5

As many as 39 elements were analyzed by XRF. Table C-1 sumarizes the results obtained after blank were substracted for the elements, which were present in significant amounts and/or served as markers for relevant sources. Among crustal element concentrations, the average *aluminum* varied from 14.1±13.2 to 84.3 ±67.5 ng/m^3, *silicon* from 34.2±42.4 to 290.7±265.2 ng/m^3, and *calcium* from 32.9±61.8 to 306.1±358.6 ng/m^3; all with the lowest levels at Blue Ash and the highest at St. Bernard.

Among traffic source elemental concentrations, *iron* varied from 56.6±57.0 ng/m^3 (Blue Ash) to 302.9 ±316.5 ng/m^3 (St. Bernard), and *zinc* varied from 12.6±7.9 ng/m^3 (Montogomery2) to 65.9±111.0 ng/m^3 (Bridgeton). The relative abundance of different trace elements varied depending on the locations and relative impact of the local pollution sources. Calcium, silicon and iron concentrations were relatively higher at Brighton, St. Bernard and Newport compared to other locations. The relatively higher variation in the trace elements compared to $PM_{2.5}$ indicates that these elements originated mostly from local pollution sources. The concentration of sulfur ranged from 946.3±294.4 ng/m^3 (St. Bernard) to 2257.6±1389.3 ng/m^3 (Covington1). Sulfur showed the highest concentration among all the elements analyzed and varied with season, which is likely due to the impact of 14 coal fired plants located along the Ohio River Valley and secondary sulfate conversion.

Table C- 1: Average $PM_{2.5}$ concentrations and its elemental compositions of samples collected at different sites (No of samples at each site is in the braket)

Sampling site	$PM_{2.5}$ Concentration ($\mu g/m^3$)	Elemental Composition of $PM_{2.5}$ (ng/m^3)										
		EC ($\mu g/ m^3$)	OC ($\mu g/m^3$)	Na	Al	K	Ca	Si	Fe	Zn	S	Other metals
Brighton (29)	17.7± 8.5	1.2± 0.7	3.5± 1.9	54.6± 51.2	60.1± 121.9	69.1± 36.5	138.5± 86.3	168.2± 242.2	181.1± 124.9	65.9± 111.1	1358.10± 895.9	70.9± 44.1
Cheviot (35)	18.4± 9.8	0.5± 0.3	3.3± 1.6	39.8± 35.8	48.7± 87.0	69.2± 58.2	64.3± 35.8	118.9± 174.9	89.7± 59.1	14.3± 8.2	2035.8± 1456.9	44.6± 21.2
Montgomery 1 (20)	16.4±10.7	0.4± 0.2	3.3± 1.6	33.6± 42.1	30.1± 25.9	67.8± 42.8	46.7± 22.9	65.9± 42.3	70.2± 34.7	15.9± 14.6	1515.3± 1121.1	38.9± 22.1
Covington 1 (21)	23.2±10.5	0.9± 0.5	4.8± 1.4	78.5± 102.2	31.1± 18.1	60.7± 24.7	78.7± 36.0	91.1± 40.2	133.5± 79.0	12.8± 5.7	2257.6± 1389.3	50.7± 20.3
Norwood 2 (33)	19.8±9.4	0.8± 0.5	4.0± 1.6	46.4± 49.2	48.4± 27.6	71.5± 31.4	88.8± 54.8	118.9± 71.7	148.0± 85.3	33.0± 21.1	1589.1± 1054.7	57.1± 20.9
Montgomery 2 (12)	13.2±5.2	0.4± 0.2	2.5± 1.3	40.1± 29.3	26.2± 23.1	52.0± 9.8	52.5±25.8	60.9± 33.8	73.0± 50.6	12.6± 7.9	1301.0± 740.4	32.8± 7.7
Newport (9)	24.2±19.5	0.5± 0.2	3.0± 0.6	139.2± 241.8	30.0± 13.2	73.9± 29.5	115.5± 61.8	105.2± 42.4	140.1± 57.0	18.6± 9.8	1369.4± 760.8	87.8± 132.9
Blue Ash (10)	14.2±3.9	0.3± 0.1	1.6± 0.8	27.3± 241.8	14.1± 13.2	44.0± 29.5	32.9± 61.8	34.2± 42.4	56.6± 57.0	30.7± 9.8	1204.4± 760.8	28.9± 132.9
Green Hills (15)	15.8± 8.1	0.3± 0.2	2.3± 1.3	38.1± 40.1	30.6± 23.1	55.4± 23.0	43.8± 27.4	69.9±46.8	59.1± 27.8	13.2± 7.1	1647.0± 1177.5	29.9± 14.2
St. Bernard (10)	15.4± 7.3	1.3± 0.8	4.1± 2.8	71.4± 65.3	84.4± 67.5	84.9± 61.2	306.1± 358.6	290.7± 265.2	302.9± 316.5	37.0± 25.4	946.3± 294.4	97.8± 81.4
Groesbeck (9)	12.6± 5.1	0.4± 0.1	2.6± 1.0	37.5± 21.8	24.2± 10.7	52.5± 19.1	58.5± 18.9	78.1± 32.1	65.7± 34.4	13.5± 9.6	1079.5± 792.8	32.6± 8.5

C.5.1.3. Elemental and organic carbon fractions

Elemental and organic carbon fractions of the measured $PM_{2.5}$ serve as markers for diesel and gasoline engine emissions. Temperature-programmed elemental and organic carbons were measured according to the IMPROVE-TOR and the NIOSH5040-TOT methods to compare results for diesel and gasoline vehicular emissions (Chow et al., 2001; Chow et al., 1993). The concentrations of the elemental and organic carbon fractions as well as

Table C- 2: Elemental and organic carbon concentrations of samples collected at different sites

Sampling site	NIOSH METHOD[a]			IMPROVE METHOD[b]		
	EC (µg/m^3)	OC (µg/m$^{3)}$	EC/OC	EC (µg/m^3)	OC (µg/m^3)	EC/OC
Brighton	1.2±0.7	3.5±1.9	0.33	1.4±0.9	2.8±1.3	0.50
Cheviot	0.5±0.3	3.3±1.6	0.15	0.8±0.5	2.6±1.1	0.29
Montgomery 1	0.4±0.2	3.3±1.6	0.13	0.7±0.5	2.5±1.1	0.30
Covington 1	1.0±0.5	4.8±1.4	0.20	1.7±0.8	3.4±0.9	0.51
Norwood 2	0.8±0.5	4.0±1.6	0.19	1.3±0.7	3.1±1.2	0.41
Montgomery 2	0.4±0.2	2.5±1.3	0.14	0.7±0.4	2.4±1.2	0.29
Newport	0.5±0.2	3.0±0.6	0.15	0.7±0.2	3.0±0.9	0.24
Blue Ash	0.3±0.1	1.6±0.8	0.18	0.5±0.3	1.2±0.6	0.38
Green Hills	0.3±0.2	2.3±1.3	0.15	0.5±0.3	2.0±1.2	0.26
St. Bernard	1.3±0.8	4.9±2.9	0.26	2.1±1.5	3.2±2.0	0.63
Groesbeck	0.4±0.1	2.6±1.0	0.15	0.5±0.2	2.2±1.0	0.23

[a] NIOSH-5040 method (Birch and Cary, 1996)

[b] IMPROVE temperature protocol (Chow et al., 1993)

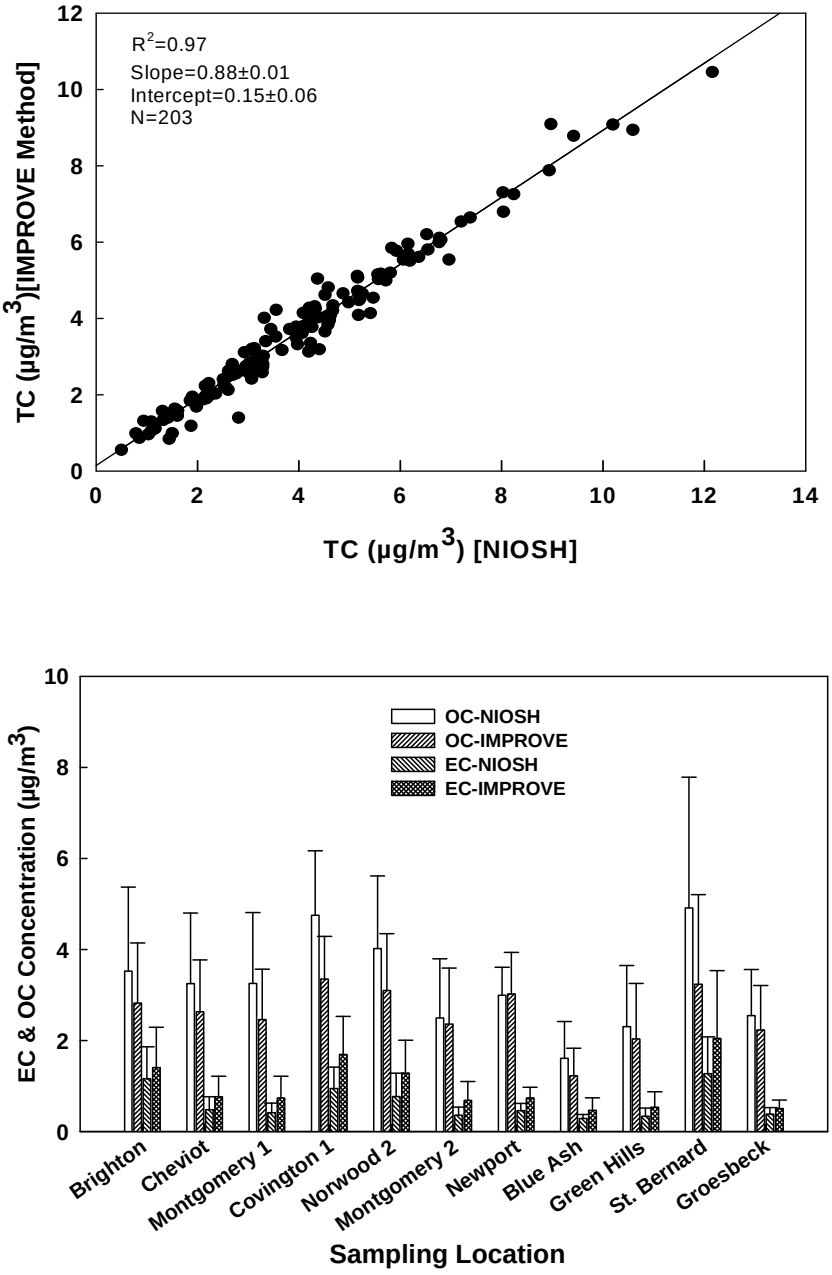

Figure C-2:(A) Correlation between TC estimated from NIOSH method and IMPROVES methodologies. (B) EC and OC variation at different sampling locations estimated from NIOSH and IMPROVE method

the EC/OC ratios are presented in Table C-2. EC concentrations ranged from 0.3±0.1 $\mu g/m^3$ (Blue Ash) to 1.3±0. 8 $\mu g/m^3$ (St. Bernard) and OC concentrations ranged from 1.6±0.8 (Blue Ash) to 4.9±2.9 $\mu g/m^3$ (St. Bernard), as determined with NIOSH-TOT. However, the IMPROVE-TOR method revealed different EC and OC concentration ranges: 0.5±0.3 to 2.1±1.5 $\mu g/m^3$ and 1.2±0.6 to 3.2±1.0 $\mu g/m^3$ respectively. Differences between the two methods are due to greater influence from charring of organic vapors adsorbed within the quartz-fiber filters on TOT compared to TOR (Chow et al., 2004) . However, the TC measured by both methods correlated very well (r^2=0.97), as shown in Figure C-2. The EC/OC ratio varied from 0.1 to 0.3 (NIOSH method) and 0.2 to 0.6 (IMPROVE method). The higher EC/OC ratio observed at St. Bernard and Brighton. The St. Bernard site located near a major industrial area and a school bus depot; it was also within 400 m from interstate highway I-75, whereas the Brighton site located in the downtown area and close to interstate highway I-75. Different EC/OC ratios reflect the degree of impact of traffic sources on the sampling locations. Certain fractions of EC and OC are rich in diesel and gasoline emissions compared to contributions from other sources, which provides signatures for understanding the difference between traffic sources (Cao et al., 2006; Watson et al., 1994). This difference is discussed in section 4.2.3 in association with the modeling results.

C.5.2. Results from UNMIX and PMF Modeling

C.5.2.1. Identified source profiles

Four factors were derived by UNMIX using both EC and OC fractions obtained with the NIOSH method and IMPROVE temperature-resolved eight carbon fractions. The major source factors derived from UNMIX, based on relative contributions included: combustion related sulfate source (61.9%), traffic source (23.5%), metal processing (11.2%) and soil /crustal source (3.9%). The relative contributions derived from the UNMIX evaluated with eight carbon fractions were similar except for traffic sources (Table C-3). PMF identified six sources using two carbon fractions, but could not clearly separate diesel emission source and gasoline vehicle sources. PMF using temperature resolved eight carbon fractions resolved seven sources with clear separation between individual traffic sources. PMF also identified two sulfate sources and one vegetative burning source; whereas these sources were regrouped into one source in UNMIX modeling. The major factors and source estimates derived by PMF are as follows: combustion sulfate (46.8%), vegetative/wood burning (15.8%), metal processing (7.5%), secondary sulfate (12.9%), soil/crustal (0.7%) diesel vehicle emission (10.9%) and gasoline vehicle emission (5.6%). Brief explanations of the derived source profiles by PMF are given below.

Table C- 3: Average source contribution (%) to PM2.5 estimated from the UNMIX and PMF models

Source	UNMIX with two carbon fractions	UNMIX with eight carbon fractions	PMF with two carbon fractions	PMF with eight carbon fractions
Soil/Crustal	3.9±4.1	4.3±4.6	0.6±0.4	0.7±0.4
Vegetative/wood Burning			25.3±1.7	15.7±1.0
Combustion sulfate	61.9±8.3	66.4±7.8	46.1±0.6	46.8±0.7
Secondary sulfate			10.8±1.3	12.9±0.5
Metal Processing	11.2±3.8	10.17±4.4	7.7±0.4	7.5±0.3
Diesel Vehicle				10.9±1.9
Gasoline Vehicle				5.6±1.4
Total Traffic	23.5±6.2	18.7±5.5	9.5±2.4	16.5

Sulfate source

PMF identified two sulfate related sources for both the datasets. The percentage contributions estimated by PMF were 46.1% and 10.8 % using two carbon fractions, whereas estimated contributions were 46.8% and 12.9% for datasets consisting of eight carbon fractions for combustion sulfate and secondary sulfate, respectively. These sources were characterized by relatively high concentrations of sulfur. The seasonal variation of sulfur concentrations (higher in summer and lower in winter) confirmed that the source is secondary sulfate. These two sources respectively contributed 73.8% and 11.1% to the total sulfur concentrations. Some trace elements Si, Fe, and Al are associated with the secondary sulfate source, which is consistent with previous studies (Liu et al., 2006). The sum of the contributions of both sulfate sources of 56.9% is consistent with the previously reported values of 56% for sulfate related sources (Kim et

al., 2004) and in good agreement with the contribution estimated by UNMIX modeling at the CCAAPS sampling site (Hu et al., 2006).

Traffic sources

A single traffic source was resolved by applying PMF to a dataset consisting of two carbon fractions. The signatures of this source were a relatively high abundance of EC, OC, Fe, Mn, Cu and Zn fraction. Fe, Cu, Zn are major additives to lubricating oils; Zn is also associated with other transportation activities such as brake and tire wear (Lough et al., 2005) and Mn is an additive are used to improve engine efficiency (Lewis et al., 2003). The estimated EC/OC ratios were 0.35 and 0.81 for two carbon fractions and eight carbon fractions datasets, respectively. The difference in the EC/OC ratios of the derived traffic source profile obtained using two carbon fractions and the temperature resolved eight carbon fractions may be attributed to the different amounts of EC and OC methods, which is consistent with our model results. In a source profile analysis by estimated by the two measurement protocols (the NIOSH and IMPROVE methods). This difference is consistent with our ambient analysis, in which the EC fraction estimated by IMPROVE was higher compared to the one determined with the NIOSH method and in most instances OC was lower, although the estimated TC values correlated very well (R^2=0.97). Lewis et al. (2003) observed the difference in source contribution by applying UNMIX modeling to two carbon fractions analyzed by the NIOSH and IMPROVE Watson et al. (1994), the EC/OC ratio was reported to be 0.45 for gasoline fueled vehicle exhaust, 0.83 for diesel-fueled vehicle exhaust, and 0.90 for a mixture of vehicle types in roadside tests from Phoenix, AZ.

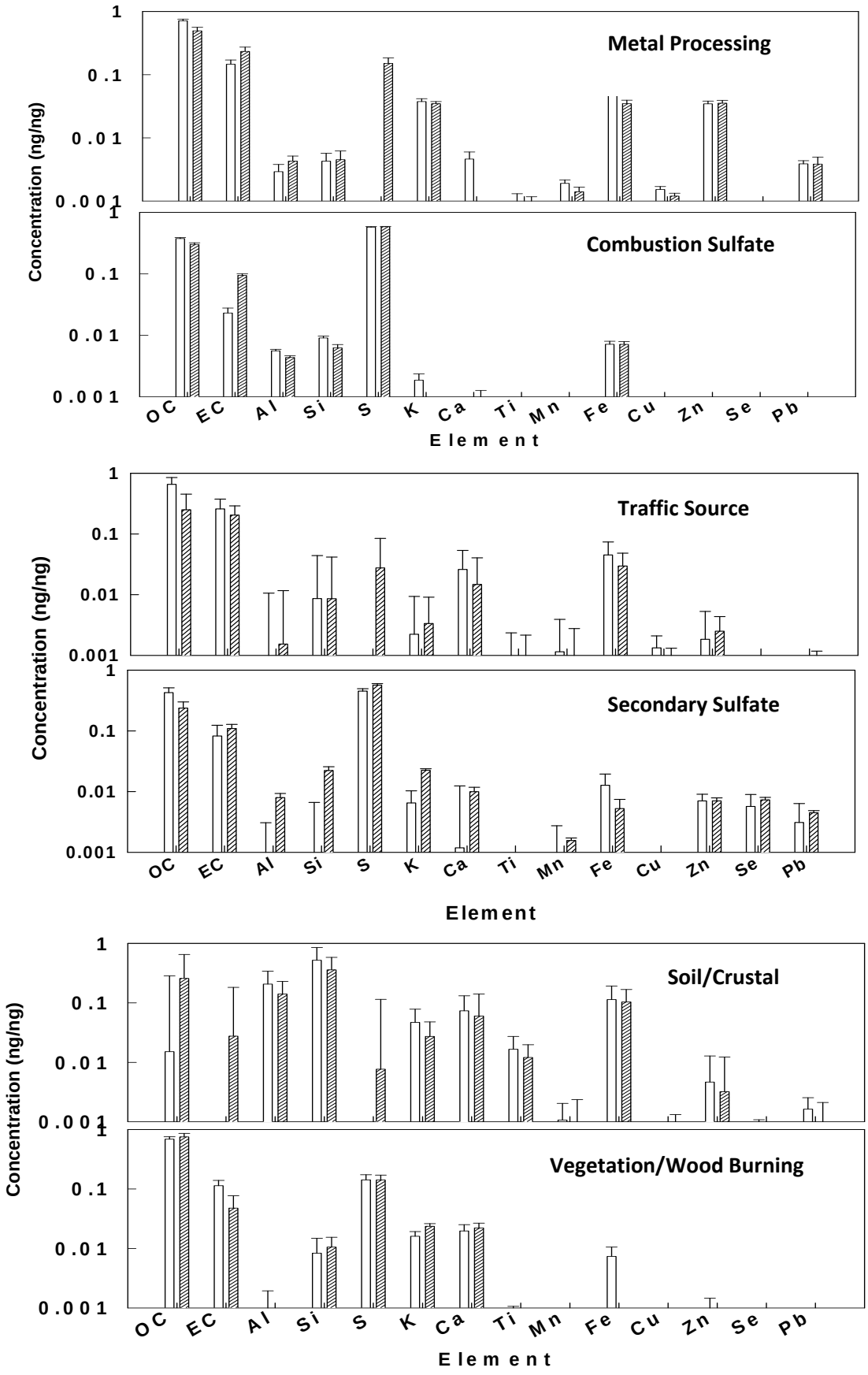

Figure C- 3: Comparison PMF derived source profiles using EC and OC carbon fraction (blank column) and temperature resolved carbon fraction (hatched column)

Cao et al. (2006) reported EC/OC ratios varying from 0.6 to 1.2 for traffic sources with an average value of 1. In this study, the EC/OC ratios were found to be 0.82 for the traffic source by using temperature resolved eight carbon fractions, which is in close agreement with Cao et al. (2006). The contributions of these two sources were 10.9% and 5.6% respectively for diesel and gasoline vehicle source. The ratio of source contribution estimates of diesel to gasoline vehicle emissions (1.95) is in good agreement with the ratio of 2.3 reported by Kim et al. (2004) at the Jefferson Street monitoring site in Atlanta. Since the E2TC and E3TC fractions present were much lower than E1TC fraction and are mostly below detection limits, the abundances of E1TC was observed in both source profiles.

Vegetative/wood burning

Vegetative burning was distinguished by high concentration of OC carbon fractions and high K. Seasonal variation for this source observed as being the highest during winter and low during summer season, confirms that the source is vegetative or wood burning. This factor contributes approximately 15.7% to the total $PM_{2.5}$ and is dominant source of potassium (45.5%).

Soil/Crustal source

This source factor has high concentrations of Si, Al, Ti, Fe, Ca and K contributing 0.7% to the total PM2.5. Crustal particles may include suspended road dust and wind-blown soil dust. The time series source contribution profiles indicated elevated air borne soil/crustal contribution during April and July, 2003 at Cheviot and Bridgeton sampling sites. The elevated soil source contribution during these periods may be caused by wind-

blown dust and Asian dust storm. Some carbon fractions were found in this source factor, suggesting some of the airborne soils are re-suspended by road traffic.

Metal processing source

Metal processing has abundances of Zn, Pb and Fe and contributes 7.5% of the ambient PM2.5 concentration and contains some amount of sulfur in its profiles. The possible reason is that there are several metal processing facilities near the CCAAPS network sampling sites (Hu et al., 2006). This source has also moderate amount of K, which is indicative of the emissions from incinerators.

Source contributions estimated by PMF using two carbon and eight carbon fractions are consistent with the major sources. The comparison of the source profiles derived from the PMF calculation is shown in Figure C-3. The source contribution estimates (Table C-3) for metal processing and traffic source by using both the data sets were different. The difference in metal processing source occurred partly because more sources were resolved using eight carbon fractions, thus effectively reducing individual source contributions. The difference in traffic source contribution may be associated with the different analytical technique adopted for EC and OC analysis as described earlier.

C.5.2.2. Comparison of source profiles derived from UNMIX and PMF

The source profiles identified from UNMIX and PMF using eight carbon fractions are compared in the Figure C-4. The larger number of sources derived from PMF modeling for identified two traffic sources, diesel and gasoline vehicular sources, which were combined to form one traffic source for comparison with UNMIX derived traffic source.

PMF also identified two additional sources, vegetative burning and secondary sulfate which were not separated in the UNMIX calculation. The traffic source contribution estimates derived were very close for the eight carbon fractions, 18.7% and 16.5% for UNMIX and PMF, respectively. PMF derived a secondary sulfate factor, sulfate source and vegetative burning source compared to a single combustion related sulfate source derived by UNMIX. Combined contribution estimates of the two sulfate sources (59.7%) is similar to the one obtained by UNMIX for combustion related sulfate source estimates (66.4%). The extra source profiles derived from PMF as vegetative burning contribute about 15.7% to $PM_{2.5}$. With seven factors derived from PMF compared to four factors by UNMIX, the crustal elements were distributed in all the sources resulting in lower contribution estimates derived by PMF for crustal source. Higher abundances of sulfur is observed in the UNMIX-derived source profiles because all the sulfur was distributed among four factors in UNMIX modeling. The major source profiles derived by both UNMIX and PMF are in good agreement and provide high confidence in the modeling results. Source contribution estimates derived from UNMIX and PMF using both two and eight carbon fractions are presented in Table C-3.

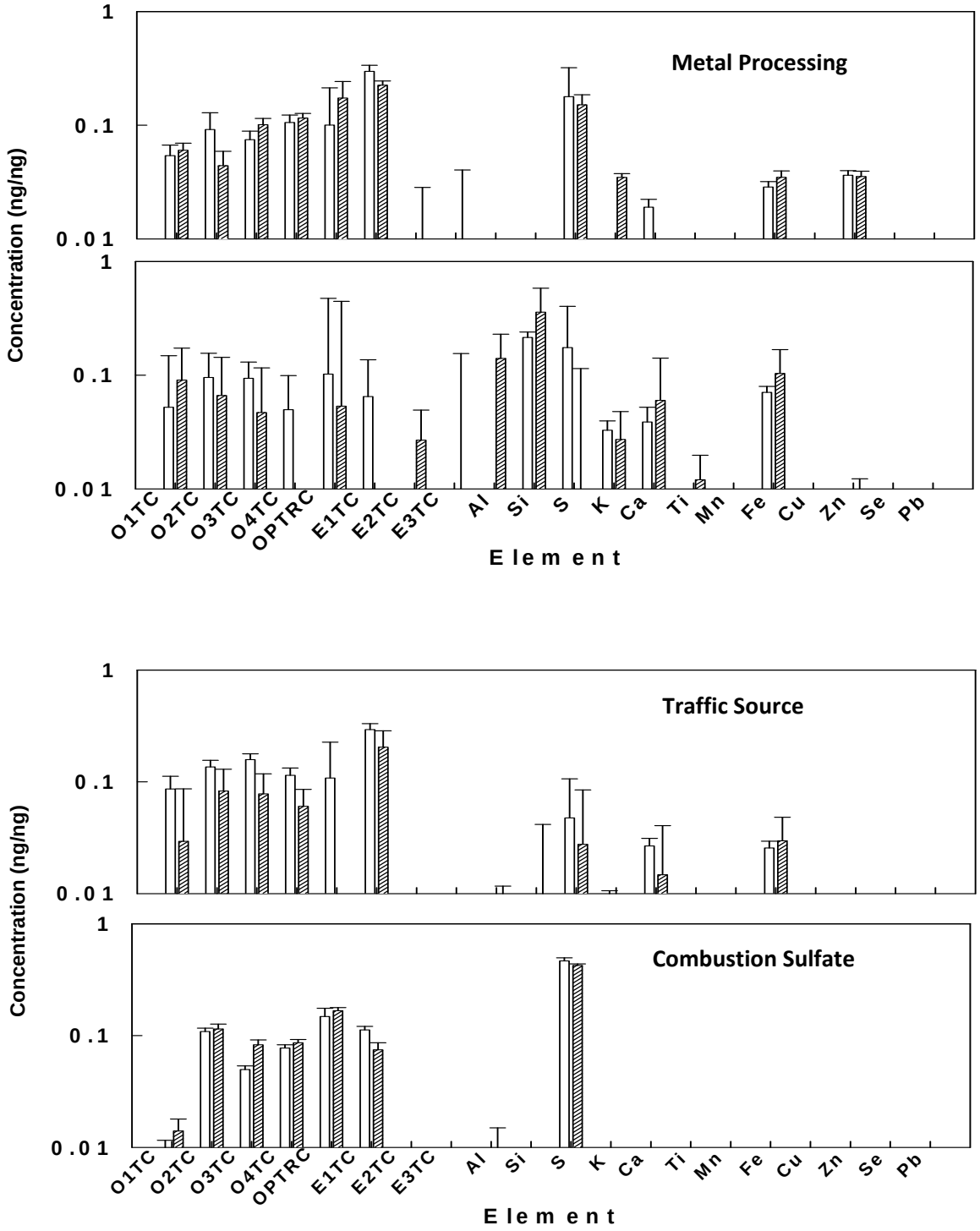

Figure C- 4: Comparison of UNMIX (blank) and PMF (hatched bar) source profiles derived from temperature resolved eight carbon fractions

(O1TC at 120 °C, O2TC at 250 °C, O3TC at 450 °C, and O4TC at 550 °C in a 100% helium (He) atmosphere. The three EC fractions were measured in a mixture of 2% oxygen/98% He: E1TC at 550 °C, E2TC at 700 °C, and E3TC at 800 °C. Pyrolyzed carbon (OPTRC) is determined based on the laser response (laser reflectance is monitored until it returns to its initial value)

C.5.2.3. Comparison of the traffic source profiles to those referred in literature

The individual EC and OC fractions attributed to gasoline and diesel emissions sources identified in this study were compared (Figure C-5) to the PMF-determined carbon

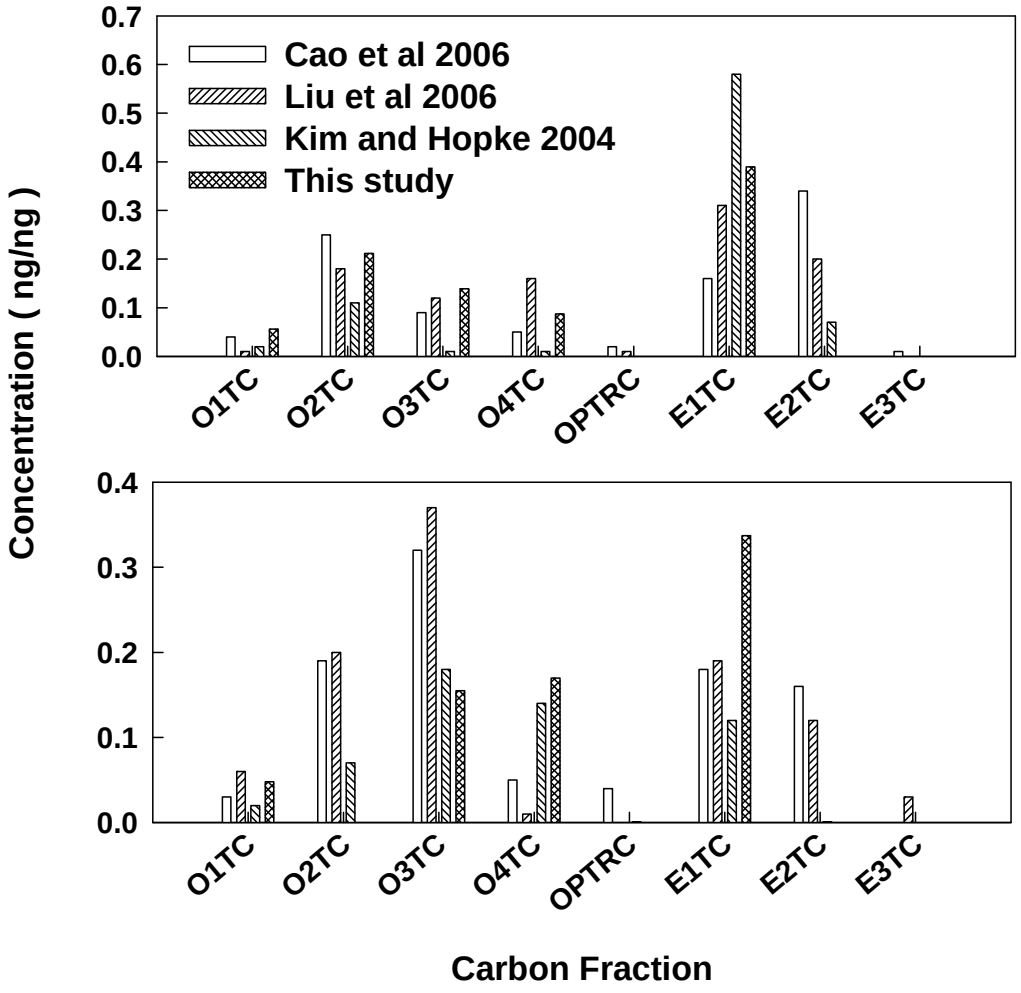

Figure C- 5:Comparison of PMF derived traffic source profiles using temperature resolved carbon fractions with literature reported values for carbon sub fractions for: (A) Diesel vehicle emissions, and (B) Gasoline vehicle emissions.. (PMF analysis for Greater Cincinnati site (this study), Urban Washington DC (Kim and Hopke, 2004), Georgia and Alabama site (Liu et al 2006), and Hong Kong, (Cao et al. 2006))

fraction reported in literature for the urban Washington DC (Kim and Hopke, 2004b), Georgia and Alabama (Liu et al., 2006), and a source sampling study performed in Hong Kong (Cao et al., 2006). The diesel vehicle source identified has high concentration of O2TC and E1TC, whereas gasoline source has high concentrations of O3TC and O4TC. This is consistent with the results reported for Washington DC and Jefferson Street in Atlanta (Kim and Hopke, 2004b; Kim et al., 2004). The source sampling study by Watson et al. (1994) found abundant E2TC and O1TC in diesel vehicle exhaust and abundant E1TC in gasoline vehicle exhaust, and Cao et al. (2006) found a greater abundance of E2TC and O2TC in diesel vehicle exhaust and abundant O3TC and O2TC in gasoline vehicle exhaust. The results qualitatively agree well with the diesel vehicle source estimated at Washington and Atlanta sites. However, large variations in the gasoline vehicle source were observed in all source apportionment studies, which is similar to the observations made by Lee et al (2006). The relatively high variations may be due to vehicles operating in stop-and-go fashion and the various intersections of interstate highways run with in the CCAAPS sampling network, since intersections create frequent traffic congestion.

C. 5.2.4. Traffic exposure ECAT and ECAD estimation

Traffic sources are the major contributor to EC and OC fractions of $PM_{2.5}$. The relative contributions estimated from PMF modeling for diesel vehicle emissions source was 10.9% compared to gasoline powered vehicle emissions of 5.6%. The elemental carbons attributed to diesel vehicle source (ECAD) and gasoline vehicle source (ECAG) were

separately calculated using the diesel vehicle and gasoline vehicle source derived from PMF. While this calculation is based on limited number of samples that may not

Table C- 4: Elemental carbon concentrations (µg / m3) attributed to different traffic sources from PMF and UNMIX model calculations: ECAT=Cumulative traffic, ECAG=Gasoline, ECAD=Diesel.

Location	8 Carbon fractions (PMF)			8-Carbon fractions (UNMIX)*	2-Carbon fractions (PMF)*	Literature Values (Ryan et al.(2007))[a]
	ECAD (Diesel)	ECAG(Gasoline)	ECAT	ECAT	ECAT	ECAT
Bridgeton	0.62±0.53	0.12±0.12	0.75±0.63	0.79±0.73	0.47±0.49	0.96
Cheviot	0.19±0.19	0.078±0.08	0.26±0.21	0.29±0.32	0.13±0.17	0.40
Montogomery1	0.22±0.23	0.07±0.07	0.28±0.25	0.45±0.39	0.12±0.14	0.28
Covington1	0.43±0.26	0.21±0.10	0.63±0.31	0.63±0.35	0.44±0.26	0.69
Norwood2	0.54±0.41	0.22±0.21	0.76±0.57	0.77±0.65	0.50±0.47	0.72
Montogomery2	0.35±0.26	0.09±0.05	0.44±0.31	0.47±0.31	0.25±0.22	0.38
Newport	0.54±0.11	0.06±0.04	0.60±0.15	0.80±0.53	0.32±0.12	0.58
Blueash	0.13±0.12	0.05±0.05	0.18±0.08	0.08±0.11	0.05±0.04	0.45
Green Hills	0.09±0.12	0.07±0.03	0.16±0.12	0.32±0.27	0.06±0.08	0.35
St. Bernard	1.22±1.00	0.45±0.77	1.66±1.71	0.87±0.77	1.09±1.23	1.02
Groesbeck	0.29±0.06	0.05±0.05	0.35±0.05	0.29±0.17	0.16±0.07	0.28
* Model results could not differentiate diesel and gasoline vehicle sources						
[a]Samples collected from December 2001-December 2004						
Sites of merging Interstates- St. Bernard and Bridgton, Covington1						
Sites within 400m of highway- Newport, Norwood2, Montogomery2, Blue Ash, Groesbeck						
Suburban beyond 400m of highway- Cheviot, Green Hills, Montogomery1						

accurately represent the EC values, it provides a comparison among different sites and relative impact of traffic sources at these sites. The estimated ECAT and ECAD values are listed in the Table 4 for various locations. ECAT values were high at sites closer to major truck routes, e.g., at St. Bernard and Bridgton (where I-74 merges with I-75),

Covington1 (close to merging point of I-71 and I-75), Newport (very close to I-471) and Norwood2 (400 m from SR-562). Lower ECAT and ECAD values were estimated at relatively clean suburban areas such as Blue Ash as well as Cheviot, Green Hills (suburbs, distant from highways), and Montogomery1 (clean area, further from I- 275). This finding confirms the association between ECAT values and relevant traffic sources. ECAT and ECAD values demonstrate that the inner city population is generally exposed to higher levels traffic emissions than the suburban population. Large variations in the ECAT and ECAD estimates were observed at sampling sites located in close proximity to major roads such as Norwood2 (400 m from SR-562), Montgomery 2 (within 400 m from I-71), Blue Ash (close to I-275), Newport (close to I-471) and St. Bernard (close to school bus depot, within 400 m from I-75). The ECAT findings from this study (i.e. combined ECAD and ECAG) are consistent with our previously reported ECAT values, which were estimated using only two carbon fractions (Ryan et al., 2007). This consistency is also related to generally the small contribution that gasoline, ECAG, makes to the ECAT values. The variations suggest that other factors such as traffic volumes and meteorological parameters are important apart from the proximity of the interstate highways (Hu, 2007). Less variation in ECAT values among suburban sites indicates that they were beyond the impact distance of traffic sources and least affected by variation in traffic pattern. Traffic source emissions and exposures depend also on vehicle operational mode and stop-and-go at specific locations (Shah et al., 2004).

C.6. Conclusions

The ambient $PM_{2.5}$ samples collected at CCAAPS monitoring sites over five years were analyzed for $PM_{2.5}$ mass, elemental and carbon (EC and OC) concentrations. Two

receptor models, UNMIX and PMF, were applied to $PM_{2.5}$ data consisting of two carbon fractions measured by NIOSH method and eight carbon fractions determined by IMPROVE method. Based on the source signatures, UNMIX identified only four major sources using both datasets. The source categories identified by UNMIX were combustion related sulfate, metal processing, traffic and soil/crustal. PMF identified six and seven sources by applying two and eight carbon fractions, respectively. Two sulfate sources were resolved, including a sulfate rich source and secondary sulfate source. One vegetation burning source was identified based on the high abundance of OC fractions. The application of PMF allowed to clearly differentiate PM emissions from diesel- and gasoline-powered vehicles using eight carbon fractions. Moreover, PMF could separate the combustion related source from the sulfate rich source which were merged in the UNMIX modeling. This study indicated that using eight carbon fractions can improve source identification and that the PMF model can extract more sources than UNMIX modeling. The difference in the two models, however, is less than one standard deviation. However, we acknowledge the limitation of modeling associated with a limited number of samples. Resolved sources from both models were compared and agreed reasonably well for the major sources identified. ECAT and ECAD values were estimated for different locations and found to vary depending on the proximity of highways as well as factors such as traffic counts, meteorology and operational mode of the vehicles. These markers of traffic-related air pollution will be utilized in land-use regression models to assess childhood exposure to particles arising from the combustion of diesel and gasoline.

C.7. References

Birch ME, Cary RA. Elemental carbon-based method for monitoring occupational exposures to particulate diesel exhaust. Aerosol Sci Technol 1996; 25: 221-241.

Cao JJ, Lee SC, Ho KF, Fung K, Chow CJ, Watson JG. Characterization of roadside fine particulate carbon and its eight fractions in Hongkong. Aerosol and Air Quality Research 2006; 6: 106-122.

Chow JC, Watson JG, Chen LWA, Arnott WP, Moosmuller H. Equivalence of elemental carbon by thermal/optical reflectance and transmittance with different temperature protocols. Environ Sci Technol 2004; 38: 4414-4422.

Chow JC, Watson JG, Chen LWA, Chang MCO, Robinson NF, Trimble D, et al. The IMPROVE-A temperature protocol for thermal/optical carbon analysis: maintaining consistency with a long-term database. J Air Waste Manage Assoc 2007; 57: 1014-1023.

Chow JC, Watson JG, Crow D, Lowenthal DH, Merrifield T. Comparison of IMPROVE and NIOSH carbon measurements. Aerosol Sci Technol 2001; 34: 23-34.

Chow JC, Watson JG, Pritchett LC, Pierson WR, Frazier CA, Purcell RG. The Dri Thermal optical reflectance carbon analysis system - description, evaluation and applications in United-States air-quality studies. Atmos Environ Part A 1993; 27: 1185-1201.

EPA US. Health assessment Document for Diesel Engine Exhaust, Prepared by by the National Center for Environmental Assessment Washington DC, for the Office of

Transportation and Air Quality. EPA/600/8-90/057F. Available: http://cfpub.epa.gov/ncea/cfm/recordisplay.cfm?deid=29060, Washington D.C 2002.

Gehrig R, Buchmann B. Characterising seasonal variations and spatial distribution of ambient PM10 and PM2.5 concentrations based on long-term Swiss monitoring data. Atmos Environ 2003; 37: 2571-2580.

Henry RC. Multivariate receptor modeling by N-dimensional edge detection. Chemom Intell Lab Syst 2003; 65: 179-189.

Hetland RB, Refsnes M, Cassee FR, Lag M, Dybing E, Schwarze PE. Cytokine release from alveolar macrophages exposed to ambient particulate matter: Relation to size, city, season and metal content. Toxicol Lett 2005; 158: S80-S81.

Hu S. Approaches to estimating exposure levels of diesel exhaust particles (DEP) in an urban airshed: Model development and applications. Department of Energy, Environmental and Chemical engineering. PhD Washington University in Saint Louis, Saint Louis, 2007.

Hu SH, McDonald R, Martuzevicius D, Biswas P, Grinshpun SA, Kelley A, et al. UNMIX modeling of ambient PM2.5 near an interstate highway in Cincinnati, OH, USA. Atmos Environ 2006; 40: S378-S395.

Jerrett M, Shankardas K, Berhane K, Gauderman WJ, Kunzli N, Avol E, et al. Traffic-related air pollution and asthma onset in children: A prospective cohort study with individual exposure measurement. Environ Health Perspect 2008; 116: 1433-1438.

Kim E, Hopke PK. Improving source identification of fine particles in a rural northeastern US area utilizing temperature-resolved carbon fractions. J Geophys Res Atmos 2004a; 109: D09204.

Kim E, Hopke PK. Source apportionment of fine particles in Washington, DC, utilizing temperature-resolved carbon fractions. J Air Waste Manage Assoc 2004b; 54: 773-785.

Kim E, Hopke PK, Edgerton ES. Improving source identification of Atlanta aerosol using temperature resolved carbon fractions in positive matrix factorization. Atmos Environ 2004; 38: 3349-3362.

Kim E, Hopke PK, Qin YJ. Estimation of organic carbon blank values and error structures of the speciation trends network data for source apportionment. J Air Waste Manage Assoc 2005; 55: 1190-1199.

Kreyling WG, Semmler M, Erbe F, Mayer P, Takenaka S, Schulz H, et al. Translocation of ultrafine insoluble iridium particles from lung epithelium to extrapulmonary organs is size dependent but very low. J Toxicol Environ Health Part A 2002; 65: 1513-1530.

Lee JH, Hopke PK, Turner JR. Source identification of airborne PM2.5 at the St. Louis-Midwest Supersite. J Geophys Res Atmos 2006; 111: D10s10.

Lewis CW, Norris GA, Conner TL, Henry RC. Source apportionment of phoenix PM2.5 aerosol with the Unmix receptor model. J Air Waste Manage Assoc 2003; 53: 325-338.

Liu W, Wang YH, Russell A, Edgerton ES. Enhanced source identification of southeast aerosols using temperature-resolved carbon fractions and gas phase components. Atmos Environ 2006; 40: S445-S466.

Lough GC, Schauer JJ, Park JS, Shafer MM, Deminter JT, Weinstein JP. Emissions of metals associated with motor vehicle roadways. Environ Sci Technol 2005; 39: 826-836.

Martuzevicius D, Grinshpun SA, Reponen T, Gorny RL, Shukla R, Lockey J, et al. Spatial and temporal variations of PM2.5 concentration and composition throughout an urban area with high freeway density - the Greater Cincinnati study. Atmos Environ 2004; 38: 1091-1105.

Maykut NN, Lewtas J, Kim E, Larson TV. Source apportionment of PM2.5 at an urban IMPROVE site in Seattle, Washington. Environ Sci Technol 2003; 37: 5135-5142.

Paatero P. Least squares formulation of robust non-negative factor analysis. Chemom Intell Lab Syst 1997; 37: 23-35.

Pandya RJ, Solomon G, Kinner A, Balmes JR. Diesel exhaust and asthma: Hypotheses and molecular mechanisms of action. Environ Health Perspect 2002; 110: 103-112.

Polissar AV, Hopke PK, Poirot RL. Atmospheric aerosol over Vermont: Chemical composition and sources. Environ Sci Technol 2001; 35: 4604-4621.

Reponen T, Grinshpun, SA., Trakumas S, Martuzevicius D, Wang Z, LeMasters G, Lockey JE, Biswas P. Concentration gradient patterns of aerosol particles near interstate highways in the Greater Cincinnati airshed. J Env Monit 2003; 5, 557–562.

Riedl M, Diaz-Sanchez D. Biology of diesel exhaust effects on respiratory function. J Allergy Clin Immunol 2005; 115: 221-228.

Ryan PH, Bernstein DI, Lockey J, Reponen T, Levin L, Grinshpun S, et al. Exposure to Traffic-related Particles and Endotoxin during Infancy Is Associated with Wheezing at Age 3 Years. Am J Respir Crit Care Med 2009; 180: 1068-1075.

Ryan PH, LeMasters GK, Biswas P, Levin L, Hu SH, Lindsey M, et al. A comparison of proximity and land use regression traffic exposure models and wheezing in infants. Environ Health Perspect 2007; 115: 278-284.

Ryan PH, LeMasters GK, Levin L, Burkle J, Biswas P, Hu SH, et al. A land-use regression model for estimating microenvironmental diesel exposure given multiple addresses from birth through childhood. Sci Total Environ 2008; 404: 139-147.

Schildcrout JS, Sheppard L, Lumley T, Slaughter JC, Koenig JQ, Shapiro GG. Ambient air pollution and asthma exacerbations in children: An eight-city analysis. Am J Epidemiol 2006; 164: 505-517.

Seagrave J, McDonald JD, Gigliotti AP, Nikula KJ, Seilkop SK, Gurevich M, et al. Mutagenicity and in vivo toxicity of combined particulate and semivolatile organic fractions of gasoline and diesel engine emissions. Toxicol Sci 2002; 70: 212-226.

Shah SD, Cocker DR, Miller JW, Norbeck JM. Emission rates of particulate matter and elemental and organic carbon from in-use diesel engines. Environ Sci Technol 2004; 38: 2544-2550.

Shi JP, Harrison RM, Brear F. Particle size distribution from a modern heavy duty diesel engine. Sci Total Environ 1999; 235: 305-317.

Sun QH, Wang AX, Jin XM, Natanzon A, Duquaine D, Brook RD, et al. Long-term air pollution exposure and acceleration of atherosclerosis and vascular inflammation in an animal model. J Am Med Assoc. 2005; 294: 3003-3010.

Sucharew H, Ryan PH, Bernstein DI, Succop P, Hershey, GKK, Lockey JE, et al 2010; Exposure to traffic exhaust and night cough during early childhood: the CCAAPS cohort. Pediatric Allergy and Immunology, 2010; 21:253-259.

Trenga CA, Sullivan JH, Schildcrout JS, Shepherd KP, Shapiro GG, Liu LJS, et al. Effect of particulate air, pollution on lung function in adult and pediatric subjects in a Seattle panel study. Chest 2006; 129: 1614-1622.

Watson JG, Chen LWA, Chow JC, Doraiswamy P, Lowenthal DH. Source apportionment: Findings from the US Supersites program. J Air Waste Manage Assoc 2008; 58: 265-288.

Watson JG, Chow JC, Lowenthal DH, Pritchett LC, Frazier CA, Neuroth GR, et al. Differences in the carbon composition of source profiles for diesel-powered and gasoline-powered vehicles. Atmos Environ 1994; 28: 2493-2505.

Wichmann HE. Diesel exhaust particles. Inhalation Toxicol 2007; 19: 241-244.

Appendix D:

Curriculum Vitae

Curriculum Vitae

Manoranjan Sahu
Email:msahu@wustl.edu
Ph: +1 (314) 458-1915

ACADEMIC QUALIFICATIONS

- **Ph.D** - Energy, Environmental and Chemical Engineering, 2011
  Washington University in St. Louis – Missouri, USA
  Advisor: Pratim Biswas

- **M.S.** - Energy, Environmental and Chemical Engineering, 2010
  Washington University in St. Louis – Missouri, USA

- **M.Tech.** - Environmental Science and Engineering, 2001
  Indian Institute of Technology (IIT) – Bombay, India

- **B.E.** - Civil Engineering, 1999
  Utkal University – Orissa, India

PROFESSIONAL EXPERIENCE

Scientific Officer, Bhabha Atomic Research Center, Mumbai, India, 2001-2006.

- Conducted field sampling, characterized atmospheric aerosols, and modeled source apportionment using different source apportionment modeling techniques
- Developed user friendly software based on dispersion modeling for prediction of ambient air pollutant concentration and heat load estimation
- Experienced in developing a regional scale atmospheric transport model for predicting of atmospheric aerosol concentration and dry and wet deposition
- Collaborated with 2 research teams and developed interface program for transport model and analyzed large datasets with statistical analysis
- Led 2 teams in conducting ambient field monitoring and advised 2 undergraduates for summer projects
- Coordinated regulatory inspection and periodic quality checks and developed safety guidelines and prepared reports
- Planned and organized safety training for a group of 25 people and performed in-house documentation of chemicals for Environmental Health and Safety (EH &S) compliance

TECHNICAL SKILLS

- **Ambient aerosol characterization techniques:** Personal Aerosol Monitor, Nanoparticle Surface Area Monitor, UCB $PM_{2.5}$ particle monitor, Cascade Impactor, High Volume Sampler, Differential Mobility Analyzer (DMA), Scanning Mobility Particle Sizer (SMPS)

- **Material synthesis techniques:** Flame Aerosol Reactor (FLAR), Furnace Aerosol Reactor (FUAR), Chemical Vapor Deposition (CVD)
- **Material characterization techniques:** Transmission Electron Microscopy (TEM), Scanning Electron Microscopy (SEM), Energy Dispersive X-ray (EDX), X-Ray Diffraction (XRD), Fourier Transform Infra Red spectroscopy (FT-IR), UV-Visible Spectroscopy (UV-vis), Differential Mobility Analyzer (DMA), Scanning Mobility Particle Sizer (SMPS), Dynamic Light Scattering (DLS), Zeta Potential, BET surface area
- **Analytical software packages:** SigmaPlot, MS Office, Origin, Surfer
- **Programming languages:** MATLAB, C, FORTRAN, Visual Basic

AWARDS/RECOGNITIONS

- McDonnell International Scholars Academy Fellowship, Washington University in St. Louis, USA, 2006-present
- Energy and Environmental Research Group Corporate Fellow, Washington University in St. Louis, 2006-present
- Best poster award, The Society of Toxicity Annual Meeting, Washington DC, USA, 2011.
- Student travel grant award, 29th AAAR conference, Portland, OR, 2010
- NSF student travel grant, 28th AAAR conference, Minneapolis, MN, 2009
- Ed. Edgerley scholarship from Washington University in St. Louis, USA, 2006
- Awarded a teaching assistantship during Masters at IIT, Bombay, 1999-2001
- Top rank in Civil Engineering at Utkal University, 1999

TEACHING EXPERIENCE

- Transport Phenomena in Biological Engineering (CHE 367), Washington University in St. Loui, Spring 2008
- Introduction to Environmental Engineering (CHE 262), Washington University in St. Louis, Fall 2008
- Aerosol Science and Engineering (ENV 518), Washington University in St. Louis, Fall 2009
- Methods of chemical analysis, Indian Institute of Technology (IIT) – Bombay, India, Fall 2000
- Conducted the examinations, help sessions, and graded assignments

PROFESSIONAL ACTIVITIES

- Member of American Association of Aerosol Research
- Served as a judge for poster session in AAAR 29th Annual Conference, Portland, OR, 2010
- Reviewed research articles in Journal of Atmospheric Environment and Environmental Science and Technology
- International student representative from School of Engineering and Applied Science to the Board of Trustees, Washington University in Saint Louis, 2007
- Coordinator in organizing Earth Day in Department of Energy, Environmental and Chemical Engineering, Washington University in St. Louis, 2008

- Served as a student assistant in AAAR 29th Annual Conference, Portland, OR, 2010
- Supervised 3 undergraduates and 3 high school students in research activity
- Teaching assistant experience for 4 courses in chemical and environmental engineering

JOURNAL PUBLICATIONS

1. Sahu, M and P. Biswas, *Concentration and Size Distribution of Nanoparticles in a Research Laboratory Working Environment with Nanomaterial Synthesis Reactors.* Journal of Nanoparticle Research, 2010, 12 (3): p 1055-1064.
2. Wu, B, R. Huang, M. Sahu, X. Feng, P. Biswas, and Y. J. Tang, *Bacterial Responses to Cu-doped TiO_2 Nanoparticles,* Science of the Total Environment, 2010, 408 (7): p 1755-1758.
3. Zeng, H, A. Singh, S. Basak, K. U. Ulrich, M. Sahu, P. Biswas, J. C. Catalano, and D. E. Giammar, *Nanoscale Size Effects on Uranium (VI) Adsorption to Hematite.* Environmental Science and Technology, 2009, 43 (5): p 1373-1378.
4. Suttiponparnit, K, J. Jiang, M. Sahu, S. Suvachittanont, T. Charinpanitku, and P. Biswas, *Role of Surface Area, Primary Particle Size, and Crystal Phase on Titanium Dioxide Nanoparticle Dispersion Properties*, Nanoscale Research Letters, 2011, 6 (27): p 1-8.
5. Kreyling, W. G, P. Biswas, M. E. Messing, N. Gibson, M. Geiser, A. Wenk, M. Sahu, K. Deppert, I. Cydzik, C. Wigge, O. Schmid, and M. Semmler-Behnke, *Generation and Characterization of Stable Highly Concentrated Titanium Dioxide Nanoparticle Aerosols for Rodent Inhalation Studies*, Journal of Nanoparticle Research, 2011, 13 (2):p 511-524.
6. Sahu, M, D. Peripert, V. Singhal, G. Yadama, and P. Biswas, *Evaluation of Mass and Surface Area Concentration of Particle Emissions And Development of Emissions Indices for Cookstoves in Rural India,* Environmental Science and Technology, 2011, 45 (6):p 2428-2434.
7. Sahu, M, S. Hu, P. Ryan, G. LeMasters, S. Grinshpun, J. Chow, and P. Biswas, *Chemical Compositions and Source Identification of $PM_{2.5}$ Aerosols for Estimation of a Diesel Source Surrogate,* Science of the Total Environment, 2011, 409 (13): p 2642-2651.
8. Sahu, M and P. Biswas, *Single-step Processing of Copper-doped Titania Nanomaterials in a Flame Aerosol Reactor*, Nanoscale Research Letters, 201, 6 (441): p 1-8.
9. Sahu, M, K. Suttiponparnit, S. Suvachittanont, T. Charinpanitku, and P. Biswas, *Characterization of Doped TiO_2 Nanoparticle Dispersions*, Chemical Engineering Science, 2011, 66 (15): p 3482-3490.
10. Wu, B W. Zhuang, M. Sahu, P. Biswas and Y. J. Tang, *Cu-doped TiO2 Nanoparticles Enhance Survival of Shewanella oneidensis MR-1 Under Ultraviolet Light (UV) Exposure*, Science of the Total Environment, 2011 (In press)
11. Sahu, M, B.Wu, L.Zhu, C.Jacobson, W. N. Wang, Y.Goyal, K. Jones, Y. J. Tang, and P. Biswas, *Role of dopant concentration, crystal phase, and particle size on microbial inactivation of Cu-doped TiO_2 nanomaterials,* Nanotechnology, 2011

12. Han, X, N. Corson, P. Wade-Mercer, R. Gelein, J. Jiang, M. Sahu, P. Biswas, J. N. Finkelstein, A. Elder, and G. Oberdörster, *The in-vivo Relevance of in-vitro Studies in Toxicological Evaluation of Nanoparticle*s, Toxicological Sciences, 2010 (Under review)
13. Seders, L. A, M. Sahu, P. Biswas, and J. B. Fein, *Experimental Study of TiO_2 Nanoparticle Adhesion to Silica and Fe(III) Oxide-coated Silica Surfaces.* Geochimica et Cosmochimica Acta, 2010 (Under review).
14. Sahu, M, J. Park, and P. Biswas, *In-Situ Charge Distribution Characterization of TiO_2 and Cu-doped TiO_2 Nanoparticles in a Flame Aerosol Reactor*, Journal of Nanoparticle Research (2011) (To be submitted).
15. Peripert, D, M. Sahu, G. Yadama, and P. Biswas, *Social Determinants of Exposure to Emissions from Household Cookstoves in India.* American Journal of Public Health, 2011(To be submitted).
16. Sahu, M, V.Singhal, J. Peipert, G.Yadama, and P. Biswas, *Aerosol Size Distribution and Surface Area Dose Characteristics from Cookstoves Emissions*, Aerosol Science and Technology, 2011 (To be Submitted)

CONFERENCE PRESENTATIONS AND PROCEEDINGS

1. Serke, B, N. Corson, P. Mercer, R. Gelein, M. Sahu, P. Biswas, G. Oberdörster and A. Elder, *Effects of Copper Doped Titanium Dioxide Nanoparticles In Vivo: Role of Soluble Metal,* The Society of Toxicity Annual Meeting, Washington DC, USA, 2011.
2. Sahu, M and P. Biswas, *Single-step Processing of Copper-doped Titania Nanomaterials in a Flame Aerosol Reactor*, International Aerosol Conference, Finland, 2010.
3. Sahu, M, B. Wu, L. Zhu, W. N. Wang, Y. J. Tang, and P. Biswas, *Role of Nanoparticle Chemical Composition and Particle Size on Toxicity of Cu-doped TiO_2 Nanomaterials in Environmental Microorganism,* AAAR 29th Annual Conference, Portland, USA, 2010.
4. Sahu, M, K. Suttiponparnit, S. Suvachittanont, T. Charinpanitkul, and P. Biswas, *Characterization of Doped TiO_2 Nanoparticle Dispersion: The Effect of Dopants*, AAAR 29th Annual Conference, Portland, USA, 2010.
5. Park, J, M. Sahu, and P. Biswas, *Characterization of In-Situ Charge Distribution of TiO_2 and Cu-Doped-TiO_2 Nanoparticles in a Flame Aerosol Reactor*, AAAR 29th Annual Conference, Portland, USA, 2010.
6. Wu, B, M. Sahu, C. Jacobson, P. Biswas, and Y. J. Tang, *Light-Dependent Antibacterial Properties of Cu-Doped TiO_2 Nanoparticles (NPs)*, AIChE, USA, 2010.
7. Seders, L. A, M. Sahu, P. Biswas, and J. B. Fein, *Experimental Study of TiO_2 Nanoparticle Adhesion to Silica and Fe(III) Oxide-coated Silica Surfaces*, Goldschmidt Conference, USA, 2010.
8. Sahu, M, B. Wu, Y. J. Tang, and P. Biswas, *Single-step Flame Aerosol Synthesis of Cu-doped TiO_2 Nanomaterials and Their Potential Toxicity*, AAAR 28th Annual Conference, Minnesota, USA, 2009.

9. Wu, B, R. Huang, M. Sahu, X. Feng, P. Biswas, and Y. J. Tang, *Assessment of Toxicity of Metal Oxide Nanoparticles to Microbial Species,* AIChE, USA, 2009.
10. Huang, R, B. Wu, M. Sahu, X. Feng, P. Wurm, H. Wynder, P. Biswas, and Y. J. Tang, *Enhanced Toxicity of Cu-doped TiO_2 Nanoparticles to Pathogenic and Environmental Microorganisms*, 1st Symposium on Nanotechnology for Public Health, Environment, and Energy, Washington University in St. Louis, 2009.
11. Sahu, M. *Energy Poverty in Rural Areas; A Challenge for New Development*, Global Leadership Vision of McDonnell International Scholars Academy, Washington University in Saint Louis, 2008.
12. Sahu, M, G. Yadama, J. Puppalla, and P. Biswas, *Personal Exposure Measurements from the Traditional Household and Commercial Scale Stoves in Rural Areas of Orissa, India*, AAAR 27th Annual Conference, Orlando, USA, 2008.
13. Peipert, J, M. Sahu, T. Severyn, E. Grimm, G. Yadama, P. Biswas, J. Puppala, R. Ravindranath, S. Pradhan, J. Topno, L. Nemali, V. Sethi, and R. S. Patil, *Adoption of Appropriate Household and Commercial Stove Technologies to Address Energy and Environmental Problems in Orissa and Andhra Pradesh, India,* McDonnell Academy Global Energy and Environmental Partnership (MAGEEP), 2008.
14. Sahu, M, D. Peipert, T. Severyn, E. Grimm, J. Puppala, R. Ravindranath, S. Pradhan, J. Topno, L. Nemali, V. Sethi, R. S. Patil, G. Yadama, and P. Biswas, *Exposure Measurements to Cooking Technology Emissions and Household Ecology in Orissa, Andhra Pradesh, & Karnataka, India,* Energy and Environment Conference, Hongkong, 2008.
15. Zeng, H, A. Singh, S. Basak, M. Sahu, P. Biswas, J. C. Catalano, and D. E. Giammar, *Nanoscale Size Effects on Uranium(VI) Adsorption and Surface Mediated Reduction on Hematite Nanoparticles*, The 236rd ACS National Meeting. Philadelphia, USA, 2008.
16. Kumar, A, J. Kayal, S. T. Manikandan, M. Sahu, S. Bhalke, R. Raghunath, B. Suseela, and R.M. Tripathi, *Elemental Composition and Source Apportionment of SPM, PM2.5-10, PM10, and PM2.5 in the Ambient Air of Anushaktinagar; A Residential Area in Mumbai, India,* 4th Asian Aerosol Conference, Mumbai, India, 2005.
17. Sahu, M, A. V. Kumar, R. M. Tripathi, S. Saundararajan, V. D. Puranik, and D. N. Sharma, *Software Package for Hazardous Risk Assessment of Toxic and Inflammable Storage Facilities*. In proceedings of XIII National Symposium on Environment, Shilong, India 377-382, 2004.